

**THE APPLICATION OF THE NUMERICAL WIND-WAVE MODEL SWAN TO  
A SELECTED FIELD CASE ON THE SOUTH AFRICAN COAST**

by

**A.J. VAN DER WESTHUYSEN**



**Thesis presented in partial fulfilment of the requirements for  
the degree of Master of Science in Civil Engineering  
at the University of Stellenbosch**

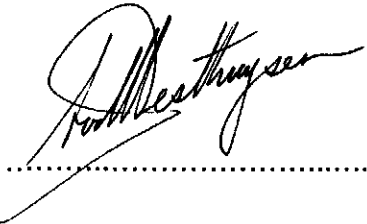
**Mr. D.E. BOSMAN  
Study leader**

**STELLENBOSCH**

**March 2002**

## DECLARATION

I, the undersigned, hereby declare that the work contained in this thesis is my own original work and that I have not previously in its entirety or in part submitted it at any other university for a degree.

Signature:  .....

Date: 25/01/2002 .....

## ABSTRACT

In this study the numerical short wave model SWAN is evaluated for application to a selected coastal region in South Africa. The aim of this study was to evaluate the degree of accuracy with which SWAN can simulate prototype nearshore wave spectra and wave parameters (e.g. wave height, mean wave direction and mean wave period) for an Algoa Bay field case. Algoa Bay represents a typical deep, sheltered embayment on the South African south coast, which is exposed to high-energy swell. Sensitivity analyses on various wave-related processes were also done, with the aim of establishing the dominant physical processes and appropriate model setup for the Algoa Bay field case. With the dominant wave-related processes and appropriate model setup for the Algoa Bay field case established, selected final runs were performed to determine the degree of accuracy with which SWAN can simulate prototype conditions, by comparing its results with available field recordings.

This study comprises a review of the SWAN evaluation work conducted to date by others, an overview of South African coastal conditions, and numerical model simulations. The model simulations, which represent the main focus of this study, were conducted for a selection of available offshore wave conditions (at 85 m water depth) observed during the Algoa Bay field case and were compared to available nearshore observations (at 17 m water depth). Environmental conditions of waves, wind and current were included in these simulations. The study focuses on model application and sensitivity analysis, rather than model development, and includes evaluation of all relevant processes, without focussing on any specific model aspect.

The results of this study show that SWAN simulations correlated well with observations at the nearshore station in Algoa Bay, both in wave spectral shape and its associated parameters. Dominant processes identified for the field case were depth-induced refraction, bottom friction and directional spreading. This finding agrees with those of previous evaluations of SWAN and previous modelling experience by others. It is shown that high-energy swell is relatively more sensitive to the choices of model setup than wind sea. Based on the simulation results of high-energy swell, it is concluded that the calculation of depth-induced refraction in SWAN seem to contain a degree of inaccuracy. It is also concluded that the findings of this study could be used as a guideline to SWAN modelling studies along the South African south coast.

## SAMEVATTING

In hierdie studie word die toepassingsmoontlikhede van die numeriese kortgolf model SWAN vir 'n geselekteerde gedeelte van die Suid-Afrikaanse kuslyn beoordeel. Die doel van hierdie studie is om die vlak van akkuraatheid waarmee SWAN prototipe golfspektra en golfparameters (bv. golfhoogte, gemiddelde golfrigting en gemiddelde golfperiode) in die vlakwater kan simuleer te beoordeel, vir 'n Algoabaai gevallestudie. Algoabaai verteenwoordig 'n tipiese diep, beskernde baai aan die Suid-Afrikaanse kuslyn, wat blootgestel is aan hoë-energie deining. Sensitiwiteitstoetse is ook uitgevoer vir verskillende golfprosesse, met die doel om die dominante fisiese prosesse en gepaste modelopstelling vir die Algoabaai gevallestudie te vind. Nadat die dominante golfprosesse geïdentifiseer is, en die toepaslike modelopstelling gevind is, is finale simulاسies uitgevoer vir geselekteerde gevalle om die mate van akkuraatheid te bepaal waarmee SWAN prototipe kondisies kan simuleer, deur simulاسie resultate met beskikbare veldmetings te vergelyk.

Hierdie studie bestaan uit 'n samevatting van die evaluasiewerk verrig op SWAN deur andere, 'n samevatting van golf-, wind- en stroomtoestande aan die Suid-Afrikaanse kus en numeriese modelsimulasies. Die modelsimulasies, wat die hoofokus van hierdie studie is, is uitgevoer vir 'n seleksie van beskikbare diepsee golftoestande (in 85 m waterdiepte) uit die Algoabaai gevallestudie en is vergelyk met beskikbare vlakwater metings (in 17 m waterdiepte). Omgewingstoestande van golwe, wind en seestrome is ingesluit in hierdie simulاسies. Die studie fokus op modeltoepassing en sensitiwiteits-analise, eerder as modelontwikkeling, en behels die beoordeeling van alle toepaslike modelprosesse, sonder om te fokus op enige spesifieke model aspek.

Die resultate van hierdie studie toon aan dat die SWAN simulاسies goed korrileer met vlakwater meetings in Algoabaai, vir beide golfspektraalvorm en verwante golfparameters. Bodemrefraksie, bodemwrywing en rigtingsspreiding is geïdentifiseer as dominante modelprosesse. Hierdie resultaat kom ooreen met bevindings van vroeëre beoordeling van SWAN en modelleer-ervaring deur andere. Dit word aangetoon dat hoë-energie deining relatief meer sensitief is vir modelopstelling as wind-see. Gebasseer op resultate van simulاسie met hoë-energie deining, word die gevolgtrekking gemaak dat die berekening van bodemrefraksie in SWAN 'n mate van onakkuraatheid toon. Die gevolgtrekking word ook gemaak dat die resultate van hierdie studie as riglyn gebruik kan word vir modelleerwerk met SWAN aan die Suid-Afrikaanse suidkus.

## ACKNOWLEDGEMENTS

I should like to express my gratitude towards a number of parties who contributed towards the successful completion of this thesis:

I should like to thank the National Ports Authority of South Africa (formerly Portnet) for their kind permission to use a collection of wave, wind and geotechnical recordings made at Algoa Bay. I should also like to thank Prof. Ian Young at the University of Adelaide, Roeland Ris, formerly at the Technical University of Delft, WL|Delft Hydraulics and the Dutch Ministry of Public Works and Coastal Management (RIKZ) for their permission to reproduce the figures included in the theory and literature sections of this thesis.

I should like to express my sincere gratitude towards IJsbrand Haagsma, Leo Holthuijsen and Prof. Jurjen Battjes at the Technical University of Delft for their technical and theoretical assistance during the preparation stages of this study.

I should like to thank Marius Rossouw, Louise Watt and Gregory Davids at the CSIR for their valuable assistance with the extraction and interpretation of wave and wind data, and for image processing. I should also like to thank Ian Hunter at the South African Weather Service for his assistance in the establishment of wind conditions over Algoa Bay for selected cases.

Lastly, I should like to thank my study leader, Eddie Bosman, for his thorough and diligent supervision of this work, and Annemarie for her patience and support.

## TABLE OF CONTENTS

	page
Abstract .....	i
Samevatting (Abstract in Afrikaans).....	ii
Acknowledgements.....	iii
Table of contents .....	iv
List of tables .....	viii
List of figures .....	ix
List of appendices.....	xiv
Nomenclature .....	xv
Definition of terms.....	xvii
<b>1 INTRODUCTION.....</b>	<b>1-1</b>
1.1 Problem statement.....	1-1
1.2 Existing work.....	1-1
1.3 Aims of study .....	1-2
1.4 Approach of study .....	1-3
1.5 Sources.....	1-4
1.6 Thesis overview .....	1-5
<b>2 THEORY .....</b>	<b>2-1</b>
2.1 Introduction .....	2-1
2.2 Background.....	2-1
2.2.1 Phase resolving and phase averaging formulations .....	2-1
2.2.2 Lagrangian and Eulerian descriptions .....	2-2
2.2.3 Model generations.....	2-2
2.3 The action balance equation .....	2-3
2.3.1 The concept of action balance .....	2-3
2.3.2 Source terms.....	2-4
2.3.3 Stationary and non-stationary simulation.....	2-10
<b>3 HISTORIC SWAN EVALUATION WORK .....</b>	<b>3-1</b>
3.1 Introduction .....	3-1
3.2 Summary of existing validation work .....	3-1
3.2.1 Academic cases .....	3-1
3.2.2 Laboratory cases.....	3-1
3.2.3 Field cases .....	3-2
3.3 Findings of historic evaluation work.....	3-4
3.3.1 Wave propagation.....	3-4
3.3.2 Fetch-limited wave growth.....	3-4
3.3.3 Depth-limited wave growth .....	3-5

3.3.4	Triad-wave interaction .....	3-5
3.3.5	Depth-induced breaking .....	3-6
3.3.6	Wave blocking .....	3-6
3.4	Recommended application of SWAN .....	3-6
3.4.1	Numerical aspects.....	3-7
3.4.2	Physical processes .....	3-7
3.5	Conclusion .....	3-8
<b>4</b>	<b>OVERVIEW OF WAVE CONDITIONS IN THE SOUTH AFRICAN COASTAL ZONE.....</b>	<b>4-1</b>
4.1	Introduction .....	4-1
4.2	Nearshore wind climate.....	4-1
4.2.1	Weather systems .....	4-1
4.2.2	Seasonal wind patterns.....	4-1
4.3	Offshore wave climate.....	4-3
4.3.1	Wave height and periodicity .....	4-3
4.3.2	Spectral shape .....	4-3
4.3.3	Directionality .....	4-4
4.4	Coastline and bathymetry.....	4-4
4.4.1	West coast.....	4-4
4.4.2	South coast.....	4-5
4.4.3	East coast .....	4-5
4.5	Coastal currents offshore, seaward of the breaker zone .....	4-6
4.5.1	East coast.....	4-6
4.5.2	South coast.....	4-6
4.5.3	South-west and west coasts.....	4-7
4.6	Discussion.....	4-8
4.7	Conclusion .....	4-8
<b>5</b>	<b>ALGOA BAY FIELD CASE: MODEL SET UP .....</b>	<b>5-1</b>
5.1	Introduction .....	5-1
5.2	Field case selection.....	5-1
5.3	Environmental conditions .....	5-2
5.3.1	Offshore wave measurements .....	5-2
5.3.2	Nearshore wave measurements.....	5-2
5.3.3	Wave measurement quality and correlation .....	5-3
5.3.4	Wind measurements .....	5-4
5.3.5	Current measurements .....	5-4
5.3.6	Bottom conditions.....	5-5
5.3.7	Selection of conditions for hindcasting .....	5-5
5.4	Computational grids and boundaries.....	5-7
5.4.1	Constraints to modelling choices.....	5-7

5.4.2	Criteria and method.....	5-7
5.4.3	Positioning of computational grids.....	5-8
5.4.4	Discussion.....	5-11
5.5	Discretization of the computational grid.....	5-12
5.5.1	Method.....	5-12
5.5.2	Results.....	5-13
5.5.3	Discussion.....	5-15
5.6	Conclusion .....	5-16
<b>6.</b>	<b>ALGOA BAY FIELD CASE: FIRST-ESTIMATE SIMULATIONS.....</b>	<b>6-1</b>
6.1	Introduction .....	6-1
6.2	Model setup.....	6-1
6.3	Simulations .....	6-3
6.3.1	Category A: Easterly wind seas.....	6-3
6.3.2	Category B: SSW swell with easterly wind seas.....	6-4
6.3.3	Category C: SSW swell.....	6-5
6.3.4	Category D: SSW swell with SW wind seas .....	6-6
6.4	Summary of results .....	6-8
6.4.1	Comparison of significant wave heights .....	6-9
6.4.2	Comparison of mean wave period.....	6-10
6.4.3	Comparison of mean wave direction .....	6-10
6.5	Conclusion .....	6-10
<b>7</b>	<b>ALGOA BAY: SENSITIVITY TESTS ON PHYSICAL PROCESSES.....</b>	<b>7-1</b>
7.1	Introduction .....	7-1
7.2	Test conditions.....	7-1
7.3	Scope of tests .....	7-1
7.4	Simulation runs .....	7-2
7.4.1	Depth-induced refraction in Algoa Bay .....	7-2
7.4.2	Energy dissipation due to bottom friction.....	7-5
7.4.3	Triad-wave interactions .....	7-9
7.4.4	Wave-current interaction.....	7-10
7.4.5	Directional spreading of waves.....	7-11
7.5	Summary of results .....	7-13
7.5.1	Summary of results for Case 9.....	7-15
7.5.2	Summary of results for Case 1.....	7-16
7.5.3	Summary of results for Case 4.....	7-16
7.6	Conclusion .....	7-17
<b>8</b>	<b>FINAL SIMULATIONS .....</b>	<b>8-1</b>
8.1	Introduction .....	8-1
8.2	SSW swell conditions.....	8-1



8.2.1	Test conditions and model setup.....	8-2
8.2.2	Simulation results.....	8-3
8.2.3	Discussion.....	8-5
8.3	ESE wind sea conditions.....	8-6
8.3.1	Test conditions and model setup.....	8-6
8.3.2	Method.....	8-7
8.3.3	Simulation results.....	8-8
8.3.4	Discussion.....	8-9
8.4	Conclusion.....	8-10
<b>9</b>	<b>RESULTS OF STUDY.....</b>	<b>9-1</b>
<b>10</b>	<b>CONCLUSIONS OF STUDY.....</b>	<b>10-1</b>
<b>11</b>	<b>RECOMMENDATIONS.....</b>	<b>11-1</b>
<b>12</b>	<b>REFERENCES.....</b>	<b>12-1</b>

## LIST OF TABLES

		page
Table 3.1	Recommended choices for computational grid discretization in SWAN.....	3-7
Table 3.2	Formulations of physical processes recommended in the SWAN manual for application of the model.....	3-8
Table 5.1	Collection of offshore wave boundary values for field case simulations.....	5-6
Table 5.2	Test cases for spatial and directional discretization tests.....	5-13
Table 5.3	Absolute errors for discretization of $\Delta x = \Delta y = 500$ m and $\Delta\theta = 10^\circ$ .....	5-15
Table 6.1	Model setup for first-estimate simulations.....	6-1
Table 6.2	Environmental conditions for first-estimate simulations.....	6-2
Table 6.3	Summary of first-estimate results for Algoa Bay field case .....	6-9
Table 6.4	Relative error of first-estimate results for Algoa Bay field case .....	6-9
Table 7.1	SWAN sensitivity tests for Algoa Bay field case.....	7-2
Table 7.2	Recommended (default) values of friction coefficients in SWAN (Holthuijsen <i>et al.</i> (1999)).....	7-6
Table 7.3	SWAN bottom friction sensitivity tests for Algoa Bay field case .....	7-7
Table 7.4	Results of sensitivity tests for Case 9 (21/04/99 at 21:00 UTC) .....	7-14
Table 7.5	Results of sensitivity tests for Case 1 (26/04/99 at 18:00 UTC) .....	7-14
Table 7.6	Results of sensitivity tests for Case 4 (case with wind) (08/04/99 at 18:00 UTC) .....	7-15
Table 7.7	Relative importance of physical processes to the nearshore results of the Algoa Bay field case .....	7-18
Table 7.8	Relative importance of physical processes on shelf seas and in the shoaling zone (excerpt) (Young, 1999, after Battjes, 1994*) .....	7-19
Table 8.1	Selection of offshore SSW swell conditions for the evaluation of proposed model setup .....	8-2
Table 8.2	Model setup for final simulation of SSW swell conditions.....	8-2
Table 8.3	Discretization of computational grids for final simulation of SSW conditions .....	8-3
Table 8.4	Simulation results for final simulation of SSW conditions.....	8-3
Table 8.5	Relative correlation error (with observations) for final simulation of SSW conditions .....	8-4
Table 8.6	Results at S4 station for wind-wave generation simulation of Case 1 .....	8-8

## LIST OF FIGURES

- Figure 1.1 Location of Algoa Bay study area
- Figure 2.1 Source terms for wind-wave generation ( $S_{in}$ ), (Young, 1999).
- Figure 2.2 Source terms for whitecapping ( $S_{bf}$ ) and bottom friction ( $S_{ds}$ ), (Young, 1999)
- Figure 2.3 Source term for quadruplet-wave interaction ( $S_{nl}$ ), (Young, 1999)
- Figure 3.1 SWAN validation laboratory cases: Wave blocking, triad-wave interaction and depth-induced breaking (Ris, 1997)
- Figure 3.2 SWAN validation laboratory cases: HISWA-tank (Ris, 1997)
- Figure 3.3 SWAN verification field cases for shallow bays: The Haringvliet (Ris, 1997), Petten and Kashimanada (Andorka Gal *et al.*, 1998)
- Figure 3.4 SWAN verification field cases: Nordermeyer Seegat and Friesche Zeegat (Ris, 1997)
- Figure 3.5 SWAN verification field cases: Westerschelde (WL|Delft Hydraulics, 2000)
- Figure 3.6 SWAN verification field cases: Mediterranean Sea (WL|Delft Hydraulics, 2000) and Duck (Rogers *et al.*, 2000)
- Figure 3.7 SWAN verification field cases: Lake George, Australia (Ris, 1997)
- Figure 4.1 Pressure and wind systems over Southern African oceans (Hurry and Van Heerden, 1982)
- Figure 4.2 Wind climate along the Southern African coast (Based on VOS data 1980 – 2000) (Rossouw, 2001)
- Figure 4.3 Wave climate along the South African coast (Rossouw, 2001)
- Figure 4.4 Contours of the Southern African seabed to 3 000 m depth (Data from: British Oceanographic Data Centre, 1997)
- Figure 4.5 Schematic trajectories of the two major Southern African ocean current system (Harris, 1978)
- Figure 4.6 Circulation patterns along the east coast of South Africa (Harris, 1978)
- Figure 4.7 Near-surface currents (with typical velocities) along west and south coast, based on ADCP data (Boyd *et al.*, 1992)
- Figure 5.1 Locations of wind and wave recording for Algoa Bay field case
- Figure 5.2 Directional wave spectra for typical ESE offshore condition
- Figure 5.3 Directional wave spectra for typical SSW offshore condition
- Figure 5.4 Directional wave spectra for typical SW offshore condition
- Figure 5.5 Test comparison between recordings of Waverider and S4, both deployed at inshore station at depth of –17 m CD

- Figure 5.6 Interpolated current pattern in Algoa Bay during November 1986 (after Goshen and Schumann, 1988)
- Figure 5.7 Seabed composition of Algoa Bay (Portnet, 2001)
- Figure 5.8(a) Polar plots of wave spectra selected for Algoa Case field case study
- Figure 5.8(b) Polar plots of wave spectra selected for Algoa Case field case study
- Figure 5.8(c) Polar plots of wave spectra selected for Algoa Case field case study
- Figure 5.9 Location of computational grid for ESE offshore direction
- Figure 5.10 Simulated and measured boundary values for Case 1 (ESE)
- Figure 5.11 Location of computational grid for SSW/SE offshore direction.
- Figure 5.12 Simulated and measured boundary values for Case 4 (SSW/SE)
- Figure 5.13 Location of computational grid for SSW offshore direction
- Figure 5.14 Simulated and measured boundary values for Case 5 (SSW)
- Figure 5.15 Simulated and measured boundary values for Case 7 (SSW/SW)
- Figure 5.16 Simulated and measured boundary values for Case 9 (SSW/SW)
- Figure 5.17 Case 4 (SSW/SE): Sensitivity tests for discretization in geographical space ( $\Delta x, \Delta y$ )
- Figure 5.18 Case 4 (SSW/SE): Sensitivity tests for discretization in directional space ( $\Delta\theta$ )
- Figure 5.19 Case 4 (SSW/SE): Sensitivity tests for total discretization ( $\Delta x = \Delta y, \Delta\theta$ )
- Figure 6.1 Case 1 (ESE): Spatial solution of significant wave height and mean direction
- Figure 6.2 Case 1 (ESE): Spectral solution of SWAN simulation at the nearshore (n/s) S4 station
- Figure 6.3 Case 2 (ESE): Spatial solution of significant wave height and mean wave direction
- Figure 6.4 Case 2 (ESE): Spectral solution of SWAN simulation at the nearshore (n/s) S4 station
- Figure 6.5 Case 3 (SSW/SE): Spatial solution of significant wave height and mean wave direction
- Figure 6.6 Case 3 (SSW/SE): Spectral solution of SWAN simulation at the nearshore (n/s) S4 station
- Figure 6.7 Case 4 (SSW/SE): Spatial solution of significant wave height and mean wave direction
- Figure 6.8 Case 4 (SSW/SE): Spectral solution of SWAN simulation at the nearshore (n/s) S4 station
- Figure 6.9 Case 5 (SSW): Spatial solution of significant wave height and mean direction
- Figure 6.10 Case 5 (SSW): Spectral solution of SWAN simulation at the nearshore (n/s) S4 station
- Figure 6.11 Case 6 (SSW/SW): Spatial solution of significant wave height and mean wave direction

- Figure 6.12 Case 6 (SSW/SW): Spectral solution of SWAN simulation at the nearshore (n/s) S4 station
- Figure 6.13 Case 7 (SSW/SW): Spatial solution of significant wave height and mean wave direction
- Figure 6.14 Case 7 (SSW/SW): Spectral solution of SWAN simulation at the nearshore (n/s) S4 station
- Figure 6.15 Case 8 (SSW/SW): Spatial solution of significant wave height and mean wave direction
- Figure 6.16 Case 8 (SSW/SW): Spectral solution of SWAN simulation at the nearshore (n/s) S4 station
- Figure 6.17 Case 9 (SSW/SW): Spatial solution of significant wave height and mean wave direction
- Figure 6.18 Case 9 (SSW/SW): Spectral solution of SWAN simulation at the nearshore (n/s) S4 station
- Figure 6.19(a) Correlation between simulated and observed  $H_{m0}$  and  $T_{m01}$
- Figure 6.19(b) Correlation between simulated and observed mean wave direction
- 
- Figure 7.1 Case 9 (SSW/SW): Absolute change in mean direction due to depth-induced refraction
- Figure 7.2 Case 9 (SSW/SW): Change in significant wave height due to depth-induced refraction
- Figure 7.3 Case 9 (SSW/SW): Spectral solution at nearshore S4 station, with and without depth-induced refraction
- Figure 7.4 Case 1 (ESE): Absolute change in mean wave direction due to depth-induced refraction
- Figure 7.5 Case 1 (ESE): Change in significant wave height due to depth-induced refraction
- Figure 7.6 Case 1 (ESE): Spectral solution at nearshore S4 station, with and without depth-induced refraction
- Figure 7.7 Case 4 (SSW/SE): Absolute change in mean wave direction due to depth-induced refraction
- Figure 7.8 Case 4 (SSW/SE): Change in significant wave height due to depth-induced refraction
- Figure 7.9 Case 4 (SSW/SE): Spectral solution at nearshore S4 station, with and without depth-induced refraction
- Figure 7.10 Case 1 (SSW/SW): Change in significant wave height due to bottom friction
- Figure 7.11 Case 9 (SSW/SW): Spectral solution at nearshore S4 station, for simulations with various friction formulations
- Figure 7.12 Case 1 (ESE): Change in significant wave height due to bottom friction
- Figure 7.13 Case (ESE): Spectral solution at nearshore S4 station, for simulations with various friction formulations

- Figure 7.14 Case 4 (SSW/SW): Change in significant wave height due to bottom friction
- Figure 7.15 Case 4 (SSW/SE): Spectral solution at nearshore S4 station, for simulations with various friction formulations
- Figure 7.16 Case 9 (SSW/SW): Change in mean wave period due to triad-wave interaction
- Figure 7.17 Case 9 (SSW/SW): Spectral solution at nearshore S4 station, for simulation with and without triad-wave interactions
- Figure 7.18 Case 1 (ESE): Change in mean wave period due to triad-wave interaction
- Figure 7.19 Case 1 (ESE): Spectral solution at nearshore S4 station, for simulation with and without triad-wave interactions
- Figure 7.20 Case 4 (SSW/SW): Change in mean wave period due to triad-wave interactions
- Figure 7.21 Case 4 (SSW/SE): Spectral solution at nearshore S4 station, for simulation with and without triad-wave interactions
- Figure 7.22 Case 9 (SSW/SW): Change in mean absolute wave period due to current
- Figure 7.23 Case 9 (SSW/SW): Change in mean wave direction due to current.
- Figure 7.24 Case 9 (SSW/SW): Change in significant wave height due to change of directional spreading to 10° standard deviation
- Figure 7.25 Case 9 (SSW/SW): Change in significant wave height due to change of directional spreading of 30° standard deviation
- Figure 7.26 Case 9 (SSW/SW): Spectral solution at nearshore S4 station, with directional spreading imposed at 10° standard deviation
- Figure 7.27 Case 9 (SSW/SW): Spectral solution at nearshore S4 station, with directional spreading imposed at 30° standard deviation
- Figure 7.28 Case 9 (SSW/SW): Correlation between simulated and observed  $H_{m0}$ ,  $T_{m01}$  and mean wave direction
- Figure 7.29 Case 1 (ESE): Correlation between simulated and observed  $H_{m0}$ ,  $T_{m01}$  and mean wave direction
- Figure 7.30 Case 4 (SSW/SE): Correlation between simulated and observed  $H_{m0}$ ,  $T_{m01}$  and mean wave direction
- Figure 8.1 Location of nested computational grid for simulation of SSW swell conditions
- Figure 8.2 Case 5 (SSW): Spectral solution at nearshore S4 station, for simulation with bottom friction of Madsen *et al.* (1988) and a nested grid
- Figure 8.3 Case 6 (SSW/SW): Spectral solution at nearshore S4 station, for simulation with bottom friction of Madsen *et al.* (1988) and a nested grid
- Figure 8.4 Case 8 (SSW/SW): Spectral solution at nearshore S4 station, for simulation with bottom friction of Madsen *et al.* (1988) and a nested grid

- Figure 8.5 Case 9 (SSW/SW): Spectral solution at nearshore S4 station, for simulation with bottom friction of Madsen *et al.* (1988) and a nested grid
- Figure 8.6 Wind measurements at Jahleel Island: Hourly averages, 1999/04/22 to 1999/04/27
- Figure 8.7 Synoptic weather chart of 1999/04/26 at 12:00 UTC (SA Weather Bureau, 1999)
- Figure 8.8 Case 1 (ESE): Development of the recorded offshore wave condition of 04/26/99 at 18:00 UTC (at Waverider)
- Figure 8.9 Case 1 (ESE): Development of the recorded nearshore wave condition of 04/26/99 at 18:00 UTC (at S4)
- Figure 8.10 Case 1 (ESE): Spatial wind distribution for stationary simulation with wind
- Figure 8.11 Case 1 (ESE): Spatial solution of significant wave height and mean wave direction for stationary simulation with wind
- Figure 8.12 Case 1 (ESE): Stationary wind-wave generation over extended Algoa Bay bathymetry – spectra at Waverider
- Figure 8.13 Case 1 (ESE): Stationary wind-wave generation over extended Algoa Bay bathymetry – spectra at S4
- Figure 8.14(a) Correlation between simulated and observed  $H_{m0}$ , and  $T_{m01}$ , for original and nested simulations
- Figure 8.14(b) Correlation between simulated and observed mean wave direction for original and nested simulations

**Figures in Appendices:**

- Figure A.1 The Eulerian representation of the energy balance equation
- Figure B.1(a) Wave data time series for offshore Waverider and inshore S4: January 1999
- Figure B.1(b) Wave data time series for offshore Waverider and inshore S4: February 1999
- Figure B.1(c) Wave data time series for offshore Waverider and inshore S4: March 1999
- Figure B.1(d) Wave data time series for offshore Waverider and inshore S4: April 1999
- Figure B.1(e) Wave data time series for offshore Waverider and inshore S4: May 1999
- Figure B.2(a) Wind measurements at Jahleel Island: 28/02/99 to 04/03/99
- Figure B.2(b) Wind measurements at Jahleel Island: 04/04/99 to 08/04/99
- Figure B.2(c) Wind measurements at Jahleel Island: 14/04/99 to 23/04/99
- Figure B.2(d) Wind measurements at Jahleel Island: 22/04/99 to 27/04/99
- Figure B.2(e) Wind measurements at Jahleel Island: 09/05/99 to 13/05/99

## **LIST OF APPENDICES**

**APPENDIX A** – Derivation of the energy balance equation on a regular grid

**APPENDIX B** – Time-series recordings waves and wind at Algoa Bay



## NOMENCLATURE

### *Symbols*

$C_f$	constant in friction formulation of Collins (1972)
$C_{JON}$	constant in friction formulation of Hasselmann <i>et al.</i> (1973)
$\lambda, C_{nl4}$	coefficients for the DIA approximation (see <i>Acronyms</i> below) of quadruplet-wave interactions
$C_{sh1}, C_{sh2}, C_{sh3}$	coefficients for the DIA approximation (see <i>Acronyms</i> below) of quadruplet-wave interactions
Dir	mean wave direction (see <i>Definition of terms</i> )
Dir <sub>p</sub>	wave direction of the peak spectral component (see <i>Definition of terms</i> )
$E$	spectral energy density
$H_{mo}$	characteristic wave height (sometimes referred to as significant wave height, $H_s$ ) calculated in the frequency domain (see <i>Definition of terms</i> )
$H_s^{x\%}$	significant wave height that is statistically exceeded $x$ percent of the time
$K_N$	constant in friction formulation of Madsen <i>et al.</i> (1988)
$N$	spectral action density
$S$	source term which represents all effects of generation and dissipation
$S_{in}$	source term for the generation of wave energy by wind
$S_{ds}$	source term for the dissipation of wave energy due to whitecapping, bottom friction and depth-induced wave breaking
$S_{nl}$	source term for the transfer of wave energy due to nonlinear wave-wave interactions
$T_{m01}$	mean absolute (first-moment) wave period (see <i>Definition of terms</i> )
$T_p$	peak absolute wave period (see <i>Definition of terms</i> )
$U_z$	wind speed at elevation $z$
$\underline{U}$	current velocity vector
$U_{rms}$	root mean squared wave-induced orbital velocity at the bottom
$c_x, c_y$	$x, y$ components of the group velocity corrected for propagation on a current with velocity $\underline{U}$
$c_\theta$	angular velocity of direction change
$c_\sigma$	propagation velocity in frequency space
$d$	water depth
$k$	wave number of spectral component
$k_p$	peak wave number in wave spectrum

$k.d$	dimensionless relative depth parameter
$f$	relative (intrinsic) wave frequency
$f_p$	peak relative (intrinsic) wave frequency
$x, y, t$	dimensions of space and time
$\alpha_{BJ}$	coefficient for the wave breaking model of Battjes and Jansen (1978)
$\gamma_{BJ}$	breaking parameter in the wave breaking model of Battjes and Jansen (1978)
$\alpha_{EB}$	coefficient for the LTA (see <i>Acronyms</i> below) approximation of triad-wave interactions
$\gamma$	peak enhancement factor for the JONSWAP wave spectrum
$\omega$	absolute radian wave frequency
$\theta$	mean wave direction
$\sigma$	relative (intrinsic) radian wave frequency
$\sigma_\theta$	directional spreading width (standard deviation)
$\Gamma$	friction coefficient
$\Gamma_{KJ}$	steepness-dependent coefficient for the whitecapping formulation of the WAMDI group (1988)
$C_{ds}, \delta, p$	coefficients of the whitecapping formulation of the WAMDI group (1988)

### *Acronyms*

CD	Chart Datum – level of the sea surface at mean spring low tide
DIA	Discrete Interaction Approximation for quadruplet-wave interactions
JONSWAP	Joint North Sea Wave Project
LTA	Lumped Triad Approximation for triad-wave interactions
MSL	land survey datum level
SADCO	Southern African Data Centre for Oceanography
SAST	South African standard time
SWAN	Simulating WAVes Nearshore
UT	Universal Time (= Greenwich Mean Time)
VOS	Voluntary Observing Ships
n/s	nearshore

## DEFINITION OF TERMS

### Wind, wave and current direction convention

Wind and wave directions indicate the directions *from which* the wind blows and *from which* the waves come. Current directions indicate the direction *into which* the current flows. The direction convention is *clockwise* from North = 0° = 360°. According to this convention, the direction range starts from North (0°) and increases over 90° (East), 180° (South) and 270° (West) back to 360° = 0° (North).

### Characteristic wave height

Characteristic wave height (sometimes referred to as significant wave height) refers to the significant height of combined sea and swell derived from the energy density spectrum.

Per definition:

$$H_{m0} = 4\sqrt{m_0}$$

where  $m_0$  is the zero<sup>th</sup> moment of the energy density spectrum  $E(\sigma, \theta)$ , defined as:

$$m_0 = \int E(\sigma, \theta) d\sigma d\theta$$

### Mean wave direction

The mean wave direction, which is the direction normal to the wave crests, is calculated from the energy density spectrum as defined in Kuik *et al.* (1988):

$$\text{Mean direction} = \arctan \left[ \frac{\int \sin(\theta) E(\sigma, \theta) d\sigma d\theta}{\int \cos(\theta) E(\sigma, \theta) d\sigma d\theta} \right]$$

### Peak wave direction

The peak wave direction is defined as the direction associated with the peak spectral frequency of  $E(\sigma, \theta)$ .

### Directional spreading width

The directional spreading width is the one-sided directional width (standard deviation) of the wave spectrum, defined as (based on Kuik *et al.*, 1988):

$$\sigma_{\theta}^2 = 2 \cdot \left( \frac{180}{\pi} \right)^2 \cdot \left( 1 - \left[ \left\{ \int \sin(\theta) \cdot \frac{\int E(\sigma, \theta) d\sigma}{\int E(\sigma) d\sigma} d\theta \right\}^2 + \left\{ \int \cos(\theta) \cdot \frac{\int E(\sigma, \theta) d\sigma}{\int E(\sigma) d\sigma} d\theta \right\}^2 \right]^{\frac{1}{2}} \right)$$

where  $\sigma_{\theta}$  = directional spreading width

### Mean absolute wave period

The mean absolute wave period considered in this study is defined as:

$$T_{m01} = 2\pi \cdot \left( \frac{\iint \omega \cdot E(\sigma, \theta) d\sigma d\theta}{\iint E(\sigma, \theta) d\sigma d\theta} \right)^{-1}$$

where  $\omega$  is the absolute radian frequency, determined by the Doppler-shifted dispersion relation:  $\omega = \sigma + \underline{k} \cdot \underline{U}$ , where  $\sigma$  is the intrinsic radian frequency,  $\underline{k}$  is the wave number vector and  $\underline{U}$  is the current vector.

### Peak absolute wave period

The peak absolute wave period is obtained as the inverse of the spectral peak frequency  $\omega$  resolved from the energy density spectrum. The standard Fast Fourier Transform (FFT) spectral analysis performed on the Waverider wave records (of approximately 17 minutes) enables the peak frequency to be resolved with a frequency resolution of 0,00977 Hz.

## **Wave Blocking**

Wave blocking is defined as follows (Ris, 1997): For waves propagating against stationary ambient current with a spatially increasing velocity, the intrinsic frequency increases, which, in turn, decreases the relative propagation speed of the wave in geographic space (group velocity relative to the current). If, at some location, the relative propagation speed has reduced to that of the opposing current velocity, the wave component is blocked. At this blocking point, the wave component is reflected and its wave energy ceases to propagate forward, and starts to travel down-current.

## **Recti-linear and curvi-linear grids**

Conventionally, numerical models feature propagation schemes which have been formulated on recti-linear grids (i.e., comprising of a grid of even-sized rectangles) in geographical space. The SWAN Cycle 2 model provides the option of using a curvi-linear grid for which the propagation scheme in geographical space has been formulated on a user-defined, irregular grid, comprising quadrangular elements. The advantage of a curvi-linear grid over a recti-linear grid is that the sizes of the quadrangular grid elements can be tailored to fit the contours of complex coastal areas, and can be decreased in areas where detail calculation is required. The use of a curvi-linear grid, therefore, removes the need for grid nesting.



# 1 INTRODUCTION

## 1.1 PROBLEM STATEMENT

In the South African coastal zone, as with coastal zones worldwide, there is an ongoing interest in obtaining dependable estimates of the nearshore wave field. In the South African context, the applications of knowledge of the nearshore wave field range from the compilation of wave climates for the design of coastal structures, morphology studies for shoreline management and offshore mining, to wave information for port operations. South Africa's 2 800 km long coastline is steep-sloped and mostly unsheltered, and is, therefore, vulnerable to wave attack. Wave conditions along the South African coastline are severe: locally generated seas incident on the coastline are supplemented by large swells, originating from around the 40° S parallel. These conditions, therefore, lead to bi-modal wave fields, with a large component of high-energy swell.

The recently-developed spectral wave model for nearshore application SWAN (Ris, 1997) has the potential of serving as a tool for obtaining accurate estimates of nearshore wave field along the South African coastline. However, the suitability and accuracy of the SWAN model for application to South African conditions have not yet been established. In terms of South African conditions, a central aspect of SWAN that requires verification is the ability of the model to simulate high-energy swell and bi-modal spectra comprising high-energy swell and seas, at sheltered inshore locations, such as those found along the South African south coasts. A second aspect that requires attention is the sensitivity of the model's performance to choices of model formulation (processes and associated coefficients), and climatic conditions (e.g. wind and currents) for South African cases. The purpose of this study is to investigate the application of SWAN to a single, typical South African field case to contribute towards the solution of the above-mentioned issues.

## 1.2 EXISTING WORK

Extensive testing has accompanied the development of SWAN (e.g. Ris, 1997 and Ris *et al.*, 1999 and WL|Delft Hydraulics, 2000). The testing has comprised comparison of model performance with linear analytical solutions, laboratory cases (termed *validation*), and with field cases (*verification*). The field cases considered in these verification tests can be classified into categories of: (a) shallow bays, (b) inter-tidal or estuarine areas and (c) open water cases. The majority of these cases dealt with North Sea situations, with environmental conditions comprising low-period wind sea

conditions with only a few conditions featuring low energy swell. Field cases included the effects of wind and tidal currents on the wave field.

Therefore, although comprehensive model evaluation exists, the testing conditions considered to date differ significantly from typical South African conditions. Therefore, the existing validation work does not provide a definite indication of how SWAN would perform for conditions along the South African coast, and a specific investigation was considered justified.

### **1.3 AIMS OF STUDY**

The overall purpose of this study was to assess the performance of the SWAN model under typical South African environmental and bathymetrical conditions. This assessment comprised a literature study and a field case study of the typical South African coastal area of Algoa Bay (Figure 1.1). The aim of the literature study was to summarize the SWAN verification work and its findings to date, to present the model developers' recommended application of SWAN, and to compare South African conditions to those considered in the SWAN verification work to date.

The field case study had two overall aims, namely the assessment of basic model performance and model sensitivity. For the former, basic model performance was evaluated, using the model developers' recommended model setup, as found in Holthuijsen *et al.* (1999). This aim comprised investigation of the following:

- a) the degree of accuracy with which SWAN could simulate nearshore wave conditions (in terms of parameters of height, period and direction) successfully in an area which is sheltered from high-energy swell by a large headland.
- b) the degree of accuracy with which SWAN could reproduce the nearshore directional wave spectra in a sheltered, deep bay accurately (i.e. whether performance under the latter condition is better than found in verification tests in shallow bays (e.g. Ris, 1997)).
- c) the degree of accuracy with which SWAN could reproduce the bi-modal, bi-directional spectra inshore, which is often found in South African field cases adequately.

The second aim of the field case study is to assess the sensitivity of model setup in application to the field case of Algoa Bay. The aspects investigated in this regard were:



- a) to identify the relative importance of the physical processes modelled by SWAN (with respect to the nearshore solution) found in the field case. The processes evaluated were: depth-induced refraction, bottom friction, triad-wave interaction, wave-current interaction, wind-wave generation and directional spreading.
- b) to assess the sensitivity of results to the choice of formulations and associated coefficients for bottom friction.
- c) to compare the findings of the investigations under (a) and (b) above with those previously found for SWAN, and also to findings on coastal wave modelling in general (Young, 1999, after Battjes, 1994).

The scope of the model evaluation described above is limited in the following ways: Firstly, the model simulations were only conducted in the stationary (time-independent) mode of SWAN. Secondly, the investigation was only conducted for the third-generation formulations in SWAN. Thirdly, model formulations were applied as they appear, without alterations to the internal coding of SWAN. Also, the coefficients of formulations for triad-wave and quadruplet-wave interactions (see Section 2) were not altered. Lastly, this study was conducted for SWAN Cycle 2 Version 40.01, which is the predecessor of the current SWAN Cycle 3 Version 40.11 (released September 2000). The latter version features improvements to the numerical scheme in geographical space (2<sup>nd</sup> order propagation scheme instead of 1<sup>st</sup> order scheme), and the adoption of spherical co-ordinates instead of (projected) geographical grid co-ordinates. These alterations had the aim of improving the numerical accuracy of SWAN over larger geographical areas. Therefore, the overall accuracy of the simulation results of this study may improve by using SWAN Cycle 3 Version 40.11. References made to SWAN in this thesis will imply version 40.01 unless otherwise indicated.

#### **1.4 APPROACH OF STUDY**

The methodology of this study is two-fold. The first component of the study is a literature survey, in which existing validation and verification work on SWAN was compiled. Conclusions were drawn from the conditions for which SWAN has been evaluated to date, and findings from the literature were summarized.

The second component of the study is the field case investigation. This part of the study takes the form of a sensitivity analysis. Environmental conditions were hindcast, using SWAN for a selection of nine representative offshore wave conditions recorded at the site of the selected field case. These simulation solutions were subsequently

compared to field recordings, and conclusions on model performance drawn. Sensitivity tests were undertaken, by conducting repeat simulations using various processes, and comparing results with field recordings. The results of these tests were used to draw conclusions on the sensitivity of SWAN's formulations and coefficients, for the particular field case.

## 1.5 SOURCES

The sources relating to this study are divided into three groups: firstly the literature on the theory of SWAN and related validation and verification work, secondly the literature on conditions in the South African coastal zone, and lastly the data relating to the South African field case investigated.

The primary sources used for the theoretical description of SWAN were the thesis on the model development by Ris (1997), the SWAN user manual by Holthuijsen *et al.* (1999) and textbooks on wind-wave theory by Young (1999) and Holthuijsen (2000). In addition, a number of supporting publications, relating to specific theoretical aspects, were consulted. The primary sources used for the compilation of the existing SWAN validation and verification work was Ris (1997) and the collection of validation work presented in WL|Delft Hydraulics (2000). In addition, publications containing the individual field case tests, as compiled in WL|Delft Hydraulics (2000) and otherwise, were consulted. Of this group of sources, not all references were available to the author. Therefore, in cases where unconsulted sources are referred to, the reference concerned is accompanied by an (\*).

The primary sources of bathymetrical and climatic conditions of the South African coastal zone were the following: For bathymetrical information, the South African Naval charts (SA Hydrographical Office, 1972-1996) were used. For the compilation of wind and weather conditions along the South African coast, data of Voluntary Observing Ships (VOS) from the database of the Southern African Data Centre for Oceanography (SADCO) were used. The latter dataset was supplemented with in-situ wave measurements around the South African coast, as compiled by Rossouw (2001). For information on currents, the sources were Harris (1978) and Boyd *et al.* (1992).

Data for the execution of the field case simulations were obtained from existing in-situ measurements. These measurements comprised: bathymetric and geotechnical surveys, time-series recordings of directional wave spectra at offshore and nearshore locations and time-series of wind measurements. These measurements were conducted by, or on behalf of, the National Ports Authority of South Africa (formerly Portnet). Measurements of near-surface current fields were taken from the literature (Goschen and Schumann, 1988).

## **1.6 THESIS OVERVIEW**

The contents of this thesis is the following: Sections 2 to 4 comprise the literature study component of this study. In Section 2 the theoretical aspects of the SWAN model, which are relevant to this study, are presented. In Section 3 a summary is given of the collection of validation and verification work that has been conducted on SWAN to date. The test conditions of this historic work are classified and findings summarized. Present recommendations for model application, as given by the model developers, are summarized. In Section 4 the conditions in the South African coastal zone, in terms of wind conditions, wave conditions, coastline and bathymetry and surface-currents are summarized, and contrasted with the conditions for which SWAN has been evaluated previously.

Sections 5 to 8 comprise the field case study component of this thesis. In Section 5 the selection of the field case of Algoa Bay is motivated, and a discription is given of the environmental data used as model input. Section 6 describes the first-estimate simulations, using the default model setup for SWAN, which was conducted for the Algoa Bay field case. A description of the sensitivity testing for physical processes which was conducted for the Algoa Bay field case is given in Section 7. Using these tests as basis, dominant physical processes for the field case are identified, and compared to findings of historic SWAN evaluation. A recommended model setup for conditions at Algoa Bay is presented. Section 8 describes the final field case simulations, by which the recommended model setup is verified. Sections 9 and 10 present, respectively, the general findings of the study, and conclusions regarding the suitability of SWAN as a modelling tool for South African conditions. Section 11 closes with recommendations on nearshore modelling studies for South African situations, further study needs along the South African coast and suggestions for model development.



## 2 THEORY

### 2.1 INTRODUCTION

The aim of this section is to provide a theoretical description of the SWAN model (Cycle 2, Version 40.01). This description identifies the application field of SWAN, the relative sophistication of the model, and its underlying theory. The following sources were used in the compilation of the description in this section Holthuijsen (2000), Holthuijsen *et al.* (1999), Ris (1997) and Young (1999).

### 2.2 BACKGROUND

#### 2.2.1 Phase resolving and phase averaging formulations

A basic classification of short wave models is into the categories of phase resolving and phase averaging formulations. These respective formulations have distinctive characteristics and, as a result, different application fields. These formulations and their applications are described below.

In *phase resolving formulations* the phase of each wave component in the wave field is retained and the displacement of the sea surface is resolved. This formulation is required where properties of the wave field vary rapidly in geographical space. Formulations that fall in this category are either linear, such as the mild slope equation (Berkhoff, 1972) or the parabolic mild slope equation (Radder, 1979), or nonlinear, such as the Hamiltonian formulation (e.g. Miles, 1981\*) or the Boussinesq formulation (e.g. Perigrene, 1966\*). Due to the fact that the wave phase is retained in these formulations, phase-dependent phenomena such as diffraction can be modelled. In addition, the nonlinear phase-resolving formulations implicitly model nonlinear processes. Due to the great computational effort (high spatial resolution) required for phase resolution, these methods are presently confined to application to relatively small areas such as harbours or around structures.

*Phase averaging formulations* describe the irregular sea surface with a spectral energy density function, and do not resolve actual sea surface displacements. Such a description is valid where wave properties vary slowly over propagation space. The phase averaging formulation takes linear wave theory as basis, and due to the spectral representation, neglects the phase of each of the spectral components. Due to the fact that energy flux is modelled and not wave profiles, a lower computation effort (spatial resolution) is required in such models. Therefore, phase averaging models are

formulated to solve wave generation and propagation over large geographical areas, such as a portion of an ocean or in a bay.

### **2.2.2 Lagrangian and Eulerian descriptions**

Limiting the discussion to phase averaging formulation, a first classification of wave models can be made in terms of basic description: The first is the Lagrangian ('wave ray') description, where wave energy propagation is described along wave rays, with change in direction in response to the bathymetry and to currents. The second is the Eulerian ('grid model') description, where the balance of wave energy is evaluated at fixed observation points on a computational grid covering the modelled area. Both classes of models may be applied to either a single frequency and directional component, or to a complete frequency and/or directional spectrum. Eulerian models has advantages over Lagrangian models in terms of the smoothness of the numerical solution – eliminating the chaotic wave ray patterns regularly found in Lagrangian solutions as well as providing the possibility of incorporating nonlinear interaction between the components of the spectrum. As a result, the development of phase averaging short wave models has favoured the Eulerian description on a regular, or curvi-linear grid.

### **2.2.3 Model generations**

A second general classification for phase averaging wave models is in terms of the formulation of the generation and transformation of the wave spectrum in the model. The classification is chiefly concerned with the presence and nature of formulations for nonlinear quadruplet wave-wave interactions (see Section 2.3.2.6.1). First-generation models lack explicit formulations for nonlinear interactions and only utilize a limit shape to spectral growth, which is usually the Pierson-Moskowitz (Pierson and Moskowitz, 1964) spectrum with a standard directional distribution. In second-generation models nonlinear interactions are parameterised, with or without using a limit spectrum shape. Where a limit spectrum is not used, the assumption is made that the nonlinear interactions are strong enough to force the spectrum into a JONSWAP (Hasselmann *et al.*, 1973) shape. Unsatisfactory performance of second-generation models under extreme wind conditions (e.g. rapidly changing wind direction) led to the development of third-generation models. In third-generation models the nonlinear interaction formulations are incorporated explicitly in the action balance equation, which is then solved without any *a priori* restrictions on the spectrum.

In terms of the classification presented above, SWAN Cycle 2 Version 40.01 can be described as a third-generation, phase-averaging, Eulerian spectral wave model for nearshore application. The theoretical formulation of SWAN is presented in the sections below.

## 2.3 THE ACTION BALANCE EQUATION

The central theoretical formulation incorporated in SWAN is the energy (or action) balance equation. This formulation is supplemented by a number of source terms for generation and dissipation of wave energy. The aim of this section is to provide an overview description of the energy balance equation and its source terms, as implemented in SWAN.

### 2.3.1 The concept of action balance

In SWAN, the evolution of the wave spectrum is described by an Eulerian formulation of the balance of wave energy density. For the purpose of the description of this formulation, spectral wave energy density is considered in its most complete form, namely as variable over time and space:

$$E = E(\sigma, \theta ; x, y, t) \quad (2.1)$$

where:  $E$  = spectral energy density  
 $\sigma$  = relative radian wave frequency  
 $\theta$  = wave direction  
 $x, y, t$  = dimensions of space and time

In the Eulerian energy balance approach, the balance of wave energy is considered in a large number of predefined cells in a grid (Figure A.1, Appendix A). The balance of energy prescribes that within every grid cell of size  $\Delta x \Delta y$ , and over a time interval  $\Delta t$ :

*'Change of Energy = Net Import of Energy + Net Local Generation'*

The application of this principle (see Appendix A) leads to the following expression, valid for every frequency component in the spectrum, which is known as the energy balance equation, for deep water:

$$\frac{\partial}{\partial t} E + \frac{\partial}{\partial x} (c_x E) + \frac{\partial}{\partial y} (c_y E) = S(\sigma, \theta ; x, y, t) \quad (2.2)$$

where:  $c_x, c_y = \underline{c}_g + \underline{U}$  = x,y components of the group velocity corrected for propagation on a current with velocity  $\underline{U}$   
 $S(\sigma, \theta ; x, y, t)$  = source term which represents all effects of generation and dissipation

If the energy balance equation is applied to shallow coastal regions and for ambient currents, three additions to (2.2) are required. Firstly, due to bottom- or current refraction, the direction in which energy propagates changes as it moves over geographical space. In analogy to energy flux in  $x,y$  space, the flux in  $\theta$ -space is accounted for by a term  $\frac{\partial}{\partial \theta}(c_\theta E)$ , where  $c_\theta$  is the angular velocity of direction change due to refraction (based on linear wave theory), for each frequency component. Secondly, the effects of the shifting of the relative frequency due to variations in depth and currents are accounted for by the term  $\frac{\partial}{\partial \sigma}(c_\sigma E)$ , with  $c_\sigma$  being the associated propagation velocity in frequency space. A last adaption is the introduction of action density,  $N(\sigma, \theta ; x, y, t) = E(\sigma, \theta ; x, y, t) / \sigma$ . This substitution is made because in the presence of currents only action is conserved, and not energy. Incorporating these additions yields the spectral action balance equation for shallow water, as is implemented in SWAN:

$$\frac{\partial}{\partial t} N + \frac{\partial}{\partial x}(c_x N) + \frac{\partial}{\partial y}(c_y N) + \frac{\partial}{\partial \sigma}(c_\sigma N) + \frac{\partial}{\partial \theta}(c_\theta N) = \frac{S(\sigma, \theta ; x, y, t)}{\sigma} \quad (2.3)$$

### 2.3.2 Source terms

$S(\sigma, \theta ; x, y, t)$  in equation (2.3) is a source term, which has the effect of changing the level of spectral energy density for which the left-hand side of the balance equation is solved.  $S(\sigma, \theta ; x, y, t)$  is the sum of a number of source terms, each representing processes which influence the shape and/or magnitude of the wave spectrum:

$$S(\sigma, \theta) = S_{in}(\sigma, \theta) + S_{ds}(\sigma, \theta) + S_{nl}(\sigma, \theta) \quad (2.4)$$

The source term  $S_{in}(\sigma, \theta)$  represents the generation of wave energy by wind. The term  $S_{ds}(\sigma, \theta)$  represents dissipation of wave energy due to whitecapping, bottom friction and depth-induced wave breaking. The last term,  $S_{nl}(\sigma, \theta)$ , represents the transfer of wave energy due to nonlinear wave-wave interactions. Each of these source terms are described in more detail below.

#### 2.3.2.1 Input by wind ( $S_{in}$ )

The transformation of the kinetic energy of a wind field into water wave energy is modelled by means of the source term  $S_{in}$ . Two mechanisms of wave energy



generation, namely the linear growth mechanism due to Phillips (1957) and the exponential growth mechanism due to Miles (1957) are included in the source term  $S_{in}$  for SWAN. The linear growth mechanism is considered to be dominant in the earliest stages of wave generation, but is overtaken by the exponential growth mechanism as the sea-state grows. The source term is expressed in the following manner:

$$S_{in}(\sigma, \theta) = A + B.E(\sigma, \theta) \quad (2.5)$$

where  $A$  represents the linear growth term and  $B$  the exponential growth term.

The formulation used for the term  $A$  is that of Cavaleri and Malanotte-Rizzoli (1981). For the exponential growth term  $B$  both the formulations of Komen *et al.* (1984) and Janssen (1989, 1991) are available in SWAN. The generation of wave energy takes into account the influence of following or opposing current on the effective fetch length of generation.

Figure 2.1(a) shows the shape of the integrated one-dimensional atmospheric input term  $S_{in}(f) = \int S_{in}(f, \theta) d\theta$  using a relationship similar to that of Komen *et al.* (1984). The term has been evaluated for a JONSWAP spectrum with a peak enhancement factor  $\gamma = 3,3$  and a range of wind speeds. The relationship between wave generation and wind speed is clear, as well as the concentration of growth at the peak spectral frequency for moderate to high wind forcing. Figure 2.1(b) compares the relative magnitudes of the integrated linear and exponential source terms, based on respectively Phillips (1957) and Miles (1957) formulations. Here the source terms have been integrated over direction ( $S_{in}(f) = \int S_{in}(f, \theta) d\theta$ ), and is shown for a wind speed  $U_{10} = 10$  m/s and a JONSWAP spectrum with a peak enhancement factor  $\gamma = 3,3$ . In Figure 2.1(b) it can be seen that the exponential growth term dominates at moderate and high wind speeds.

### 2.3.2.2 Dissipation of wave energy

Three processes of wave energy dissipation are included in SWAN, namely whitecapping, bottom friction and depth-induced wave breaking. These three mechanisms are included in the source term  $S_{ds}(\sigma, \theta)$  in the following manner:

$$S_{ds}(\sigma, \theta) = S_{ds,w}(\sigma, \theta) + S_{ds,b}(\sigma, \theta) + S_{ds,br}(\sigma, \theta) \quad (2.6)$$

where:  $S_{ds,w}(\sigma, \theta)$  = white-cap dissipation

$$\begin{aligned}
S_{ds,b}(\sigma, \theta) &= \text{bottom friction dissipation} \\
S_{ds,br}(\sigma, \theta) &= \text{depth-induced breaking dissipation}
\end{aligned}$$

### 2.3.2.3 Whitecapping

The source term for whitecapping dissipation accounts for the loss of energy due to deep water wave breaking. In theoretical formulations, this energy loss is assumed to be proportional to wave steepness. The source term used in SWAN is based on the model of Hasselmann (1974), as adapted by the WAMDI group (1988):

$$S_{ds,w}(\sigma, \theta) = -\Gamma_{KJ} \tilde{\sigma} \frac{k}{\tilde{k}} E(\sigma, \theta) \quad (2.7)$$

where:  $k$  = wave number of spectral component  
 $\tilde{\sigma}, \tilde{k}$  = mean frequency and wave number, respectively

The quantity  $\Gamma_{KJ}$  is a steepness-dependent coefficient, defined by the WAMDI group (1988):

$$\Gamma_{KJ} = C_{ds} \cdot \left( (1-\delta) + \delta \cdot \frac{k}{\tilde{k}} \right) \left( \frac{\tilde{s}}{\tilde{s}_{PM}} \right)^p \quad (2.8)$$

where  $\tilde{s}$  is the overall wave steepness =  $\tilde{k} \sqrt{E_{tot}}$   
 $\tilde{s}_{PM}$  is the steepness value of the Pierson-Moskowitz spectrum  
 $C_{ds}, \delta$  and  $p$  are tunable coefficients

The values of the tunable coefficients  $C_{ds}, \delta$  and  $p$  are obtained by closing the energy balance of waves in fully developed conditions, for the wind input formulation ( $S_{in}$ ) used. Therefore, for the purposes of this study, these tunable coefficients of  $\Gamma_{KJ}$  will be considered as fixed for its corresponding wind input formulations.

In Figure 2.2(a) the whitecapping formulation (2.7) is evaluated for a mean JONSWAP spectrum ( $f_p = 0,3$  Hz,  $\gamma = 3,3$ ) for a range of depths. Two aspects emerge from this figure: firstly, whitecap dissipation is the largest at the peak spectral frequency (0,3 s), and secondly, the dependance of whitecap dissipation on relative depth ( $k_p \cdot d$ ). As

waves enter nearshore regions and shoal (decreasing relative depth), they become steeper and whitecapping increases.

#### 2.3.2.4 Bottom friction

When waves move over areas of finite depth (relative depth  $k.d < \pi$ ), the drag between orbital water motion and the seabed results in energy loss. The energy loss per spectral energy component is dependent on the relative depth (represented by  $k.d$ ), intrinsic wave frequency, spectral energy level and bed roughness. The source term for bottom friction is expressed in the following generic form (Holthuijsen *et al.*, 1999):

$$S_{ds,b}(\sigma, \theta) = -\Gamma \cdot \frac{\sigma^2}{g^2 \sinh^2(k.d)} \cdot E(\sigma, \theta) \quad (2.9)$$

with  $\Gamma$  = bottom friction coefficient  
 $k.d$  = dimensionless depth parameter

The friction coefficient  $\Gamma$  has been formulated in a number of ways, and is the tunable parameter in this formulation. Three approaches to the formulation of  $\Gamma$  are available in SWAN, namely:

- a) Madsen *et al.* (1988): Calculation of  $\Gamma$  by means of an eddy-viscosity (mobile bed) model, taking into account a bottom roughness length scale ( $K_N$ ) and variable values of the near-bottom excursion amplitude and orbital velocity ( $U_{rms}$ ) based on the actual wave conditions. The bottom roughness scale  $K_N$  is the tunable constant of the calculation.
- b) Collins (1972): Simplification by assuming that  $\Gamma = C_f \cdot g \cdot U_{rms}$ , where  $C_f$  is a tunable constant.
- c) Hasselmann *et al.* (1973): Simplification by taking the entire coefficient  $\Gamma$  as constant =  $C_{JON}$ .

Figure 2.2(b) shows the integrated source term of Hasselmann *et al.* (1973) evaluated for a JONSWAP spectrum with  $f_p = 0,3$  Hz and  $\gamma = 3,3$  for a range of relative depths ( $k_p \cdot d$ ) values. It can be seen that dissipation is the largest at the spectral peak, and increases for decreasing values relative depth.

### 2.3.2.5 Depth-induced breaking

When waves propagate into shallow water they shoal, and as a result, gradually increase in steepness. As the depth decreases into very shallow water, a point is reached where the wave steepness cannot be supported and the wave breaks. In the surf zone (extremely shallow water) breaking becomes dominant over all other processes. Breaking is incorporated in SWAN through the formulation of Battjes and Janssen (1978), as adapted for a wave spectrum by Eldeberky and Battjes (1996\*). Led by experimental findings, the latter formulation calculates dissipation proportional to energy density:

$$S_{ds,br}(\sigma, \theta) = \frac{D_{tot}}{E_{tot}} E(\sigma, \theta) \quad (2.10)$$

where  $D_{tot}$  is the total energy dissipation given by Battjes and Janssen (1978):

$$D_{tot} = -\frac{1}{4} \alpha_{RJ} Q_b \left( \frac{\tilde{\sigma}}{2\pi} \right) H_m^2 \quad (2.11)$$

where  $\alpha_{RJ}$  is a tunable coefficient,  $\tilde{\sigma}$  is the mean (first moment) spectral frequency, and  $Q_b$  the portion of broken waves determined by means of the Rayleigh distribution, in the expression:

$$\frac{1 - Q_b}{\ln Q_b} = -8 \frac{E_{tot}}{H_m^2} \quad (2.12)$$

in which  $H_m$  is the maximum wave height that can exist at a given depth ( $d$ ), given by  $H_m = \gamma_{RJ} \cdot d$ . The coefficient  $\gamma_{RJ}$  is known as the *breaking parameter*, and relates the highest unbroken wave that can exist at a given depth.

### 2.3.2.6 Nonlinear wave-wave interactions

Resonant sets of wave components exchange energy resulting in the distribution of wave energy over the energy density spectrum. In deep water, SWAN models this energy transfer by means of four-wave (or *quadruplet*) interactions and in shallow water by means of three-wave (or *triad*) interactions. These nonlinear interactions are incorporated in SWAN through the source term  $S_{nl}(\sigma, \theta)$ , and are discussed below.

### 2.3.2.6.1 Quadruplet-wave interactions

Quadruplet-wave interaction is the main contributor to the evolution of the wave spectrum in deep water. By quadruplet interaction energy is transferred from the peak frequency to lower frequencies, and partially to higher frequencies. This process is particularly important during situations of wind-wave generation. Quadruplet interactions have the effect of stabilising the spectral shape and determining its directional spreading.

The exact formulation of quadruplet interactions is given by the Boltzmann integral (e.g. Hasselmann, 1962\*, 1963(a)\* and 1963(b)\*) but is computationally intensive to solve and is, as a result, not applied. However, an approximation, the Discrete Interaction Approximation (DIA) derived by Hasselmann *et al.* (1985), is implemented in SWAN. This formulation is computationally more efficient, but still captures the key elements of the exact formulation. The DIA is governed by five coefficients, namely  $\lambda$ ,  $C_{nl4}$ ,  $C_{sh1}$ ,  $C_{sh2}$ , and  $C_{sh3}$  (see Holthuijsen *et al.*, 1999)

Figure 2.3 shows the form of the Boltzmann integral, which is directly related to  $S_{nl}(\sigma, \theta)$ . The expression shown has been integrated over direction and is evaluated for a JONSWAP spectrum with  $f_p = 0,3$  Hz and  $\gamma = 3,3$ . The source term has a characteristic plus-minus-plus shape which allows for the shifting of energy from the peak frequency to lower and higher frequencies. A second point of note is the effect of the relative depth ( $k.d$ ) on the shape and magnitude of the interactions. In shallow waters the amount of interaction is much greater than in deep water, and the transfer to higher frequencies grows in proportion to that of transfer to lower frequencies. To incorporate the enhanced shallow-water quadruplet interaction in SWAN, the transfer rates for each spectral component are scaled with a depth-dependent scaling factor.

### 2.3.2.6.2 Triad-wave Interactions

Triad-wave interaction is of minor importance in deep water, but can be significant in the shoaling zone. During triad-interactions, sub- and super-harmonics are generated through resonant non-linear interactions between frequency components. These interactions have the effect of transforming a single peaked spectrum into a multi-peaked spectrum. These resonant interactions are only possible in very shallow water where waves are non-dispersive. In intermediate water, where waves are weakly dispersive, non-resonant or bound interactions are found, the amplitudes of which remain small.

In SWAN, an approximation of the triad-interaction mechanism, namely the Lumped Triad Approximation (LTA) of Eldeberky (1996), is applied. The LTA uses a single

tunable proportionality coefficient,  $\alpha_{EB}$ , (see Holthuisen *et al.*, 1999). With this formulation, the development of super-harmonics is modelled (sub-harmonic development is not considered).

### 2.3.3 Stationary and non-stationary simulation

The complete action balance equation incorporated in SWAN has been given in Section 2.3.1 as the following:

$$\frac{\partial}{\partial t} N + \frac{\partial}{\partial x} (c_x N) + \frac{\partial}{\partial y} (c_y N) + \frac{\partial}{\partial \sigma} (c_\sigma N) + \frac{\partial}{\partial \theta} (c_\theta N) = \frac{S(\sigma, \theta ; x, y, t)}{\sigma} \quad (2.3)$$

If (2.3) is implemented as it appears above, using boundary conditions and/or source terms which vary in time, then SWAN is operated in a *non-stationary* or time-dependent mode. Conversely, if the all boundary conditions and all source terms are constant in time, equation (2.3) simplifies to:

$$\frac{\partial}{\partial x} (c_x N) + \frac{\partial}{\partial y} (c_y N) + \frac{\partial}{\partial \sigma} (c_\sigma N) + \frac{\partial}{\partial \theta} (c_\theta N) = \frac{S(\sigma, \theta ; x, y)}{\sigma} \quad (2.13)$$

Simulations in which conditions are considered to be independent of time, and effectively use (2.13), are termed *stationary* simulations. Stationary simulation is considered appropriate in cases where boundary wave conditions and source term forcings vary slowly relative to the propagation time of waves inside the computational area.

## **3 HISTORIC SWAN EVALUATION WORK**

### **3.1 INTRODUCTION**

This section gives an overview of the SWAN validation and verification work that has been undertaken to date by others, as found in literature. The aim of this section is to give an overview of the conditions tested in these studies and the corresponding findings. The present section is concluded with a summary of the recommended application of SWAN, as provided by the model developers. The primary sources for this section is Ris (1997) and WL|Delft Hydraulics (2000).

### **3.2 SUMMARY OF EXISTING VALIDATION WORK**

A substantial amount of validation and verification work has accompanied the ongoing development of SWAN to its present state. Initial model testing was conducted by Ris (1997) during the inception of the model. This testing comprised comparison of model performance with academic cases, laboratory cases (termed *validation*), and with field cases (*verification*). Subsequently, a number of additional field case studies were undertaken. These included additional testing based on the original case studies (e.g. Holthuijsen *et al.*, 1998 and Holthuijsen *et al.*, 2000), as well as additional field cases (e.g. Andorka Gal *et al.*, 1998 and Rogers *et al.*, 2000). A selection of these case studies, plus some additional work, have been compiled in WL|Delft Hydraulics (2000).

The conditions and phenomena for which SWAN has been evaluated to date are summarized below under the headings of academic cases, laboratory cases and field cases.

#### **3.2.1 Academic cases**

Academic cases were modelled to validate the ability of SWAN to reproduce the following analytically solvable phenomena or processes: (a) depth-induced refraction and shoaling, (b) current-induced refraction and shoaling, (c) refraction, shoaling and set-up on curvi-linear grids and (d) the numerical behaviour of SWAN (diffusiveness).

#### **3.2.2 Laboratory cases**

Laboratory cases were modelled to verify the ability of SWAN to reproduce the results found in a selection of experiments for shallow water processes. These experiments are (original experiment cited in brackets): depth-induced breaking of random waves (Battjes and Janssen, 1978, see Fig. 3.1(a)), (b) triad interaction of random wave

spectra over a shoal (Beji and Battjes, 1993, Fig. 3.1(b)), (c) wave induced set-up, (d) current-induced wave blocking (Lai *et al.* 1989\*, see Fig 3.1(c)), (e) transformation of the wave spectrum over a submerged bar with current, in the so-called 'HISWA-tank' (Dingemans *et al.*, 1987, Fig. 3.2) and (f) wave propagation around a barrier island using regular and curvi-linear grids (Holthuijsen *et al.*, 1993).

### 3.2.3 Field cases

The field cases completed for SWAN to date are summarized in terms of their bathymetry types and environmental conditions.

#### 3.2.3.1 Bathymetry types

Field cases considered to date can be classified into three basic bathymetry types, namely shallow bay areas, restricted inter-tidal areas and open-water cases. These are summarized below:

The three cases with *shallow bays* where: *The Haringvliet* (e.g. Ris, 1997 and Holthuijsen *et al.*, 1998) shown in Figure 3.3(a), a shallow bay area (depths 6 to 4 m) with a large shoal of minimum depth of 2 m, covering an area of 10 x 10 km<sup>2</sup>. *Petten* (Andorka Gal *et al.*, 1998) shown in Figure 3.3(b), a shallow, parallel beach (depths of 22,0 – 4,2 m) on the North Sea coast with numerous shoals, covering a cross-shore distance of 8,3 km. *Kashimanada* (Andorka Gal *et al.*, 1998) shown in Figure 3.3(c), a shallow beach (depths 5,4 to 0,5 m) on the Pacific coast, covering a cross-shore distance of 300 km.

Three cases of *inter-tidal or estuarine areas* were tested: *Norderneyer Seegat* (Ris, 1997) with total area 20 x 25 km<sup>2</sup>, shown in Figure 3.4(a) and *Frieche Zeegat* (Ris, 1997), with total area 25 x 15 km<sup>2</sup>, shown in Figure 3.4(b). These two cases feature tidal gaps between barrier islands (depths <15 m), with shoals and channels. *Westerschelde* (WL|Delft Hydraulics, 2000, after Andorka Gal and Roelse, 1997\* and Kamsteeg *et al.*, 1998\*) shown in Figure 3.5(a) and (b) – an estuary with a long, narrow tidal area (depths < 15 m), with an area of 60 x 10 km<sup>2</sup>.

Five studies with *open-water areas* have been published. Three of these studies focused on deepwater areas and two on shallow areas. The cases with deep water areas are: *Idealized wave growth* (Ris, 1997) - deep water 'basin' for evaluating computed wave growth against measurements. *Mediterranean Sea* (WL|Delft Hydraulics, 2000, after Holthuijsen *et al.*, 1996) shown in Figure 3.6(a) – large body of open water (depths > 1 000 m), with area of 3 700 x 1 800 km<sup>2</sup>. *Duck* (Rogers *et al.*, 2000) shown in Figure 3.6(b) - open shelf area with depths > 100 m to shore, with an area of 300 x 520 km<sup>2</sup>. The two cases with depth-limited areas are: *Idealized wave*



*growth* (Ris, 1997) - depth-limited 'basin' for evaluation of calculated wave growth against measurements. *Lake George* (Ris, 1997) (Fig. 3.7) – a shallow lake (depths < 2 m) with flat bottom, with area of 20 x 10 km<sup>2</sup>.

### 3.2.3.2 Purpose of tests

The purpose of the field cases conducted are linked to the bathymetry types used. Therefore, similar classifications as those used above are used for the description of test aims:

The purpose of the *shallow bay* cases were to model wind-wave generation in shallow water of variable depth and with shoals. Wave propagation and transformation were evaluated, with respect to refraction, triad-wave interactions, depth-induced breaking and bottom friction.

The purpose of cases with *inter-tidal or estuarine areas* was to evaluate wind-wave generation, depth-induced refraction, triad-wave interactions, wave-current interaction and depth-induced breaking in shallow, complex bathymetry with islands, shoals and channels.

The purpose of the cases with *open-water areas* was to evaluate stationary and non-stationary generation of wind-waves in deep and shallow water. The aspects evaluated were quadruplet-wave interactions, whitecapping (with and without the presence of swell), bottom friction and depth-induced breaking.

### 3.2.3.3 Environmental conditions

The environmental conditions for which the field case testing have been conducted were taken from measurements at the respective sites (mostly of extreme nature). The test conditions are discussed below, under the headings of wave conditions, wind conditions and currents:

The *wave conditions* for the collection of field cases were both single-peaked and multi-peaked spectra. The cases of the Haringvliet, Norderneyer Seegat, Friesche Zeegat and Petten represented single-peaked spectra of peak periods within the range of  $T_p = 7-10$  s, with mostly significant storm events modelled. For the cases of Duck, Kashimanada and Westerschelde, multi-peaked spectra were modelled. For these cases the swell component varied from fairly low periods ( $T_p = 8$  s) to fairly high periods ( $T_p = 15$  s, for Kashimanada). However, swell energy was low relative to that of the wind sea for all cases considered.

*Wind conditions* covered a wide range of values, from relatively low ( $U_{10} = 11,5$  m/s for Friesche Zeegat) to very high ( $U_{10} = 19,1$  m/s for Petten,  $U_{10} = 28$  m/s for Westerschelde). Current flows were found for the cases of inter-tidal or estuarine areas, and had velocities of up to 1 m/s (e.g. Friesche Zeegat).

### **3.3 FINDINGS OF HISTORIC EVALUATION WORK**

The findings of the SWAN validation and verification tests to date are summarized below. The majority of findings are those of Ris (1997), based on the original release of SWAN (Version 30.51). Between this release and the version under investigation in the present study (Version 40.01), a number of improvements have been made (see Holthuijsen *et al.*, (1999)). Therefore, only the findings still valid for Version 40.01 are reproduced. Findings from other sources than Ris (1997) are given with a reference.

#### **3.3.1 Wave propagation**

Simulation of idealized conditions showed excellent agreement between analytical solutions and simulations of depth-induced refraction, shoaling and wave-current interaction. First order upwind numerical scheme (in geographical space) was found to be diffusive. As a result, it was recommended that the distance over which wave propagation is modelled in SWAN Version 40.01 should be limited to 25 km.

The results of the field cases of the Haringvliet, Nordemeyer Seegat and Friesche Zeegat, showed that over quite complex bathymetry wave conditions were reasonably modelled in terms of significant wave height and mean direction. In shallow regions, currents were found to have a significant influence on wave height, mean period and direction in these case studies. For example, at station 5 in the Friesche Zeegat field case, differences between simulation results and observations in significant wave height of 33 percent, in mean wave period of up to 53 percent and in mean wave direction of 10 degrees were found if the following current of about 60 cm/s was neglected.

#### **3.3.2 Fetch-limited wave growth**

In idealized wave growth simulations, which include quadruplet-wave interaction, the formulations of Komen *et al.* (1984) gave generally good agreement with measurements of total energy and wave period. However, over very short fetches, it was found that wave energy was significantly over-estimated and peak frequency under-estimated. This over-estimation was ascribed to the linear growth term  $A$  (Section 2.3.2.1). The implemented formulations of Janssen (1989\*, 1991) significantly

over-estimated wave energy over short fetches and under-estimated energy over large fetches.

In the field case of Duck (Rogers *et al.*, 2000), wind-wave generation in the presence of low-energy swell over a shelf sea was investigated. It was found that SWAN predicted the total wave energy well, but predicted the spectral distribution of energy poorly, as reflected in the under-estimation of mean wave period. It was suspected that the error was due to inaccurate whitecapping formulation which over-dissipates the swell component of the spectrum, while under-dissipating the wind sea component. This result was confirmed by Holthuijsen *et al.* (2000) who found that, in the presence of swell, SWAN erroneously decreases the (steepness-dependent) whitecapping, causing under-dissipation of high frequencies. This model error was shown to affect wave growth in idealized conditions noticeably, but not the shallow water field case of the Haringvliet.

### **3.3.3 Depth-limited wave growth**

Idealized wave growth in depth-limited conditions showed good correspondence with measurements. It was found that the three available friction formulations yielded very similar results. Bottom friction was shown to be important to the accurate computation of total energy level and peak frequency in shallow water.

It was shown that wind-wave generation was required to represent conditions in the shallow and sheltered interior regions of the Haringvliet, Norderneyer Seegat and Friesche Zeegat field cases accurately. However, it was found that SWAN significantly over-estimated locally generated waves close to leeward edges of landforms and under-estimated their periods. In the field case of Lake George, where depth-limited wave growth was modelled, it was found that all formulations of bottom friction showed fairly similar results. However, the formulation of Hasselmann *et al.* (1973) with a friction coefficient of  $\Gamma = 0,067 \text{ m}^2 \cdot \text{s}^{-3}$  gave slightly better agreement with measurements. It was observed that the levels of dissipation by bottom friction are such that it could often be neglected in areas of significant wave breaking.

### **3.3.4 Triad-wave interaction**

Ris (1997) showed that triad-wave interactions caused wave energy to shift from the peak to twice the peak frequency in the shoaling area of the Haringvliet field case. In the presence of wind, however, the effect of the interactions was submerged in the generated high-frequency energy. In the HISWA-tank laboratory experiment, it was found that triad interactions were under-estimated.

Holthuijsen *et al.* (1998) demonstrated the impacts of triad-wave interactions on the field cases of the Haringvliet and Norderneyer Seegat. It was shown that omission of triad-wave interactions in very shallow water leads to errors in wave period, which in turn leads to errors in wave direction and height, due to its effect on wave refraction.

Andorka Gal *et al.*, (1998) confirmed the impacts of triad-wave interactions, on a relatively deepwater case with a uni-modal spectrum (Petten), and a shallow water case with a bi-modal spectrum (Kashimanada). For these shallow, parallel coastlines, it was found that the mean wave period was greatly affected by triad-wave interactions but that significant wave height was only slightly affected. The finding that wave heights were unaffected were ascribed to the absence of depth-induced refraction. The inclusion of triad-wave interactions significantly improved agreement between calculated and observed spectra.

### **3.3.5 Depth-induced breaking**

It was found that depth-induced breaking effectively described the total dissipation rate of energy. For the field cases of the Haringvliet, Norderneyer Seegat and Friesche Zeegat, integral wave heights in the nearshore/surfzone were well reproduced, and depth-induced breaking simulated the total rate of dissipation accurately. It was confirmed that the total dissipation rate is dominated by the breaking parameter  $\gamma_{BJ}$  (maximum wave height to depth ratio).

### **3.3.6 Wave blocking**

Comparison between computational results for wave blocking and laboratory measurement showed that wave periods were well modelled, but wave heights were over-estimated.

## **3.4 RECOMMENDED APPLICATION OF SWAN**

It was shown in Section 2 that various options with respect to physical processes and model set-up are available in SWAN. In addition, the user has great freedom with respect to choices regarding the numeral aspects (e.g. grid discretization) of the model. Compiled at the time of the release of SWAN version 40.01, the user manual (Holthuijsen *et al.*, 1999) contains a number of recommendations on model configuration and application. A selection of these recommendations is repeated below.

### 3.4.1 Numerical aspects

Various sets of grids are used for computation in SWAN: Input quantities (e.g. bottom description, current fields, etc.) are provided on input grids which have a discretization in geographical (x,y) space. The action balance calculation takes place on a computational grid, which has discretization in geographical (x,y), directional ( $\theta$ ), frequency ( $\sigma$ ) and time (t) space. The appropriate definition of these grids is important for the accuracy of model results. Recommended grid definitions are summarized in Table 3.1 below:

Table 3.1: Recommended choices for computational grid discretization in SWAN

Component	Specification
Directional resolution:	
- Wind sea conditions	$\Delta\theta = 15^\circ-10^\circ$
- Swell conditions	$\Delta\theta = 5^\circ-2^\circ$
Frequency resolution	$\Delta\sigma/\sigma = 0,1$
Frequency range	$f_{low} = 0,04$ Hz
	$f_{high} = 1,00$ Hz
Spatial resolution	$\Delta x, \Delta y = 50-1000$ m

In applying the recommendations of Table 3.1, it should be ensured that the discretizations resolve the modelled quantity sufficiently. The spatial resolution should be fine enough to resolve bathymetrical detail, directional resolution should be fine enough to resolve the distribution of directional wave components and the frequency resolution should be fine enough to resolve relevant spectral details. The recommended upper and lower frequency limits are to allow for wind-wave growth and nonlinear interaction between components of the spectrum. It was recommended that the overall dimensions of the computational grid be limited to 25 km in the direction of wave propagation (see Section 3.3.1).

The choice of discretization is, therefore, dependent on the specific conditions of the modelled case. For every simulation, the option of nesting a secondary grid of higher discretization is available, if more detailed calculations are required for a specific area.

### 3.4.2 Physical processes

Physical process refer to the collection of formulations of physical processes and their associated coefficients (refer Section 2) available in SWAN. The recommended default

form of these formulations (Holthuijsen *et al.*, 1999) are summarized below. This selection of formulations and coefficients is defined as the 'standard' configuration of SWAN:

*Table 3.2: Formulations of physical processes recommended in the SWAN manual for application of the model*

Physical process	Formulation	Coefficient
Linear wave growth	<i>Deactivated</i>	<i>None</i>
Exponential wave growth	Komen <i>et al.</i> (1984)	
Whitecapping	Hasselmann (1974) and WAMDI group (1988)	$C_{ds} = 2,36 \times 10^{-5}$ $\delta = 0$ $p = 4$ $\tilde{s}_{PM} = 3,02 \times 10^{-3}$
Quadruplet-wave interactions	Hasselmann <i>et al.</i> (1985)	$\lambda = 0,25$ $C_{n4} = 3 \times 10^7$ $C_{sh1} = 5,5$ $C_{sh2} = 6/7$ $C_{sh3} = -1,25$
Bottom friction	Hasselmann <i>et al.</i> (1973)	$C_{JON} = 0,067 \text{ m}^2 \cdot \text{s}^{-3}$
Triad-wave interactions	Eldeberky (1996)	$\alpha_{EB} = 0,1$
Depth-induced wave breaking	Battjes and Janssen (1978) as adapted by Eldeberky and Battjes (1996)	$\alpha_{BJ} = 1$ $\gamma_{BJ} = 0,73$

The above 'standard configuration' of SWAN was first defined by Ris (1997), and subsequently refined into the form it has in Holthuijsen *et al.* (1999). This configuration embodies most of the evaluation work summarized in this section, and is regarded as an appropriate form for first-estimate simulations of a field case. Therefore, this form was used in the initial series of simulations conducted for the South African field case of Algoa Bay described in later chapters.

### 3.5 CONCLUSION

In this section it was shown that extensive historic validation work on the SWAN model has been performed, including a comprehensive selection of academic, laboratory and field cases. The field cases investigated focused on shallow bays, shallow inter-tidal areas and open water conditions. The environmental conditions modelled were mostly those found in the North Sea, and mostly comprised uni-modal spectra generated by local storms. In most cases the peak spectral period was below 10 s.

Testing revealed that SWAN produces reasonable results, even over complex bathymetry, with respect to significant wave height, period and direction. It was, however, found that over short fetches wave growth is significantly over-estimated. In wave growth over large fetches with swell, mean wave periods tended to be somewhat under-estimated. For most cases considered, the degree of correlation between calculated wave spectra and measurements tended to be only average.

Processes that were found to be of importance in the historic cases considered were the following: For deeper regions, the important processes were found to be depth-induced refraction and shoaling, and wind-wave growth (which includes quadruplet-wave interactions and whitecapping). In intermediate to shallow water, the dominant processes were found to be wind-wave growth, depth-induced refraction and shoaling, wave-current interaction, triad-wave interaction and depth-induced breaking. Bottom friction was found to be important in very shallow areas, but only if wave breaking is absent.

A summary of the recommended configuration, as given by Holthuijsen *et al.* (1999), has been presented. This summary includes guidelines with respect to numerical formulation (discretization) of the model, as well as the choice of physical processes.





## **4 OVERVIEW OF WAVE CONDITIONS IN THE SOUTH AFRICAN COASTAL ZONE**

### **4.1 INTRODUCTION**

In this section, the South African coastal zone is described in general terms, with respect to its physical form, atmospheric conditions, wave climate and water circulation patterns. The aim of this section is to contrast the general conditions in the South African coastal zone with the conditions for which SWAN has been evaluated to date (Section 3), to provide a background for the SA case study to be presented.

### **4.2 NEARSHORE WIND CLIMATE**

Wind regimes over the South Atlantic and Indian Oceans adjacent to the Southern African continent are the driving force of the wave fields found in the South African coastal zone, as well as an important generating force of coastal currents. The South African wind climate is described below, using Hunter (1987) and Rossouw (1989) as main sources.

#### **4.2.1 Weather systems**

Wave conditions on the South African coastline are mainly the result of wind fields caused by a near-permanent arrangement of high- and low-pressure systems in the South Atlantic and Indian Oceans (Figure 4.1, Hurry and Van Heerden, 1982). The first two components are two near-stationary high-pressure systems, respectively the South Atlantic high (offshore to the west of South Africa) and the South Indian high (offshore to the east of South Africa) produced by the hot-air Hadley cell. Disturbed air in the Ferrel westerlies creates low-pressure systems which move from west to east, to the south of the two high-pressure systems, with intervals of about three to five days. The wind fields associated with the west-to-east moving low-pressure systems are the main sources of the higher energy wave climate to which the South African coastline is exposed.

#### **4.2.2 Seasonal wind patterns**

Due to combined workings of the systems described above, two distinctive weather patterns are found for winter and summer, as shown in Figure 4.1. During winter, the South Atlantic high and South Indian Ocean high systems are situated around 30° S latitude. Depressions from the Ferrel westerlies, with their associated cold fronts, pass with regular intervals, along the latitude 40° S beneath these two systems just south of

the African continent. In the deep sea, the passing low-pressure systems result in strong south-westerly winds, which generate swell over considerable fetches to the south-west of the African continent. Wind conditions along the coastline undergo a characteristic pattern of change during this passing: Due to the clock-wise (cyclonic) rotation of the passing depression, winds on the west and south coasts change direction from an initial NW, through W to SW. Upon reaching the east coast, the depression is normally deflected by the South Indian high, and moves south-eastwards, away from the continent.

During summer months, the whole system of high and low pressure moves southwards, with the South Atlantic high and South Indian high residing between the latitudes 30° S and 40° S (Figure 4.1). The belt of the Ferrel westerlies is pushed to the south, so that the influence of the passing depressions is only occasionally felt along the continent. However, the presence of the anti-cyclonic South Atlantic high results in S to E winds along the west and south coasts.

Weather conditions along the east coast are less regular than those of the west and south coast. It was observed that east of Port Elizabeth the influence of the regularly passing cold fronts of the Ferrel westerlies is less intense Rossouw (1989). This was presumed to be due to a combination of the decreasing intensity of cold fronts east of Port Elizabeth, the deflection of the depressions by the South Indian high and the north-eastwards swing of the coastline to the east of Port Elizabeth.

The resultant local offshore wind climate is presented in Figure 4.2. The wind roses presented are based on measurements of Voluntary Observing Ships (VOS). For a discussion on the reliability of VOS measurements, see Hunter (1987). The wind roses are in general agreement with the description of the underlying weather system. The dominant wind directions along the west coast are S to SE, along the south-west coast W to SE and along the south coast W, SW and E. Less pronounced dominant wind directions are found along the east coast. In the vicinity of East London wind is found from a wide spectrum of directions, but the dominant directions are SW and NE. Dominant wind directions offshore off Durban are in the S and N – NE sectors. Along the entire coast wind speeds of 5-15 m/s are frequently found, and speeds in excess of 25 m/s on occasions.

An important factor in the description of the east coast climate is the presence of tropical cyclones highlighted by Rossouw (1999). Rossouw concludes that at coastal locations between the latitudes 2,5° S and 32,5° S, tropical cyclones occur with a return period of one in a hundred years.

### 4.3 OFFSHORE WAVE CLIMATE

Due to the characteristic wind patterns of the region, the South African wave climate is essentially bi-modal. This climate comprises a dominant high-energy swell component generated by winds over the South Atlantic to the SW of the continent, and lower energy wind seas, generated by local winds. An overview of the offshore design wave climate is given below, using as main source an analysis made by Rossouw (1989).

#### 4.3.1 Wave height and periodicity

Using a selection of simultaneous Waverider records, Rossouw (1989) showed that the offshore wave climate along the westerly and southerly coastlines (Oranjemund to Port Elizabeth) display a similarity in significant wave height ( $H_{m0}$ ) and peak period ( $T_p$ ) during storm events. Wave heights offshore along the south west and south coasts, up to Port Elizabeth, displayed nearly identical  $H_{m0}$  and  $T_p$ , with peak energy periods ranging between 9 s and 16 s during 80 per cent of the time (with median 12,5 s). A gradual reduction in wave height and period were found moving northwards up the west and east coasts. A summary of wave height and periodicity, as compiled by Rossouw (2001), is given in Figure 4.3.

The similarity in wave conditions along the west and south coasts was ascribed by Rossouw (1989) to the common weather system (as related in Section 4.2 above) over this region. The gradual reduction in wave heights along the west coast was attributed to the decreasing intensity of the passing depressions with increasing distance from the eye of the storm. Wave heights along the east coast were also found to decrease with increasing distance from the passing depressions, but are also influenced by weaker local weather systems.

#### 4.3.2 Spectral shape

Two years of measured spectra at two locations, Slangkop (just west of Cape of Good Hope – refer Figure 4.3) and SEDCO-K (on the Agulhas Bank – refer Figure 4.3), were used by Rossouw (1989) to formulate an average energy density spectrum. Although great variation was reportedly found in spectral form, the highest energy levels were found between 13 s and 16 s. According to Rossouw, this energy range applies for the entire South African coast. To obtain an indication of the shape of the design spectrum, the spectra of 43 records of high wave occurrences ( $H_{m0} > 6$  m) at the Slangkop station were analyzed. These spectra fitted the JONSWAP spectral shape (Hasselmann *et al.*, 1973) with the value of the peak enhancement factor  $\gamma$  ranging between 1 and 6, with a mean value of 2,2 and a standard deviation of 1,0.

Due to wind-wave generation near the coast, spectra are often found which display a secondary, higher frequency peak. This peak represents a growing wind sea state, which is superimposed on the ambient high-energy swell, and gives the spectrum a bi-modal character.

### **4.3.3 Directionality**

An overview of directionality of waves along the South African coastline is given in Figure 4.3, using the VOS dataset of 1960-2000 (Rossouw, 2001). The wave roses presented here include both wind sea and swell. However, it should be noted that VOS directions tend to be somewhat biased towards wind sea directions (M Rossouw, CSIR, pers. comm., 2001). As a general rule, the sea component of these roses correlates well with the local wind climate (Figure 4.2), while a consistent south-westerly component is added by high-energy swell. This distinctive bi-directional nature of swell and sea components adds to the bi-modal character of the South African wave climate.

Figure 4.3 shows that along the west coast, southerly seas dominate, but that a strong SW swell component is present. Along the south-west coast, wave directions from W to SE are found, with the S direction slightly dominant. Along the south coast, SW swell dominates, but wind seas are found from both W and E directions. Along the south-east coast wave directions from W to N are found, but SW swell is the most significant. Along the east coast, the dominant direction is southerly, although relatively high occurrences from SW to N are present.

## **4.4 COASTLINE AND BATHYMETRY**

The South African coastline and bathymetry (Figure 4.4) can be described as generally straight, open and steep, reaching intermediate to deep water close offshore. A continental shelf is present on the southern coastline, and a number of large, deep bays are also found on this section of coastline. Three distinctive coastal regions can be identified, namely the west-, south- and east coasts. These regions are described below, using the SA Naval charts (SA Hydrographical Office, 1972–1996) as source.

### **4.4.1 West coast**

The west coast (Oranjemund to Green Point, Cape Town) is mainly long and straight, and is steep-sloped between the depth of 50 m and the shore. Most of the bays on the west coast are small. Only two significant bays are found - the open, north-facing St. Helena Bay (95 km<sup>2</sup>) and the sheltered Saldanha Bay (100 km<sup>2</sup>). Two islands of noteworthy proportion are found on the southern part of the coast, namely Dassen

Island (2,4 km<sup>2</sup>) and Robben Island (5,4 km<sup>2</sup>). These islands have some sheltering effect on local wave conditions (CSIR, 1998).

Regarding the bathymetry of the west coast, the depths along the straight coastlines vary essentially along one dimension only. In the part north of St. Helena Bay the seabed slopes are 1:90 to 1:40 (100 m to shore), and to the south of it (to Green Point) somewhat milder at 1:250 to 1:75 (100 m to shore). In the bay area of St. Helena Bay the bottom slopes from 20 m depth to the shore are 1:450 to 1:100.

#### **4.4.2 South coast**

The south coast (Green Point to East London) is bordered by a broad continental shelf, the Agulhas Bank, which extends up to approximately 250 km to the south. On the south coast, numerous large, deep bays are found, which are mostly southerly or south-easterly facing. The largest bays found on this coast are False Bay (1 040 km<sup>2</sup>) and Algoa Bay (800 km<sup>2</sup>). These bays are formed by one or two prominent headlands typically found on the western side of the bay, which provide some shelter from south-westerly swell.

The bed slopes of the south coast vary considerably. For areas deeper than 50 m, bed slopes varies between 1:60 on the sides of headlands to 1:1 800 for areas leading into the Agulhas Bank. For areas shallower than 50 m, slopes between 1:200 and 1:45 are found. In False Bay the bottom slope is relatively mild, from 1:450 in deeper regions, to 1:150 in areas shallower than 30 m. In Algoa Bay the corresponding bottom slopes are 1:500 and 1:200, respectively.

#### **4.4.3 East coast**

The east coast (East London to Ponta do Ouro, Mozambique) is similar to the west coast, open, straight and steep-sloped. The coastline is without prominent bays, containing a number of river mouths only. These rivers, however, have generally low run-off, and do not regularly form open estuarine areas. One significant coastline feature is the relatively shallow Natal Shelf, between Green Point near Durban and Port Dunford. The Durban Bluff provides some shelter against southerly wave conditions for the beaches immediately to its north.

The seabed of the east coast is generally steep, with slopes in the 100–50 m depth range generally being between 1:150 and 1:100, and from 20 m to shore as steep as 1:40. The exception is the Natal Shelf region, where slopes of 1:400 are found in depths of 100–50 m and slopes of 1:600 to 1:300 from 50 m to shore.

## **4.5 COASTAL CURRENTS OFFSHORE, SEAWARD OF THE BREAKER ZONE**

The water circulation around the Southern African continent can be divided into three main regions (see Figure 4.5): the Agulhas Current system, the central and eastern Agulhas Bank and the Benguela system. The primary driving forces in the current regime of South Africa are: the Agulhas Current – a south-moving continuity current, local winds, density differences and waves. Tidal currents are insignificant in almost all cases. A description of the average climate of coastal currents are given below for the east, south and west coasts, using as source Harris (1978).

### **4.5.1 East coast**

The coastal currents along the east coast (Figure 4.6) are generated by the Agulhas Current and local winds, with the former being dominant. The largest part of the east coast is steep sloped, and as a result the Agulhas Current (which is deep-running and meandering) can come into close proximity of the coastline. On the coastline north of Durban, current velocities within 10 km from the shore are frequently in excess of 0,5 m/s (southwards). The velocity of the Current increases southwards, with speeds on the coastline south of Durban reaching values of up to 1,0-1,5 m/s within 10 km of the shore.

On the Natal Shelf (between Port Dunford and Green Point) an exception is found to the general current pattern. Due to the shelf, the Agulhas Current diverges from the coast, and a large cyclonic circulation pattern, the Natal Gyre, is found. The result of this cyclonic circulation is that north-going currents of up to 1 m/s are found off Durban regularly. The cyclonic Natal Gyre is also found to cause smaller anti-cyclonic circulation patterns on the Natal Shelf. A similar flow diversion and cyclonic circulation is observed at Cape Hermes to the south of the Natal Shelf.

### **4.5.2 South coast**

The Agulhas Current separates from the continent in the region of Port Elizabeth, to follow the contour of the shelf edge to the WSW. This leaves the central and eastern Agulhas Bank free of the direct influence of the Current, and weak and variable currents are found. In this region, wind forcing is considered very important, and the flow pattern is mainly due to the prevailing E and W winds (Goschen and Schumann, 1988). The net direction of currents close to the coast would, therefore, reflect the wind and swell angle, and is expected to be predominantly to the east (Schumann *et al.*, 1982).

The description above was supported by Boyd *et al.* (1992), who produced a schematic flowfield of near-surface currents (at 30–50 m depth) of the west coast, southern coast

and the Agulhas Bank (Figure 4.7). His findings were based on two years' Acoustic Doppler Current Profiler (ADCP) measurements taken over the region. The current field shown in this chart cannot be directly related to surface currents, but a fair indication of flow patterns may be deduced. According to this chart, current flow has typical values of 10–40 cm/s (easterly/westerly) on the central-eastern side of the Agulhas Bank and 25–50 cm/s (easterly) at Port Elizabeth. The latter increase in easterly velocity at Port Elizabeth was ascribed to retroflexion (reverse flow along the edge) of the inshore margin of the Agulhas Current.

#### 4.5.3 South-west and west coasts

The flow on the western Agulhas Bank and south-west coast is driven by local winds, and varies seasonally. Between Cape Agulhas and Cape Point, the coastal currents are either NW-going or SE-going. Boyd *et al.* (1992), using ADCP measurements, revealed typical current velocities in this region to be in the order of 0–40 cm/s (Figure 4.7). The existence of slack and slightly onshore currents was also found. Current movements in the numerous bays on the south-western coast display characteristic patterns: False Bay, for example, displays cyclonic and anti-cyclonic flow due to wind, and tidal flow patterns. Velocities for the former group are in the order of 50 cm/s and smaller, and for the latter 25 cm/s and smaller (Harris, 1978, after Atkins, 1970\*).

From the Cape Peninsula north-westwards the Benguela system is found. Its flow is mainly north-westwards past the Peninsula, with typical velocities of 50–75 cm/s measured near the surface (Figure 4.7). Between the Cape Peninsula and St. Helena Bay, current velocities reduce. Surface currents in this region are in response to the prevailing SE and NW winds, with NW-going currents dominating. Current velocities are in the order of 20–30 cm/s (Harris, 1978), but slack currents are common. Wave driven currents are common up to 3 km from the coast. At Saldanha Bay, tidal currents of 15 cm/s are found. Locally, at the Langebaan lagoon mouth in Saldanha, a significant tidal current of 100 cm/s prevails at spring-tide (Shannon and Stander, 1977).

At Cape Columbine, the Benguela current speeds up and diverges into a major offshore arm and a minor northward arm (Shannon, 1985). The northward arm is found within the 500 m isobath and reach velocities of 50 cm/s regularly. Inshore the flow is weaker and variable. Current flow is predominately southerly with velocities of 0–25 m/s, but cross shelf flow is relatively common (Boyd *et al.*, 1992).

## 4.6 DISCUSSION

Based on the description of this section, conclusions can be drawn on the sea conditions along the South African coastal zone. The characteristic element of this region is the presence of strong SW swell conditions (with  $H_s^{1\%} = 4,5-6,0$  m), resulting and peak periods between 9 and 16 s. This swell condition dominates along the west and south coasts. In addition to this, moderate to strong local winds prevail, which cause the development of local seas. The result is a wave climate of bi-modal nature with regard to both frequency and direction.

The South African coastline is exposed and the bathymetry, between 50 m and the shore, generally steep-sloped. On the south coast, shelter is provided by large headlands, which form a number of large, deep bays. Average coastal offshore currents along the east and west coast of up to, respectively, 150 cm/s and 75 cm/s are found. The main driving forces of coastal currents are winds and ocean-scale continuity currents.

Comparison between these conditions and those for which SWAN has been evaluated to date (Section 3), show significant differences. The most prominent differences are in terms of wave periodicity (the presence of high-energy swell), spectral shape (bi-modality) and bathymetry (steep, open coastlines and deep, sheltered bays). These differences justify an evaluation of the performance of SWAN model for a typical South African field case. For this field case, the propagation of swell-dominant bi-modal wave condition over a typical sheltered bay area will be investigated. Aspects which might yield unique results are wave generation in the intermediate depths of the bay, the impacts of triad-wave interaction, wave-current interaction and bottom friction. The relative importance of these effects will be assessed.

## 4.7 CONCLUSION

The sea conditions on the SA coastline as described above, differ considerably from the sea conditions to which SWAN has been evaluated to date. The field cases for which SWAN have been evaluated to date are either shallow and sheltered inter-tidal areas and bays, or open water areas. Wave conditions of these field cases are those corresponding to shorter fetches of local storms, with peak periods that are generally below 10 s. A few cases were tested which featured bi-modality in frequency, and generation over shelf seas (e.g. Duck), but in these spectra the swell component was less dominant.

In contrast to the conditions of the historic SWAN evaluation (Section 3), the following environmental conditions characterize the South African coastal zone: Bi-modal wave conditions, both in frequency and direction with a strong swell component, prevailing.



The coastline and bathymetry is open and steep-sloped, or in the form of large, deep bays. Coastal currents are generated by local winds or ocean-scale continuity currents. These differences justify an investigation of the performance of SWAN for a typical SA field case.



## **5 ALGOA BAY FIELD CASE: MODEL SETUP**

### **5.1 INTRODUCTION**

This section, together with Sections 6 to 8, describe the evaluation of SWAN for the field case of Algoa Bay, South Africa (Figures 1.1 and 5.1). The overall aim of this field case study is to investigate the performance of SWAN at a site, and with environmental conditions (wave, wind and current), which are typical of the South African south coast. The field case evaluation takes the form of initial first-estimate model simulations, using the model configuration recommended by the model developers (Section 3.4.2) and subsequent sensitivity tests and model calibration for a selection of offshore conditions and processes. The study is concluded by final simulations for the calibrated model setup. Issues that are investigated in this study are: (a) refraction of high-energy swell around the headland of Cape Recife, (b) simulation of bi-modal offshore spectra and (c) an evaluation of the influence of various physical processes on modeling results. The results of these investigations are brought into relation with the historic evaluation work conducted on SWAN.

The present section describes the input conditions and model set-up for the field case study, and comprises the following aspects:

- a) the selection of a field case
- b) selection of environmental conditions for modelling
- c) positioning of computational grids and boundary value specification
- d) discretization of computational grids

### **5.2 FIELD CASE SELECTION**

The field case of Algoa Bay is presented in Figure 5.1, and shows the location of the Bay on the south-east coast of South Africa. This site was selected as a study area due to three main reasons: Firstly, simultaneous measurements of offshore and nearshore directional wave spectra are available for this site. Secondly, geographically this site represents a large, deep bay, sheltered by a prominent cape on its western boundary, which is typical of an embayment on the southern coastline of South Africa. Thirdly, the wave climate of Algoa Bay comprises the characteristic bi-modal spectra of high-energy swell superimposed by local wind seas. This field case, therefore, is an example of one typical situation on the South African coastline. Insights into modeling aspects of this case would, therefore, contribute to its appropriate application to other sites along the South African south coasts. The Algoa Bay field case is also significantly different to previous published cases for which SWAN has been evaluated

(Section 3), which would allow this study to add to the corpus of SWAN evaluation work.

### **5.3 ENVIRONMENTAL CONDITIONS**

In this section a description of environmental conditions at Algoa Bay, as was used as input for the SWAN simulations, is given. The environmental conditions considered were: the offshore wave data, nearshore wave data, winds, current and seabed conditions. In the case of the wave and wind data, near-continuous, concurrent, time-series measurements were available over a four and a half month period, from 01/01/99 to 18/05/99. Field measurements of a typical current pattern were available. These measurements are described in the sections below. From these measurements a selection of representative climatic conditions are drawn, for which SWAN simulations for Algoa Bay were conducted.

#### **5.3.1 Offshore wave measurements**

Measurements of conditions offshore of Algoa Bay were taken by a directional Waverider buoy, deployed in a water depth of –85 m below Chart Datum (CD), directly south of Cape Recife (Figure 5.1). These measurements yielded an hourly time series of directional wave spectra, sampled over approximately 17 minutes, for the period 01/01/1999 to 26/05/1999. Figures B.1(a)-(e) in Appendix B show for this time series the parameters of significant wave height ( $H_{m0}$ ), peak period ( $T_p$ ) and the mean direction of the spectral peak. This data series captures a period of South African summer and autumn.

Visual inspection of this record shows a definite seasonal character of wave conditions: During the summer months of January and February, significant wave heights were between 1 and 2 m, with mean directions from SE. Peak wave periods were found between 8 and 12 s. During autumn and the start of winter (April to June) the character of the wave climate changed noticeably: Swell from SSW started occurring, with significant wave heights rising frequently above 2 m (maximum 6 m recorded), and peak period often rising above 12 s. By regarding wave spectra at selected storm events during the period April to June (not shown here), SSW swell was often found in combination with wind seas from either ESE-SE or SW, resulting in bi-directional spectra for swell and wind sea.

#### **5.3.2 Nearshore wave measurements**

A time series of nearshore wave conditions was obtained from measurements by an S4 pressure/current meter which was deployed in Algoa Bay over the period 01/01/99 to

18/05/99, in a water depth of  $-17$  m CD (Figure 5.1). This nearshore time series of measurements is also presented in Appendix B, Figures B.1(a)-(e), in terms of the parameters  $H_{m0}$ ,  $T_p$  and the mean direction of the spectral peak. The S4 meter is a bottom-mounted electromagnetic pressure/current recorder. Directional wave spectra can be derived from pressure and orbital velocities measured by this device. However, wave frequencies higher than  $0,2$  Hz cannot be reliably interpreted, and, therefore, the recorded spectrum is truncated at this frequency.

Measured nearshore wave spectra are discussed here in relation to offshore conditions at Cape Recife. The S4 current meter was located in a position which is fairly sheltered from SSW swell by the landmass of Cape Recife. This situation provided an opportunity of investigating, amongst other issues, the sheltering of the inshore bay area from high-energy swell by a large headland. By comparing offshore and nearshore observations (denoted as WR and S4 respectively in Figures 5.2 to 5.4), the following typical cases of wave transformation were found:

- a) Seas from an *offshore ESE to SE* direction (see Figure 5.2), moving directly into the open bay, resulted in relatively high wave energy at the nearshore station. Wave energy from the wind sea conditions remained above frequencies of  $0,1$  Hz. In the example shown, the mean direction of the peak frequency changed from  $100^\circ$  TN offshore to  $\pm 120^\circ$  TN inshore, presumably due to refraction.
- b) Swell from an *offshore SSW* direction (Figure 5.3) was registered at the inshore station with a marked decrease in energy. Wave energy remained in the lower frequency band of  $< 0,12$  Hz, but the mean direction of the peak frequency of the inshore spectrum swung around to  $150^\circ$  TN.
- c) Wave components from an *offshore SW* direction pass Cape Recife without being registered at the S4 location. This is shown in Figure 5.4 for the SW seas component of a bi-modal spectrum.

### 5.3.3 Wave measurement quality and correlation

Verification of the correlation between the time series measurements of wave spectra was required before they could be reliably applied to the field case study. Such verification was conducted prior to their simultaneous deployment in January 1999, by means of simultaneous recording of the two devices at a common location (final S4 position) in nearshore Algoa Bay. A comparison of the respective test time series recordings by these two devices are shown in Figure 5.5. This comparison shows generally good correlation between the wave height ( $H_{m0}$ ) recordings of the Waverider and the S4 meter. However, an average difference of about seven degrees was found between the mean direction of the spectral peak recorded by the two devices, with the

S4 reading being generally to the south of that of the Waverider. Also, the peak period recordings of the S4 differed by + and – 0,9 s to that of the Waverider. This difference in peak period values was ascribed to differences in the frequency discretizations ('binning') assigned to the two sets of spectra by post-processing software. In terms of the mean period parameter  $T_{m01}$ , differences were below these values (A Holtshauzen, PRDW Consulting Engineers, pers. comm., 2001).

Inspection of the offshore wave height time series between 01/04/1999 and 19/04/1999 (Figure B.1(d)) reveals an isolated period of erroneous 'spikiness' in recording. This is believed to be due to the tendency of the Waverider buoy to malfunction during periods of rough seas (M Rossouw, CSIR, pers. comm., 2001). These periods of erroneous recording were avoided in the selection of modelling conditions.

#### **5.3.4 Wind measurements**

Time series measurements of wind speed and direction were made at the offshore station of Jahleel Island (Figure 5.1), at a height of +21 m above land survey datum (MSL), over the period 01/01/1999 to 30/06/1999. A selection of five periods of wind recording is presented in Appendix B, Figures B.2 (a)-(e). These records show the mean hourly wind speed and direction. It can be seen that maximum mean hourly speeds of between 15 and 18 m/s were recorded, mostly associated with westerly winds, although easterly winds were also frequent. These records correspond to the collection of test conditions for the SWAN simulation to be selected in a later section.

The measurement location of Jahleel Island had the disadvantage of being downwind of the fetch area, and also quite near the coast. A description of the wind climate over the larger Algoa Bay area is provided by Schumann *et al.* (1991). In their review, measurements from 1986 to 1988 of two offshore and two onshore stations, Cape Recife and Bird Island, respectively and Port Elizabeth Airport and Sundays river (see Figure 5.1), were analyzed. On the basis of measurements from May to July, averaged over both yearly and daily periods, similar results for wind conditions were found at the two offshore stations. This indicates that, at least over the offshore area of Algoa Bay, the wind field can, as a first approximation, be modelled with spatially uniform speed and direction.

#### **5.3.5 Current measurements**

No simultaneous surface current measurements over Algoa Bay were available for the period over which waves and wind were recorded. It was, therefore, necessary to reconstruct a representative current flow pattern over the Bay, which could be used in the SWAN simulation.

It was shown in Section 4 that coastal currents in the region of Algoa Bay are mainly driven by the prevailing E and W winds, and would, consequently, reflect the strength and direction of the wind. Goschen and Schumann (1988) presented measurements of a cyclonic near-surface current field which typically forms in the Bay during a period of consistent westerly to south-westerly winds. These measurements were taken along sampling lines, which ran perpendicular to the coast, and were linearly interpolated to obtain the flow field presented in Figure 5.6. As an approximation, it is assumed that a similar flow field would result after a similar period of persistent westerly winds, for example, on the day of 12/05/1999 (see Figure B.2(e)). This measured flow field will, therefore, be applied to an appropriate case in the field case study.

It should be noted that Goschen and Schumann (1988) found the measurements of Figure 5.6 to be quite high compared to other measurements that existed at the time. Their measurements showed inshore value on average of 49 cm/s compared to an average value of 11 cm/s found earlier by others (Harris 1978). The conservative nature of this data set was considered in the interpretation of the results in this study.

### **5.3.6 Bottom conditions**

Establishment of conditions on the seabed of Algoa Bay was important to the selection of appropriate bottom friction formulations for the field case simulations. A summary of seabed composition is given in Figure 5.7 (Portnet, 2001). This summary shows that the seabed is mostly comprised of sand, with small patches of muddy sand and gravelly sand. The median grain size of this offshore area was given as approximately 190 micron.

### **5.3.7 Selection of conditions for hindcasting**

To evaluate the performance of SWAN for the Algoa Bay field case, a collection of offshore cases was selected which represents typical conditions in the Bay. These cases featured, notably, conditions with high-energy SSE swell and bi-modal spectra. The selection also included records with SE wind sea conditions, which are similar to those tested in historic validations (Section 3), to serve as reference condition. To obtain clear results, records were chosen on the basis of significant properties. Cases with properties such as high wave energy, the distribution of energy spectra (such as clear high and low frequency peaks) and high wind speed were selected. Wave records in the month of April 1999 were selected in such a manner as to avoid the erroneous 'spikiness' present in the time series (refer Section 5.3.3). The time span of available records was also limited by the need for simultaneous measurements of offshore and inshore waves and wind. The following categories of offshore conditions were selected for simulation:

- A. *ESE wind seas*: spectra with peak period between five and 10 s, originating from a dominant ESE to SE direction.
- B. *SSW swell with SE wind seas*: spectra where SSW swell with peak periods of above 10 s is found in conjunction with SE wind seas (bi-directional).
- C. *SSW swell*: boundary spectra containing a SSW swell of high energy.
- D. *SSW swell with SW wind seas*: spectra where SSW swell is found in conjunction with wind seas from SW with periods between 5 and 10 s (bi-directional).

To obtain results over a range of conditions for the evaluation of the performance of SWAN, a total of nine cases, representing the categories above, were selected for simulation. These cases are indicated on the time series of Figures B.1(a)-(e) in Appendix B, listed in Table 5.1 below, and shown in terms of spectra as polar plots in Figures 5.8 (a), (b) and (c):

*Table 5.1: Collection of offshore wave boundary values for field case simulations*

<b>Case no.</b>	<b>Category</b>	<b>Date and time (Mm/dd, UT)</b>	<b>Description</b>
1	A	04/26 at 18:00	Single peaked seas from ESE, with 5 to 10 s period
2	A	04/27 at 19:00	Single peaked seas from ESE, with 5 to 10 s period
3	B	03/03 at 23:00	SSW swell in combination with SE wind seas
4	B	04/08 at 18:00	SSW swell in combination with SE wind seas
5	C	05/13 at 18:00	SSW swell with peak period at 13 s
6	D	04/23 at 21:00	SSW swell in combination with SW wind seas
7	D	04/18 at 12:00	SSW swell in combination with SW wind seas
8	D	04/19 at 08:00	Highly developed SW wind sea in combination with SSW swell
9	D	04/21 at 15:00	SSW swell in combination with SW wind sea



## 5.4 COMPUTATIONAL GRIDS AND BOUNDARIES

This section describes the positioning of computational grids and the specification of boundary values for the SWAN simulation of the Algoa Bay field case. This description comprises the following aspects: a discussion of the constraints to the model setup of the field case, the choice of the computational grids and boundary values, and lastly a description of the tests performed to verify the accuracy of the choices made.

### 5.4.1 Constraints to modelling choices

Before the specification of model grids and boundary values are described, some consideration is given to the constraints to these selections. The first limitation is that of geographic scale: The area of Algoa Bay (see insert in Figure 5.1) covers a geographical surface of approximately 80 km x 60 km. As discussed in Section 3, the recommended usage of SWAN version 40.01 limits the model application to distances of approximately 25 km, due to the numerically diffusive nature of the model. It was therefore required to define some arbitrary computational area within the Bay, limited in size to these dimensions. All influences outside this grid had to be compensated for.

The second limitation is the position of the offshore wave measurement station: Offshore wave information was only known at the location offshore and to the south of Cape Recife (Figure 5.1), which is fairly close inshore. No concurrent, truly deep-sea recordings were available. This limitation is significant, given the large surface area of this open bay. A technique was, therefore, required to relate wave information at the Waverider location to other offshore locations in the Bay.

The combination of these constraints led to the choice of selecting computational areas of approximately 25 km x 25 km in size, which explicitly incorporated, in its boundaries, all influences outside the computational area which would enter it. These influences are, firstly, the ambient swell condition, and secondly the wind, which is incorporated through its associated sea condition. A second consequence of these constraints to model setup is the decision that simulations was to be done in a 'case-per-case' stationary mode. This was necessary, because as was motivated above, restrictions on input data required the setting up of cases on an individual basis, with *ad-hoc* specification of wave and wind conditions, as will be shown below.

### 5.4.2 Criteria and method

The position and extent of the computational grids were chosen with attention to the location and orientation of the offshore boundary. The offshore boundary is defined here as the boundary at which the offshore wave condition is specified (e.g. in Figure 5.9). The choice of the offshore boundary position was made on the basis of the deep-

sea wave period (versus local depth) and wave direction of the offshore wave conditions to be modeled. Two aspects were considered in this choice: Firstly, it was sought to place the offshore boundary such that the incoming wave components were not yet affected by the sea bottom, so that wave conditions could be specified uniformly along the boundary. Secondly, the offshore boundary orientation was required to be such that the entire directional spectrum could enter the computational field.

The specification of the offshore boundary values on the computational grid was done using the directional spectra at the offshore Waverider buoy (Figure 5.1). The procedure was to apply the single-location data of the Waverider to the *entire* offshore boundary, perform test runs using this boundary condition, and compare the newly computed spectra at the offshore buoy location with the originally measured values. With this technique, in essence two uncertainties were tested: (a) whether the boundary allows all directional components to enter the computational field, and (b) whether any significant changes occur within the propagation distance between the computational boundary and the offshore buoy.

It was accepted that if, firstly, the boundary was chosen so that the wave field could be assumed uniform along it, and secondly that the measured spectra were 'recovered' at the offshore buoy, that the placing of the computational grid and the boundary values were satisfactory. It was found that to succeed in both these goals, slight adjustments had to be made to some of the spectra applied to the computational boundaries. These adjustments were case-specific and will be described below.

#### 5.4.3 Positioning of computational grids

The Cartesian co-ordinate system of the bathymetical area ( $X', Y'$ ) for the SWAN simulations is defined, relative to the co-ordinate system of the geographical area ( $X, Y$  - in SA Lo 25 projection), as follows:

$$\begin{aligned}X' &= + 63\,015 - Y \\Y' &= + 3\,769\,097 - X\end{aligned}$$

The offshore boundary of the computational area was chosen at the 100 m contour, for all cases (e.g. in Figure 5.9). This choice was made because geographically this contour forms a well-defined limit to the area of interest, and because at this depth the upwave area can still be regarded as deep-sea for spectral components with periods of up to 11,5 s. Therefore, wave conditions along the 100 m contour were assumed to be uniform for the purpose of simulation. The computational grids were extended shoreward to include the location of the S4 station.

To allow the complete directional sector of energy to enter the computational area, the orientation of the boundary was chosen in accordance with the direction of the spectra of the offshore wave condition<sup>1</sup>. The placing of the boundary was, however, limited to orientations that represent the course of the 100 m contour. Three boundary positions were chosen: at angles of 10-, 20- and 30 degrees to the E-W direction, for mean wave directions of WSW to SSW, SE and ESE respectively (see Figures 5.9, 5.11 and 5.13). These boundaries are described below, moving clockwise from ESE to WSW:

#### 5.4.3.1 ESE direction

For the ESE wind sea condition of offshore category A, an offshore boundary orientation of 30 degrees to the E-W line was chosen (Fig. 5.9), and the measurements at the Waverider position taken as its boundary values. For the ESE wave and wind condition this situation is not ideal, as this position of the boundary is significantly upwind of the location at which offshore conditions were known. It should, therefore, be realized that by applying the downwind Waverider measurements to the upwind offshore boundary, all energy generated by easterly winds between the boundary and Waverider position is *already incorporated in the boundary condition*. This implies that wind forcing between the offshore boundary and the Waverider position should be neglected, for all wind conditions from an easterly sector. Using the selected offshore boundary in a trail SWAN computation (with wind neglected), the above approximation was assessed. The results of the simulation (see Figure 5.10) show that the offshore spectra at the Waverider were acceptably recreated at most frequencies. Figure 5.10 shows the comparison between observed (the original) and calculated spectra at the Waverider for Case 1 (ESE wind sea).

However, as a different issue, the offshore boundary was unable to describe the full incoming directional wave spectrum. Wave components, at mean wave directions smaller than 100° TN, were truncated. This introduced errors in the simulated mean wave direction (lower plot, Figure 5.10) and spectral energy density (upper plot, Figure 5.10), at the Waverider location and inside the computational area. However, observing the geometry of the field case, the truncation of directional components from N of E along the offshore boundary would not affect the solution inside the Bay area and at the inshore S4 station. This misrepresentation at the offshore boundary was, therefore, accepted.

To allow for the influx of wave energy from the eastward area of the bay (which falls outside the geographic area modelled), representative boundary values were required for the eastern lateral computational boundary (see Figure 5.9). This was provided by conducting a separate simulation with SWAN in one spatial dimension, by which the

---

<sup>1</sup> There is, however, no theoretical restriction in the SWAN formulation on the allowable orientation of the boundary relative to the mean propagation direction.

effects of depth-induced refraction and shoaling the along the boundary were accounted for. This simulation used the depths along the line of the lateral boundary, and the Waverider spectrum for the (single) boundary value at the starting position at 100 m depth. The success of this boundary value specification is confirmed by the good correlation obtained between the recorded and recreated (simulated) spectra presented in Figure 5.10.

#### **5.4.3.2 SE/SSW direction**

For the bi-directional wave field of the SE/SSW spectra (category B), the offshore boundary was rotated to 20 degrees to the E-W line, as is shown in Figure 5.11. This orientation of the computational grid allowed swell from SSW to enter the computational area. Similar to the observation made in Section 5.4.3.1 above, the selected boundary position is somewhat upwind of the Waverider location from where its boundary values are taken. The fact that the boundary contains some effects of down-wind generation was taken into account in the compilation of the spatial wind field for wind-wave generation.

Along the eastern lateral boundary, one-dimensional SWAN simulations were performed to reproduce the effects of refraction and shoaling in the boundary condition. Implementing the selected offshore and eastern boundaries, the measured and recreated spectra for Cases 3 and 4 were evaluated. Figure 5.12 shows, for the example of Case 4, that good correlation between simulated and measured spectra was obtained.

#### **5.4.3.3 SSW direction**

To accommodate directional components from a westerly sector the boundary orientation for the group of cases from WSW to SSW was chosen at 10 degrees to the E-W line (Figure 5.13). With this boundary orientation the complete SSW directional spectrum was able to propagate into the computational field. This was verified by comparing measured and recreated spectra for Case 5, as shown in Figure 5.14. However, a discrepancy of about 15 degrees in the direction of components with periods above 12 s was found. This directional change was ascribed to refraction (components with longer wavelength feeling the bottom), and was compensated for in an iterative process of slightly correcting and re-testing directions for these frequencies at the offshore boundary. This adjustment is incorporated in the spectrum shown in Figure 5.14.

Considering the geometry of the simulated area it can be seen that because the energy of the offshore wave condition is eastward-moving, no energy input was needed along the eastern lateral boundary.

#### **5.4.3.4 SW direction**

For the SW offshore condition, a boundary orientation of  $10^\circ$  to the E-W line was again used (Figure 5.15). As was the case with the SSW spectra, wave components entering with a mean direction of up to 225 degrees were able to enter the computational area nearly completely and be recomputed acceptably at the offshore buoy location. An example of this result is shown in Figure 5.15 for Case 7. However, wave spectra entering with a mean direction greater than 225 degrees were not represented accurately. For mean directions beyond 225 degrees, the far-lying directional components of the spectra were truncated, introducing errors in the mean direction in excess of five degrees. This was coupled with proportionate loss of energy at the corresponding frequency components<sup>2</sup>. The boundary values and layout were, however, accepted on the assumption (to be confirmed by simulation results) that the energy of the WSW-moving wave components would propagate completely out of the computational area, without affecting the conditions inside the Bay. It was, therefore, assumed that this deficiency in the offshore boundary would not affect the solution in the inshore area of interest.

Compensation was made for directional errors due to refraction of longer-period components. As for SSW cases described above, no boundary values were assigned to the eastern lateral boundary.

#### **5.4.3.5 WSW direction**

Using an offshore boundary with a 10 degree orientation relative to the E-W line (Figure 5.14), the bi-directional spectra of SSW/WSW were recreated satisfactorily. As an example, the measured and recreated spectra for bi-directional WSW and SSW Case 9 is given in Figure 5.16. It was again found that directional components from directions greater than  $225^\circ$  were truncated from the spectra, but was accepted on the same grounds as stated above. As done previously, the effects of refraction of longer-period components were compensated by correction of their boundary directions.

#### **5.4.4 Discussion**

In the selection computational grids and offshore boundaries, a number of aspects were revealed and a few assumptions were made. These are discussed below:

- a) Limitations on grid size and the position of the offshore measuring station resulted in approximations in the choices of the computational grid and boundaries. Most notably, for easterly wave and wind conditions, boundary

---

<sup>2</sup> A partial solution to this problem is the inclusion of the offshore buoy data on the west-facing lateral boundary.

conditions on the upwave (easterly boundary) were specified in terms of measurements on the downwind (westerly) side. This resulted in the simplification that effects of wind-wave generation over the modelled area were incorporated in the upwind boundary. The acceptability of this approximation was tentatively verified (refer Section 5.4.3.1).

- b) Wave conditions were specified at the up-wave (offshore) model boundaries, which were placed along the 100 m contour. At this depth, the wave field was taken as unaffected by shallow-water effects over most of the frequency spectrum. Therefore, the wave conditions were specified as being uniform along the offshore boundary by applying a single offshore spectrum. The acceptability of this approximation was tentatively verified (refer Section 5.4.3.2 to 5.4.3.5).
- c) It was shown that boundary wave conditions should be assigned with care, especially in situations where wave energy is incident from a wide sector of directions. Neglecting directional components was found to lead to errors in the average direction as well as in the total energy density inside the computational area. This confirms the recommendation on the same topic given in Holthuijsen *et al.* (1999).
- d) It was tentatively assumed that for WSW wave components, the insufficient representation at the offshore boundary would have little effect over the part of the inshore solution that is of interest to this study.

## **5.5 DISCRETIZATION OF THE COMPUTATIONAL GRID**

The aim of this section is to find optimal settings for the numerical discretization in geographical space ( $\Delta x$  and  $\Delta y$ ) and direction ( $\Delta\theta$ ) of the computational grid, for the Algoa Bay case study. These optimal discretizations would be such as to provide sufficiently accurate modelling results while being computationally efficient.

### **5.5.1 Method**

The discretization in the geographical (spatial) and directional domain was established separately. The method followed was to isolate one of the two discretizations, for instance that of the spatial dimension. The directional discretization was chosen relatively fine, while the discretization in space was varied over a range of values. Starting from a coarse value, the spatial discretization (both  $\Delta x$  and  $\Delta y$ ) was incrementally reduced until differences in simulation results, as evaluated at the nearshore S4 station, became acceptably small. A similar process (keeping the spatial

discretization constant and varying  $\Delta\theta$ ) was followed to obtain the optimal discretization in the directional dimension ( $\Delta\theta$ ). The frequency resolution was fixed throughout at a fine  $\Delta\sigma/\sigma = 0,04$ .

This evaluation was conducted for four offshore conditions covering the directional sector from ESE to WSW, to ensure a solution that is applicable to all field case conditions. These field cases, together with the ranges for which the discretizations were evaluated, are presented in Table 5.2 below.

*Table 5.2: Test cases for spatial and directional discretization tests*

Case no.	Date and time (Mm/dd, UT)	$\Delta x, \Delta y$ (m)	$\Delta\theta$ (°)	$\Delta\sigma/\sigma$
1	04/26 at 18:00	2000 - 250	40 – 5	0,04
4	04/08 at 18:00	2000 - 250	40 – 5	0,04
7	04/18 at 12:00	2000 - 250	40 – 5	0,04
9	04/21 at 15:00	2000 - 250	40 – 5	0,04

The evaluations were conducted using SWAN with standard model formulation (Section 3), including processes such as bottom friction and whitecapping. However, for sake of comparison between cases, wind-wave generation was not included in the simulations.

## 5.5.2 Results

### 5.5.2.1 Discretization in geographical space

For the establishment of the discretization in geographical space ( $\Delta x$  and  $\Delta y$ ), directional discretization ( $\Delta\theta$ ) was fixed at five degrees, while  $\Delta x$  and  $\Delta y$  was varied (by subsequent halving) between 2 000 m and 250 m. Figure 5.17 shows the result of these tests in terms of the calculated solution at the nearshore S4 station, for the representative example of Case 4 (SSW swell with SE seas).

The plots in Figure 5.17(b) and (c) show the respective differences in solution between simulations with 2 000 m and 250 m, 1 000 m and 250 m, and 500 m and 250 m, to indicate the error made by using the coarser discretization in each case. The discretization error in energy density is defined as:

$$\text{Percentage absolute error} = \frac{\text{abs}[E(f)_{\Delta x} - E(f)_{250m}]}{E(f)_{250m}} \times 100 \quad (5.1)$$

where  $\Delta x$  is the increment investigated and 250 m is a relatively fine, arbitrarily chosen, increment of discretization

These plots show that the reduction of the error in solution decreases as the increments  $\Delta x$  and  $\Delta y$  are reduced. It can be seen in Figure 5.17(b) that when spatial increments are reduced to 500 m, the next reduction (to 250 m) would result in an improvement in calculated energy density of less than eight percent for the SSW swell (< 3 percent in  $H_{m0}$ ) and 3 percent (< 2 percent  $H_{m0}$ ) for the SE wind sea component. Similarly, a reduction spatial increment from 500 m to 250 m resulted in an absolute difference in mean direction of less than 0,5 degree. For all cases considered (Table 5.2) the discretization error for energy density and mean direction was, respectively, below eight percent and one degree for SSW swell, and three percent and one degree for SE and SW wind sea conditions.

#### **5.5.2.2 Discretization in directional space**

For the establishment of an acceptable discretization resolution of direction ( $\Delta\theta$ ), directional discretization ( $\Delta x$  and  $\Delta y$ ) was fixed at 250 m, while  $\Delta\theta$  was varied (by subsequent halving) between 40 and five degrees. Figure 5.18 shows the result of these tests in terms of the calculated solution at the nearshore S4 station, for the example of Case 4.

The plots in Figure 5.18(b) and (c) show the respective differences in solution between simulations with  $\Delta\theta$  of 40° and 5°, 20° and 5°, and 10° and 5°, to demonstrate the reduction of the error in solution with the decrease of  $\Delta\theta$ . It can be seen in Figure 5.18(b) that when the directional increment is reduced to 10 degrees, the next reduction (to five degrees) resulted in an improvement in energy density of two percent for the SSW swell and one percent for the SE wind seas. The corresponding discretization errors in direction was less than 0,5 degree. It was found in all cases that when the increments are reduced to 10 degrees, the next reduction (to five degrees) would result in an improvement in the solution of energy density and mean direction of eight percent and one degree for SSW swell, and three percent and two degrees for SE and SW wind seas.

#### **5.5.2.3 Combined discretization**

The final step in the discretization process was to evaluate the combined error for discretization in geographical space and direction. Simulations were performed for the four test cases to establish the differences in solution between simulations with the fine discretization of  $\Delta x = \Delta y = 250$  m and  $\Delta\theta = 5^\circ$ , and the discretization of  $\Delta x = \Delta y = 500$  m



and  $\Delta\theta = 10^\circ$ , to indicate the error made by using the coarser discretization in each case

Figure 5.19 shows the result of this test in terms of the calculated solution at the nearshore S4 station, for the example of Case 4 (SSW swell with SE wind sea). Figure 5.19(b) shows that when spatial and directional increments are reduced to  $\Delta x = \Delta y = 500$  m and  $\Delta\theta = 10^\circ$ , a further reduction to  $\Delta x = \Delta y = 250$  m and  $\Delta\theta = 5^\circ$  would result in an improvement in calculated energy density of less than eight percent for the SSW swell ( $< 3$  percent in  $H_{m0}$ ) and three percent ( $< 2$  percent  $H_{m0}$ ) for the SE wind sea component. This reduction in spatial and directional increments resulted in an absolute difference in mean direction of one degree for the swell component, and three degrees for wind sea component. A summary of the combined discretization errors of all cases investigated are presented in Table 5.3 below:

*Table 5.3: Absolute errors for discretization of  $\Delta x = \Delta y = 500$  m and  $\Delta\theta = 10^\circ$*

Case	E(f) (m <sup>2</sup> /Hz)		Dir (°)	
	Swell	Sea	Swell	Sea
1	-	3	-	1,5
4	7,5	4	1	3
7	11	9,2	0,1	0,4
9	7,5	3,5	<0,5	<0,5

### 5.5.3 Discussion

The results of the analysis in Sections 5.5.2.1 and 5.5.2.2 showed the errors for spatial and directional discretization to be of similar magnitude, and relatively small. When the discretization choices of  $\Delta x = \Delta y = 500$  m and  $\Delta\theta = 10^\circ$  are combined, the relative errors given in Table 5.3 were made: maximum error in  $H_{m0}$  of three percent and maximum error in mean direction (at the peak frequency) of three degrees. Considering the results of the above analysis, the scale of the computational area and its significant bathymetric features (Figure 5.1), computational efficiency and relative accuracy, the discretization of the computational grid of the Algoa Bay field case study was chosen at  $\Delta x = \Delta y = 500$  m,  $\Delta\theta = 10$  degrees and  $\Delta\sigma/\sigma = 0,04$ .

The error margin contained in the above choice (the error made by not using the next better numerical solution) can be defined as a model uncertainty, and weakens the ability to resolve correlation errors between simulation results and observations. This uncertainty, which will be regarded in the sections to follow is, however, considered acceptably small.

## 5.6 CONCLUSION

This section described the preparatory work completed for the execution of the Algoa Bay case study. In this section descriptions were given for the selection of Algoa Bay as case study, the selection of environmental conditions and of the positioning and discretization of the computational grids to be used. The following aspects of these choices are highlighted:

- (i) Algoa Bay was selected as a field case, based on the availability of sufficient environmental data, its resemblance to a typical sheltered bay on the South African coast and its bi-modal wave climate.
- (ii) Concurrent time-series measurements of offshore and nearshore directional wave spectra and nearshore wind conditions were available over the period March 1999 to May 1999 at Algoa Bay. From these records, nine characteristic offshore wave conditions were selected for simulation. Conditions inside Algoa Bay were further described by seabed conditions and an estimated typical current flow pattern.
- (iii) It was chosen to use the computational grid at three orientations, depending on the direction of the offshore wave condition. In all cases the offshore boundary, at which the offshore wave condition was applied, was placed approximately along the 100 m contour. Where required, wave input was simulated along lateral model boundaries. Simulation tests were used to tentatively verify the accuracy of the specified boundary values. Due to restrictions on input data, which necessitated the individual model setup of each simulation case, it was decided to employ the time-independent (stationary) mode of SWAN simulation.
- (iv) The discretization of the computational grid was chosen at a spatial increment of  $\Delta x = \Delta y = 500$  m, a directional increment of  $\Delta\theta = 10$  degrees and a frequency resolution of  $\Delta\sigma/\sigma = 0,04$ . The discretization error (defined as the percentage error in nearshore solution incurred by the chosen discretization, above a halving of the spatial and directional increments) was found to be within acceptable limits, i.e. below 11 percent in energy density (< 3 percent in  $H_{m0}$ ) and three degrees in mean direction.

## 6 ALGOA BAY FIELD CASE: FIRST-ESTIMATE SIMULATIONS

### 6.1 INTRODUCTION

This section forms the first part of simulations for the Algoa Bay field case. The aim of this section is to obtain a first-estimate of the performance of SWAN for the Algoa Bay area and conditions. The aspects of the performance of SWAN that were of specific interest were: (a) the refraction of high-energy SSW swell around the headland of Cape Recife to the sheltered nearshore S4 station and (b) the simulation of swell, wind-sea and bi-modal spectra at the S4 station. To this purpose, stationary SWAN simulations were conducted for the nine selected offshore conditions and their corresponding model setup, as was discussed in Section 5. For these first estimates, all simulations were conducted using the developers' recommended (standard) configuration of SWAN (Table 3.2).

The outcome of this section is a comparison between the results of the SWAN simulations and nearshore field recordings in Algoa Bay, in terms of directional wave spectra and integral wave parameters. In addition, the results of this section were used in the selection of conditions for the sensitivity test simulations conducted in subsequent sections.

### 6.2 MODEL SETUP

The model configuration used for the simulations conducted in this section is similar to the recommended configuration presented in Section 3. In addition, the grid layouts, boundary values and discretizations discussed in Section 5 are implemented. Together, the recommended physical processes and parameters, and the selected discretizations will be referred to as the 'default configuration' for the first-estimate simulations of the Algoa Bay field case study. Table 6.1 summarizes the generic configuration used in the simulations of this section:

*Table 6.1: Model setup for first-estimate simulations*

Computational grid					
X length (m)	Y length (m)	Orientation	$\Delta x$ (m)	$\Delta y$ (m)	$\Delta\theta$ (°)
50 000 - 55 000	40 000	10°–30°	500	500	10

Table 6.1: Model setup for first-estimate simulations (continued)

Physics				
Generation	Breaking	Friction	Triads	Quadruplets
Komen <i>et al.</i> (1984)	Battjes and Janssen (1978), $\alpha_{BJ}=1, \gamma_{BJ}=0,73$	Hasselmann <i>et al.</i> (1973), $C_{JON} = 0,067 \text{ m}^2 \cdot \text{s}^{-3}$	off	Hasselmann <i>et al.</i> (1985)
Whitecapping	Refraction	Frequency shift	Setup	Simulation mode
Komen <i>et al.</i> (1984)	on	on	off	Stationary

It is noted that the total dimensions of the computational grid are in excess of the suggested limit of 25 km for wave propagation. However, regarding the geometry of the individual cases, the propagation of wave energy is limited to distances of 35 to 40 km in all cases. Triad-wave interactions were expected to be of low importance at the depth of deployment of the S4, and was, therefore, not included in the first-estimate simulations. Regarding the processes modelled (physics), formulations of wave generation and quadruplet-wave interaction are only included in the cases where wind generation is modelled. A listing of the environmental conditions for each of the nine cases is given in Table 6.2 below (see also Figures 5.8(a)-(c)). The cases are organized into the four categories of offshore wave conditions defined in Section 5 (refer Table 5.1), namely: easterly wind seas (Cat. A), SSW swell with easterly wind seas (Cat. B), SWW swell (Cat. C) and SSW swell with south-westerly wind seas (Cat. D).

Table 6.2: Environmental conditions for first-estimate simulations

Environmental conditions						
Case no.	Cat.	Spectral shape	$H_{m0}$ (m)	$T_p$ (s)	$Dir_p$ ( $^{\circ}$ TN)	$U_{21}$ wind (m/s, dir TN)
1	A	Single peaked seas	3,45	7,69	101,3	10,4 E
2	A	Single peaked seas	3,13	7,14	101,1	8,6 E
3	B	Bi-modal	3,35	15,38	213,5	8,7 W
4	B	Bi-modal	2,80	12,50	197,8	4,0 S
5	C	Single peaked swell	3,48	13,33	200,6	8,8 E
6	D	Bi-modal	4,37	14,29	210,5	5,1 W
7	D	Bi-modal	3,04	11,76	187,8	16,6 W
8	D	Bi-modal	3,67	10,00	229,7	15,1 NW
9	D	Bi-modal	4,69	15,38	195,1	18,9 WSW

The offshore wave conditions and relevant wind fields, as listed above, were included in simulations. No concurrent surface current measurements were available, and were therefore not included in simulations. However, the effect of a typical current field on simulation results is investigated as part of the sensitivity analyses of Section 7. The tidal range for Port Elizabeth is in the order of 2 m. The hourly values of tidal level at the time of simulation (SA Hydrographical Office, 1999) were added to the mean water level in each case.

## **6.3 SIMULATIONS**

In this section the execution of the nine first-estimate simulations are described and the respective results discussed. These descriptions are grouped into the four categories of offshore conditions defined.

### **6.3.1 Category A: Easterly wind seas**

#### **6.3.1.1 Case description**

In this section the two easterly wave conditions of 26/04/99 at 18:00 UT (Case 1) and 27/04/99 at 19:00 UT (Case 2) are described. The test scenarios for these conditions are shown in Figures 6.1 and 6.2 for Case 1, and in Figures 6.3 and 6.4 for Case 2, respectively. The prevailing wind conditions (measured at Jahleel Island) during these wave events are given in Figure B.2(d) in Appendix B.

Figures 6.2(a) and 6.4(a) show the offshore spectra measured at the Waverider station (identified as WR in the legend) which corresponds to the offshore boundary values. These two spectra contain dominant wind seas from around 100° TN, and are similar in shape, being the result of a common storm condition. Of the two spectra, Case 1 is somewhat higher in energy.

Wind generation is not included in the simulation of Case 1 and 2. The reason for this is the following: From Figure B.2(d) in Appendix B it is seen that during both events, the ambient wind was easterly. Furthermore, as described in Section 5, the spectra measured at the Waverider were applied as boundary values to the southerly offshore boundary and easterly lateral boundary. This would imply that all energy generated over the fetch up to the Waverider location is artificially included in the boundary as wave energy. Therefore, for correct energy levels it would only be necessary to apply wind field in the fetch downwind of the offshore station, up to the point of the nearshore station. However, seeing that for an easterly wind the fetch between the offshore and inshore stations is negligible, wind forcing is neglected.

### 6.3.1.2 Results

The plots of Figures 6.1 and 6.3 show the spatial solution of significant wave height and mean direction for Cases 1 and 2. According to this solution, the wave direction (perpendicular to the crests, as denoted by the arrows) is fairly constant over Algoa Bay. Wave directions are uniform ESE along the offshore boundaries, focus at the headland of Cape Recife, and diverge somewhat inside the Bay. Significant wave heights are shown to increase over and behind the Ruy Bank shoal, and to decrease uniformly into the Bay.

Considering the wave spectra in Figures 6.2 and 6.4, it can be seen that the calculated nearshore wave spectra compares generally well with the nearshore observations of between zero and two hours later. For Case 2, correlations for energy density spectra and mean direction are excellent. Nearshore observations show a rotation of mean wave direction from  $100^\circ$  TN to  $120^\circ$  TN, which was reproduced in Cases 1 and 2 with a maximum difference of 10 degrees. However, in Case 1 the levels of the energy density spectrum were significantly over-estimated.

### 6.3.2 Category B: SSW swell with easterly wind seas

#### 6.3.2.1 Case description

In this section the simulations for the two bi-modal wave conditions of 03/03/99 at 23:00 UT (Case 3) and 04/08/99 at 18:00 UT (Case 4) are described. Figures 6.5 and 6.6 show the test scenario for Case 3, and in Figures 6.7 and 6.8 show the scenario for Case 4. The prevailing wind conditions during these two events are given in Figures B.2(a) and B.2(b) in Appendix B, for Cases 3 and 4 respectively.

The offshore energy density spectrum of Case 3 (labelled WR in Figure 6.6(a)) shows a dominant swell component from SSW, in combination with SE wind seas of lower energy. During this event, winds of  $U_{21} = 8,7$  m/s were recorded at Jahleel Island, coming from a westerly direction. However, considering that the nearshore station has virtually no fetch on its westerly side, this wind field was neglected.

The offshore energy density spectrum of Case 4 (labelled Figure 6.8(a)) contains a combination of SSW swell and SE seas, with energy peaks of comparable magnitude. Winds of  $U_{21} = 4,0$  m/s, from a southerly direction, were recorded at Jahleel Island during this event. This wind field was related to a reference wind speed at  $U_{10}$  and included in the simulation.

### 6.3.2.2 Results

Figures 6.5 and 6.7 show the solutions of significant wave height and mean direction over the Bay for Cases 3 and 4, respectively. It is seen that for Case 3 (Figure 6.5) the mean wave direction takes the orientation of the dominant swell, while in Case 4 (Figure 6.7), the mean wave direction is found between the directions of the wind-sea and swell components. The wave directions in the spatial solution of Case 3 display a large amount of rotation and spreading of wave fronts in the lee of Cape Recife. In Case 4, where swell is less dominant, the wave field appeared to be greatly affected by the SE wind sea. Wave directions in the lee of Cape Recife were similar for both cases, but away from the shelter of Cape Recife, wave directions of Case 4 were uniformly more easterly than for Case 3.

Figures 6.6 and 6.8 provide the spectral solutions of Cases 3 and 4 at the S4 station. Figure 6.6 shows that for the simulation of Case 3 both the spectral energy levels and mean directions are in very good correlation with observations. It is seen that the dominant swell component is considerably reduced at the inshore station, and its mean direction greatly changed (215° TN to 150° TN). Both these changes are well reproduced by SWAN. The sea component retains its SE direction and about half of its spectral energy, and was equally well reproduced. In Case 4 (Figure 6.8) the correlation of nearshore results varied. The reduction and rotation of the SSW swell correlated well with observed values, and the direction of the wind-sea component is reproduced to within 10 degrees of observations. However, similar to what was found in Case 1 above, the spectral energy level of the easterly seas component appears to be over-estimated.

### 6.3.3 Category C: SSW swell

#### 6.3.3.1 Case description

This category comprises the single condition of 13/05/99 at 18:00 UT (Case 5), of which the test scenario and wave conditions are presented in Figures 6.9 and 6.10. The corresponding wind condition is presented in Figure B.2(e) in Appendix B.

Case 5 represents a condition of single-peaked, high-energy swell from SSW, originating from a distant offshore storm. Winds of speed  $U_{21} = 8,8$  m/s, from an easterly direction, were recorded during this event. This wind field was included in the simulation.

### 6.3.3.2 Results

Figure 6.9 shows the spatial solution of significant wave height and mean wave direction for Case 5. From the arrows indicating mean wave direction it is seen that significant rotation of wave fronts occurs around Cape Recife and inside the Bay. The wave height plot shows that energy is focussed behind the Ruy Bank shoal, but otherwise reduce gradually as energy diverges in the Bay. It is significant that an area of low wave height is found in the lee of Cape Recife.

The calculated and observed wave spectra at the offshore and nearshore stations are presented in Figure 6.10. It is shown that, in both simulation and observation, the energy density of the SSW swell is greatly reduced by the sheltering of Cape Recife, and that mean wave directions changed from 200° TN to 155° TN. In the simulation results, the rotation of mean wave directions is over-estimated, but is within 10 degrees of measured values. The reduction of spectral wave energy is well represented in the model results, although under-estimated. Between the frequencies of 0,15 and 0,2 Hz evidence of wind-wave growth is found in the observed S4 spectrum. By the incorporation of an easterly wind field this wave growth was reproduced with a reasonable degree of success.

### 6.3.4 Category D: SSW swell with SW wind seas

#### 6.3.4.1 Case description

Category D comprises wave conditions of SSW swell combined with seas spanning the directional sector of SW to WSW. The following records fall in this category: 23/04/99 at 21:00 UT (Case 6), 18/04/99 at 12:00 UT (Case 7), 19/04/99 at 08:00 UT (Case 8), and 21/04/99 at 15:00 UT (Case 9). These are presented in Figures 6.11 to 6.18. The corresponding wind conditions during these events are shown in Figure B.2(c) in Appendix B. The simulation conditions are described, in turn, below:

- Case 6 (Figure 6.12) features high energy SSW swell, with a minor component of SW wind sea. The wind during this event was westerly.
- Case 7 (Figure 6.14) comprises a low energy SSW swell coupled with WSW wind sea of similar energy. Wind during this event was westerly.
- Case 8 (Figure 6.16) features high energy SW swell, with a minor component of WSW wind sea. The wind during this event was north-westerly.
- Case 9 (Figure 6.18) comprises high-energy SSW swell coupled with a minor component of WSW wind sea. Wind during this event was west-south-westerly.



In all these cases, the prevailing winds were westerly. Considering that no fetch exists to the west of the inshore station, these wind fields were not included in the simulations.

#### **6.3.4.2 Results**

Figures 6.11, 6.13, 6.15 and 6.17 show the solutions of significant wave height and mean direction for the cases of south-westerly wave conditions considered. These cases display similar results in terms of mean wave direction and significant wave height distribution. Wave directions changed noticeably in the shallower regions inside the Bay, and wave crests rotated significantly around Cape Recife. For all cases, significant wave heights reduced gradually from the offshore to the nearshore as wave energy diverged in the Bay. It was found in all cases that significant wave heights increased downwave of the Ruy Bank shoal, as found consistently for the Cases 1 to 5.

Figures 6.12, 6.14, 6.16 and 6.18 show the simulation results of wave spectra at the nearshore station. These figures show that a generally good correlation was found between the calculated and observed inshore spectra. Figure 6.12 (Case 6) show that the reduction of wave energy by sheltering is in excellent agreement with observations. The rotation of wave direction ranges from 205° to 265° TN, to 155° to 175° TN, and was reproduced with a difference of about 10 degrees relative to observations (simulated directions to the east of observations).

Figure 6.14 (Case 7) shows the inshore result for a bi-modal condition (SSW swell and WSW), with swell and wind-sea components of similar magnitude. The correlation between the observed and calculated spectra for this case is not good. For the swell component of the spectrum the reproduction of the inshore spectrum was reasonable, both in energy density and mean direction. However, over the seas portion of the spectrum, wave direction differed by about 20 degrees, and energy density was underestimated. Considering the rapid change in the inshore energy density levels, this lack of correlation would appear to be due to the non-stationary nature of the environmental conditions modelled.

Figure 6.16 (Case 8) presents the nearshore spectral results of the offshore condition with a dominant SW swell. The observations show that wave energy of the SW swell condition is significantly reduced, and its mean direction changed from 230° TN to between 150° and 170° TN. The reduction in energy density and change in mean direction of the simulation corresponds well with these observations. The difference between the calculated and observed mean wave direction is about 10 degrees (simulated direction to the south of observations).

Figure 6.18 (Case 9) shows the spectral results of an offshore SW swell and a WSW seas condition. Comparing calculated and observed nearshore spectra, it is seen that the correlation is quite good. However, energy density was somewhat overestimated by the model, and the mean direction differed from the observed values by about 10 degrees (simulated direction to the east of observations).

In summary, correlation between the calculated and measured spectra at the nearshore station was generally good. There was, however, a tendency for the calculated mean wave direction to be about 10 degrees to the east of observations. In addition, energy densities and mean wave periods at the nearshore S4 station tended to be somewhat over-estimated by the model.

#### 6.4 SUMMARY OF RESULTS

The simulation results of Section 6.3 are summarized in Tables 6.3 and 6.4 and plotted Figures 6.19(a) and (b). In this summary the calculated integral parameters of significant wave height ( $H_{m0}$ ), mean period ( $T_{m01}$ ) and mean wave direction at the nearshore S4 station are compared against observations. Although conditions were generally stationary, the nearshore measurements used in the comparison are those taken one hour later than the offshore measurement, to allow for the propagation of peak energy components (in prototype) across the simulated area.

Due to the high-frequency cut-off of the measured spectra (refer Section 5.3.2), all three integral parameters in the simulated and observed results are calculated only up to the 0,2 Hz spectral component, for sake of comparability. Due to this choice, the calculated values of  $T_{m01}$  are somewhat biased (1 – 2 s higher than their true value), and are therefore denoted as  $T_{m01}'$ . The values of  $H_{m0}$  and mean direction are also calculated in this manner, but are not significantly affected by this definition. Differences between the simulated and observed nearshore parameters are given in terms of relative errors in Table 6.4. The relative errors in  $H_{m0}$ ,  $T_{m01}'$  and mean wave direction are defined as follows:

$$\% \text{ rel. error in } H_{m0} = 100 \times (H_{m0, SWAN} - H_{m0, observed}) / H_{m0, observed} \quad (6.1)$$

$$\text{rel. error in } T_{m01}' = T_{m01, SWAN}' - T_{m01, observed}' \quad (6.2)$$

$$\text{rel. error in } Dir = Dir_{SWAN} - Dir_{observed} \quad (6.3)$$

Using the indices of (6.1), (6.2) and (6.3), positive values of relative errors imply over-estimation of significant wave height and mean wave period, and a mean wave direction which is to the south of the observed value.

*Table 6.3: Summary of first-estimate results for Algoa Bay field case*

Case no.	$H_{mo, obs}$ (m)	$T_{m01', obs.}$ (s)	$Dir_{, obs.}$ (° TN)	$H_{mo, SWAN}$ (m)	$T_{m01', SWAN}$ (s)	$Dir_{, SWAN}$ (° TN)
1	1,8	7,1	118,6	2,2	7,3	115,5
2	2,1	7,3	122,5	2,0	7,2	115,5
3	1,5	8,6	140,6	1,6	8,3	133,5
4	1,4	7,7	132,4	1,7	7,7	132,1
5	1,3	8,9	152,2	1,5	10,6	147,5
6	1,4	11,3	156,8	1,5	11,2	149,6
7	1,2	9,2	139,2	1,0	9,9	147,2
8	0,7	10,6	148,7	0,7	10,0	153,9
9	1,7	12,0	153,6	1,9	13,4	145,9

*Table 6.4: Relative error of first-estimate results for Algoa Bay field case*

Case no.	Rel. error in $H_{mo}$ (%)	Rel. error in $T_{m01'}$ ( $\Delta s$ )	Rel. error in $Dir$ ( $\Delta^\circ$ )
1	19,2	0,2	-3,0
2	-1,2	-0,1	-7,0
3	3,2	-0,3	-7,1
4	23,5	0,0	-0,3
5	9,5	1,6	-4,8
6	7,7	-0,1	-7,3
7	-19,2	0,7	8,1
8	0,9	-0,6	5,2
9	12,0	1,4	-7,7

#### 6.4.1 Comparison of significant wave heights

The comparison between simulated and observed significant wave height is presented in Tables 6.3 and 6.4 and Figure 6.19(a). In three cases (Case 2 from Cat. A (ESE), Case 3 from Cat. B (SSW/SE) and Case 8 from Cat. D (SSW/SW)), calculated and observed values compared within three percent accuracy, which is within the limits of the discretization error (Section 5). However, there appeared to be a tendency for calculated wave heights to be over-estimated. Two simulated conditions with SE/ESE

seas, Cases 1 and 4, significantly over-estimated the nearshore wave energy (19 percent and 23,5 percent respectively). Over-estimation was also found for three cases with offshore SSW swell, namely Cases 5, 6 and 9. In contrast, Case 7, featuring a bi-modal spectrum with SW seas, displayed significant under-estimation of nearshore wave energy. This lack of correlation was shown to be due to the development of high-frequency peak in the spectrum, which was recorded at the S4 station (Figure 6.14).

#### **6.4.2 Comparison of mean wave period**

Tables 6.3, 6.4 and Figure 6.19(a) show a good correlation between calculated and observed values of  $T_{m01}$ . Correlations for south-easterly wind sea cases appear to be better than for the south-westerly swell cases. Two notable differences appear for two SSW swell conditions, Cases 5 and 9, where periods were over-estimated by 1,6 s and 1,4 s respectively.

#### **6.4.3 Comparison of mean wave direction**

In Section 5.5 the discretization error in mean direction was established as about three degrees. In Section 5.3.3 it was shown that instrument observations were estimated to be accurate to within seven degrees. Tables 6.3, 6.4 and Figure 6.19(b) show a generally good correlation between calculated and measured values of mean wave direction for all cases. The maximum difference in mean direction was about eight degrees, which is significantly above the estimated discretization error, but within the recording error of the instrumentation. There was a tendency in the calculated results, both for ESE wind sea and SSW swell, to be to the east of observed values (negative relative difference in Table 6.4).

Two exceptions to the general findings were Cases 7 and 8 where nearshore mean directions were found to err to the south of the observed values. In the example of Case 8, the offshore swell direction was quite westerly ( $229,3^\circ$  TN) compared to the other swell cases, and the calculated inshore direction south of the observed direction.

### **6.5 CONCLUSION**

In this section, simulations were conducted for the Algoa Bay field case, using the 'default configuration' of SWAN which is based on the recommendations given in Holthuijsen *et al.* (1999). Simulations were conducted for a selection of nine observed offshore spectra, representing typical conditions for the field case. From the simulation results presented, it is concluded that the SWAN simulations for Algoa Bay, using the 'default configuration' model setup, shows generally good comparison with



observations, both in terms of wave spectra and integral parameters. This conclusion is based on comparisons of both directional wave spectra and their integral parameters, for a relatively large selection of offshore wave conditions, containing swell, wind sea and combinations thereof, for a wide sector of directions. However, the simulation results identified the following aspects:

- a) For easterly sea conditions, calculated nearshore wave energy appeared over-estimated (by about 20 percent of the observed  $H_{m0}$ ). Reasons for the discrepancy may be erroneous boundary values and/or the treatment of wind-wave generation, or the selection of physical processes (refraction, bottom friction, etc.). It was found that simulated mean directions were constantly to the east of observations, which corresponds to the recording bias of the S4, as indicated in Section 5.3.3.
- b) For the SSW swell conditions, significant wave heights tended to be over-estimated by about 10 percent, and mean periods were over-estimated by a maximum of 1,6 s. Reasons for these differences, which fall outside of the recording and discretization errors, could be depth-induced refraction or other physical process (bottom friction, etc.), excessive directional spreading, or the influence of current. Wave directions were found to differ from observations by a maximum of about eight degrees, with a tendency of simulation results to be to the east of observations. This difference in mean direction falls within the measurement accuracy of the recording equipment.
- c) For one bi-modal condition, inaccuracy in simulation results was found to be due to the generation of a high-frequency component from SE, which could not be reproduced in the present stationary simulations. Due to the non-stationary nature of the observation, this case will not be pursued further.

The investigation of possible causes of inaccuracy in these first-estimate simulations is the subject of the next section of this report. In this section, various components of the SWAN simulation are considered and their effect on the nearshore solution result quantified.

## **7 ALGOA BAY: SENSITIVITY TESTS ON PHYSICAL PROCESSES**

### **7.1 INTRODUCTION**

In Section 6 a first estimate of the performance of SWAN for the Algoa Bay field case was made by means of simulations based on the model developers' recommended (default) setup for physical processes of SWAN. The aim of the present section is to investigate, for the Algoa Bay field case, the relative influence of these physical processes on the results produced by SWAN, and the sensitivity to the choice of their coefficients.

The sensitivity evaluation was limited to processes that were expected to affect the wave conditions up to the nearshore S4 station, which was at 17 m water depth. The processes selected for investigation were: depth-induced refraction, bottom friction, triad-wave interactions, wave-current interaction and directional spreading. These evaluations were done for a sub-set of the nine offshore wave conditions selected for simulation (Section 5).

### **7.2 TEST CONDITIONS**

For the investigation of wave processes in Algoa Bay, a sub-set of three representative offshore wave conditions were selected, from the nine conditions selected in Section 5 and modeled in Section 6. The three selected conditions are: a condition with ESE wind sea – 26/04/1999 at 18:00 UT (Case 1), a bi-modal condition with SSE swell and SE wind sea – 08/04/1999 at 18:00 UT (Case 4) and a bi-modal condition with SSE swell and WSW wind sea – 21/04/1999 UT (Case 9).

These three offshore conditions were selected on two criteria: Firstly, these conditions represent good examples of the characteristic conditions found in Algoa Bay during the measurement period, namely dominant ESE wind sea (with E wind), SSW swell with SE wind sea (with S wind), and a dominant SSW swell with WSW wind sea. Secondly, the first-estimate simulation results of the conditions showed the largest differences with respect to observations (Section 6).

### **7.3 SCOPE OF TESTS**

A series of sensitivity tests were conducted for each of the three selected offshore conditions. These tests investigated the processes in SWAN which were expected to have an influence over the deeper regions of Algoa Bay and up to the moderate depth

of 17 m in which the nearshore S4 station was located. Because of the absence of calibration information in regions shallower than 17 m, the scope of tests was limited to the following: depth-induced refraction, wave-current interaction, directional spreading, bottom friction and also the shallow water process of triad-wave interaction. Sensitivity of the process of depth-induced breaking was not included. A listing of the simulations that were conducted is presented in Table 7.1 below. Descriptions of each of the tests, as well as reasons for choices of coefficients, are given in later sections. All simulations were conducted in the stationary mode of SWAN.

*Table 7.1: SWAN sensitivity tests for Algoa Bay field case*

Test series	Cases tested	Test description
a	1,4,9	Default configuration (as in Section 6)
b	1,4,9	Default configuration, refraction disabled
c1	1,4,9	Default configuration, bottom friction disabled
c2	1,4,9	Bottom friction of Hasselmann <i>et al.</i> (1973), $C_{JON} = 0,038 \text{ m}^2\text{s}^{-3}$
d1	1,4,9	Bottom friction of Collins (1972), with $C_f = 0,015$
d2	1,4,9	Bottom friction of Collins (1972), with $C_f = 0,10$
e1	1,4,9	Bottom friction of Madsen <i>et al.</i> (1988), with $K_N = 0,01 \text{ m}$
e2	1,4,9	Bottom friction of Madsen <i>et al.</i> (1988), with $K_N = 0,05 \text{ m}$
e3	1,4,9	Bottom friction using Madsen <i>et al.</i> (1988), with $K_N = 0,10 \text{ m}$
f	1,4,9	Triad-wave interactions of Eldeberky (1996), with $\alpha_{EB} = 0,1$
g	9	Default configuration, current field imposed
h1	9	Directional spreading width imposed at $10^\circ$ standard deviation
h2	9	Directional spreading width imposed at $30^\circ$ standard deviation

## 7.4 SIMULATION RUNS

### 7.4.1 Depth-induced refraction In Algoa Bay

In this section the investigation into the influence of depth-induced refraction on wave height and direction in Algoa Bay is described. This investigation was conducted using the model developers' recommended (default) SWAN configuration, as applied in Section 6. The influence of refraction on the simulation results is obtained by conducting two successive simulations with the default SWAN configuration - one with depth-induced refraction included and the second with refraction disabled. The results of the two simulations were analyzed graphically, by means of spatial *difference plots* (subtraction of two spatial solutions) and by inspecting the differences between the two calculated nearshore directional spectra.



#### **7.4.1.1 Results: Case 9**

Figure 7.1 shows a difference plot for wave direction for the typical SSW swell condition of Case 9. The shaded contour areas in the plot represent the absolute magnitude of the difference in mean wave direction between the simulation solutions with and without depth-induced refraction. The plot, therefore, shows how mean wave direction was influenced by depth-induced refraction in the different areas of the Bay. This plot shows how a SSW swell field is refracted around Cape Recife during its propagation into the Bay, resulting in increasing differences in mean wave direction as it moves around the Cape, compared to the non-refraction solution.

Figure 7.1 shows that refraction has a significant influence on mean wave direction in the Bay for the SSW swell condition. Differences in wave direction become notable inshore of the 60 m contour where wave-front rotation of five degrees was calculated, and are most prominent in the lee of Cape Recife, where rotation of up to 50 degrees were found. At the location of the nearshore S4 station refraction caused a change in mean direction of 18 degrees. Significant wave rotation was also found leeward of the Riy Bank shoal.

Figure 7.2 presents the influence of depth-induced refraction on the simulated wave height in Algoa Bay. Areas where refraction caused, respectively, increases and decreases in significant wave height are displayed. From the plot it is seen that refraction increases the wave height in the Bay area in the lee of Cape Recife and down-wave of the Riy Bank shoal, as expected. It was found that depth-induced refraction accounts for increases in significant wave height at the nearshore S4 station of 0,22 m (about 11 percent of default simulation value inshore). Figure 7.1 and 7.2 confirm the assumption made in Section 5 at the selection of boundary position, namely that only minor refraction effects occur offshore of the 85 m contour.

Figure 7.3 compares the calculated nearshore spectra at the S4 station for the cases with and without refraction. In terms of energy density, the absence of refraction has a significant effect, and would appear to bring the peak energy level down to that of the observed values. However, this apparent improvement is misleading, because the correlation between mean wave direction and observations decreased with the disabling of refraction.

#### **7.4.1.2 Results: Case 1**

The influence of refraction on Case 1 is presented in Figures 7.4 to 7.6. The difference plot of Figure 7.4 shows significant change in wave direction on the north and south faces of Cape Recife, as well as inside the Bay, immediately north of the nearshore

station. The change in wave direction at the nearshore S4 station caused by refraction is 3,5 degrees. Figure 7.4 shows that a small amount of wave rotation was calculated down-wave of the Riy Bank, and that, as in Case 9, the wave field at the offshore Waverider station experienced minimal rotation due to refraction.

Figure 7.5 shows the difference plot for significant wave height due to refraction. This plot shows a general decrease (divergence) of wave energy inside the Bay, although some localized increase of wave energy was found at the tip of Cape Recife. Notable localized increase of wave height is also found at the Riy Bank. Figure 7.5 shows that refraction caused a reduction in significant wave height at the nearshore S4 station of 0,11 m (about five percent of default simulation value inshore).

Figure 7.6 presents the calculated nearshore spectra for the cases with and without refraction. The plot of energy density shows a slight decrease in energy at the peak spectral frequency due to refraction, corresponding to the results in Figure 7.5. The plot of the frequency distribution of mean wave direction reveals a small change in direction due to refraction.

#### **7.4.1.3 Results: Case 4**

The influence of depth-induced refraction on Case 4 is presented in Figures 7.7 to 7.9. The difference plot of Figure 7.7 shows the calculated change of mean direction due to refraction. The directional change displayed in this plot is due to the combination of swell and wind sea, and is, therefore, be similar to a combination of Cases 9 and 4 (Figures 7.1 and 7.4, respectively).

Figure 7.7 shows that for most of the Bay, depth-induced refraction accounted for changes in wave direction of two to six degrees. The largest wave-front rotation was found at the northern face of Cape Recife, where refraction caused changes in mean wave direction of up to about 24 degrees. In contrast, the region north of the nearshore S4 station experienced little wave-front rotation. At the nearshore station the influence of refraction on mean wave direction was 4,1 degrees. As for Cases 1 and 9, refraction accounts for significant change in wave direction at the Riy Bank.

Figure 7.8 presents the calculated difference plot for significant wave height due to refraction. This plot presents interesting results of the combined effect of refraction of swell and wind sea on the significant wave height parameter. Increases in wave height were found at the tip of Cape Recife. Significant increase of wave height was also found at the Riy Bank. However, over the greater Bay region, the significant wave height was only slightly reduced. This finding contrasts with the results of Cases 1 and 9 where refraction caused, respectively, notable reduction and increase in wave height.

Significant wave height at the nearshore S4 station was virtually unaffected by refraction (0,01 m, which is one percent of the default simulation value nearshore).

Figure 7.9 reveals the effect of refraction on the bi-modal spectrum at the S4 station. It is shown that the swell component increased in energy due to the inclusion of refraction around Cape Recife, while the wind sea component experienced a reduction in energy due to the refraction-induced divergence of wave energy nearshore. However, the netto effect of these movements was nearly zero when integrated into a significant wave height, which accounts for the results of Figure 7.8. In terms of mean wave direction per frequency component, Figure 7.9 shows that the swell component was most strongly affected by refraction, as expected.

#### **7.4.1.4 Discussion**

The results of this section showed that depth-induced refraction has a significant influence on the simulation results at the S4 station for the three cases investigated. Refraction plays a significant role in establishing the inshore result of the high-energy SSW swell condition of Case 9, where it accounts for about 11 percent of significant wave height and an 18 degree change in wave-direction. In comparison, it was found that the effect of depth-induced refraction was relatively smaller for Case 1 (3,5 degree in direction and five percent in  $H_{m0}$ ) and Case 4 (4,1 degree in direction and one percent in  $H_{m0}$ ). This indicates that these lower-period and lower-energy wave conditions are less affected by depth-induced refraction than Case 9, as expected.

#### **7.4.2 Energy dissipation due to bottom friction**

In this section the investigation into the effect of bottom friction in the Algoa Bay field case is described. The aim of this investigation was, firstly, to establish the magnitude of depth-induced dissipation over the study area, and secondly to compare the simulation results of the three friction formulations available in SWAN (see Section 2) with observations. The investigation was conducted for Cases 9 (high-energy swell in bi-modal spectrum), Case 1 (moderate-energy wind sea) and Case 4 (moderate-energy bi-modal spectrum).

##### **7.4.2.1 Input values**

Three formulations for bottom friction are available in SWAN, representing three basic types of friction formulation (see Section 2). Simulations were conducted for all three of these formulations, using a selection of values for their coefficients, based on recommendations in the literature.

For the formulation of Hasselmann *et al.* (1973), coefficient values of  $C_{JON} = 0,038 \text{ m}^2 \cdot \text{s}^{-3}$  are recommended for swell conditions and  $0,067 \text{ m}^2 \cdot \text{s}^{-3}$  for a wind sea condition (Bouws and Komen, 1983). The coefficient  $C_f$  in the formulation of Collins (1972) is frequently taken as 0,015 in models (value proposed by Collins), but has been found to increase up to 0,10 for large grain diameters of seabed material (Hsiao and Shemdin, 1978). For the Madsen *et al.* (1988) model, applied to a sandy sea bed, Tolman (1991) considered the possible range of bottom roughness values to be from  $K_N = 200 \text{ } \mu\text{m}$  (grain roughness) to  $K_N = 0,2 \text{ m}$  (ripple roughness). After calibration over various depths (120 m – 7,5 m) Tolman recommended a value of  $K_N = 0,05 \text{ m}$  as the best general fit to his test cases.

Table 8.2 below lists the default values of the friction coefficients, per formulation, as recommended by Holthuijsen *et al.* (1999). As was listed in Table 3.2, of these three formulations, the one proposed by Hasselmann *et al.* (1973) is recommended by Holthuijsen *et al.* (1999) as the overall default choice.

*Table 7.2: Recommended (default) values of friction coefficients in SWAN (Holthuijsen et al. (1999))*

Formulation	Default SWAN coefficient values
Hasselmann <i>et al.</i> (1973) (default formulation)	$C_{JON} = 0,067 \text{ m}^2 \cdot \text{s}^{-3}$
Collins (1972)	$C_f = 0,015$
Madsen <i>et al.</i> (1988)	$K_N = 0,05 \text{ m}$

For the SWAN simulations presented in this section, the following choices of coefficients were made (Table 7.3 below, refer Table 7.1): For Hasselmann *et al.* (1973) (default formulation), the default value of  $C_{JON} = 0,067 \text{ m}^2 \cdot \text{s}^{-3}$  was tested as well the value of  $C_{JON} = 0,038 \text{ m}^2 \cdot \text{s}^{-3}$ , the latter being appropriate to swell conditions. For the Collins (1972) formulation, simulations were conducted at moderate roughness ( $C_f = 0,015$ ) and at high roughness ( $C_f = 0,10$ ). For the formulation of Madsen *et al.* (1988) simulations were conducted for the following roughness length scales:  $K_N = 0,01 \text{ m}$ ,  $K_N = 0,05 \text{ m}$  and  $K_N = 0,10 \text{ m}$ . For comparison, for each offshore condition, a simulation was also conducted with bottom friction disabled.

Table 7.3: SWAN bottom friction sensitivity tests for Algoa Bay field case

Test series	Cases tested	Test description
c1	1,4,9	Default configuration, bottom friction disabled
c2	1,4,9	Bottom friction of Hasselmann <i>et al.</i> (1973), $C_{JON} = 0,038 \text{ m}^2\text{s}^{-3}$
d1	1,4,9	Bottom friction of Collins (1972), with $C_f = 0,015$
d2	1,4,9	Bottom friction of Collins (1972), with $C_f = 0,10$
e1	1,4,9	Bottom friction of Madsen <i>et al.</i> (1984), with $K_N = 0,01 \text{ m}$
e2	1,4,9	Bottom friction of Madsen <i>et al.</i> (1984), with $K_N = 0,05 \text{ m}$
e3	1,4,9	Bottom friction using Madsen <i>et al.</i> (1984), with $K_N = 0,10 \text{ m}$

#### 7.4.2.2 Results: spatial distribution

Simulation results for Cases 9, 1 and 4 with various bottom friction formulations are given in Figures 7.10 to 7.15. Figures 7.10, 7.12 and 7.14 present, for each case, the spatial difference plots for wave height for two consecutive simulations, respectively with bottom friction enabled (default simulation as in Section 6) and bottom friction disabled. These plots, therefore, show the effect of the Hasselmann *et al.* (1973) friction formulation (with default coefficient value of  $C_{JON} = 0,067 \text{ m}^2\text{s}^{-3}$ ) on the result of simulated wave height.

The spatial difference plot of Figure 7.10 shows that for the high-energy swell condition of Case 9, bottom friction was responsible for reduction in significant wave height of up to about 0,5 m. At the nearshore station, bottom friction accounted for a significant wave height reduction of 0,26 m (about 14 percent of default simulation value nearshore). Figure 7.10 shows that the cumulative height loss increased gradually over the Bay, but increased rapidly in areas shallower than 30 m. The most significant losses occurred north of the nearshore S4 station where high levels of wave energy were incident. Local increases in bottom friction dissipation were also found at Cape Recife, and on the Ruy Bank shoal.

The difference plot of Figure 7.12 shows that for the wind sea condition of Case 1 bottom friction accounted for significant wave height loss of up to 0,2 m, which is less than half of the result for Case 9. At the nearshore S4 station, reduction of significant wave height was 0,1 m (about five percent of the default simulation value). Energy loss due to bottom friction was experienced over the entire bay area, but was most significant in regions shallower than 30 m.

Figure 7.14 shows the spatial difference plot for the combined wind sea and swell condition of Case 4. The maximum dissipation of significant wave height in the bay

was found to be 0,16 m. At the nearshore S4 station loss of wave height due to bottom friction dissipation was 0,08 m (about five percent of the default simulation value). The spatial distribution of bottom friction dissipation shows, as in the previous cases, gradual loss of energy over the entire bay, increasing significantly in regions shallower than 30 m. In contrast to Cases 1 and 9, the solution of Case 4 displays its maximum level of dissipation along the entire coastline northwards of Cape Recife.

#### 7.4.2.3 Results: Spectra

The calculated spectra at the nearshore S4 station for the simulations with the selected bottom friction formulations and coefficients are shown in Figures 7.11, 7.13 and 7.15. The simulation results of Cases 9, 1 and 4 have the following in common: Firstly, it is clear that dissipation was the greatest at the peak spectral frequency. Secondly, the solutions obtained by the formulations of Hasselmann, Collins and Madsen, using the values recommended in Holthuijsen *et al.* (1999), displayed a similar relation for all three cases: It was found throughout that Madsen *et al.* (1988), with  $K_N = 0,05$  m produced the most dissipation, followed by Hasselmann *et al.* (1973) with  $C_{JON} = 0,067 \text{ m}^2 \cdot \text{s}^{-3}$ , with Collins (1972) with  $C_f = 0,015$  producing the least amount of dissipation. When the coefficients were varied from the default values, it was found that the formulation of Hasselmann *et al.* (1973) with  $C_{JON} = 0,038 \text{ m}^2 \cdot \text{s}^{-3}$  produced the least amount of dissipation, while the formulation of Collins (1972) with  $C_f = 0,10$  produced the most. The formulation of Madsen *et al.* (1988) with  $K_N = 0,10$  m appeared to produce the best correlations with observations.

Sensitivity to friction formulation and coefficients were the most pronounced for Case 9 (high-energy swell), where dissipation was significant. Cases 1 and 4, which feature wind sea and lower energy swell, bottom friction dissipation was comparatively low, especially for the wind sea component.

#### 7.4.2.4 Discussion

The results of the sensitivity tests for bottom friction are in good correlation with the theoretical behaviour of the bottom friction source term (Figure 2.2). It was found that dissipation was the largest at the peak spectral frequency, and that dissipation increased with decreasing relative depth ( $k.d$ ). Furthermore, it was found that dissipation increased with increased wave energy. This explanation agrees with the finding that the highest dissipation was calculated for the high-energy swell of Case 9, in areas shallower than 30 m.

It was found that for the recommended (default) friction coefficients taken up in SWAN, the formulation of Madsen yielded the largest dissipation and that of Collins the least, with the result of Hasselmann in between. This finding corresponds to a

recommendation to the same effect given by Holthuijsen *et al.* (1999). Based on the results of this section, the sensitivity to bottom friction is the most significant to Case 9. For this condition, significantly improved correlation between simulation results and observations was obtained by the formulation of Madsen *et al.* (1988), with  $K_N = 0,10$  m. This formulation also improved correlation for Cases 1 and 4, although energy was still not deduced to desired levels.

### **7.4.3 Triad-wave interactions**

In this section the contribution of triad-wave interaction to the results of the Algoa Bay field case is considered. The aim of this investigation is to determine the relative magnitude of the influence that triad interactions have on the results at the nearshore station. This investigation was conducted for the offshore conditions of Case 1, 4 and 9, by means of consecutive simulations with triad-wave interactions respectively activated and de-activated.

#### **7.4.3.1 Results: Spatial distribution**

The results of the simulations for triad-wave interactions are presented in Figures 7.16 to 7.21. The results of the spatial distribution of triad interactions are presented as difference plots in Figures 7.16, 7.18 and 7.20. In these plots the occurrence of triad-wave interactions are represented by their influence on the mean wave period  $T_{m01}$ . The relative change in  $T_{m01}$  is obtained in these difference plots by taking, in each case, the difference of the spatial solutions for  $T_{m01}$  with and without triad interactions.

The difference plots for Cases 1, 4 and 9 reveal the simulated contribution of triad interactions to mean wave periodicity in Algoa Bay to be minor. The most significant occurrence of triad interactions was for Case 9 (Figure 7.16). For this high-energy swell condition, the mean wave period was shifted by up to 4 s at locations along the coast inshore of the 10 m contour, in the lee of Cape Recife and over the Riy Bank. However, at the nearshore S4 station, a reduction in mean wave period of only 0,2 s was calculated. For Cases 1 and 4 (Figures 7.18 and 7.20, respectively) the effect of triad-interactions was confined to the coastline, inshore of the 10 m contour. The reduction in mean wave period at the nearshore S4 station was generally between zero and 1 s for both these cases. For these cases mean wave periods were unaffected at the S4 station.

#### **7.4.3.2 Results: Spectra**

The spectra at the nearshore S4 station, for the simulations with and without the inclusion of triad interactions are presented in Figures 7.17, 7.19 and 7.21. These plots show that the effect of the interactions at the nearshore station, in terms of energy

density and direction distribution, was generally very small. The only evidence of the generation of high-frequency harmonics can be seen for Case 9 in Figure 7.17(a), where an amount of energy was distributed to a frequency of 0,13 Hz.

#### **7.4.4 Wave-current interaction**

This section describes the investigation into wave-current interaction for the Algoa Bay field case. The aim of this investigation was to determine the magnitude and spatial distribution of changes in mean wave direction and absolute wave period due to currents in the Bay. The investigation was conducted only for Case 9, for which the appropriate environmental conditions prevailed.

##### **7.4.4.1 Test conditions**

It was pointed out in Section 5 that no surface current measurements are available over the period considered for the Algoa Bay study. No numerical current modelling was conducted either, as this was considered to fall outside the scope of this study. Rather, typical current flow conditions, as presented in the literature, were considered. A typical surface current pattern during a period of moderate ( $U_{10} = 8-11$  m/s) south-westerly winds has been measured by Goschen and Schumann (1988) along sampling tracks. These measurements were linearly interpolated to cover the complete Bay area (Section 5, Figure 5.6). The wind conditions leading up to the time of Case 9 (Fig B.2(c) in Appendix B) correspond to those observed by Goschen and Schumann. It is, therefore, reasonable to assume that a similar current flow to that presented in Figure 5.6 may have been found during the observation period of Case 9. Therefore, the flow pattern based on the observations by Goschen and Schumann was applied as environmental condition for the wave-current simulation of Case 9.

##### **7.4.4.2 Results: Spatial distribution**

The results of the simulation with wave-current interaction for Case 9 are presented in Figures 7.22 and 7.23. The results are presented in terms of spatial difference plots, showing the change in absolute mean period ( $T_{m01}$ ) and mean wave direction, respectively, for simulations with and without wave-current interaction.

Figure 7.22 presents the spatial change in mean absolute period ( $T_{m01}$ ) due to current, by showing the difference between simulations with and without the current field. The simulation conditions without current is equal to that of Section 6. The difference plot shows distinctive areas where the absolute wave period was somewhat increased or reduced. The wave periods were found to increase where strong following currents were found, and decrease where weak or opposing currents occurred. The maximum increase in absolute wave period was about 0,5 s, found to the east of the Bay, while



the maximum reduction was about 0,6 s. At the nearshore S4 measuring station, a reduction in mean absolute period of 0,2 s was found for the SWAN simulation.

Figure 7.23 shows the corresponding difference plot for change in mean wave direction. In this difference plot, regions where wave directions changed clockwise (positive values, darker shade) and anti-clockwise (negative values, lighter shade) are distinguished. From the difference plot it is seen that over most of the Bay gradients in current velocity caused wave crests to rotate anti-clockwise, although areas of clockwise rotation were also found. The maximum change in wave direction due to wave-current interaction was about four degrees, while the change in direction at the nearshore station were found to be less than one degree.

#### **7.4.4.3 Discussion**

The simulation conducted in this section shows that wave-current interaction appears to have had notable influence on wave period and direction where strong currents were found. Mean wave periods were increased or decreased by maxima of, respectively, 0,5 s and 0,6 s. Mean wave direction were changed by as much as four degrees, and mostly in an anti-clockwise direction. Increase in wave period was experienced where strong currents followed the wave field, and current-refraction was found where waves encountered velocity gradients in the cross-current.

However, at the nearshore S4 location the weak local currents appeared to have had a minor effect on simulated wave conditions, with the mean absolute wave period and mean wave direction changing by 0,2 s and by less than one degree respectively.

#### **7.4.5 Directional spreading of waves**

The directional spreading of a given wave spectrum describes the distribution in direction of wave components about the mean direction of propagation. Contrary to the complete directional wave spectra used in the present study, measurements of directional spreading may not be available as model input, or may be considered uncertain, so that it would be regarded as a 'tuning parameter' to a wave simulation study.

From the geometry of the Algoa Bay field case, it is apparent that the amount of directional spreading of wave energy could significantly affect the conditions at the nearshore S4 station, which is sheltered from SSW swell energy by Cape Recife. It is, therefore, the aim of this section to investigate, in a quantitative sense, the sensitivity of the choice of directional spreading of an offshore swell condition on the results at the nearshore S4 station.

#### **7.4.5.1 Test conditions**

The effects of directional spreading in the Algoa Bay field case were investigated for the SSW swell condition of Case 9. The offshore condition of Case 9 contains a dominant SSW swell component and a WSW wind sea component with directional spreading of approximately 20 and 30 degree standard deviation, respectively.

To investigate the impact of directional spreading on the nearshore simulation results, two repeat simulations of Case 9 were conducted with varying magnitudes of directional spreading. For the two consecutive simulations, directional spreading of, respectively, 10 and 30 degree standard deviation were assigned to all frequency components of the observed offshore spectra, as applied to the offshore model boundary. The former condition, therefore, represented a directionally focused wave field (distant swell condition), while the latter represented a locally generated wave field (wind sea).

#### **7.4.5.2 Results**

Plots showing the spatial difference between simulations with the recorded offshore spectrum and those with imposed 10- and 30-degree standard deviation directional spreading widths are presented in Figures 7.24 and 7.25. From these results it is seen that for the imposed narrower directional spreading of 10 degrees standard deviation (Figure 7.24), a reduction in overall energy in the lee of Cape Recife was found, when compared to the simulation results using the original (observed) offshore spectrum. At the nearshore S4 station the simulated significant wave height was decreased by 0,3 m. The focusing of wave energy around the mean direction, therefore, enhances the sheltering effect of Cape Recife. On the other hand, by imposing a wider directional spread (Figure 7.25), an increase in energy in the lee of Cape Recife was found. For this simulation, significant wave height at the S4 station increased by 0,1m.

Figures 7.26 and 7.27 show a comparison between the spectral results for the above simulations, simulations with the original offshore spectra, and observations at the nearshore S4 station. Figure 7.26 shows that the reduction of directional spreading to 10 degrees standard deviation resulted in a reduction of the nearshore energy density associated with the SSW swell, and a significant decrease in energy associated with the SW wind sea components. Due to the large reduction in nearshore energy of the offshore SW wind sea, the mean wave period was found to increase significantly, from 13,38 s (original simulation) to 14,26 s. Due to the specification of a 10-degree standard deviation, a southward shift in mean wave direction (2,2 degrees) was found.

Figure 7.27 shows that with a directional spreading imposed at 30 degrees standard deviation, the nearshore energy of the swell component was somewhat increased

relative to the original simulation. The mean wave period was found to decrease from 13,38 s (original simulation) to 13,03 s. The mean wave direction changed by 1,2 degrees, so that newly simulated directions were somewhat to the east of the simulated directions with the original offshore spectrum.

#### **7.4.5.3 Discussion**

The results presented in this section confirm that for a broader directional spreading more wave energy enters into the sheltered region downwave of Cape Recife, and that for a spectrum with a narrow spreading (distant-generated swell), wave penetration behind the Cape is less. It was also shown that for wave components which are more westerly in direction (greater sheltering), nearshore results are very sensitive to directional spreading. In a quantitative sense, the differences in significant wave height, mean wave direction and mean period due to the change in directional spreading were shown to be significant. In the case considered, this effect was enhanced by the presence of a SW wind-sea component. However, the correlation between simulated results and observations were not convincingly improved by alteration to the observed offshore directional spreading.

### **7.5 SUMMARY OF RESULTS**

A summary of the results of the sensitivity tests conducted in this section are given in Figures 7.28 to 7.30 and in Tables 7.4 to 7.6 below. In these figures and tables the sensitivity results at the nearshore S4 station are given together with the corresponding observations and also with the results of the default simulations (Section 6), as reference. In these results, the same meaning applies to  $T_{m01}$  as that given in Section 6. Descriptions of test conditions can be found in Table 7.1.

Table 7.4: Results of sensitivity tests for Case 9 (21/04/99 at 21:00 UT)

Test	$H_{m0}$ (m)	$T_{m01}$ (s)	Dir (° TN)
Observation	1,71	12,03	153,6
SWAN, test a	1,92	13,38	145,9
SWAN, test b	1,70	13,13	163,9
SWAN, test c1	2,18	13,52	145,8
SWAN, test c2	2,03	13,44	145,8
SWAN, test d1	2,02	13,45	145,9
SWAN, test d2	1,44	13,08	146,7
SWAN, test e1	2,01	13,44	145,9
SWAN, test e2	1,83	13,34	146,0
SWAN, test e3	1,68	13,24	146,2
SWAN, test f	1,93	13,18	146,0
SWAN, test g	1,83	13,21	146,3
SWAN, test h1	1,60	14,26	148,1
SWAN, test h2	2,01	13,03	144,7

Table 7.5: Results of sensitivity tests for Case 1 (26/04/99 at 18:00 UT)

Test	$H_{m0}$ (m)	$T_{m01}$ (s)	Dir (° TN)
Observation	1,81	7,12	118,6
SWAN, test a	2,16	7,33	115,5
SWAN, test b	2,27	7,35	112,0
SWAN, test c1	2,26	7,39	115,7
SWAN, test c2	2,20	7,35	115,6
SWAN, test d1	2,22	7,37	115,7
SWAN, test d2	2,04	7,27	115,6
SWAN, test e1	2,18	7,43	115,6
SWAN, test e2	2,11	7,30	115,5
SWAN, test e3	2,02	7,25	115,4
SWAN, test f	2,16	7,33	115,5

Table 7.6: Results of sensitivity tests for Case 4 (with wind) (08/04/99 at 18:00 UT)

Test	H <sub>m0</sub> (m)	T <sub>m01</sub> ' (s)	Dir (° TN)
Observation	1,38	7,65	132,40
SWAN, test a	1,70	7,70	132,1
SWAN, test b	1,69	7,70	136,2
SWAN, test c1	1,78	7,93	132,0
SWAN, test c2	1,72	7,84	131,8
SWAN, test d1	1,74	7,88	132,0
SWAN, test d2	1,57	7,65	131,9
SWAN, test e1	1,73	7,85	131,9
SWAN, test e2	1,65	7,74	131,7
SWAN, test e3	1,57	7,62	131,5
SWAN, test f	1,68	7,77	131,8

### 7.5.1 Summary of results for Case 9 (SSW swell/SW wind sea)

Table 7.4 and Figure 7.28 summarize the simulation results for the sensitivity tests of Case 9. Figure 7.28 shows that the simulation results varied quite significantly in terms of significant wave height, with the variation in values being 0,7 m. This range of solutions included values near to the observed value. Variation in mean wave direction was within three degrees, with all values to the east of observations, except where depth-induced refraction was de-activated. Variation in mean wave period was small (0,4 s), except for the cases where directional spreading was altered, and still overestimating the observed value.

The results presented in this section show that for Case 9 the most significant physical processes were depth-induced refraction, bottom friction and directional spreading. The inclusion of depth-induced refraction accounted for 11 percent of the significant wave height and 18 degrees change in mean wave direction at the nearshore S4 station in the result of the default simulation. In terms of bottom friction, choices of formulation and coefficients are shown to change the significant wave height solution at the nearshore station by +14 percent (no friction) to -25 percent (intense friction) of the default simulated value. Altering directional spreading between standard deviations of 10 and 30 degrees respectively changed calculated significant wave height by, respectively, -17 percent and 5 percent. Therefore, with respect to significant wave height, simulation results show the greatest sensitivity to bottom friction formulation. In terms of mean wave direction, the most important process was depth-induced refraction. Directional spreading was found to have a significant effect on mean wave period.

Wave-current interaction displayed notable influence in areas where strong currents were found. The maximum change in mean wave period was 0,6 s and the maximum change in mean wave direction four degrees. However, at the nearshore S4 station the influence of currents was small, with changes of only 0,2 s in mean period and less than one degree in direction. This difference in direction is even below the numerical accuracy (three degrees) of the evaluation (Section 5.5). The influence of triad-wave interactions was limited to very shallow regions of the bay (< 10 m) and in the lee of Cape Recife. Triad-wave interaction had a minor influence on the solution at the S4 station, being only 0,2 s in mean period.

### **7.5.2 Summary of results for Case 1 (ESE wind sea)**

Table 7.5 and Figure 7.29 summarize the simulation results for the sensitivity tests for Case 1. Figure 7.29 shows that the simulation results were quite insensitive to the varying simulation formulations. The variation between nearshore results for significant wave height was only 0,2 m, and still over-estimated by the observed value. Mean wave direction displayed almost no change, except with the de-activation of depth-induced refraction where a difference of 3,5 degrees was found. Mean wave period, which correlated well with observations, was not sensitive to model formulation, with the variation in results being only 0,1 s.

The simulation results presented in the sections above displayed the most sensitivity towards depth-induced refraction and bottom friction, although the sensitivity was notably less than for Case 9. It was found that depth-induced refraction accounted for five percent of the significant wave height and 3,5 degrees change in wave direction of the result at the S4 station of the default simulation. In terms of bottom friction it was shown that significant wave height was either increased by five percent (no friction) or decreased by six percent (intense friction), depending on the coefficients chosen. It can, therefore be concluded that in terms of significant wave height, depth-induced refraction and bottom friction are of similar importance. Depth-induced refraction is, however, important for obtaining better correlation with observations in terms of mean wave direction.

Triad-wave interactions were found to act only inside the 10 m contour and therefore to have no influence on the results at the nearshore S4 station. The effects of wind-wave generation of easterly winds were not considered in this section.

### **7.5.3 Summary of results for Case 4 (SSW swell/SE wind sea)**

The results of the sensitivity tests for Case 4 are presented in Table 7.6 and Figure 7.30. It can be seen in Figure 7.30 that, as for Case 1, the results at the

nearshore S4 station were insensitive towards model formulation. The variation in the result for significant wave height is 0,2 m, which still over-predicts the observed value. Mean wave period, which correlated well with observations, varied by 0,3 s. The mean wave direction, which showed equally good correlation with observations, was virtually unchanged, except for the case where depth-induced refraction was disabled. In the latter case a variation of 4,1 degrees was found.

The simulation of Case 4 was found as for Cases 1 and 9 to be the most sensitive to depth-induced refraction and bottom friction. Bottom friction showed the largest influence, with possible increase in significant wave height of five percent (no friction) or a decrease of eight percent (intense friction). In terms of significant wave height, depth-induced refraction accounted for one percent of the simulated nearshore wave height. In terms of spectral components, bottom refraction was shown to increase and reduce the swell and wind-sea components of the offshore wave spectrum respectively.

Simulations showed that the effect of triad-wave interactions are small at the nearshore S4 station, causing a change of less than 0,1 s in the mean wave period.

## **7.6 CONCLUSION**

In this section, sensitivity testing on the solutions of the Algoa Bay field case have been conducted for a number of physical processes included in SWAN. These tests were conducted for three characteristic offshore conditions found in the Bay, namely: a bi-modal condition with high-energy SSW swell, a bi-modal condition with SSW swell and SW wind sea, and an ESE wind sea condition. The purpose of the sensitivity testing was to investigate the influence of the relevant processes on the nearshore solution, with specific attention to the nearshore S4 station, and to establish optimal simulation settings. Considering the findings of this section, the following conclusions are made:

- a) In this section sensitivity tests were conducted for the following physical processes: depth-induced refraction, bottom friction, triad-wave interaction and wave-current interaction. Of the selection considered, the dominant processes with respect to the simulation results at the nearshore station appeared to be depth-induced refraction, bottom friction and directional spreading. The influence of triad-wave interactions and wave-current interaction at the nearshore station appeared to be small.
- b) The degree to which the simulations were sensitive to physical processes depended on the direction, period and energy level of the offshore condition modelled. Of the conditions considered, the high-energy swell condition of

Case 9 appeared to be the most sensitive to model setup. This can be seen if the simulations for depth-induced refraction, bottom-friction and triad-wave interaction are compared: For Case 9, which contains high-energy SSW swell, variation in significant wave height for the range of simulations was 0,7 m, compared to the variation in significant wave height of Cases 1 and 4, which were both 0,2 m. Likewise, the variation in mean wave period, although small, was the largest for the swell condition of Case 9 ( $T_{m01}' = 0,4$  s, compared to  $T_{m01}' = 0,3$  s and 0,1 s for Cases 4 and 1, respectively). The largest variation in mean wave direction was found for Case 9 (18 degrees, due to refraction), compared to the variations of 4,1 degrees and 3,4 degrees respectively for Cases 4 and 1. These results are in qualitative agreement with the composition of the source terms plotted in Figure 2.2, where it was shown that energy dissipation increases for increasing wave energy and decreasing relative depth ( $k.d$ ). The offshore direction of the swell, which resulted in sheltering, further increases this latter sensitivity.

Based on the simulation results of this section, a qualitative judgement is made of the relative sensitivity to physical processes experienced at the nearshore S4 station (17 m depth) for the three offshore conditions considered. The results of the evaluation are presented in Table 7.7 below, using the following key:

••• - dominant, •• - significant, • - minor importance, NT – not tested.

*Table 7.7: Relative importance of physical processes to the nearshore results of the Algoa Bay field case*

Physical process	SSW swell (Case 9)	SSW swell/SW sea (Case 4)	ESE sea (Case1)
Depth-induced refraction	•••	••	••
Bottom friction	•••	•••	••
Triad interactions	•	•	•
Wave-current interaction	•	NT	NT
Directional spreading	•••	NT	NT

Table 7.7 reflects the fact that depth-induced refraction and bottom friction were found to be dominant and especially important to high-energy SSW swell. Due to the sheltered nature of the nearshore station, directional spreading was also found to be a dominant influence on SSW swell. Triad-wave interaction and wave-current interaction are considered of low importance. Table 7.8 presents an excerpt of a classification of the importance of physical processes, given by Young (1999), after Battjes (1994\*). In this classification, the dominant processes on shelf seas were considered to be bottom



friction and processes associated with wind-wave growth. In the shoaling zone, depth-induced refraction, shoaling and depth-induced breaking were given as dominant. The findings summarized in Table 7.7 are in general agreement with those of Battjes (1994\*). However, due to the relatively deep-water location of the S4 station, depth-induced breaking and triad interactions were not found to be as significant (more akin to the shelf sea classification). The importance of wind-wave generation in the Algoa Bay field case was not considered in this section, but is shown in Section 8 to be dominant for Case 1 (ESE wind sea).

*Table 7.8: Relative importance of physical processes on shelf seas and in the shoaling zone (excerpt) (Young, 1999, after Battjes, 1994\*)*

<b>Physical process</b>	<b>Shelf seas</b>	<b>Shoaling zone</b>
Diffraction	-	•
Depth refraction and shoaling	••	•••
Current refraction	•	••
Quadruplet-wave interactions	•••	•
Triad-wave interactions	•	••
Atmospheric input	•••	•
Whitecapping	•••	•
Depth-induced breaking	•	•••
Bottom friction	•••	••

The results of the sensitivity tests presented in Figures 7.28 to 7.30 can be regarded as a measure for calibration of the Algoa Bay field case. It is seen in all cases that the simulated significant wave height and mean wave period tend to over-estimate observations. In terms of these parameters, the simulation results of Madsen *et al.* (1988) with  $K_N = 0,10$  m produced the best correlation with observations. It is, however, observed that even with the application of this model setup with enhanced friction, an over-estimation in mean wave period remains for the swell condition of Case 9. For Cases 1 and 4 the significant wave heights would still be over-estimated. In terms of mean wave direction, correlation errors are within seven degrees and were relatively unchanged by the enhanced friction.

Considering the overall correlation of results, it is proposed that the following model setup for physical processes be used for the Algoa Bay field case, which is essentially the recommended version of Holthuijsen *et al.* (1999), but with enhanced bottom friction:

- Depth-induced refraction – included
- Bottom friction – formulation of Madsen *et al.* (1998), with  $K_N = 0,10$  m
- Triad-wave interactions – neglected
- Wave-current interaction – neglected

This model setup is implemented in Section 8, in which a set of final simulations for Algoa Bay is conducted. However, considering the remaining uncertainties which were identified above, additional tests are included in Section 8: Firstly, the process of depth-induced refraction, which was shown to be dominant for SSW swell conditions, is re-evaluated. By means of this re-evaluation, it is investigated whether the discrepancies in mean wave period and wave direction, which fall within the sensitivity influence of refraction, could be reduced. Secondly, the remaining over-estimation of wind-sea energy in Cases 1 and 4 prompts a re-evaluation of the simulation of ESE wind seas. The simulation of Case 1 is revised by neglecting the boundary values chosen in Section 5, and including wind-wave generation.

## 8 FINAL SIMULATIONS

### 8.1 INTRODUCTION

This section conducts a final verification, and partial improvement, of the modelling choices proposed in Section 7. The sensitivity tests conducted in Section 7 revealed that the dominant processes for the SWAN simulation of the Algoa Bay field case were *depth-induced refraction, bottom friction and directional spreading*. This sensitivity was especially found for high-energy SSW swell conditions offshore. It was shown that for these conditions, the best correlation with observations were obtained by a model setup which includes depth-induced refraction and which uses the friction formulation of Madsen *et al.* (1988), with a friction coefficient  $K_N = 0,10$  m. These choices are verified in the present section.

Prompted by the evident importance of depth-induced refraction to SSW swell conditions of this field case, the effect of including a nested computation grid with a higher spatial and directional discretization was investigated. It was established for a selection of SSW offshore cases to what extent correlation with observations improves with this increased detail of, amongst others, refraction calculation.

In Sections 6 and 7 it was found that for ESE wind seas the SWAN simulation significantly over-estimates the observed nearshore wave energy. The sensitivity testing in Section 7 showed that this correlation error was affected little by the different choices of the physical processes evaluated. The present section shows how this correlation can be improved for ESE wind wave cases by discarding the boundary condition derived in Section 5, and incorporating time-independent generation by wind instead.

The aims of this section are, therefore, to conclude the Algoa Bay field case simulations by: (a) the verification of the choices of model setup chosen in Section 7 for the dominant SSW swell condition, (b) to investigate the effect of increased computational grid resolution for simulations of the dominant SSW swell condition and (c) to show how improved nearshore results for the ESE wind wave conditions can be obtained by the modelling of wind-sea generation.

### 8.2 SSW SWELL CONDITIONS

In this section the modelling choices proposed in Section 7 are verified by applying them to four of the SSW swell conditions contained in the original set of nine testing conditions (Section 5). It is shown to what extent the nearshore simulation results at

the S4 station improved for the proposed model setup. This section also describes the investigation into the effect of increasing the discretization of the computational grid by means of grid nesting, for the same three SSW swell conditions.

### 8.2.1 Test conditions and model setup

For the verification of the model setup proposed in Section 7, four SSW swell conditions were evaluated. These four cases were selected from the original selection of nine conditions evaluated in Section 6, and are given in Table 8.1 below. These offshore conditions were simulated by SWAN for the model setup proposed in Section 7, which is given in Table 8.2.

*Table 8.1: Selection of offshore SSW swell conditions for the evaluation of proposed model setup*

Case no.	Category	Date and time (Mm/dd, UT)	Description
5	C	05/13 at 18:00	SSW swell with peak period at 13 s
6	D	04/23 at 21:00	SSW swell in combination with SW wind sea
8	D	04/19 at 08:00	Highly developed SW wind sea in combination with SSW swell
9	D	04/21 at 15:00	SSW swell in combination with SW wind sea

*Table 8.2: Model setup for final simulation of SSW swell conditions*

Physics				
Generation	Breaking	Friction	Triads	Quadruplets
Komen <i>et al.</i> (1984)	Battjes and Janssen (1978)	Madsen <i>et al.</i> (1988) Initially $K_N = 0,10$ m adapted to $K_N = 0,08$ m	off	Hasselmann <i>et al.</i> (1985)
Wcapping	Refraction	Frequency shift	Setup	Simulation
Komen <i>et al.</i> (1984)	on	on	off	Stationary

The simulations of the above offshore conditions were conducted for the computational grid discretization selected in Section 5, which is repeated in Table 8.3 below. In addition, the grid discretization was increased by using a nested computational grid in

the area surrounding the contours of Cape Recife. The discretization of the nested grid is given in Table 8.3 below, and its positioning is shown in Figure 8.1. The aim of using a higher resolution nested grid was to obtain a higher accuracy nearshore result with respect to depth-induced refraction, which was shown to be a dominant process.

*Table 8.3: Discretization of computational grids for final simulation of SSW conditions*

<b>Grid</b>	<b><math>\Delta x, \Delta y</math> (m)</b>	<b><math>\Delta\theta</math> (°)</b>	<b><math>\Delta\sigma/\sigma</math></b>
Original	500	10	0,04
Nested	250	5	0,04

### 8.2.2 Simulation results

The results of the simulations for the SSW swell conditions, using the proposed model setup, are shown in Figures 8.2 to 8.5 and Tables 8.4 and 8.5 below. The relative correlation shown in Table 8.5 was defined by (6.1) to (6.3) in Section 6.4. Figures 8.2 to 8.5 show the simulated wave spectra at the nearshore S4 station, for both the original computational grid discretization and the simulation using the nested grid (refer Table 8.3). Also shown on these plots, for comparison, are the results of the first-estimate SWAN simulations (Section 6) and the wave spectra observed at the S4 station.

*Table 8.4: Simulation results for final simulation of SSW conditions*

<b>Case no. and grid type</b>	<b><math>H_{m0}</math> (m)</b>	<b><math>T_{m01}</math> (s)</b>	<b>Dir (° TN)</b>
5, original	1,35	10,41	147,5
5, nested	1,33	10,41	146,9
6, original	1,37	11,10	150,0
6, nested	1,30	11,05	149,3
8, original	0,67	9,95	153,9
8, nested	0,65	10,10	152,6
9, original	1,74	13,28	146,1
9, nested	1,72	13,34	145,2

Table 8.5: Relative correlation error (with observations) for final simulation of SSW conditions

Case no. and grid type	Rel. error in $H_{m0}$ (%)	Rel. error in $T_{m01}'$ ( $\Delta$ s)	Rel. error in Dir ( $\Delta$ °)
5, original	1,70	1,47	-4,7
5, nested	0,63	1,46	-5,3
6, original	-1,68	-0,19	-6,8
6, nested	-7,01	-0,24	-7,5
8, original	-6,39	-0,62	5,2
8, nested	-10,06	-0,47	3,9
9, original	1,51	1,25	-7,5
9, nested	0,08	1,31	-8,4

Inspection of the results in Figures 8.2 to 8.5 and Tables 8.4 and 8.5 reveals the following, for cases where the original grid discretization were used:

- (a) In all cases the basic shape of the simulated spectra remained similar to those found in the first-estimate simulations of Section 6. In all cases the correlation between simulated and observed mean wave directions was quite similar to, although slightly better than, that of the first-estimate results (refer Table 6.4). Comparison with observations shows that differences in the estimation of mean wave direction of up to 7,5 degrees remained.
- (b) For Cases 5, 6 and 9, which over-estimated wave energy in the first-estimate simulations, the results of the proposed adjusted model setup displayed a significant decrease of wave energy. This decrease in calculated wave energy amounts to a general improvement in the correlation between the simulated results and measurements. Application of the friction coefficient of  $K_N = 0,10$  m yielded slight under-estimation of nearshore observations. An adjustment of the coefficient to  $K_N = 0,08$  m yielded the results presented in Tables 8.4 and 8.5 and Figure 8.14, which represents an improved fit to observations for this sample set of conditions.
- (c) For Case 8, which displayed good correlation with observations in the first-estimate simulations (Section 6), the proposed model formulation resulted in decreased correlation with observations, with respect to significant wave height.

The results of simulations using a nested computational grid of higher resolution yielded the following:

- (a) The computational time required to perform the simulations with a nested grid was found to be a factor three greater than those for the simulations with the original (single) computational grid. This figure is a function of the relatively large nested area modelled, and significantly detracts from the practicality of exercising this option.
  
- (b) The inclusion of the nested grid appears to have had a slight enhancing effect on the effects of depth-induced refraction. It was found that wave-front rotation around Cape Recife was increased (by a maximum of 1,3 degrees) so that mean wave directions calculated at the S4 station were somewhat more easterly than for simulations using the original computational grid. This relates to a somewhat worse correlation than found for the original grid. The expected accompanying increase in wave height and mean period was, however, not detected. Instead, the increased discretization resolution appeared to enhance the influence of bottom friction, which yielded decreases in significant wave height of between 1,3 and 5,3 percent relative to simulations with the original grid. Mean wave periods were affected by a maximum of 0,2 s.

### **8.2.3 Discussion**

The results of the simulations presented in this section indicates that the proposed model setup indeed significantly improves correlation between the nearshore simulation results and observations for SSW offshore conditions found in Section 6. This improvement is mainly seen in the results of significant wave height, where the simulations, which showed over-estimation of observations, now show good correlation. Marginal improvements in mean wave period and mean wave direction were found.

The inclusion of a nested computational grid of finer discretization changed the simulation results marginally. Compared to simulations with the original computational grid, the inclusion of the nested grid caused somewhat greater wave-front rotation around Cape Recife (at the S4 station), and a general decrease in wave energy. This leads to the conclusion that both processes of depth-induced refraction and energy dissipation were somewhat enhanced. Considering that the simulation with the nested grid (finer computational resolution) represents the more precise numerical solution, results-correlation worsened somewhat with a more precise calculation of SWAN's depth-induced refraction. Although the correlation errors of these simulation results fall within the recording accuracy of the instrumentation (Section 5.3.3), this finding would suggest that a degree of inaccuracy exists in the calculation of depth-induced refraction of the SSW swell.

The finding that the effect of bottom friction is enhanced by the use of a nested grid implies the need for a re-calibration of the friction coefficient to a lower value. This re-calibration was not conducted here, and the value of  $K_N = 0,08$  m is accepted.

The simulation results (original computational grid) presented for the sub-set of SSW swell conditions showed the best correlation between simulations and observations for a Madsen *et al.* (1988) friction coefficient of  $K_N = 0,08$  m. This result was, however, based on a limited sample set. Fine-tuning of this coefficient would be best conducted on a greater sample of conditions, such as a complete simulated time series which includes SSW conditions. Such simulation would best be conducted by non-stationary (time-dependent) SWAN simulation, which falls outside the scope of this study

### 8.3 ESE WIND SEA CONDITIONS

In this section the generation of ESE wind sea over the Algoa Bay study area is investigated. It was found in Section 6 that the boundary wave conditions selected for conditions with ESE wind sea components (Cases 1, 2, 3 and 4), yielded nearshore results which over-estimated nearshore observations. Sensitivity tests conducted in Section 7 showed little improvement of this result for Cases 1 and 4, even with the adoption of the proposed model setup (as given in Table 8.2).

The aim of this section, therefore, is to determine whether the nearshore wave conditions can be simulated accurately by time-independent wind generation, without using the pre-defined boundary wave conditions set up in Section 5. The simulation was conducted for Case 1, using the downwind directional wave spectra (Waverider and S4), and the following wind information: wind measurements at Jahleel Island, synoptic weather charts, and interpretations from shipping charts.

#### 8.3.1 Test conditions and model setup

During the period 25/04/99 – 26/04/99, easterly wind conditions were experienced at Jahleel Island in Algoa Bay, as shown in the time series of wind, reproduced in Figure 8.6. In this figure it can be seen that easterly wind speeds rose from  $U_{21} = 4\text{--}6$  m/s to  $U_{21} = 14$  m/s on 26/04/99 at 12:00 UT. Figure 8.7 shows the synoptic weather chart for the corresponding time (SA Weather Bureau, 1999).

The change in offshore and nearshore wave conditions during this wind event is seen in the time-series wave recording of Figure B.1(d) in Appendix B. The peak wave direction and period changed from that of a SSW swell condition to that of an ESE wind sea condition. During this time a peak in the significant wave height was also observed to develop. The corresponding recorded wave spectra at the offshore and nearshore



stations are presented in Figures 8.8 and 8.9. These figures show the development, over a period of about 24 hours, which produced the conditions measured on 26/04/99 at 18:00 UT (Case 1). The SWAN simulation described in this section aimed to reproduce this development of wave energy at the offshore and nearshore stations. The model setup used for the simulation is that given in Table 8.2.

### 8.3.2 Method

Figure 8.10 shows the bathymetry of Algoa Bay, extended by 100 km to the east. In terms of geography, the fetch area is unlimited to the east, extending beyond the continental shelf into the Indian Ocean. According to the synoptic weather chart of 26/04/99 at 12:00 UT (Figure 8.7), the large-scale high-pressure system affords a fetch length of many hundreds of kilometres easterly. Detailed wave information was available only at the downwind measurement locations. It was, therefore, necessary to arbitrarily demarcate a fetch to be used in the simulation. This fetch was estimated by means of the Sverdrup-Munk-Bretschneider (SMB) nomograms, as presented in CERC (1984), using as input the average wind velocity over the generation period and the downwind wave height observations.

By means of the SMB curves, it was determined that to generate an offshore significant wave height of 3,3 m (wind sea component observed at the S4 station on 26/04 at 18:00) with an average wind speed  $U_{10} = 11$  m/s (average observed at Jahleel Island during generation period, related to 10 m reference height), a fetch of 200 km is required. For the purpose of the stationary (time-independent) SWAN simulation conducted, the wind velocity was taken as constant in time, at  $U_{10} = 11$  m/s. Due to a lack of more detailed information, the wind field was initially assumed uniform in space.

The computational grid for Case 1 was defined on the extended bathymetry as shown in Figure 8.11. On this large, deep-water extent, the computational grid discretization was reduced to  $\Delta x = \Delta y = 1000$  m,  $\Delta\theta = 10^\circ$  and  $\Delta\sigma/\sigma = 0,04$ . For wind sea generation, the length of the computational grid in the direction of generation is interpreted as the fetch area. Therefore, the east-west dimension of the computational grid (upwind of the nearshore station) was set equal to the fetch. However, the total fetch of 200 km is not incorporated in the configuration of Figure 8.11. Instead, an offshore boundary condition (East) was generated using a preceding SWAN computation, using the constant  $U_{10} = 11$  m/s wind condition, over a generation distance of 100 km in deep water.

### 8.3.3 Simulation results

#### 8.3.3.1 Spatial distribution

The results of the simulation for wind-wave generation are presented in Figures 8.11 to 8.13. Figure 8.11 shows the spatial plot of significant wave height and mean wave direction of the wave field generated over the 100 km of fetch upwind of the Waverider and S4 observation stations. This plot is the end result of a calibration process described in Section 8.3.3.2 below. Figure 8.11 shows a general increase of significant wave height in the downwind direction, but also that greater wave heights were found in the open sea, south of Cape Recife, than inside of Algoa Bay. This result corresponds with the observations at the offshore Waverider and nearshore S4 stations. The correlation of simulation results at the S4 station are given in Table 8.6 below:

*Table 8.6: Results at S4 station for wind-wave generation simulation of Case 1*

Item	$H_{m0}$ (m)	$T_{m01}$ (s)	Dir (° TN)
Observed	1,8	7,1	118,6
Simulated	1,8	6,9	123,6
Relative error	0,0 %	0,2	5,0°

#### 8.3.3.2 Wave spectra

Figures 8.12 and 8.13 present the simulation results in terms of the energy density spectra, at the offshore (Waverider) and nearshore (S4) stations, respectively. The results of four simulations are plotted on each of the figures. The first of these results were obtained in the simulation with an assumed uniform wind field of  $U_{10} = 11$  m/s (Jahleel Island average). Figures 8.12 and 8.13 show that the spectra generated by this wind significantly under-estimated offshore and nearshore observations. Based on this result, the assumption of spatial uniformity of the wind field over the fetch was re-assessed.

According to interpretations of 6-hourly shipping charts for the period 25/04/99 to 26/04/99 (Hunter, SA Weather Service, pers. comm., 2001), winds just outside Algoa Bay of approximately 160 percent of the values at Jahleel Island were reported. Based on this finding, it is conceivable that wind speeds could have been higher over the larger Bay area than those measured at Jahleel Island. Subsequent runs were conducted using constant wind speeds at 125 percent (13,5 m/s) and 140 percent (15,4 m/s) of the Jahleel Island values. These results are incorporated in Figures 8.12

and 8.13. The increase of wind speed to 15,4 m/s (140 %) resulted in a good correlation with the offshore observation (Figure 8.12). However, at the inshore station this wind speed yielded an over-estimation of energy, although the peak frequency correlated well with observations. Due to this result, the assumption of spatial uniformity of the wind field over the extended Algoa Bay area was dropped.

In a simulation with a spatially non-uniform wind field, the wind field was schematized into two areas, as shown in Figure 8.10. The schematization comprises a deep-sea region outside the Bay where wind speeds were set to 140 percent of the value at Jahleel Island (15,4 m/s), and a Bay region where wind speeds were taken equal to the average observed at Jahleel Island (11 m/s). The spatial solution of this simulation is shown in Figure 8.11, and was discussed in Section 8.3.3.1 above. The spectral results of the simulation are presented in Figures 8.12 and 8.13. Figure 8.12 shows that the calculated spectrum at the offshore station corresponds well with observations, being somewhat lower than for the run with a uniform wind field of 15.4 m/s. At the nearshore station the correlation between the calculated and observed spectrum is much improved by the decrease of wind speed in the Bay, and now correlates well with observations. Correlation between calculated and measured wave direction for the nearshore S4 station is also good, displaying a degree of wave front rotation inside the Bay.

#### **8.3.4 Discussion**

In Section 8.3 it was shown that with a sufficiently detailed spatial description of the offshore wind field, SWAN was able to estimate the observed downwind wind sea conditions for Case 1, without the use of offshore boundary wave information. These simulations demonstrated the effective functioning of the source functions for wind-wave generation and quadruplet-wave interactions to simulate the observed spectra with high accuracy.

The spatial plot of significant wave height and mean wave direction displayed greater wave energy outside the Bay than inside, which corresponds to observations at the Waverider and S4 stations. This finding could account for the correlation errors found in Sections 6 and 7 for easterly wind sea conditions, in which offshore wind sea observations were used as boundary condition for conditions inside the Bay.

The simulations presented in this section have a number of shortcomings. Firstly, the assumption of time-independence in the generation of wind waves is a rather great approximation, but was made to remain within the scope of the study. Secondly, the outcome of the simulation was largely determined by the choice of spatial wind field distribution. The study would have benefited from more detailed measurements over the Bay area and offshore. Lastly, the simulation area over which wave generation

was modelled (200 km fetch) is long compared to the recommended limit for SWAN Cycle 2 Version 40.01, which is 25 km (Section 3). Nevertheless, the results obtained in this section displayed good correlation with observations, and a significant improvement to the simulation results of Section 6.

#### 8.4 CONCLUSION

In this section, final verification simulations were conducted for offshore SSW swell conditions and an ESE offshore wind sea condition. The aims of these simulations were to evaluate the model setup proposed in Section 7, to test the sensitivity of SSW swell conditions to the addition of a nested computational grid, and to investigate the generation of ESE wind sea conditions. The results of these final simulations are presented in Figures 8.14(a) and (b).

For the SSW swell conditions it was found that by incorporating the model setup (with increased bottom-friction dissipation of Madsen *et al.* (1988)) proposed in Section 7, the correlation between simulated results and observations significantly improved. Reasonable correlation between observations and simulations was obtained for a friction coefficient of  $K_N = 0,08$  m (as opposed to  $K_N = 0,10$  m proposed in Section 7). The improvement was mainly seen in the results of significant wave height, where a notable reduction height improved the over-estimation reported in Sections 6 and 7. However, the correlation errors of mean wave direction and mean wave period of, respectively, up to 7,5 degrees and 1,5 s remained. It was proposed that a slight adjustment to the friction coefficient could be required if the simulation results of a complete time series of observations were considered.

The inclusion of a nested grid of higher discretization resolution yielded correlation errors in mean wave direction that were somewhat higher (greater rotation) than for simulations with the original discretization. This finding would appear to indicate that the dominant process of depth-induced refraction was calculated with a degree of inaccuracy. It is suspected that this inaccuracy was enhanced by the long period and high-energy nature of the swell conditions considered in this study. Bottom friction dissipation was found to be enhanced by the incorporation of the nested grid. It was found that the computational time required by simulations with a nested grid was a factor three of that required for a simulation without.

For the ESE wind sea condition of Case 1 it was found that the inclusion of wind-wave generation, as opposed to the use of an approximated offshore boundary value, yielded good correlation with the down wind Waverider and S4 stations. This finding would indicate that the simulation of the wind sea components of conditions such as Cases 3 and 4, which were both over-estimated in Section 6, could also be improved

by the simulation of wind-wave generation. These cases were, however not considered in this study. The effect of the presence of high-energy swell on the wind-wave generation in the Bay, which could be significant (refer Rogers *et al.*, 2000 and Holthuijsen *et al.*, 2000), was also not considered.

It was pointed out that the simulation of the wind sea in Section 8.3 was simplified by the stationary application of SWAN. Furthermore, it was pointed out that the results of the simulation would probably have been more precise if a more detailed wind field (in space and time) had been available.



## 9 RESULTS OF STUDY

In this study the numerical wave simulation model SWAN Cycle 2 Version 40.01 was applied in a stationary (time-independent) mode to the field case of Algoa Bay, South Africa. This field case featured a deep bay formed by a large cape, with wave conditions of high-energy swell and local wind sea, which were frequently found as bi-modal wave fields. For model verification, observations at two recording locations were used – one offshore (at 85 m water depth) and one nearshore (at 17 m water depth). The aims of this field case study were, firstly, to evaluate the performance of SWAN in terms of the modelling of wave spectra and integral wave parameters at an inshore observation station in the lee of the sheltering cape. Secondly, it was aimed to evaluate the sensitivity of the model results to model setup and the relative importance of physical processes, for typical conditions found in the field case. These findings were to be related to the findings of previous verification work on SWAN. Lastly, it was aimed to provide general guidelines towards the implementation of SWAN for wave modeling on the South African coast. The following findings were made this study:

- a) A review of the literature (Section 3) showed that to date, SWAN has been comprehensively validated for a large selection of academic, laboratory and field cases. The field cases considered in these validations were classified here as shallow inter-tidal areas, shallow bays and open-water conditions. Typical wave conditions for these field cases were wind seas and low-energy swell. These tests showed that SWAN simulation results compared well with observations in terms of the parameters of significant wave height, mean period and mean direction, but tended to fare less well in terms of the prediction of wave spectra. For the cases considered, it was shown that the important simulation processes in deep water were regarded to be depth-induced refraction and shoaling, and wind-wave growth. In intermediate to shallow water, important processes were regarded to be wind-wave growth, depth-induced refraction and shoaling, wave-current interaction, triad-wave interaction and depth-induced breaking, depending on the situation.
- b) In contrast to the cases on which the historic verification of SWAN has focused, the South African coastal zone was shown (in Section 4) to feature the following differentiating characteristics: The South African coastal zone was shown to be characterized by a high-energy swell component ( $H_s^{1\%} = 4,5$  to  $6,0$  m and  $T_p = 9$  to  $16$  s) which frequently occurs as a bi-modal wave spectrum with wind seas. The coastline is open and steep-sloped along the west and east coasts of the country, and forms large bays along the south coast. Coastal currents were shown to be wind-driven or to form part of oceanic-scale continuity currents, with tidal currents mostly absent.

- c) Initial simulations of the Algoa Bay field case were conducted for nine wave conditions (Section 6), using a model setup for SWAN based on recommendations by Holthuijsen *et al.* (1999). These initial simulations yielded generally good comparison with instrument observations in terms of both wave spectra and integral wave parameters. However, in using the recommended model setup, it was found that for the high-energy SSW swell conditions, nearshore results over-estimated significant wave height (differences of about 10 percent of observed values) and mean wave frequency (differing with up to 1,6 s from observed values). Correlation errors of about seven degrees were found in mean wave direction, which was within the recording accuracy of the observations. For conditions containing ESE and SE wind sea, over-estimations were found in significant wave height (about 20 percent of observed values), and again errors in mean wave direction of up to seven degrees. For one simulation condition it was found that wave conditions changed too rapidly for time-independent simulation to be successful.
- d) Sensitivity tests (Section 7), for a set of three offshore wave conditions, demonstrated that the dominant processes at the nearshore observation station of the Algoa Bay field case were depth-induced refraction, bottom friction and directional spreading of the wave spectrum. The sensitivity of these processes was shown to depend on the direction, periodicity and direction of the offshore conditions. The greatest sensitivity to model setup was displayed by a high-energy SSW swell condition, for which the parameter of relative depth ( $k.d$ ) was small. The processes of triad wave-interaction and wave-current interaction were found to be relatively unimportant at the nearshore location considered.
- e) The results of the sensitivity tests conducted in this study are in general agreement with a classification of shoaling-zone wave processes provided by Battjes (1994\*), in which depth-induced refraction was considered a dominant process and bottom friction significant. The generation of wind sea over shelf seas (e.g. the open bay area of Algoa Bay) was found dominant both in this study and by Battjes. However, in contrast to the classification of Battjes, the processes of depth-induced breaking, triad-wave interaction and wave-current interaction were not found to be significant in the Algoa Bay study case, at the nearshore location considered.
- f) In the final, calibrated simulations of the Algoa Bay field case (Section 9) it was shown that for the existing model formulation, the best correlation between simulation results and observations was obtained for the friction formulation of Madsen *et al.* (1988), with a friction coefficient of  $K_N = 0,08$  m. Applying this



model setup, in three out of four tested cases the difference between simulated and observed significant wave height was below two percent. However, correlation errors of up to 7,5 degrees in mean wave direction and 1,5 s in mean wave period remained. By conducting simulations with a finer computational grid discretization, it was shown that a degree of inaccuracy exists in the formulation for depth-induced refraction. In a next category of testing, it was shown that, by modelling wind-wave generation by offshore ESE winds without imposing boundary wave conditions, improved results of simulated nearshore wind sea conditions could be obtained. In a single simulation case, using a schematized wind field, observed significant wave height was simulated exactly, while simulated and observed values of mean wave direction and mean wave period differed by only five degrees and 0,2 s respectively.

- g) It was shown (in Section 3) that the Algoa Bay field case physically resembles a typical large-scale embayment on the South African south-west and south coasts. It was also shown, through investigations by others, that in this coastal area, wave, wind and current conditions are very similar.



## 10 CONCLUSIONS OF STUDY

Considering the findings of this study, as set out in Section 9, the following final conclusions are drawn:

- a) To date SWAN has been comprehensively validated for the simulation of wind sea conditions and low energy swell, for various bathymetrical forms in both deep sea and coastal areas. However, it was shown in this study that typical South African coastal conditions differ from these previous validation cases, with respect to bathymetry, wave climate and current climate. It is, therefore, concluded that the historical evaluation work conducted on SWAN is not directly applicable to the South African situation.
- b) In contrast to the findings of the historical SWAN validation work, the findings of the Algoa Bay field case study leads to the conclusion that *where high-energy, long period swell is found, such as typically along the South African south coast, the processes of depth-induced refraction and bottom friction are the dominant processes in the simulation, for regions outside of the surf zone. In addition, an accurate specification of directional spreading width is important to the correct simulation of wave conditions at sheltered nearshore areas in deep bays. It is further concluded that wave conditions featuring high-energy, SSW swell are typically the most sensitive to model setup.*
- c) With due consideration to the accuracy of wave and wind recordings used in this study, it is concluded that *SWAN, once calibrated, is capable of simulating the nearshore wave field of the Algoa Bay field case with sufficient accuracy.* However, it is also concluded that due to the bi-modal nature of the offshore wave fields considered in the field case, the single offshore wave recording station and the lack of offshore wind measurements presented constraints to modelling setup, thereby limiting modelling accuracy.
- d) Due to the characteristic similarity between environmental and bathymetrical conditions along the South African south coast, it is concluded that the findings of this study can be applied as a guideline to short wave simulations over this entire region. It was, however, shown that conditions along the South African west and east coasts, comprising steep, straight, open coastlines and the large-scale current systems (notably the Agulhas Current on the east coast), differs significantly from the conditions considered in the present study. For these situations, closer resemblance may be found to historic SWAN field case studies, for example the cases of Duck (Rogers *et al.*, 2000), Petten and Kashiminada (Andorka Gal *et al.*, 1998).

- e) Considering the results of simulations with various grid discretizations and for various storm events, it is concluded that SWAN appears to contain a degree of inaccuracy with respect to depth-induced refraction. This inaccuracy is presumably magnified by the characteristic South African wave climate of high-energy swell.
  
- f) Time-independent simulation with SWAN yielded generally good comparison with observations. However, as was shown in one case where observed nearshore conditions changed rapidly, the assumption of time-independency was not always valid.

## 11 RECOMMENDATIONS

Based on the conclusions drawn from the results of this study, the following recommendations are made with regard to the application of SWAN to field cases on the South African south coast, the improvement of the SWAN model, and with regard to further model applications to the general validation of SWAN for the South African coastal region:

- a) For the modelling of short waves in deep bays along the South African south coast, the wave-related physical processes to be considered dominant up to the outside of the surf zone, are depth-induced refraction and bottom friction. It is also recommended that care should be taken in the correct specification of directional spreading. Offshore conditions which feature swell originating from the south-westerly quarter should be considered the most sensitive to the formulation of the SWAN model setup. It was found that the best correlation with observations was obtained for a setup of physical processes as recommended by Holthuijsen *et al.* (1999), but with the friction formulation of Madsen *et al.* (1988) and a friction coefficient of  $K_M = 0,08$  m.
- b) Based on the finding that high-energy swell was somewhat excessively refracted (too much wave-front rotation) around Cape Recife, it is recommended that the formulations for depth-induced refraction in SWAN be reviewed. Such a revision should use as subject wave spectra of high energy and period, and steep-sloped topography such as that of Cape Recife.
- c) Considering the difficulties experienced with the accurate specification of boundary wave conditions on the eastern computational boundary during simulation, it is recommended that, where possible, the information on offshore wave conditions be expanded. For the Algoa Bay field case, which represents a large, open bay, the single offshore wave observation station could be supplemented by a second, situated to the east of the Bay. Also, the specification of offshore boundaries would be significantly enhanced using a nesting in an oceanic-scale wave prediction model such as WAM (WAMDI group, 1988). This option already exists in SWAN.
- d) It was shown that for at least one offshore condition modelled, the choice of time-independency made in this study was not valid. It is, therefore, recommended that non-stationary (time-dependent) simulations be conducted for, for example, the three characteristic offshore conditions considered in this study – SSW swell, ESE wind sea and a bi-modal condition. Time dependent

simulations of typical storm events would also provide a basis for the improved calibration of the model setup proposed for the Algoa Bay field case.

- e) It is recommended that the validation on SWAN for conditions in the South African coastal zone be extended. Application to typical south coast conditions was considered in this study. However, it was shown that special cases exist along the South African coast, for example: strong current action in the open bay area at the Durban Bluff (east coast), and possible interaction between high-energy swell and wind-sea generation on the west coast (which is related to the field case of Duck (Rogers *et al.*, 2000)). The modelling of such cases using SWAN requires further investigation.

## 12 REFERENCES

- \*ANDORKA GAL, JH and ROELSE, P (1997). Wave Modelling in the Westerschelde Estuary and Wave Conditions Along the Sea Defences, *Rep. RIKZ/AB-96.868x*, Ministry of Transport, Public Works and Water Management, The Hague, The Netherlands.
- ANDORKA GAL, JH, HOLTHUIJSEN, LH, DE JONG, JCM and KIEFTENBURG, ATMM (1998). Wave Transformation Near a Quasi-1D Coast, *Proc. 26<sup>th</sup> Int. Conf. Coastal Eng.*, pp. 150-160.
- \*ATKINS, GF (1970). Winds and Current Patterns in False Bay. *Trans. R. Soc. S. Africa XXXIX*. Part 2, pp. 139-148.
- \*BATTJES, JA (1994). Shallow Water Wave Modelling, *Proc. Int. Symp.: Waves – Physical and Numerical Modelling*, Vancouver, pp. 1-23.
- BATTJES, JA and JANSSEN, JPFM (1978). Energy Loss and Set-Up due to Breaking of Random Waves. *Proc. of 16<sup>th</sup> Int. Conf. on Coastal Eng. ASCE*. pp. 569-587.
- BEJI, S and BATTJES, JA (1993). Experimental Investigation of Wave Propagation Over a Bar. *Coastal Engineering*, 19, pp. 151-162.
- BERKHOFF, JCW (1972). Computations of Combined Refraction-Diffraction, *Proc. 13<sup>th</sup> Int. Conf. on Coastal Eng.*, Vancouver, pp. 471-490.
- BOUWS, E and KOMEN, GJ (1983). On the Balance Between Growth and Dissipation in an Extreme, Depth Limited Wind-Sea in the Southern North Sea, *Journ. Phys. Oceanogr.*, 13, pp. 1653-1658.
- BOYD, AJ, TAUNTON-CLARK, J and OBERHOLSTER, GPJ (1992). Spatial Features of the Near-Surface and Midwater Circulation Patterns off Western and Southern South Africa and their Role in the Life Histories of Various Commercially Fished Species. *Benguela Tropic Functioning. S. Afr. J. mar. Sci.* 12, pp. 189-206.
- BRITISH OCEANOGRAPHIC DATA CENTRE (1997). General Bathymetric Chart of the Oceans (GEBCO) '97. Birkenhead, United Kingdom.
- CAVALERI, L and MALANOTTE-RIZOLLI, P (1981). Wind Wave Prediction in Shallow Water: Theory and Applications. *Journ. Geophys. Res.*, 86, (C11), pp.10961-10,973.

CERC (1984) Shore Protection Manual, US Army Corps of Engineers, *Techn. Rep.* No. 4.

COLLINS, JI (1972). Prediction of Shallow-Water Spectra. *Journ. of Geophysical Research*, 77 (15) pp. 2693-2707.

CSIR (1998). SFF Milnerton Installation: Environmental Data for the Feasibility Study of a SPM in Table Bay. *Confidential CSIR Report ENVIS-C 98013*, Stellenbosch.

\*DINGEMANS, MW, STIVE, MJF, BOSMA, J, DE VRIEND, HJ and VOGEL, JA (1987). Directional Nearshore Wave Propagation and Induced Currents, *Proc. 20th Int. Conf. Coastal Engineering, ASCE*, pp. 1092-1106.

ELDEBERKY, Y (1996). Nonlinear Transformation of Wave Spectra in the Nearshore Zone, *Ph.D thesis*, Delft University of Technology, Department of Civil Engineering, The Netherlands.

\*ELDEBERKY, Y and BATTJES, JA (1996). Spectral Modelling of Wave Breaking. Application to Boussinesq Equations, *J Geophys. Res.*, 101, (C1), pp. 1253-1264.

GOSCHEN, WS and SCHUMANN, EH (1988). Ocean Current and Temperature Structures in Algoa Bay and Beyond in November 1986. *S. Afr. J. mar. Sci.* 7: pp. 101-116.

HARRIS, TFW (1978). Review of Coastal Currents in Southern African Waters. *Rep. S. Afr. Nat. scient. Progrms* 30, 103 pp.

\*HASSELMANN, K (1962). On the Nonlinear Energy Transfer in a Gravity Wave Spectrum. Part 1: General Theory. *Journ. Fluid Mech.*, 12, pp. 481-500.

\*HASSELMANN, K (1963a). On the Nonlinear Energy Transfer in a Gravity Wave Spectrum. Part 2: Conservation Theorems; Wave-Particle Analogy; Irreversibility, *Journ. Fluid Mech.*, 15, pp. 273-281.

\*HASSELMANN, K (1963b). On the Nonlinear Energy Transfer in a Gravity Wave Spectrum. Part 3: Evaluation of Energy Flux and Sea-Swell Interaction for a Neumann Spectrum, *Journ. of Fluid Mech.*, 15, pp. 385-398.

HASSELMANN, K (1974). On the Spectral Dissipation of Ocean Waves due to Whitecapping. *Boundary Layer Meteorology*, Vol. 6, pp. 107-127



HASSELMANN, K, BARNETT, TP, BOUWS, E, CARLSON, H, CARTWRIGHT, DE, ENKE, K, EWING, JA, GIENAPP, H, HASSELMANN, DE, KRUSEMAN, P, MEERBURG, A, MÜLLER, O, OLBERS, DJ, RICHTER, K, SELL, W and WALDEN, H (1973). Measurement of Wind-Wave Growth and Swell Decay During the Joint North Sea Wave Project (JONSWAP), *Dtsch. Hydrogr. Z. Suppl.*, 12 (A8).

HASSELMANN, S, HASSELMANN, K, ALLENDER, JH and BARNETT, TP (1985). Computations and Parameterizations of the Linear Energy Transfer in a Gravity Wave Spectrum. Part II: Parameterizations of the Nonlinear Transfer for Application in Wave Models, *Journ. Physical Oceanography*, 15 (11) pp. 1378-1391.

HOLTHUIJSEN, LH (2000) Wind Waves (Lecture Notes). *Collegehandleiding Ctwa 9991*, Delft University of Technology.

\*HOLTHUIJSEN, LH, BOOIJ, N, and RIS, RC (1993). A Spectral Wave Model for the Coastal Zone, *Proc. of 2<sup>nd</sup> Int. Symposium on Ocean Wave Measurement and Analysis*, New Orleans, pp. 630-641.

\*HOLTHUIJSEN, LH, BOOIJ, N and BERTOTTI, L (1996). The Propagation of Wind Errors through Ocean Wave Hindcasts, *J. of Offshore Mech. and Arctic Eng.*, 118, pp. 184-189.

HOLTHUIJSEN, LH, BOOIJ, N and HAAGSMA, IJ G (1998). Comparing 1<sup>st</sup>-, 2<sup>nd</sup>- and 3<sup>rd</sup>-generation Coastal Wave Modelling, *Proc. 26<sup>th</sup> Int Conf Coastal Engrg*, pp. 140-149.

HOLTHUIJSEN, LH, BOOIJ, N, RIS, RC, HAAGSMA, IJ G, KIEFTENBURG, ATMM and PADILLA-HERNANDEZ, R (1999). *SWAN Cycle 2 version 40.01 User Manual*. Delft University of Technology, Delft.

HOLTHUIJSEN, LH, RIS, RC and CECCHI E (2000). Swell and Whitecapping, A Numerical Experiment, *Proc. 27<sup>th</sup> Int Conf Coastal Engrg*, pp. 346-354.

HSIAO, SV and SHEMDIN, OH (1978). Bottom dissipation in finite depth water waves, *16<sup>th</sup> Int. Conf. Coastal Eng.*, ASCE, Hamburg, pp 434-448.

HUNTER, IT (1987). The Weather of the Agulhas Bank and the Cape South Coast. *CSIR Report 634*. Stellenbosch.

HURRY, L and VAN HEERDEN, J (1982). *South Africa's Weather Patterns*, Via Africa Ltd., Cape Town.

JANSSEN, PAEM (1989). Wave-induced Stress and the Drag of Air Over Sea Waves, *J Phys Oceanogr*, Vol. 19, pp. 745-754.

JANSSEN, PAEM (1991). Quasi-linear Theory of Wind-wave Generation Applied to Wave Forecasting, *J Phys Oceanogr*, Vol. 21, pp. 1631-1642.

\*KAMSTEEG, AT, ANDORKA GAL, JG, DE RONDE, JG and DE JONG, JCM (1998). Wave Boundary Conditions on the Westerschelde, Given a 1/400 Wind Velocity. *RIKZ Report No. 98.018*, Ministry of Transport, Public Works and Water Management, The Hague, The Netherlands.

KOMEN, GJ, HASSELMANN, S and HASSELMANN, K (1984). On The Existence of a Fully Developed Wind-Sea Spectrum. *Journ. of Phys Oceanogr*, Vol. 14, pp. 1271-1285.

KUIK, AJ, VAN VLEDDER, G PH, HOLTHUIJSEN, LH, (1988). A Method for the Routine Analysis of Pitch-and-Roll Bouy Wave Data, *J Phys Oceanogr*, Vol. 18, pp. 1020-1034.

\*LAI, RJ, LONG SR and HUANG, NE (1989). Laboratory Studies of Wave-Current Interaction: Kinematics of the Strong Interaction, *Journ. Geophysical Research*, 94, (C11) pp. 16,201–16,214

MADSEN, OS, POON, Y-K and GRABER, HC (1988). Spectral Wave Attenuation by Bottom Friction: Theory. *Proc. of 21th Int. Conf. Coastal Eng. ASCE*. pp. 492-504.

MILES, JW (1957). On the Generation of Surface Waves by Shear Flows. *Journ. of Fluid Mech*, 3, pp. 185-204

\*MILES, JW (1981). Hamiltonian Formulations for Surface Waves, *Applied Scientific Research*, 37, pp. 103-110.

\*PERGRENE, DH (1966). Long Waves on a Beach, *Journ. of Fluid Mech.*, 27 (4) pp. 815-827.

PHILLIPS, OM (1957). On the Generation of Waves by Turbulent Wind. *Journ. of Fluid Mech*, 2, pp 417-445.

PIERSON, WJ and MOSKOWITZ, L (1964). A Proposed Spectral Form for Fully Developed Wind Seas Based on the Similarity Theory of SA Kitaigorodskii, *Journ. Geophys. Res.*, Vol. 69, No. 24, pp. 5181-5190.

PORTNET (2001). Coega Port: Maritime Works. Subtask G: *Site Investigations*, Vol.1. Portnet Head Office, Braamfontein, p. A-2.

RADDER, AC (1979). On the Parabolic Equation Method for Water-Wave Propagation, *Journ. Fluid Mech.* 95(1), pp. 159-176.

RIS, RC (1997). Spectral Modelling of Wind Waves in Coastal Areas. Communications on Hydraulic and Geotechnical Engineering. *Report No. 97-4*. Delft University of Technology. Delft.

RIS, RC, BOOIJ, N and HOLTHUIJSEN, LH (1999). A Third-Generation Wave Model for Coastal Regions. Part II: Model Description and Validation, *Journ. Geographical Research*, 104(C4), pp. 7667-7682.

ROGERS, WE, HWANG, PA, WANG, DW and KAIHATU, JM (2000). Analysis of SWAN Model with In-situ and Remotely Sensed Data from SandyDuck '97, *Proc. 27<sup>th</sup> Int Conf Coastal Engrg*, pp. 812-825.

ROSSOUW, C (1999). The Probability of Occurrence and the Intensity of Tropical Cyclones along the Southern African East Coast. *M.Sc Thesis*. University of Stellenbosch.

ROSSOUW, J (1989). Design Waves for the South African Coastline. *Ph.D Thesis*. University of Stellenbosch.

ROSSOUW, M (2001). Re-evaluation of the Extreme Wave Climate of Southern Africa. *Ph.D thesis* (in preparation). University of Stellenbosch, South Africa.

SA HYDROGRAPHICAL OFFICE (1972–1996). *Naval Charts*, Tokai, South Africa.

SA HYDROGRAPHICAL OFFICE (1999). *South African Tide Tables 1999*. SAN HO-2, Tokai, South Africa.

SA WEATHER BUREAU (1999). *Daily Weather Bulletin for the Month April 1999*. ISSN 0011-5517.

SCHUMANN EH, PERRINS L-A and HUNTER IT (1982). Upwelling along the South Coast of the Cape Province, South Africa. *S. Afr. J. Sci.* 78(6): pp. 238-242.

SCHUMANN, EH, ILLENBERGER, WK and GOSCHEN, WS (1991). Surface winds over Algoa Bay, South Africa. *S. Afr. J. of Sci.* Vol. 87: 202-207.

SHANNON LV (1985). The Benguela Ecosystem. 1. Evolution of the Benguela, Physical Features and Processes. *Oceanography and Marine Biology. An Annual Review* 23. Aberdeen: University Press. pp. 105-182.

SHANNON, LV and STANDER, GH (1977). Physical and Chemical Characteristics of Water in Saldanha Bay and Langebaan Lagoon. *Trans. R. Soc. S Afr.* 42, Parts 3 and 4. pp. 441-459.

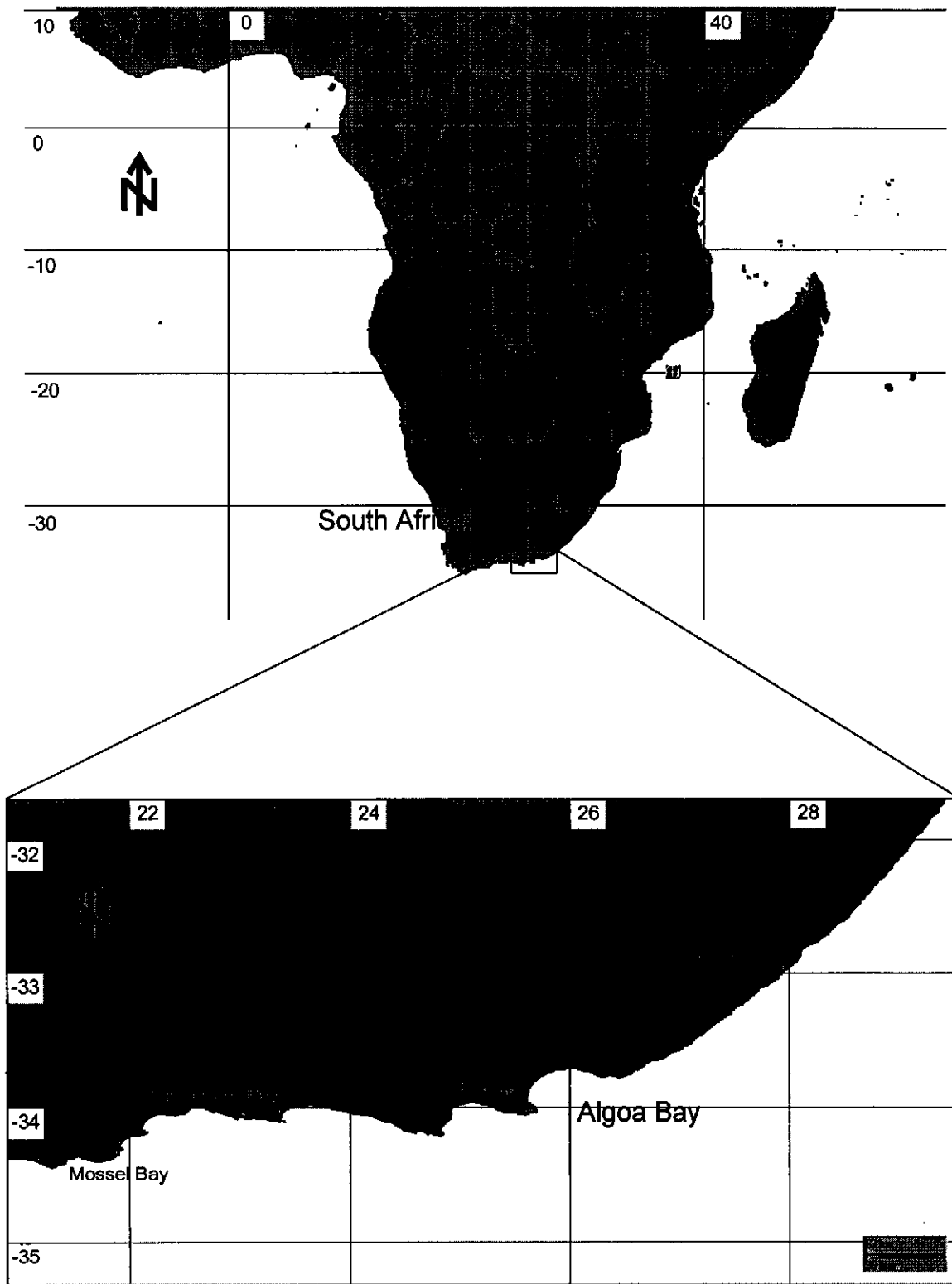
TOLMAN, HL (1991). A Third-Generation Model for Wind Waves on Slowly Varying, Unsteady and Inhomogeneous Depths and Current, *Journ. of Physical Oceanography*, 21(6) pp. 782-797.

WAMDI GROUP (1988). The WAM Model – A Third Generation Ocean Wave Prediction Model, *Journ. of Physical Oceanography*, 18, pp. 1775-1810.

WUDELFT HYDRAULICS (2000). *Suite of Bench Mark Tests for the Shallow Water Wave Model SWAN. SWAN Cycle 2, Version 40.01 and Updates.* Delft.

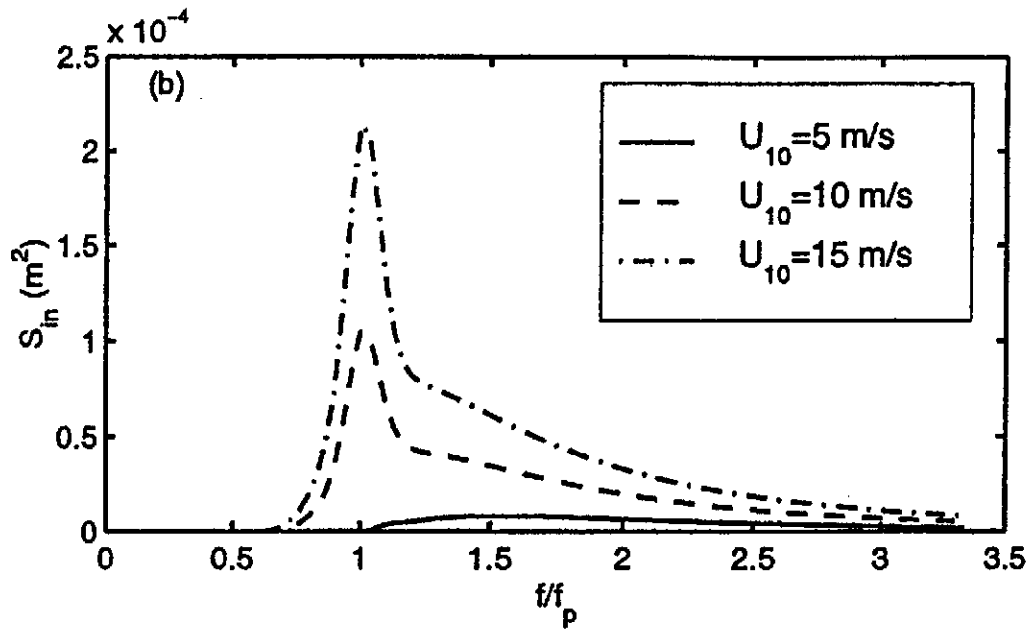
YOUNG, IR (1999). *Wind Generated Ocean Waves.* Elsevier Ocean Engineering Book Series Volume 2.

**FIGURES**

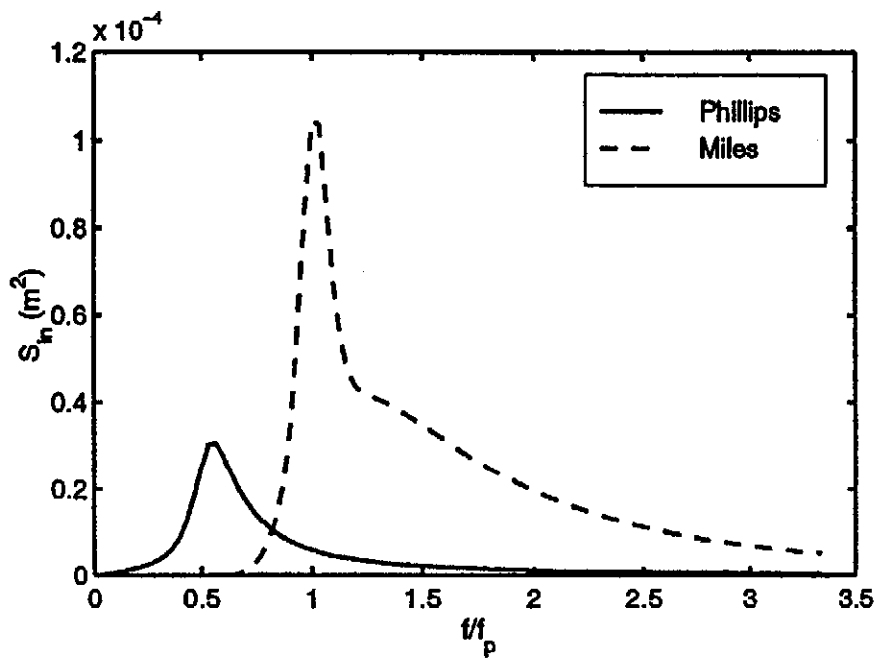


Location of Algoa Bay study area

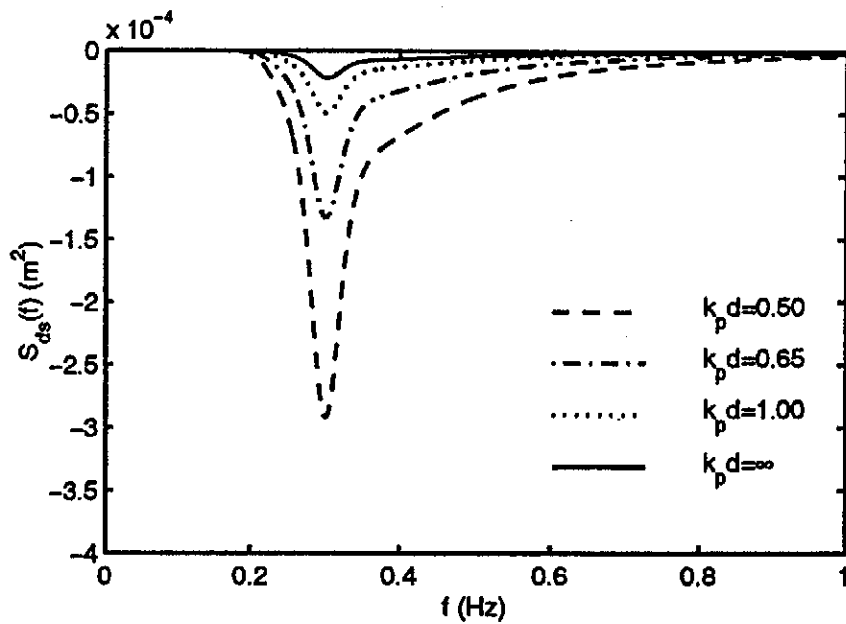
FIGURE  
1.1



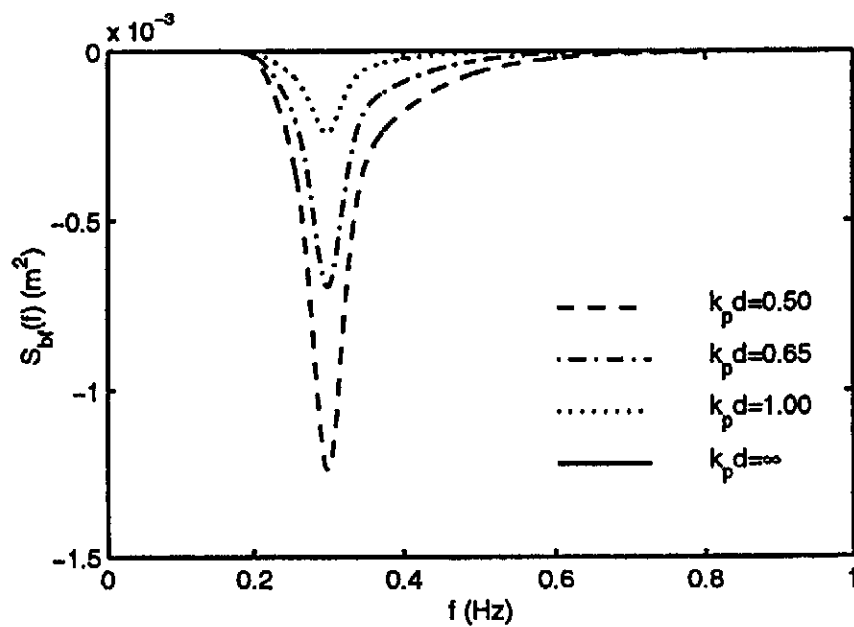
(a) Source term of Komen et al. (1984), integrated over direction and evaluated for a JONSWAP spectrum with  $\gamma = 3,3$ . Calculation shown for a range of wind speeds.



(b) Comparison of linear source term (Phillips, 1957) and exponential source term (Miles, 1957), integrated over direction. Evaluated with  $U_{10} = 10$  m/s, for a JONSWAP spectrum with  $\gamma = 3,3$ .



(a) Source term for whitecapping (Hasselmann, 1974), integrated over direction. Evaluated for a JONSWAP spectrum with  $f_p = 0,3$  Hz and  $\gamma = 3,3$ . Calculation shown for a range of relative depths.

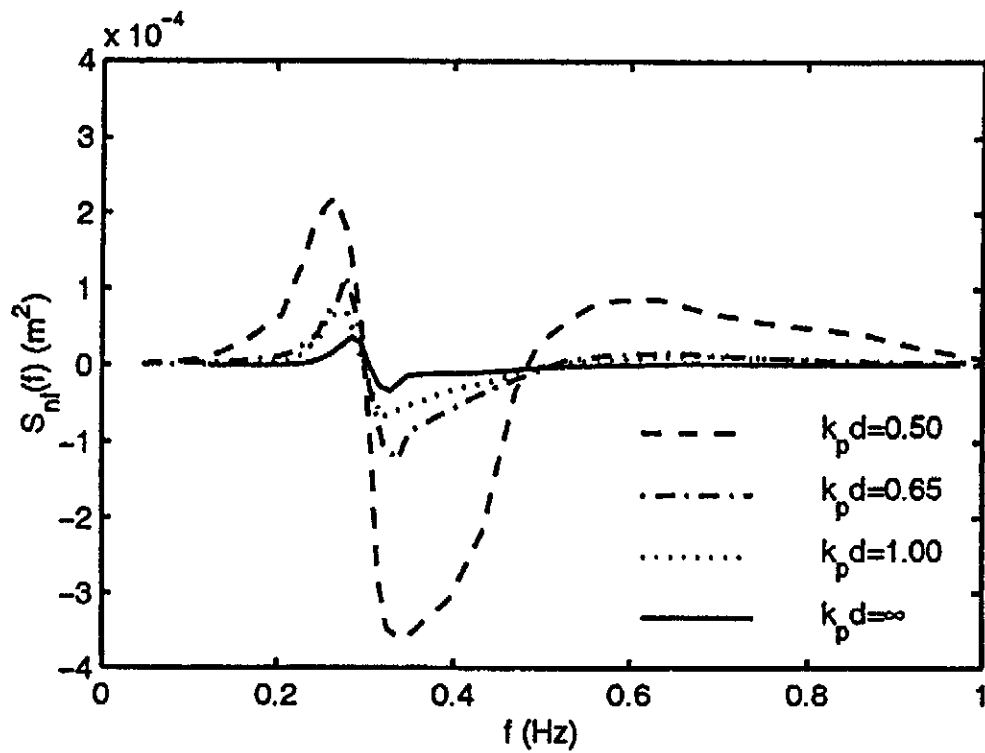


(b) Source term for bottom friction (Hasselmann et al., 1973), integrated over direction. Evaluated for a JONSWAP spectrum with  $f_p = 0,3$  Hz and  $\gamma = 3,3$ . Calculation shown for a range of relative depths.

Source terms for whitecapping ( $S_{bf}$ ) and bottom friction ( $S_{ds}$ )  
(Young, 1999)

FIGURE  
2.2

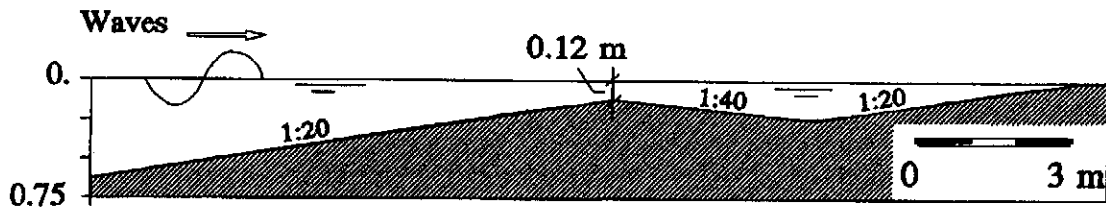




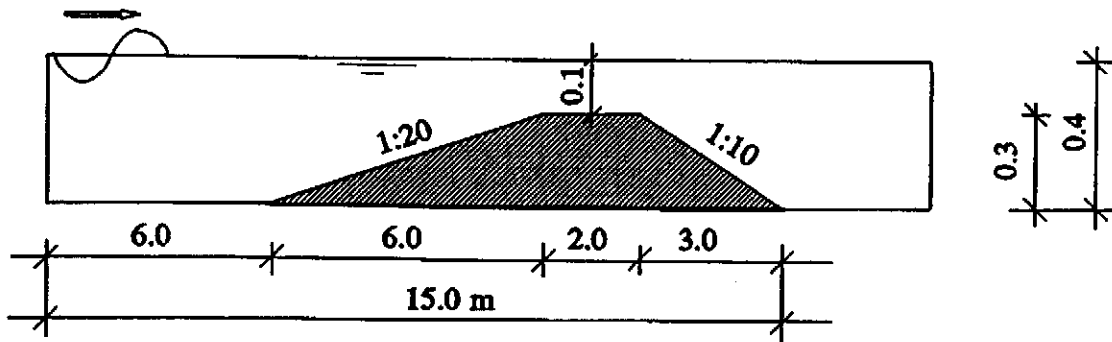
Boltzmann integral for quadruplet-wave interaction (Hasselmann et al., 1962\*, 1963a\* and 1963b\*), integrated over direction. Evaluated for a JONSWAP spectrum with  $f_p = 0,3$  Hz and  $\gamma = 3,3$ , for a range of relative depths.

Source term for quadruplet-wave interaction ( $S_{nl}$ )  
(Young, 1999)

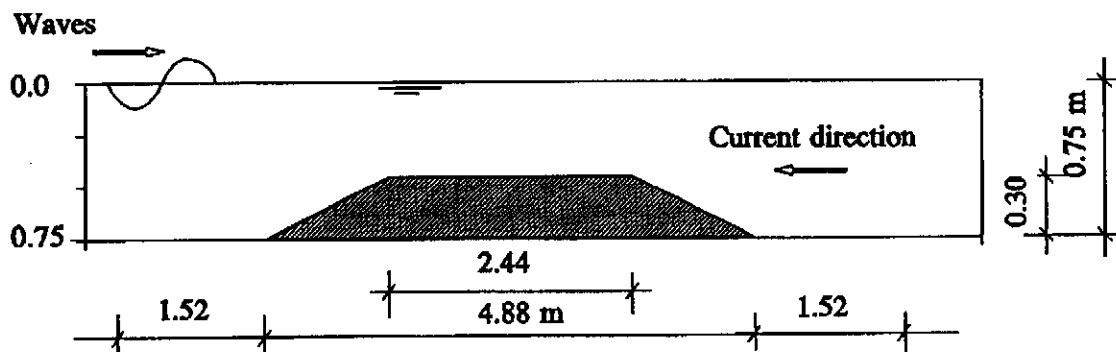
FIGURE  
2.3



(a) Depth-induced wave breaking experiment of Battjes and Janssen (1978)



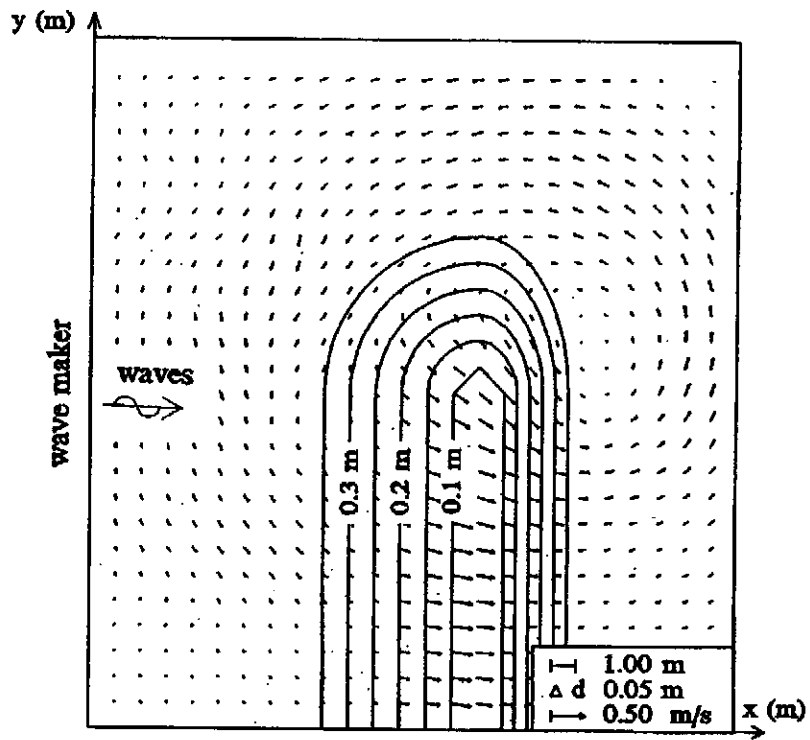
(b) Triad-wave interaction experiment of Beji and Battjes (1993)



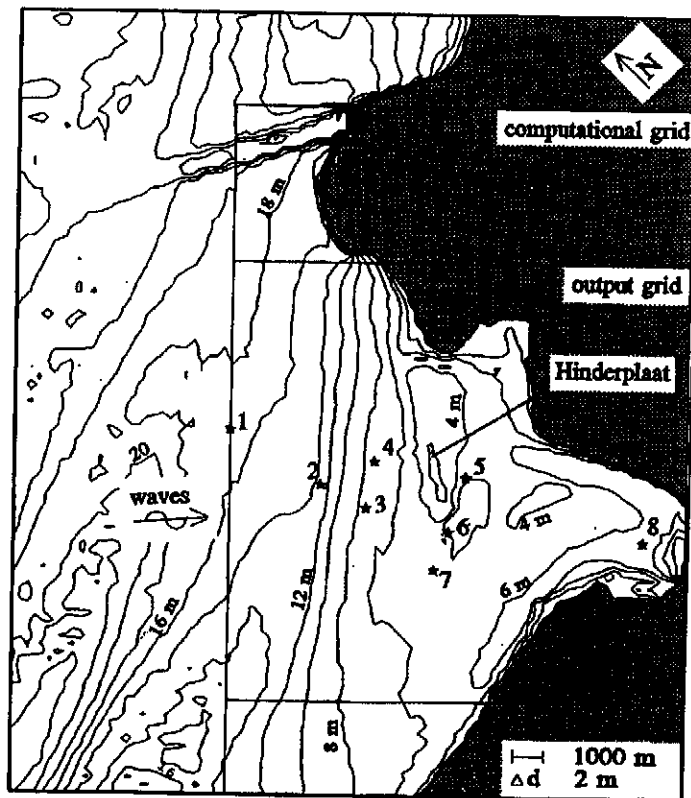
(c) Wave-blocking experiment of Lai et al. (1989)

SWAN validation laboratory cases:  
Wave blocking, triad-wave interaction and depth-induced  
breaking (Ris, 1997)

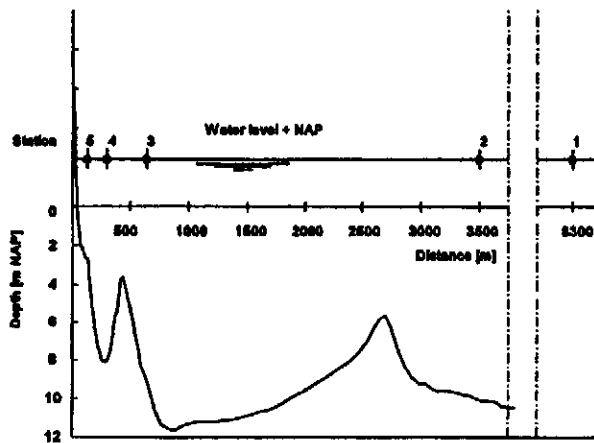
FIGURE  
3.1



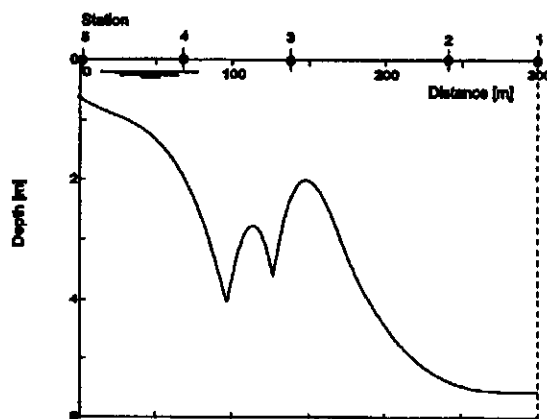
Bathymetry and current pattern of HISWA-tank experiment of Dingemans et al. (1987)  
 (arrows indicate current velocity vectors)



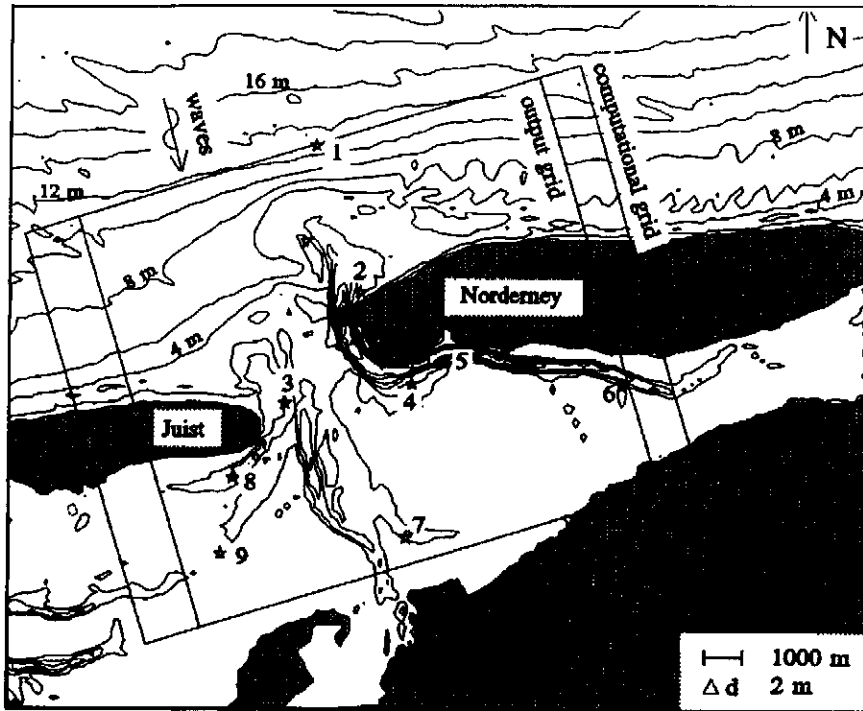
(a) Bathymetry of the Haringvliet estuary, the Netherlands (★ indicates wave recording locations and  $\Delta d$  depth contour intervals)



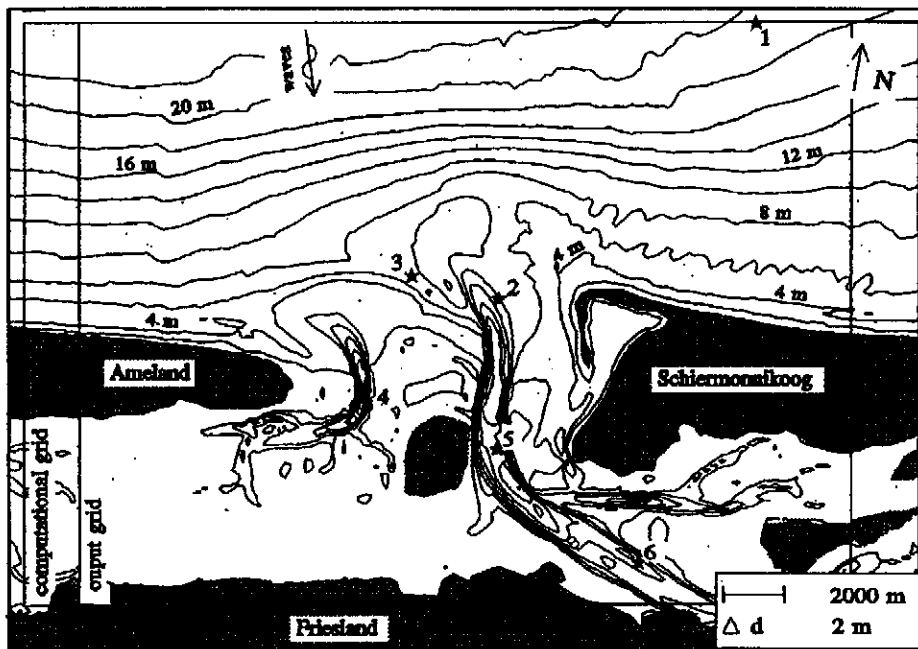
(b) Seabed profile of Petten, the Netherlands



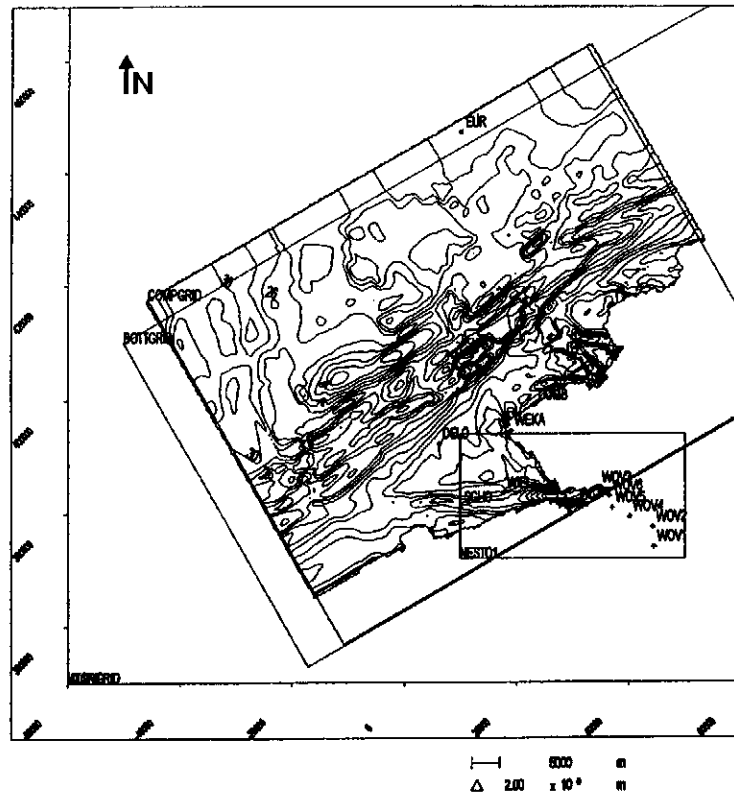
(c) Seabed profile of Kashimanada, Japan



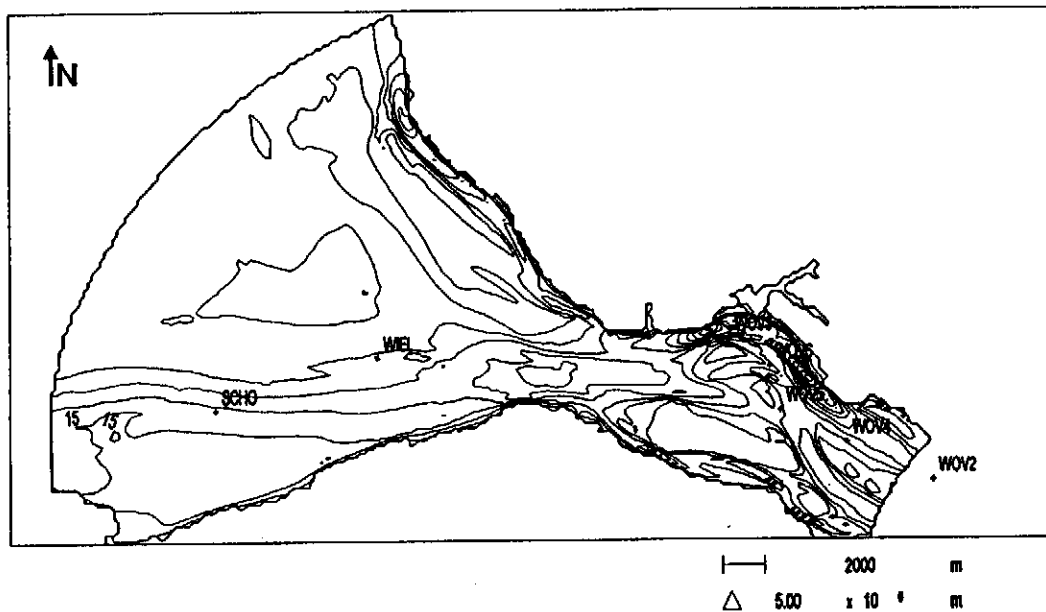
(a) Bathymetry of the Nordemeyer Seegat, Germany (★ indicates wave recording locations)



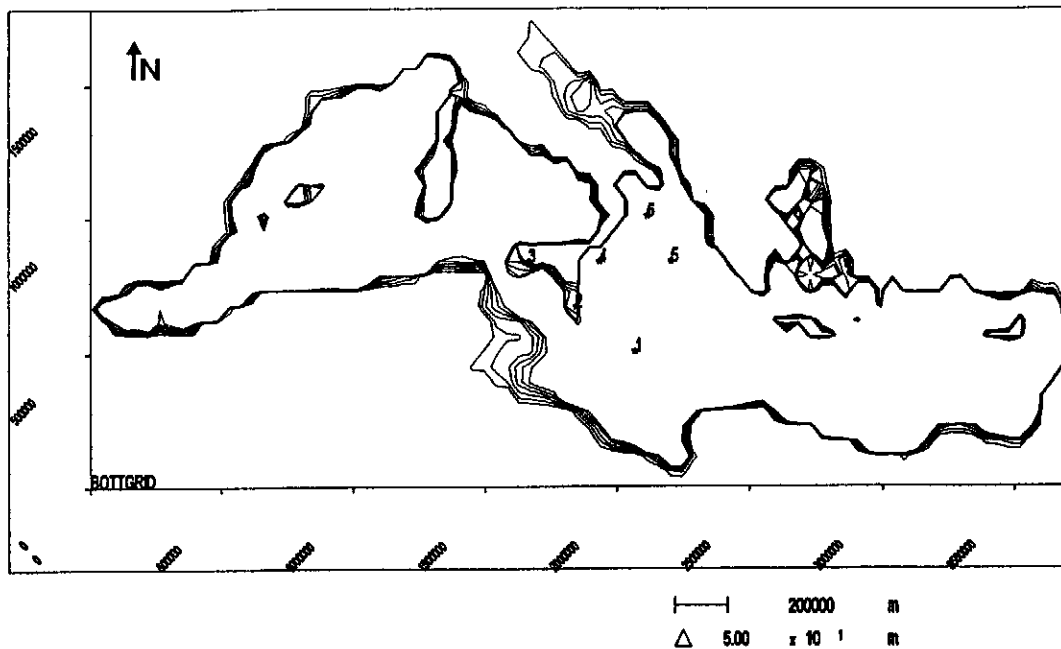
(b) Bathymetry of the Friesche Zeegat, the Netherlands (★ indicates wave recording locations)



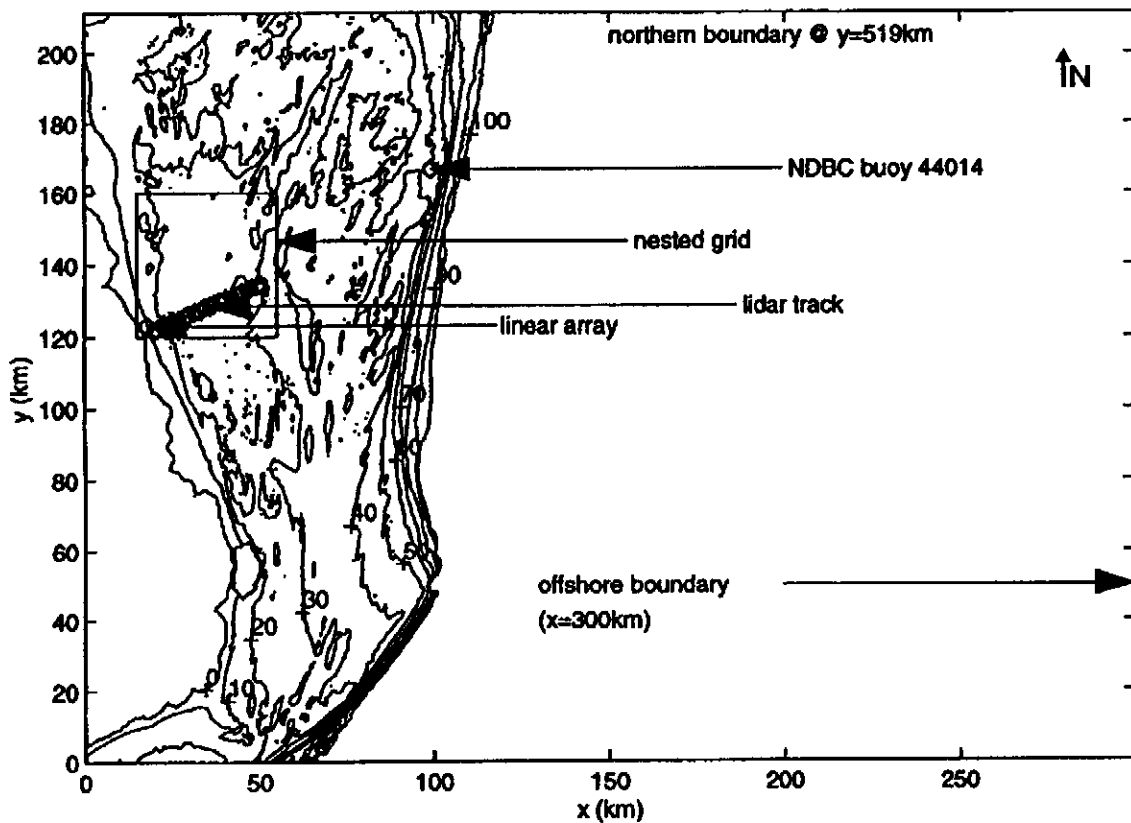
(a) Bathymetry of the outer region of the Westerschelde estuary, the Netherlands (+ indicates wave recording locations, and  $\Delta$  depth contour intervals)



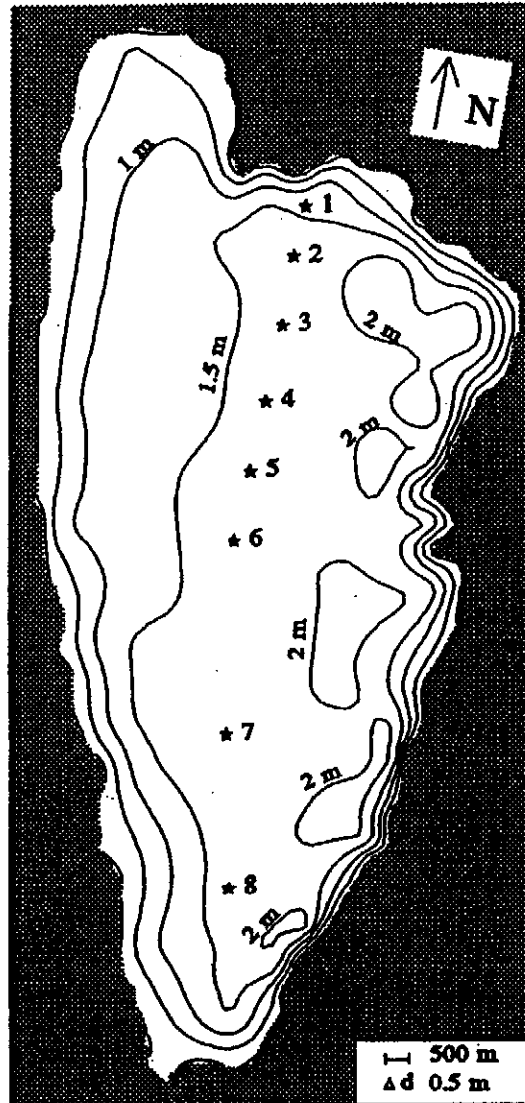
(b) Bathymetry of the inner region of the Westerschelde estuary (+ indicates wave recording locations, and  $\Delta$  depth contour intervals)



(a) Bathymetry of the Mediterranean Sea (★ indicates wave recording locations, and  $\Delta$  depth contour intervals)

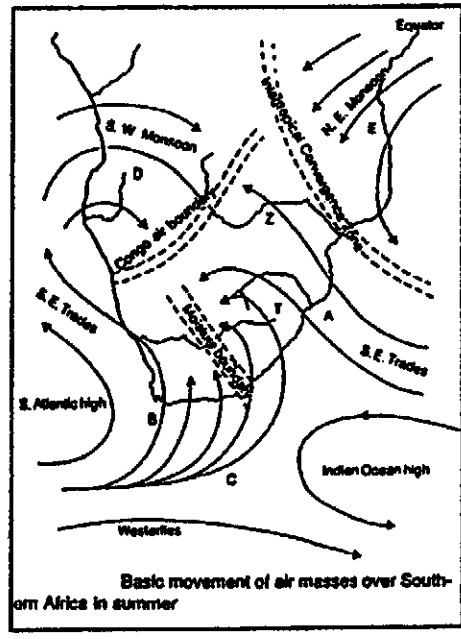
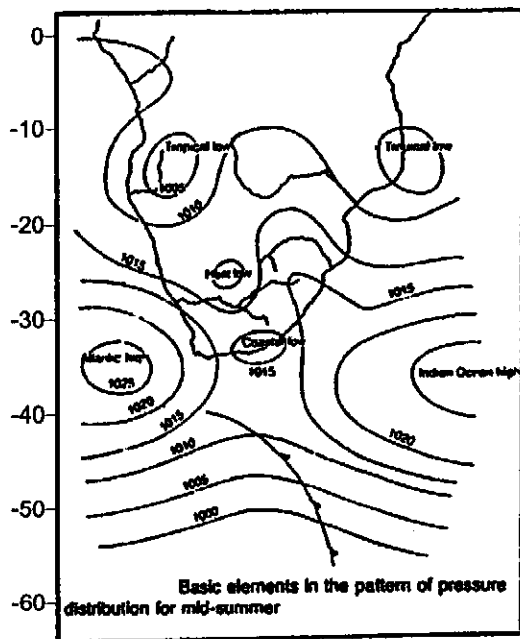
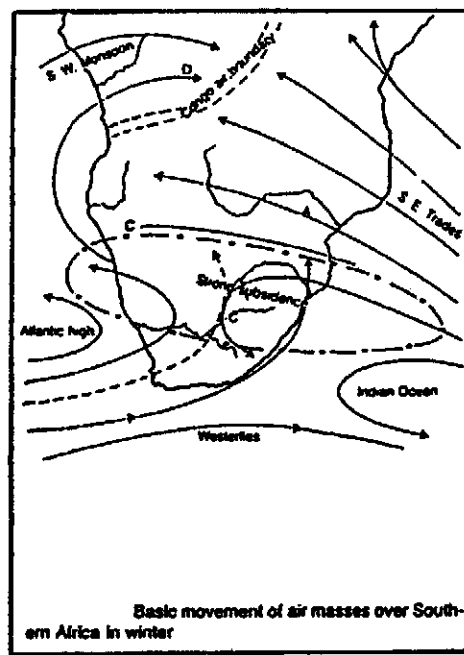
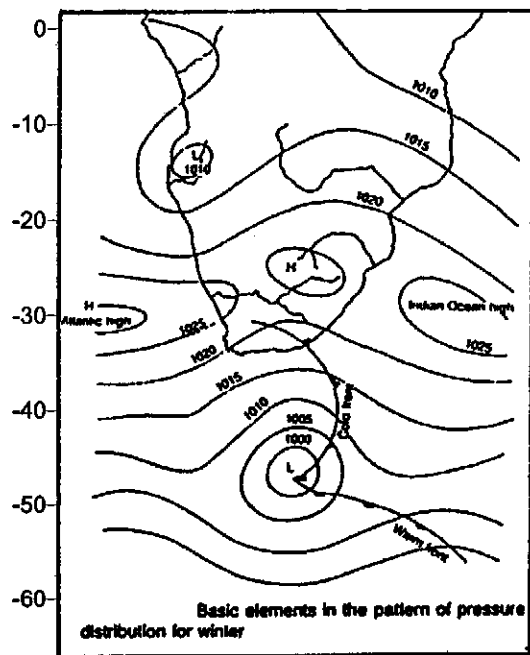


(b) Bathymetry of Duck, USA (+ indicates depth contour values)



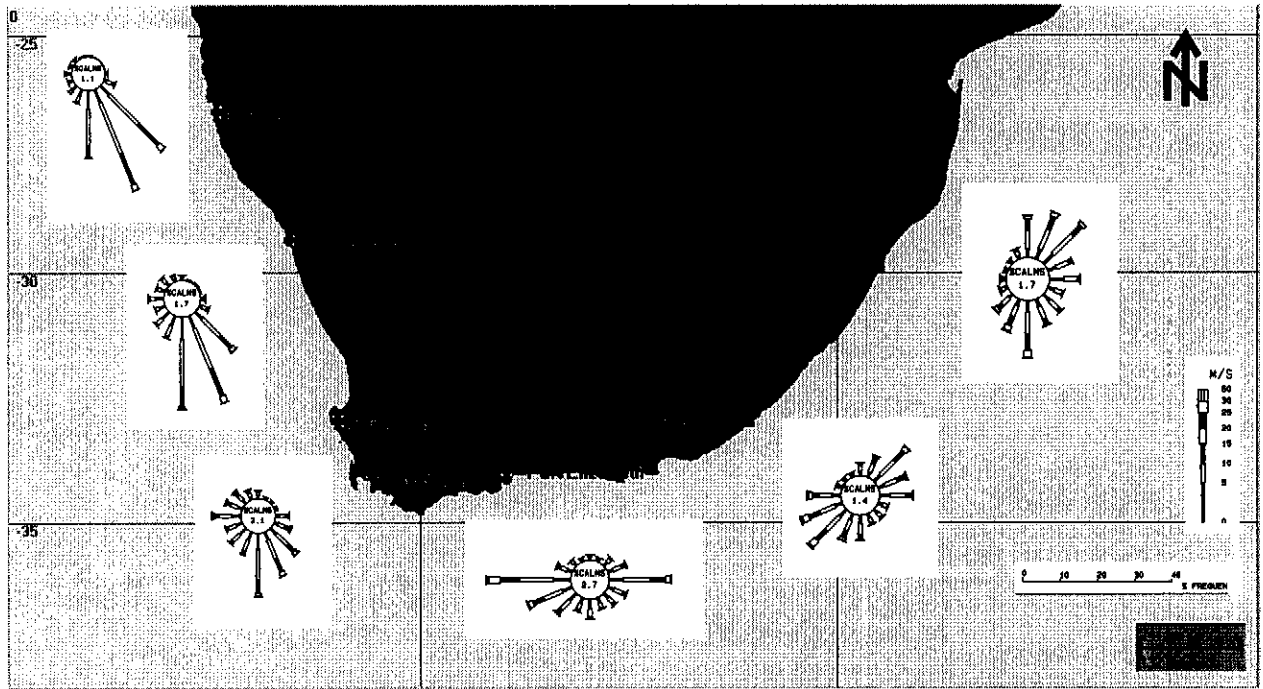
Bathymetry and measurement stations for Lake George field case  
(★ indicates wave recording locations)





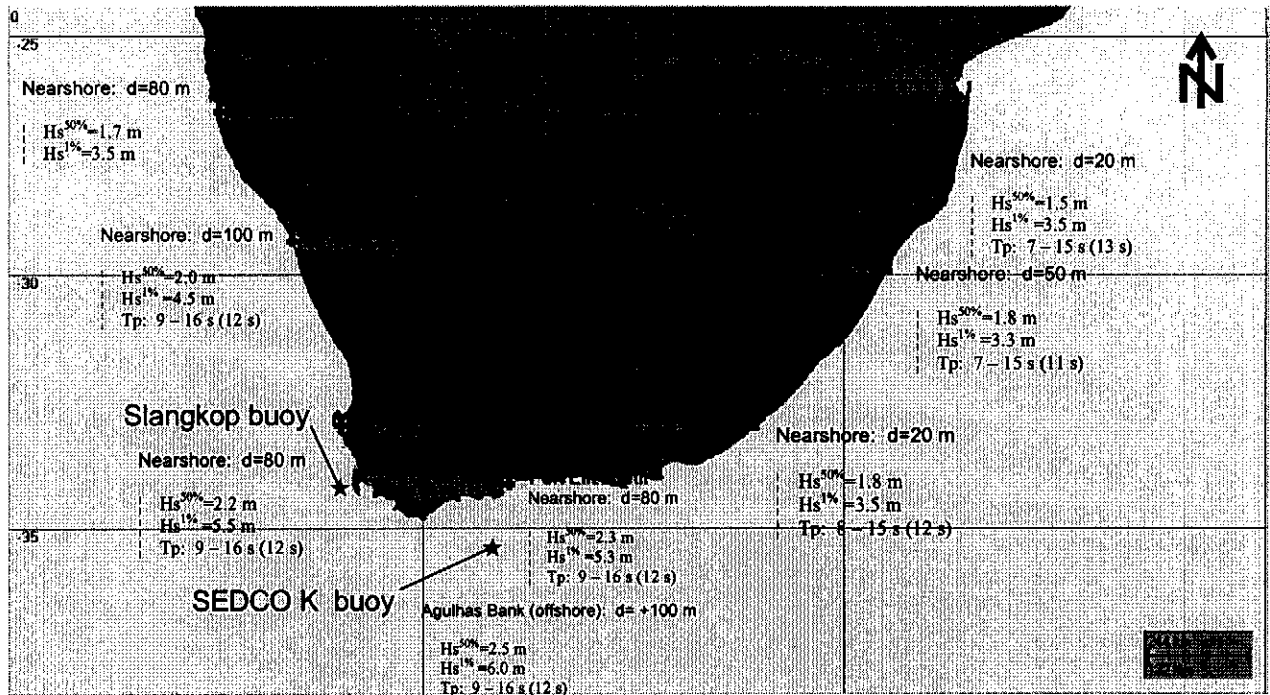
Pressure and wind systems over Southern African oceans (Hurry and Van Heerden, 1982)

FIGURE 4.1

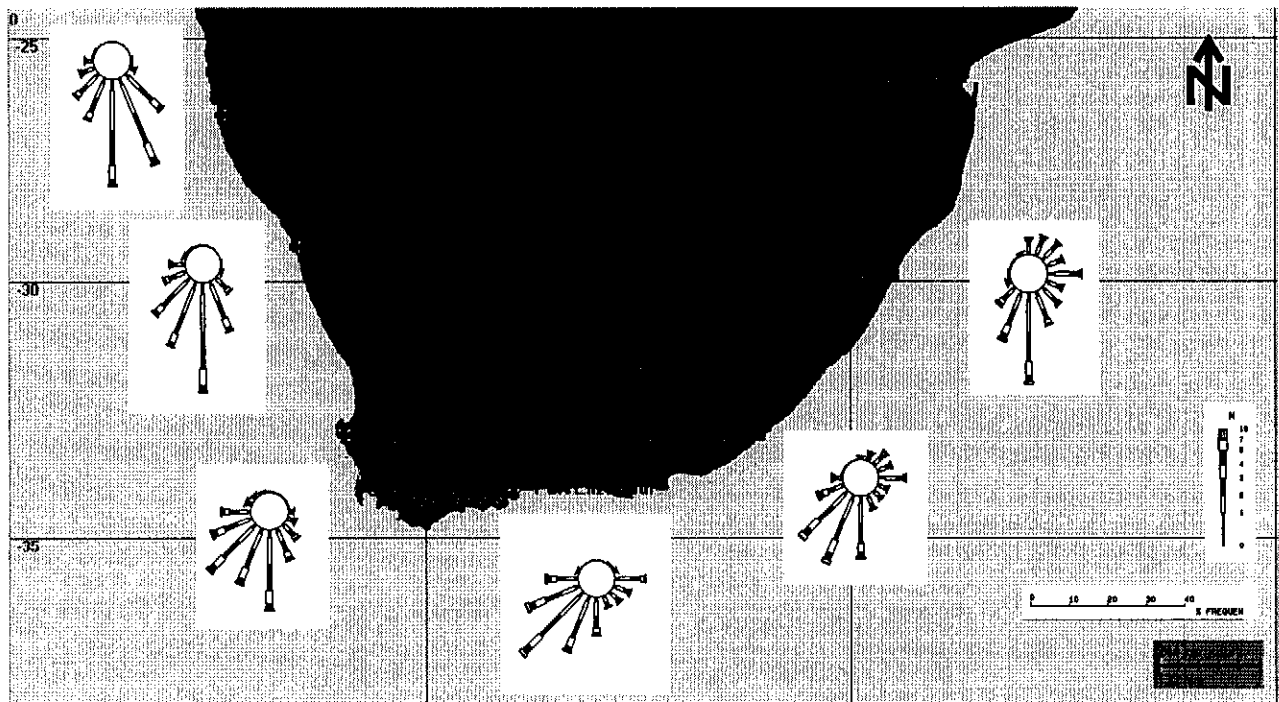


Wind climate along the Southern African coast, based on VOS data (1980-2000) (Rossouw, 2001)

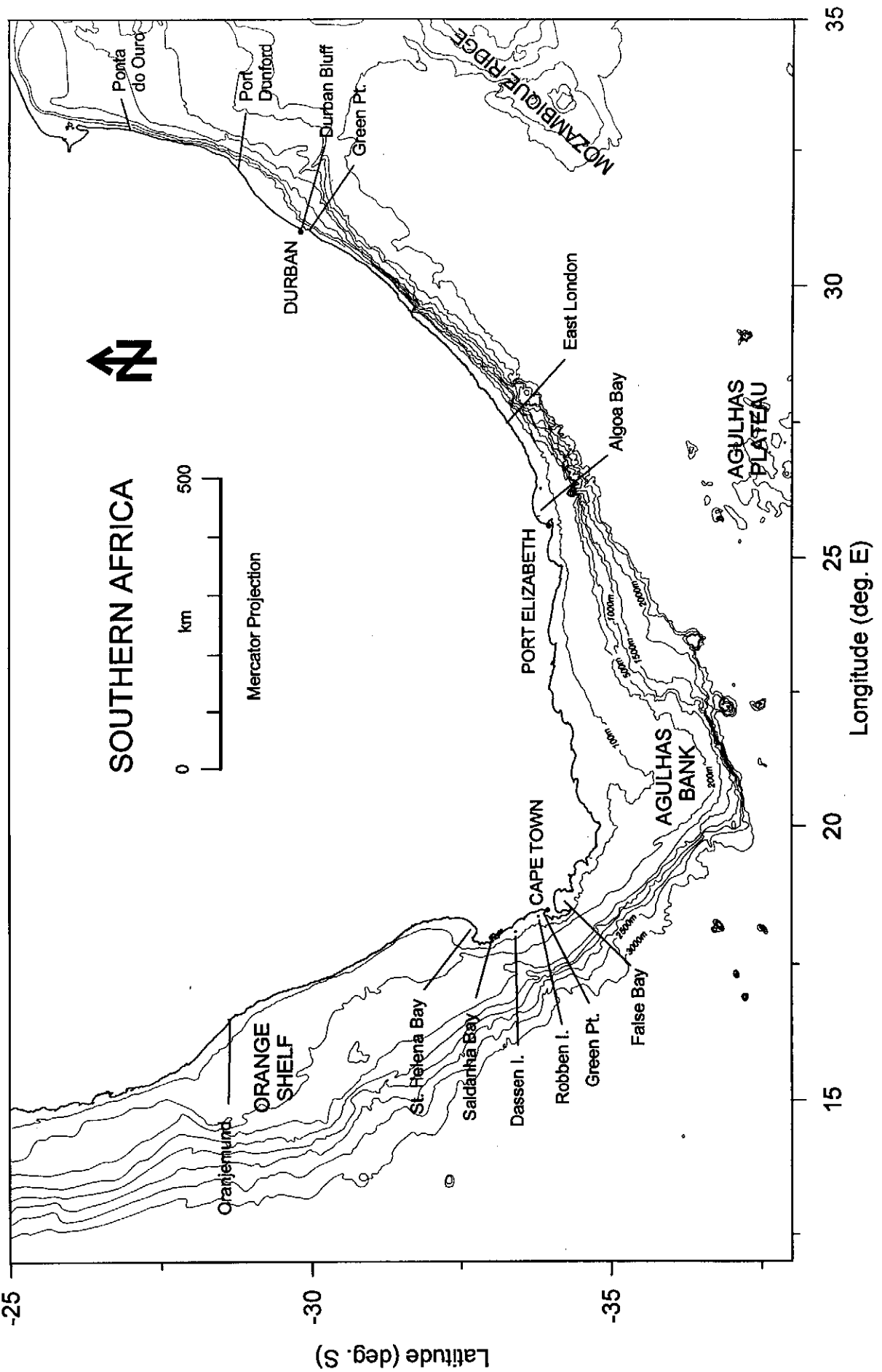
FIGURE 4.2



(a) Statistics of wave height and periodicity along the South African coastline

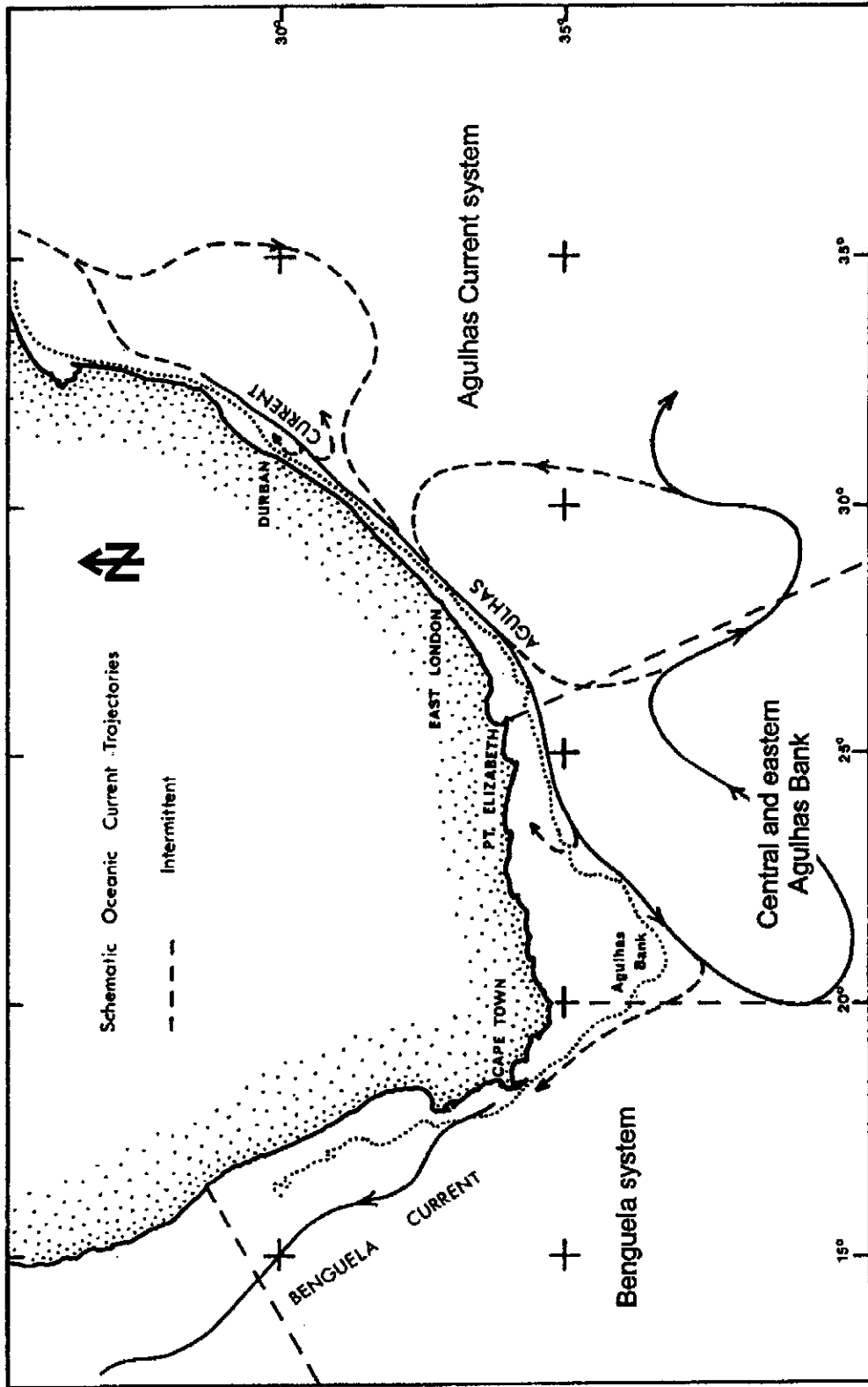


(b) Offshore wave climate of South Africa (VOS data 1980-2000)



Contours of the Southern African seabed to 3 000 m depth  
 (Data from: British Oceanographic Data Centre, 1997)

FIGURE  
 4.4

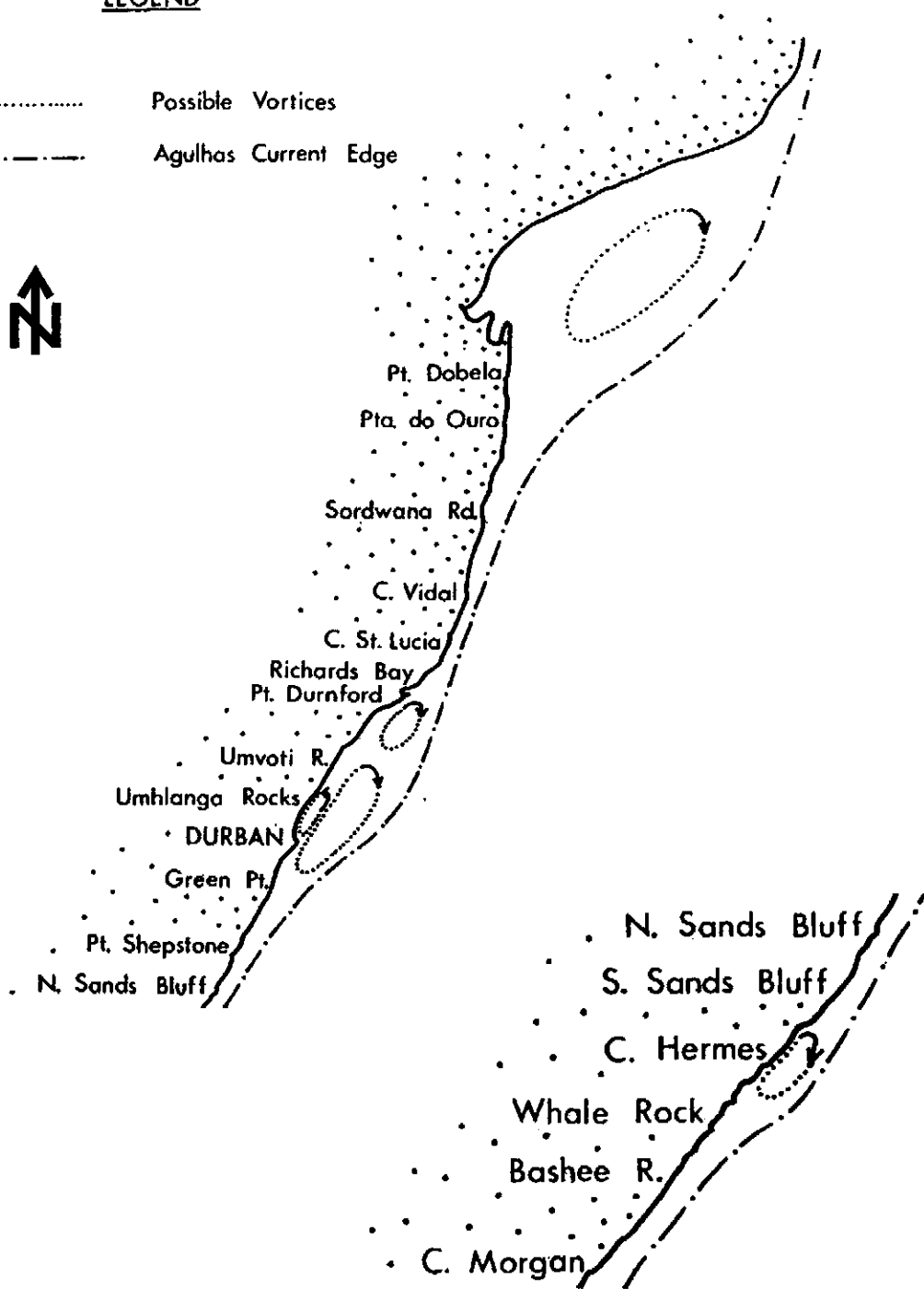


Schematic trajectories of the two major Southern African ocean current system (Harris, 1978)

FIGURE 4.5

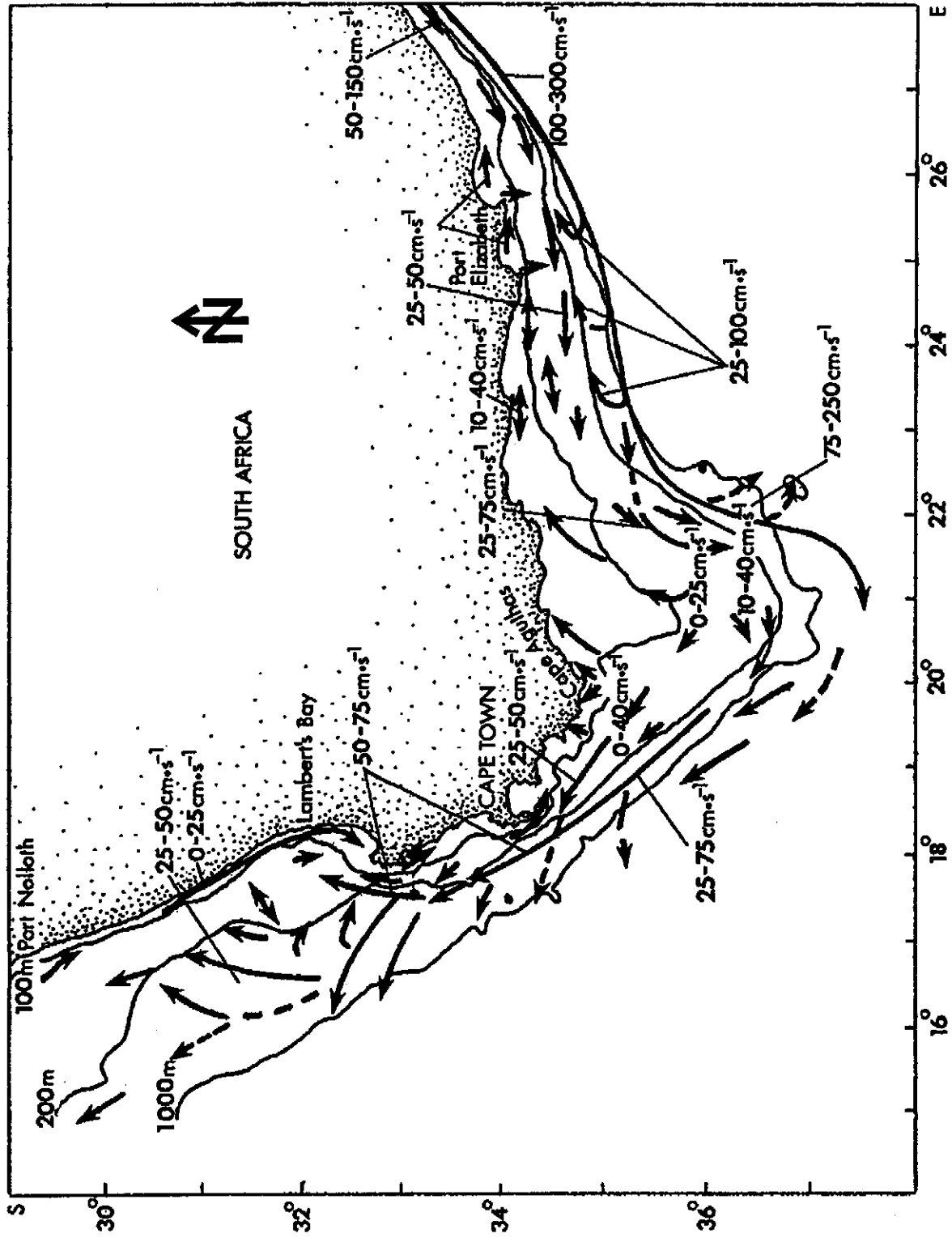
LEGEND

- ..... Possible Vortices
- - - - - Agulhas Current Edge



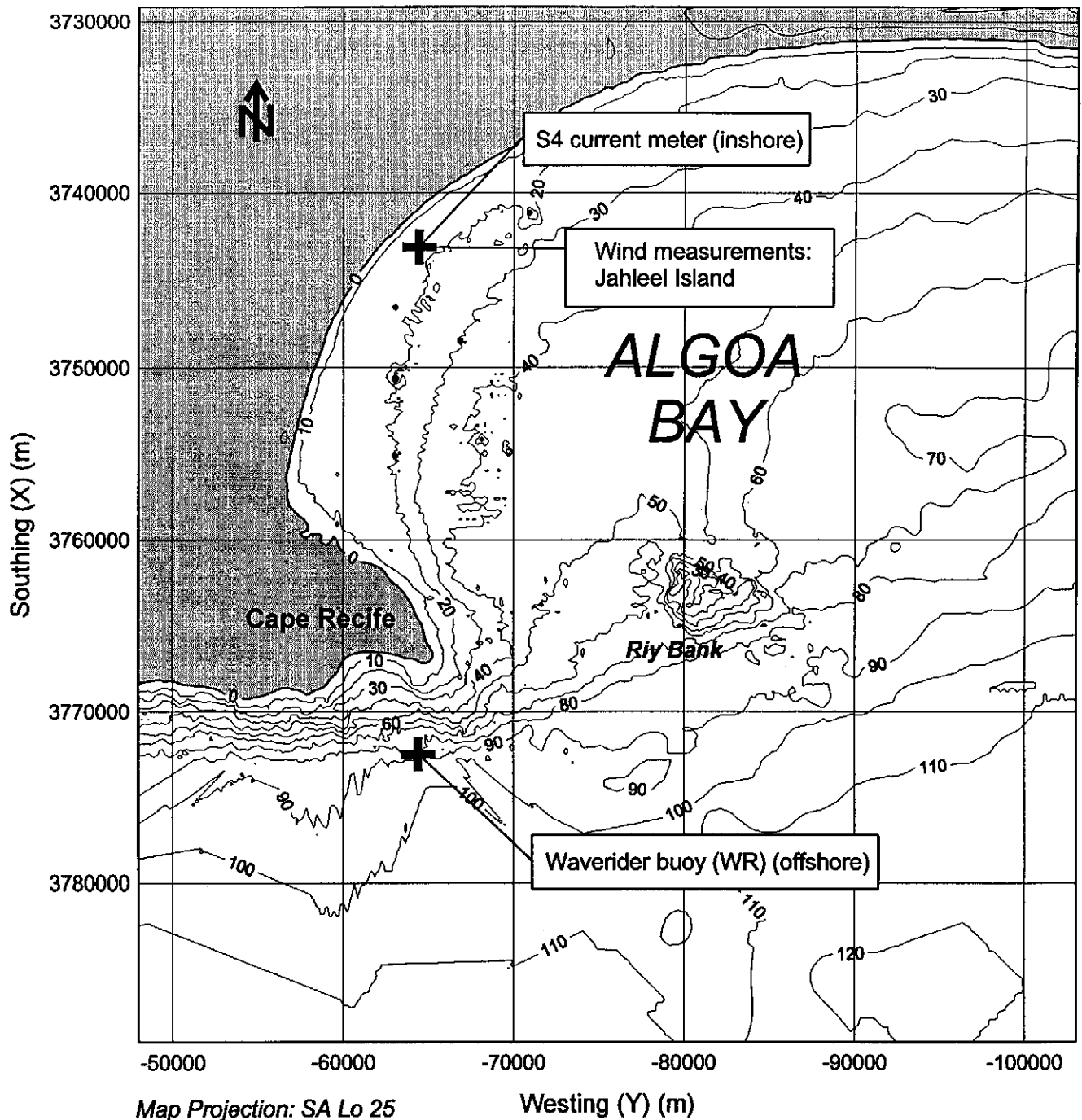
Circulation patterns along the east coast of South Africa  
(Harris, 1978)

FIGURE  
4.6



Near-surface currents (with typical velocities) along west and south coast, based on ADCP data (Boyd et al., 1992)

FIGURE 4.7



**Wave recording locations**

**Directional Waverider**  
 Lat.: 34° 04' 50,6" S  
 Long.: 25° 41' 54,8" E

**S4 current meter**  
 Lat.: 33° 48' 54,6" S  
 Long.: 25° 41' 45,9" E

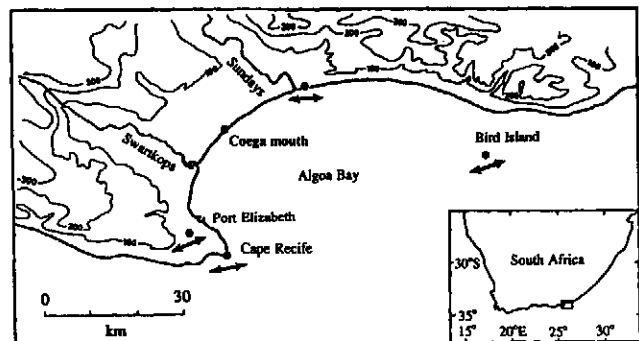


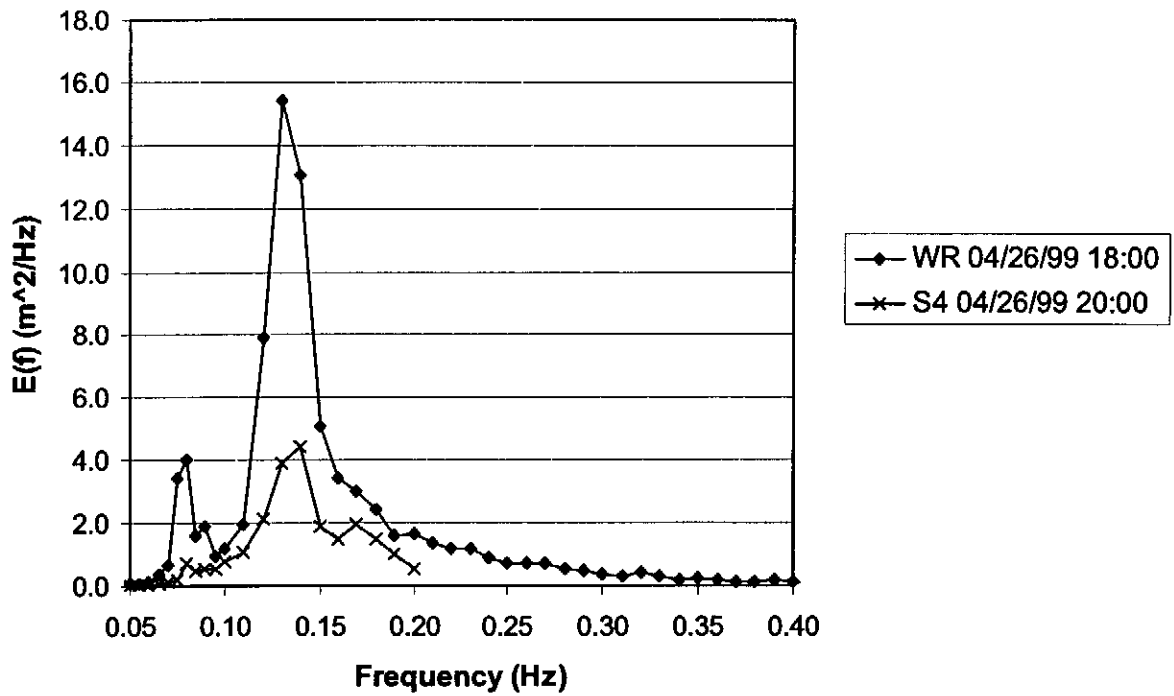
(Chart insert from: Schumann et al., 1991)

**ALGOA BAY FIELD CASE: MODEL SETUP**  
 Locations of wind and wave recording for  
 Algoa Bay field case

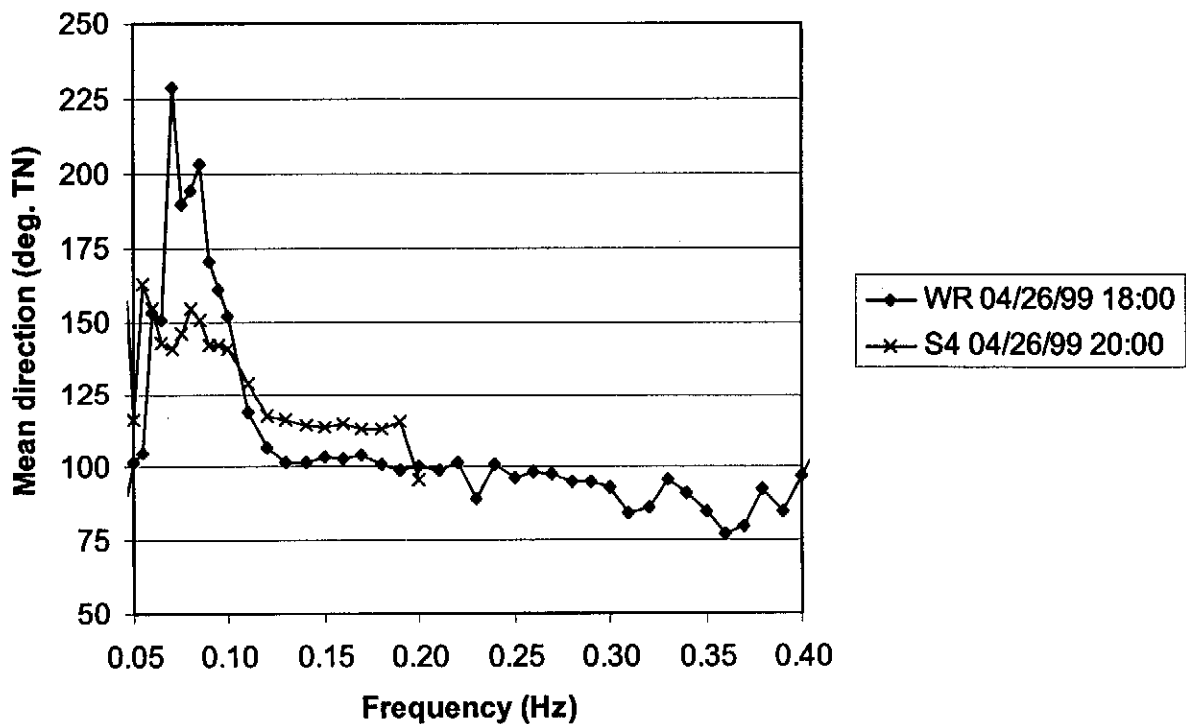
**FIGURE**  
 5.1



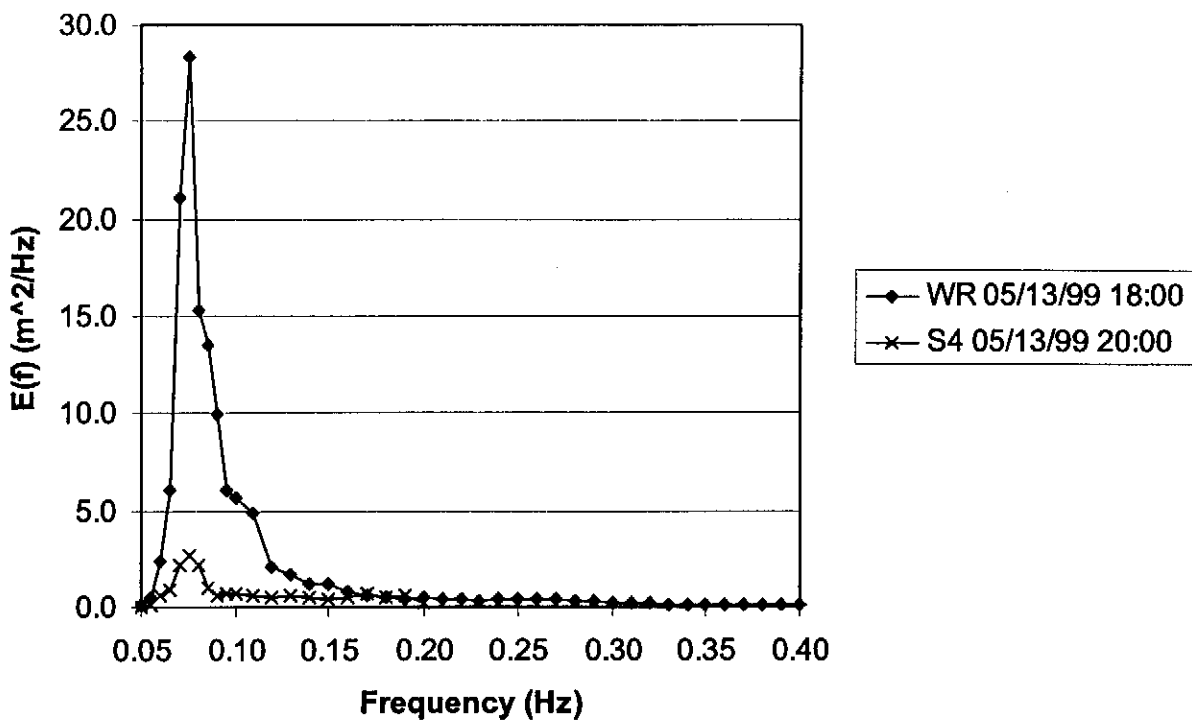
(a) Energy density spectra for ESE offshore condition



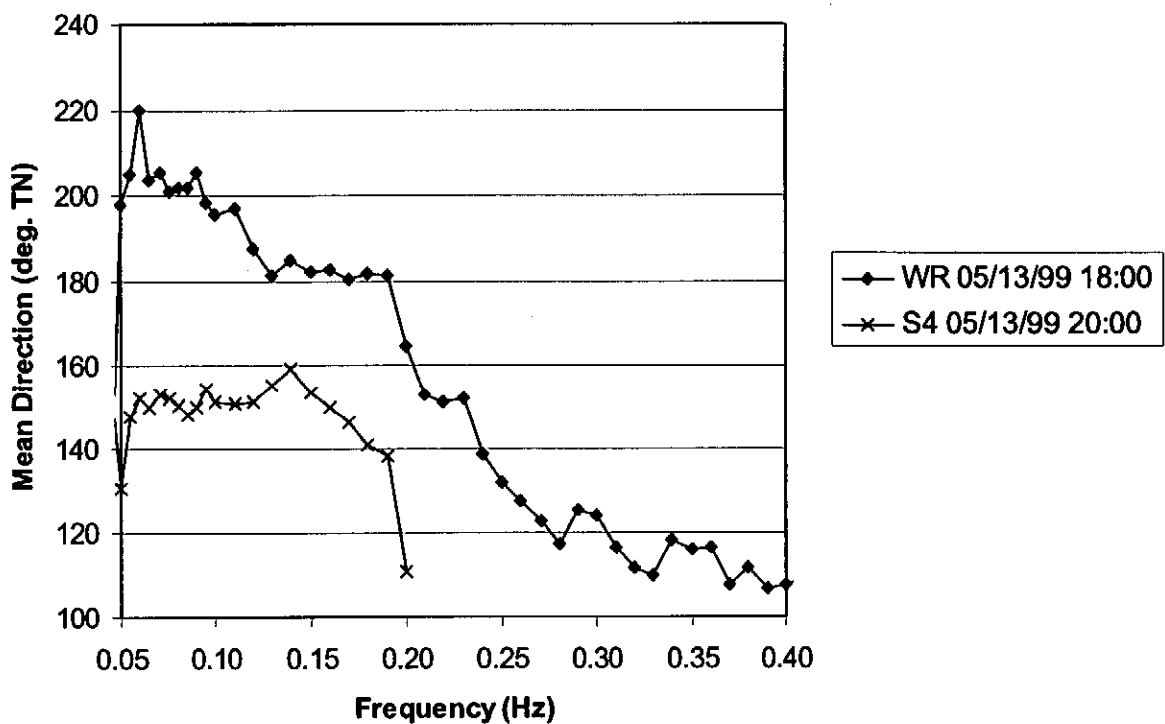
(b) Mean direction per frequency component for ESE offshore direction



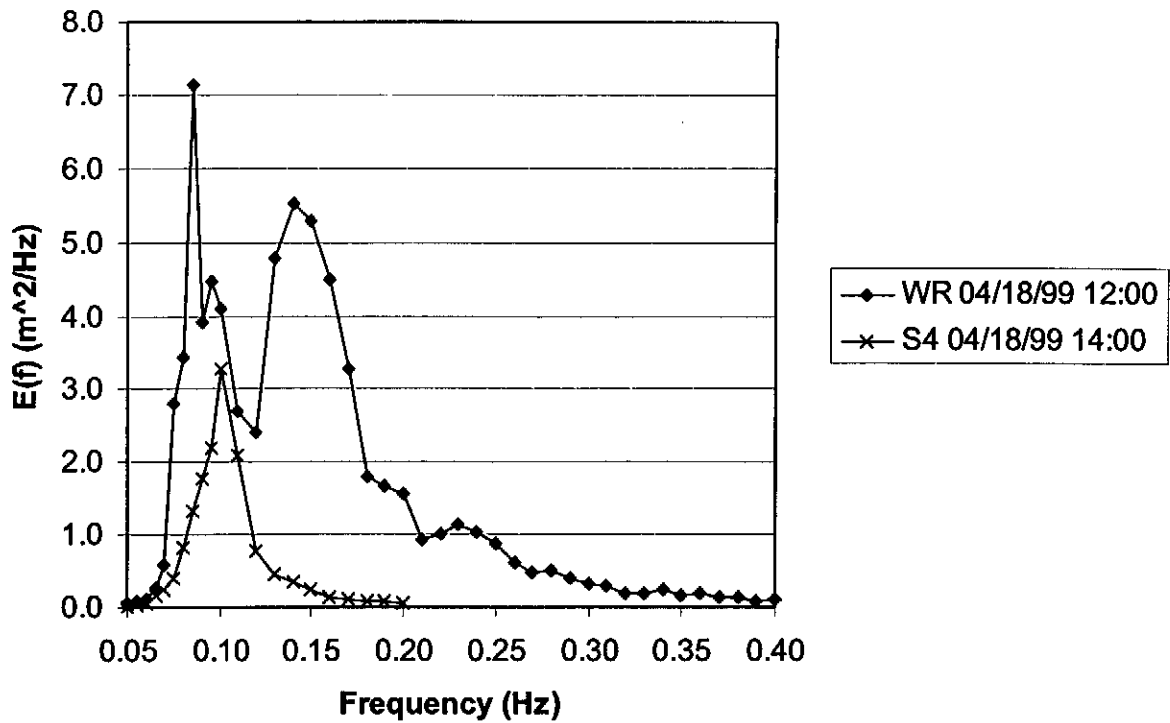
(a) Energy density spectra for SSW offshore condition



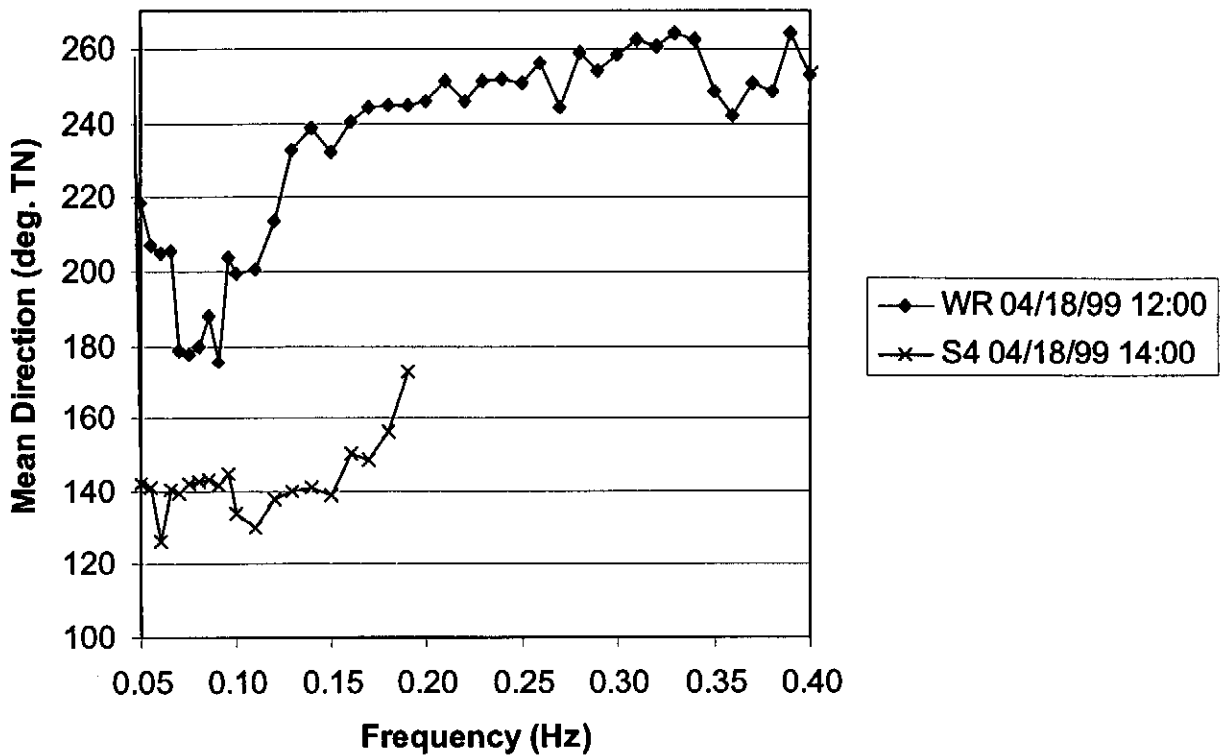
(b) Mean direction per frequency component for SSW offshore direction



(a) Energy density spectra for SW offshore condition



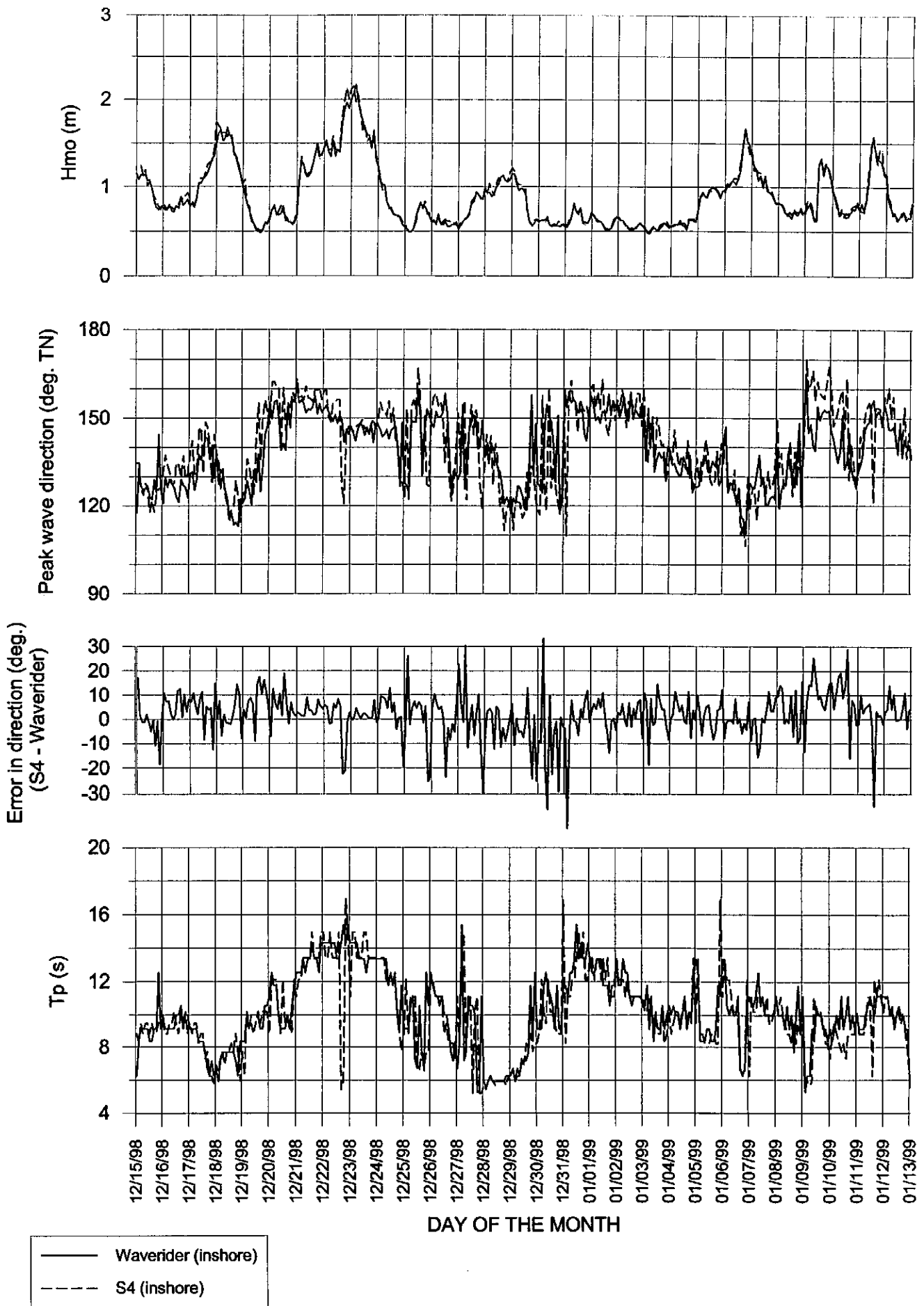
(b) Mean direction per frequency component for SW offshore direction



ALGOA BAY FIELD CASE: MODEL SETUP

Directional wave spectra for typical SW offshore condition

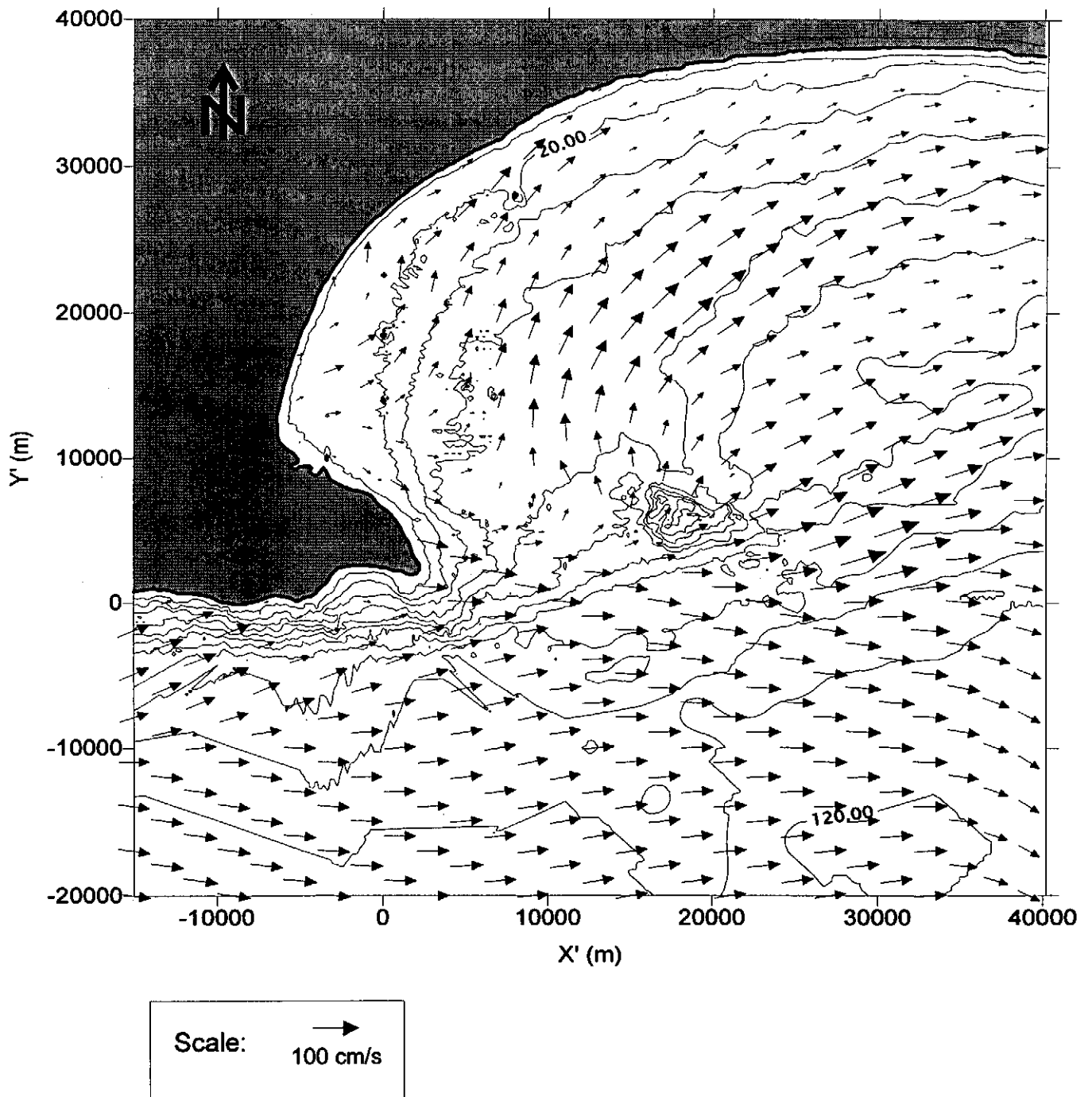
FIGURE 5.4



ALGOA BAY FIELD CASE: MODEL SETUP

Test comparison between recordings of Waverider and S4,  
both deployed at inshore station at depth of -17 m CD

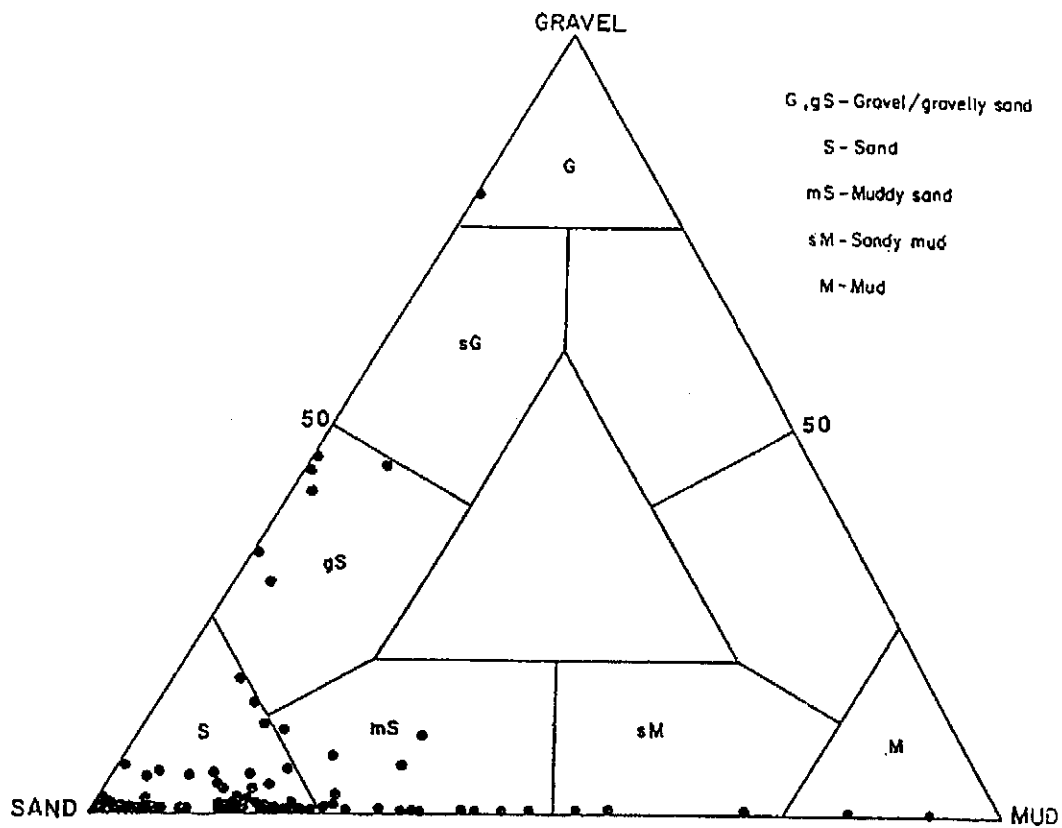
FIGURE  
5.5



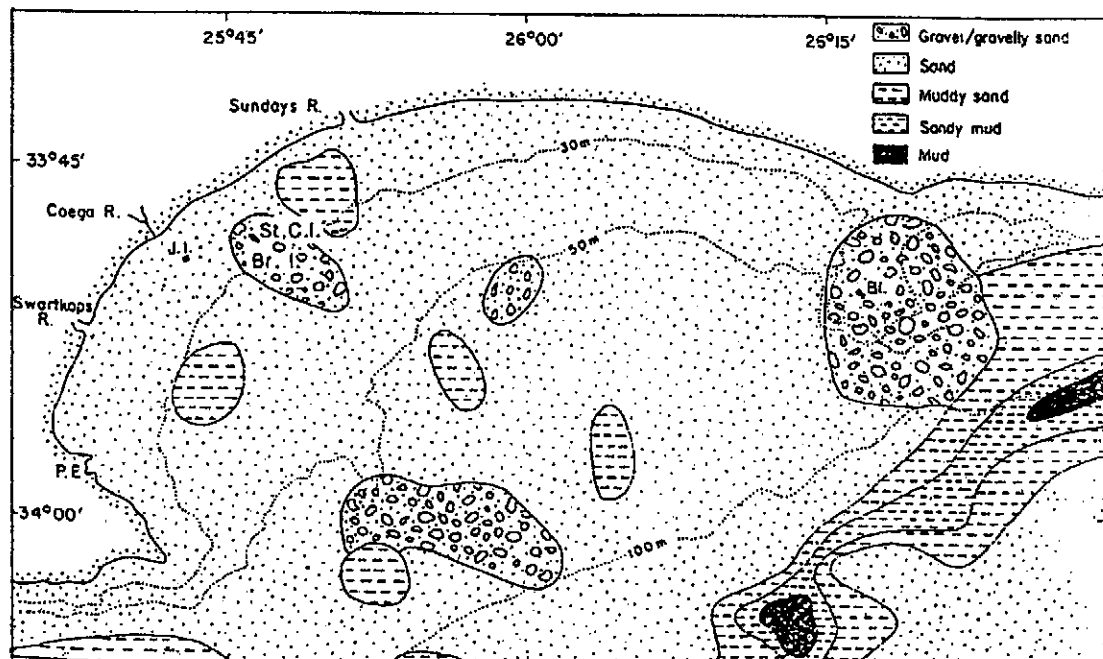
ALGOA BAY FIELD CASE: MODEL SETUP

Interpolated current pattern in Algoa Bay during  
November 1986 (after Goshen and Schumann, 1988)

FIGURE  
5.6



(a) Ternary diagram of sediment texture



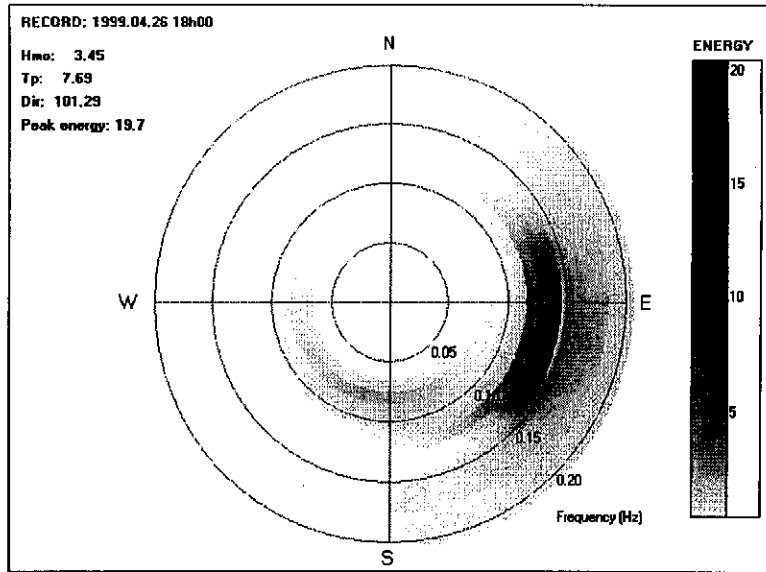
(b) Textural facies map of Algoa Bay

ALGOA BAY FIELD CASE: MODEL SETUP

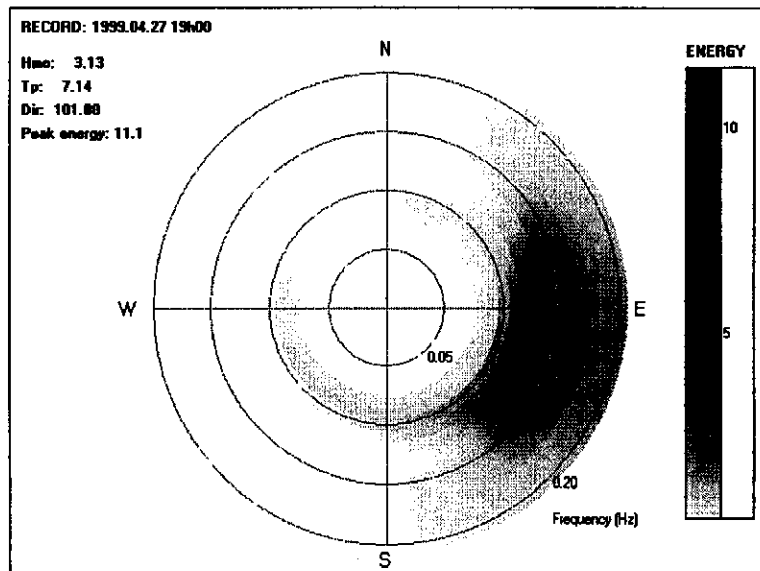
Seabed composition of Algoa Bay (Portnet, 2001)

FIGURE  
5.7

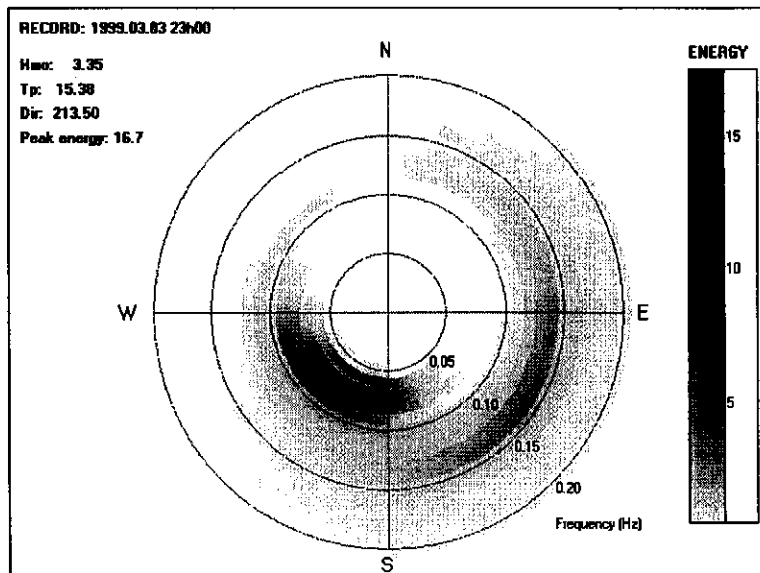
(1) Cat. A: 04/26 at 18:00 UT



(2) Cat. A: 04/27 at 19:00 UT



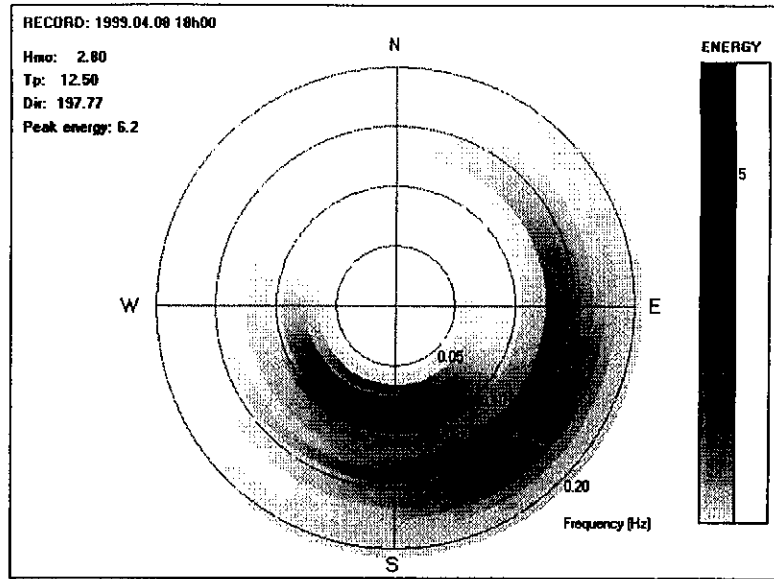
(3) Cat. B: 03/03 at 23:00 UT



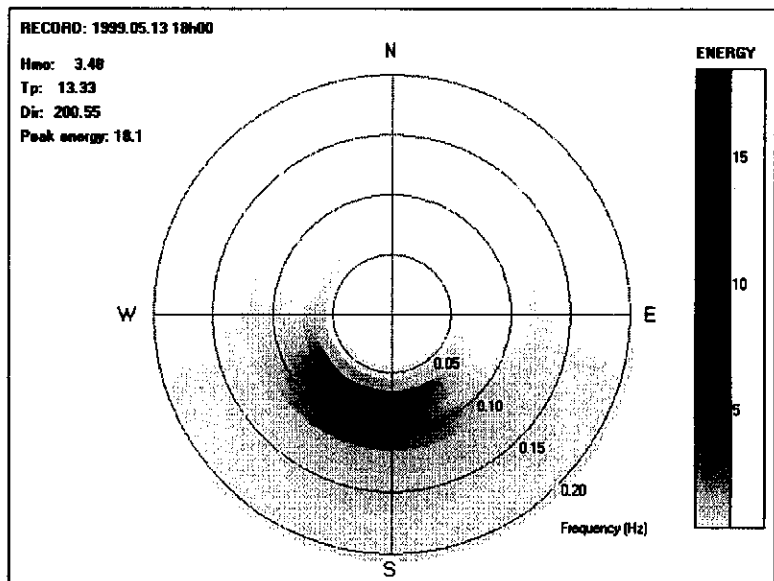
ALGOA BAY FIELD CASE: MODEL SETUP  
Polar plots of wave spectra selected  
for Algoa Case field case study

FIGURE  
5.8(a)

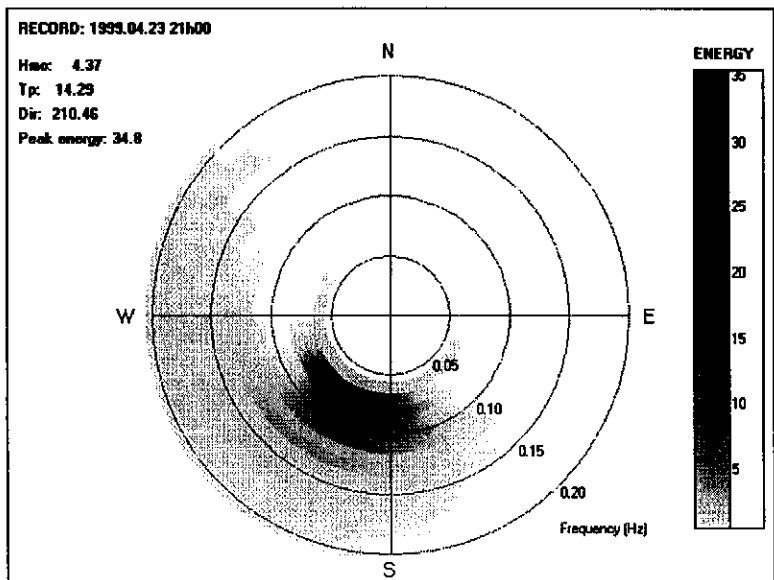
(4) Cat. B: 04/08 at 18:00 UT



(5) Cat. C: 05/13 at 18:00 UT



(6) Cat. D: 04/23 at 21:00 UT



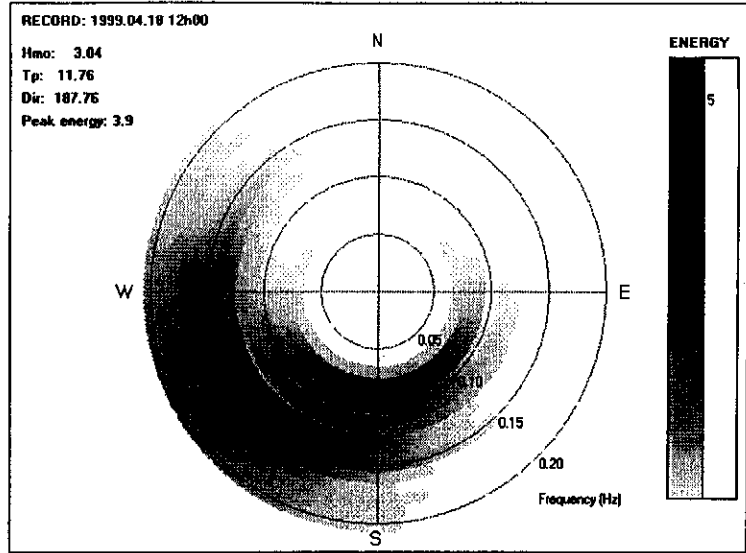
ALGOA BAY FIELD CASE: MODEL SETUP

Polar plots of wave spectra selected  
for Algoa Case field case study

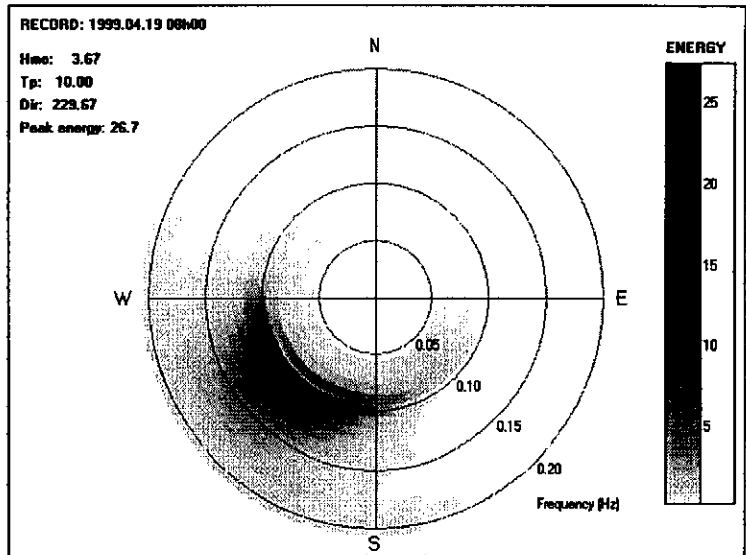
FIGURE  
5.8(b)



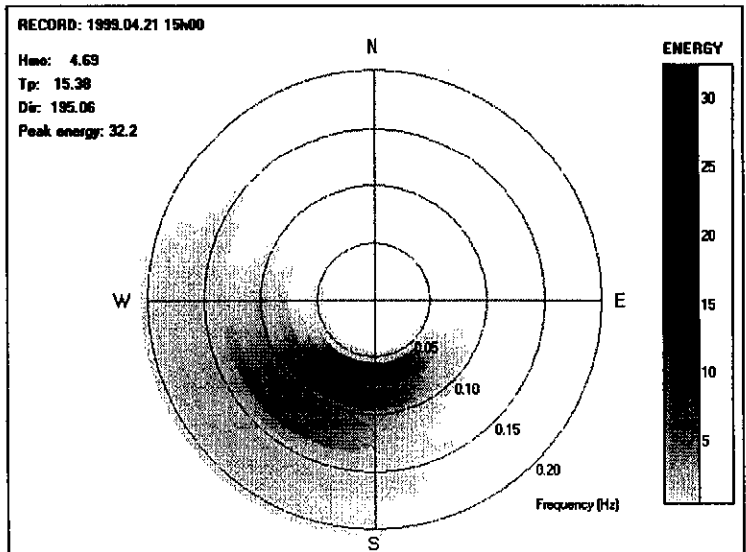
(7) Cat. D: 04/18 at 12:00 UT



(8) Cat. D: 04/19 at 08:00 UT



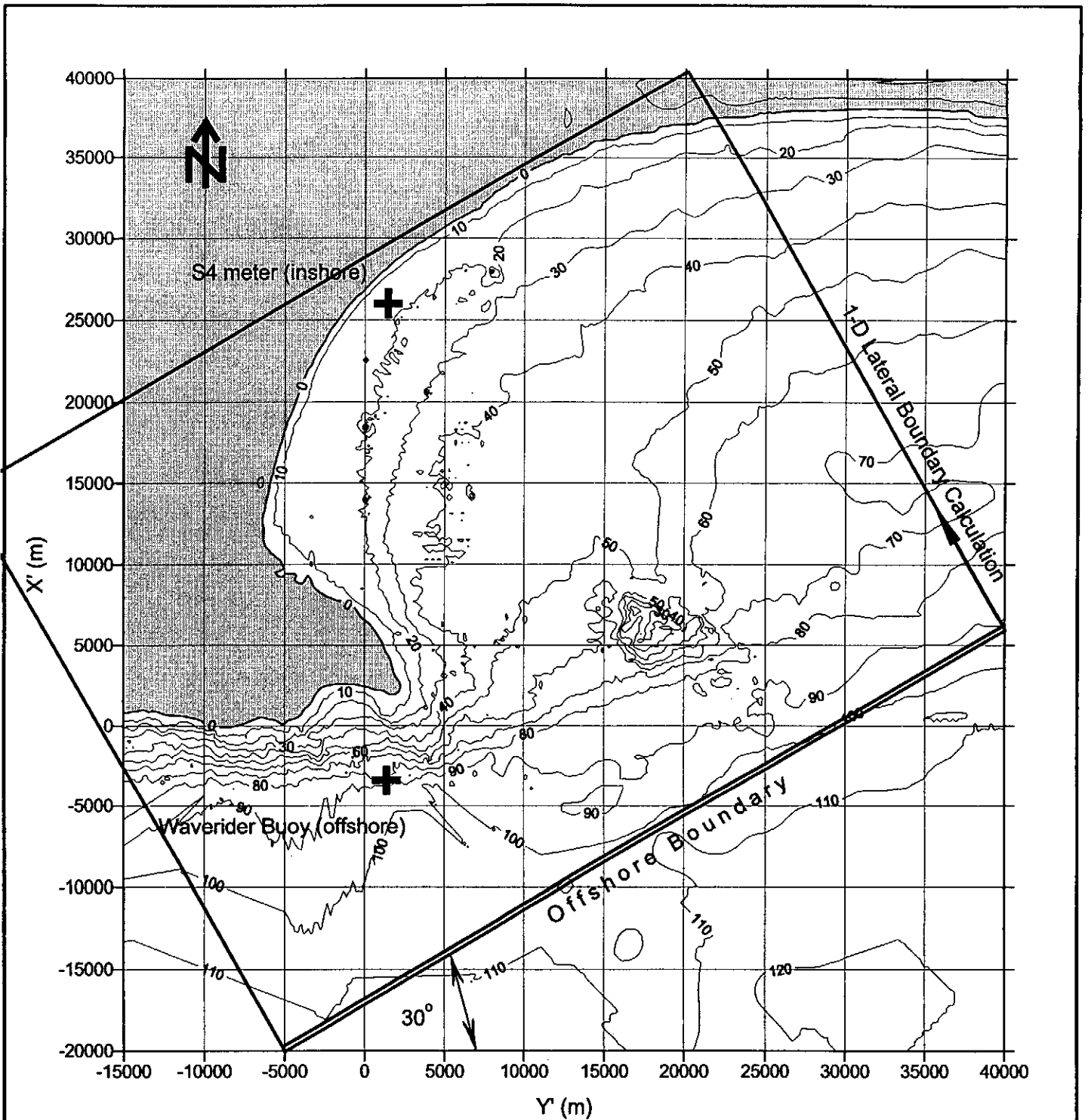
(9) Cat. D: 04/21 at 15:00 UT



ALGOA BAY FIELD CASE: MODEL SETUP

Polar plots of wave spectra selected  
for Algoa Case field case study

FIGURE  
5.8(c)



Model convention:

Model co-ordinate system relative to:  
 Southing: 3 769 097 X  
 Westing: -63 015 Y

Computational grid dimensions:

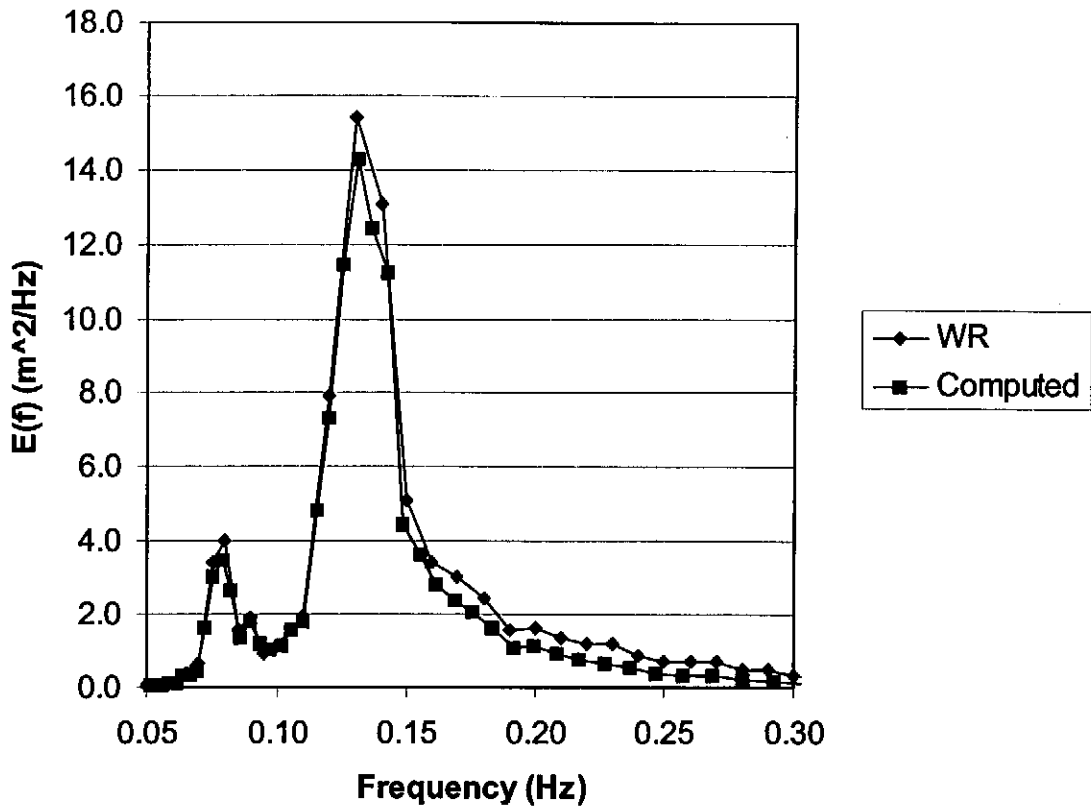
55 000 x 40 000 m

ALGA BAY FIELD CASE: MODEL SETUP

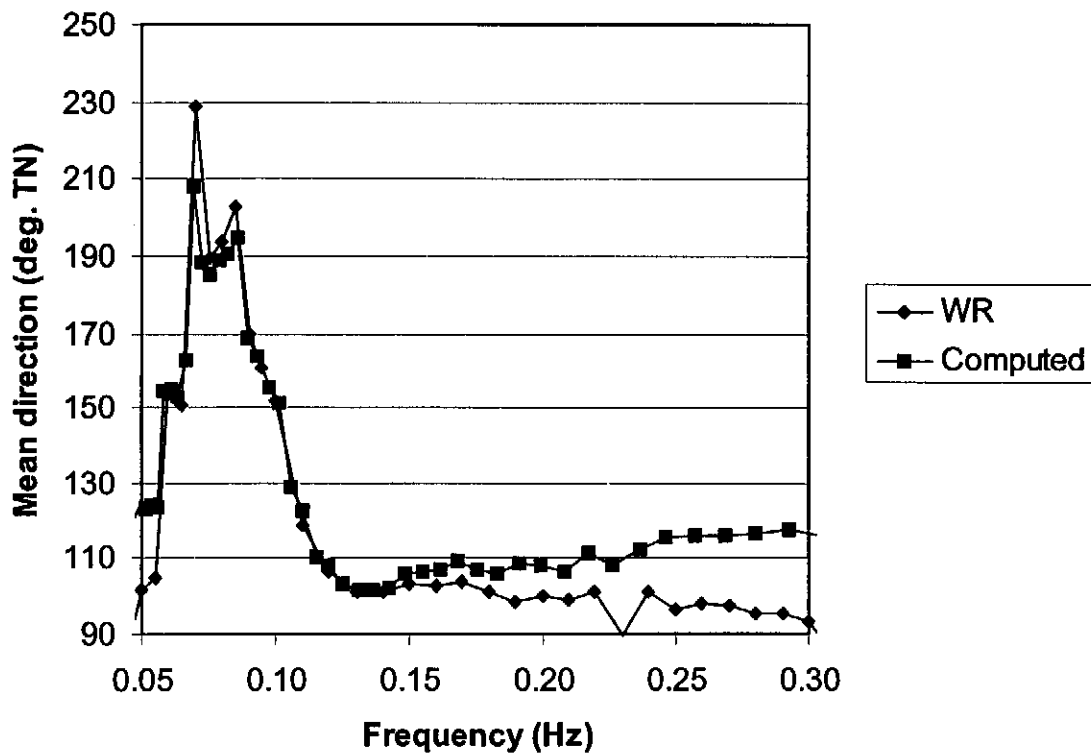
Location of computational grid for  
 ESE offshore wave direction

FIGURE  
 5.9

(a) Energy density spectrum at boundary



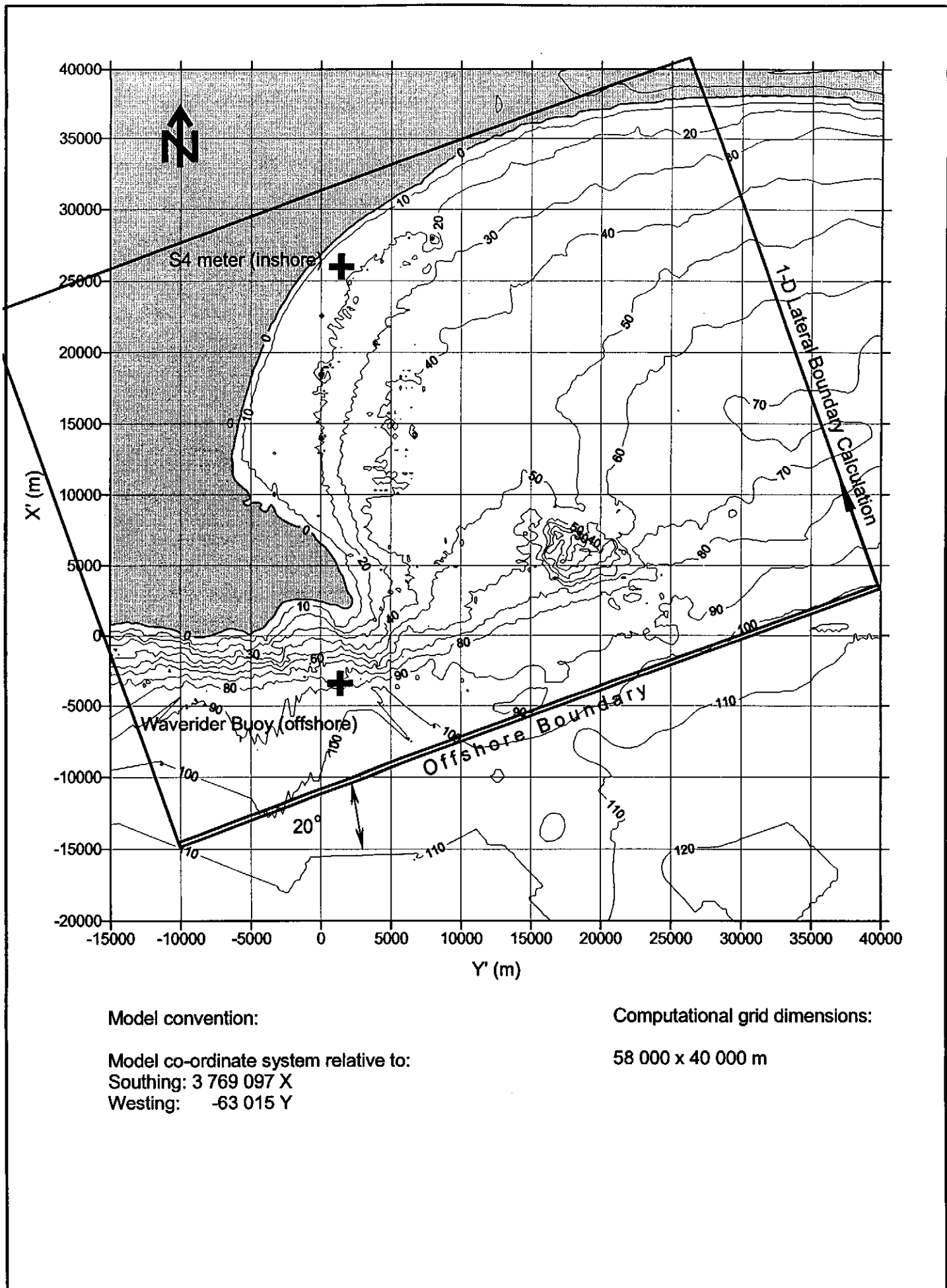
(b) Mean direction per frequency component



ALGOA BAY FIELD CASE: MODEL SETUP

Simulated and measured boundary values for Case 1 (ESE)

FIGURE  
5.10

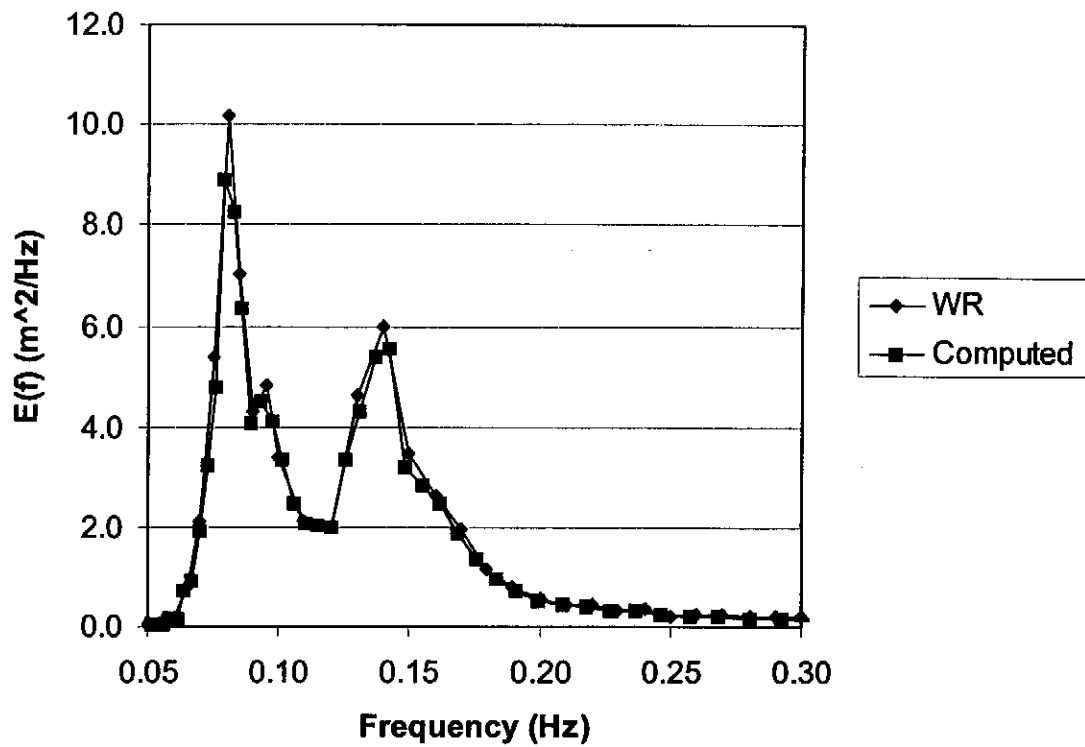


ALGA BAY FIELD CASE: MODEL SETUP

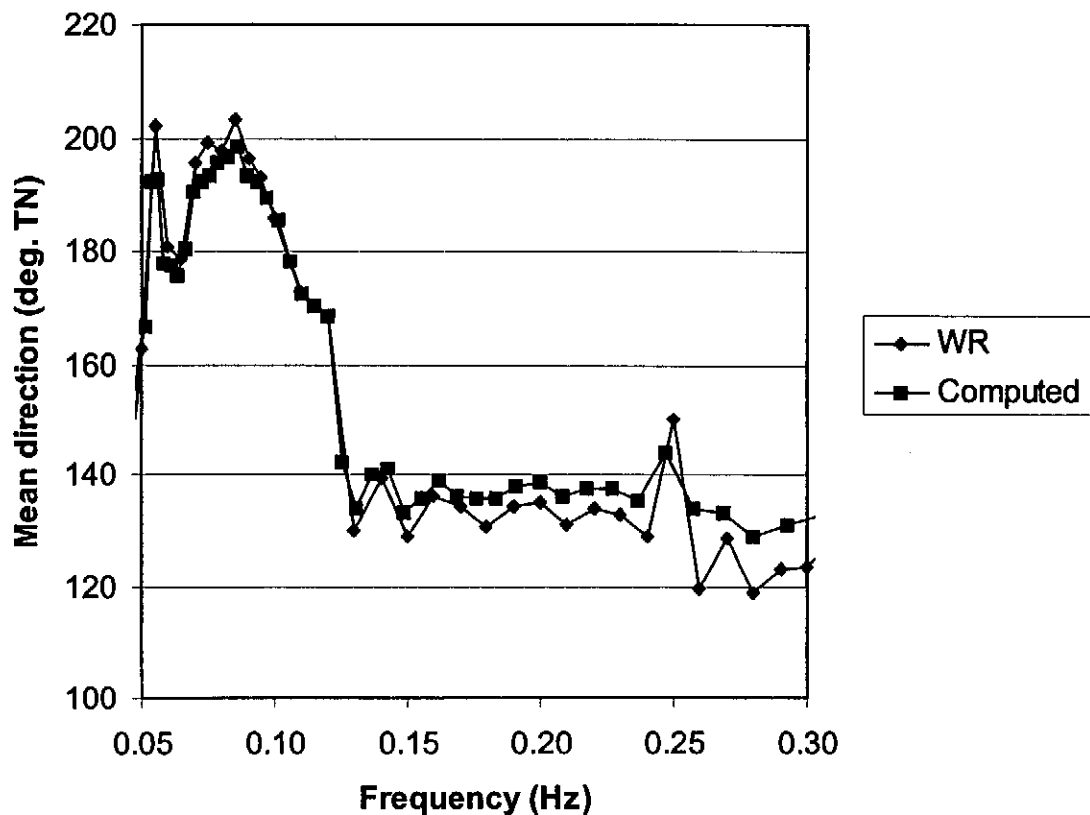
Location of computational grid for  
SSW/SE offshore wave direction

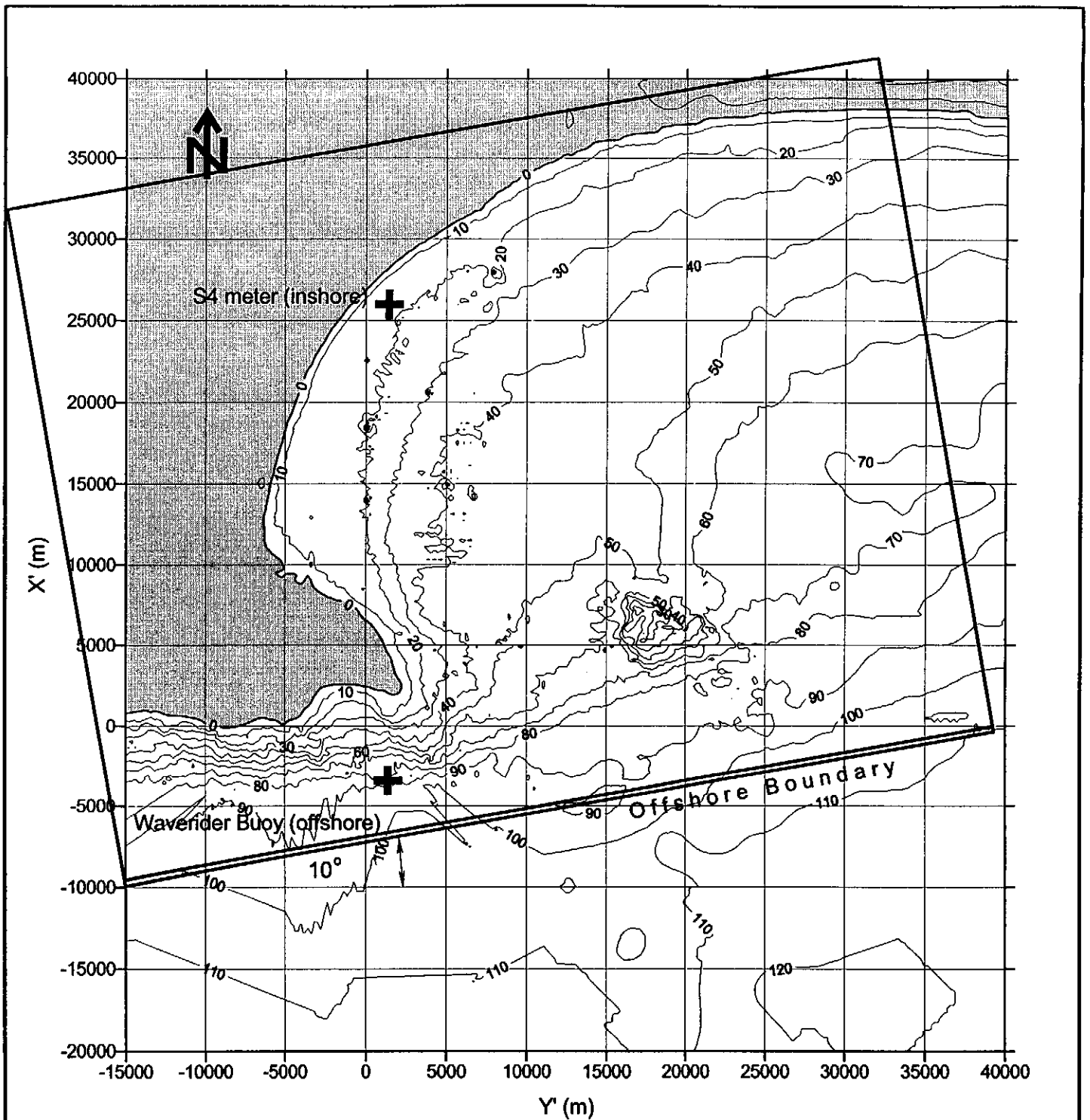
FIGURE  
5.11

(a) Energy density spectrum at boundary



(b) Mean direction per frequency component





Model convention:

Model co-ordinate system relative to:  
 Southing: 3 769 097 X  
 Westing: -63 015 Y

Computational grid dimensions:

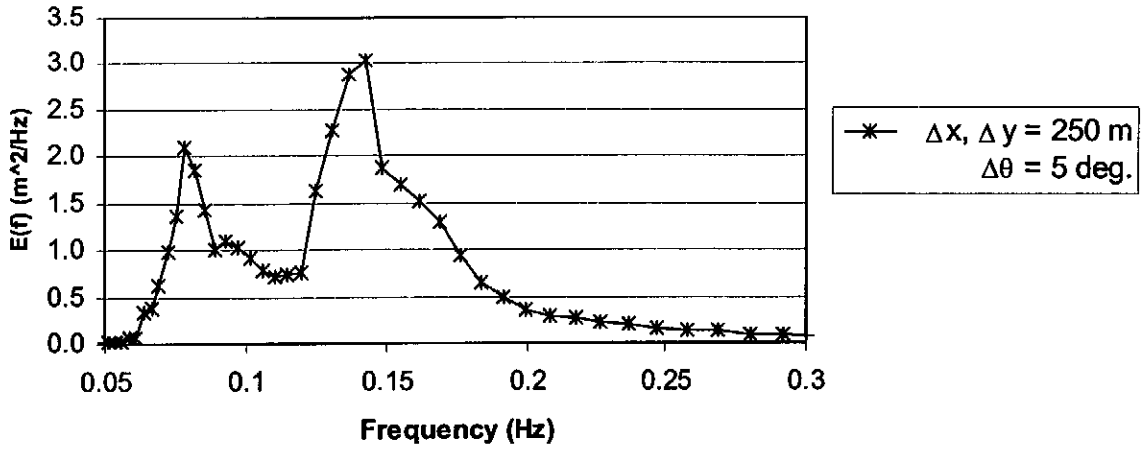
55 000 x 45 000 m

ALGOA BAY FIELD CASE: MODEL SETUP

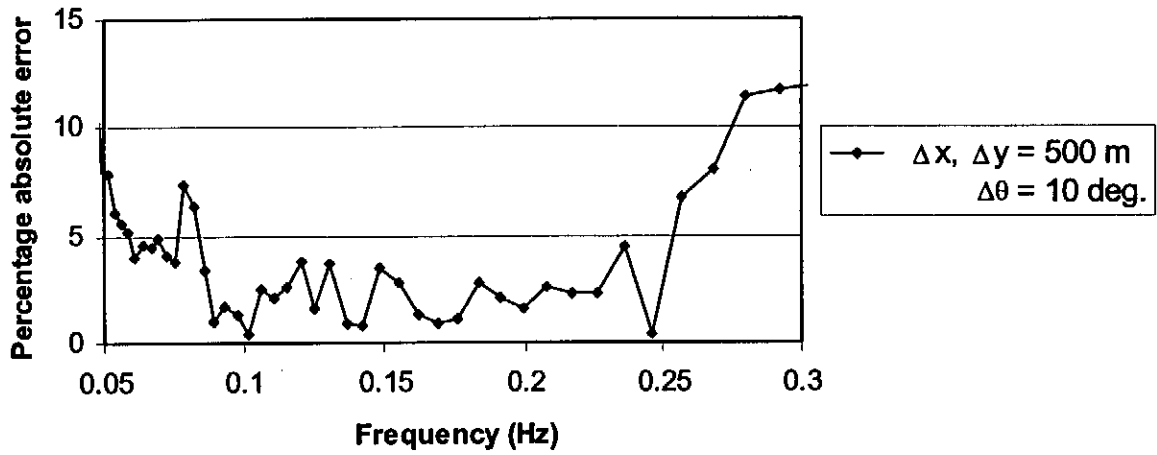
Location of computational grid for  
 SSW offshore wave direction

FIGURE  
 5.13

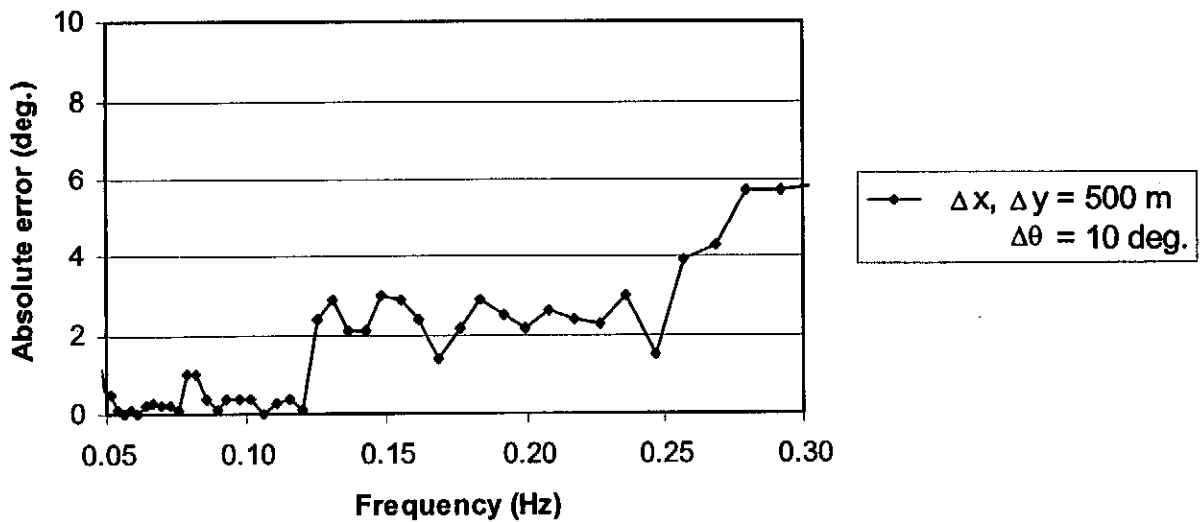
(a) Energy density spectrum at S4, calculated by fine SWAN simulation



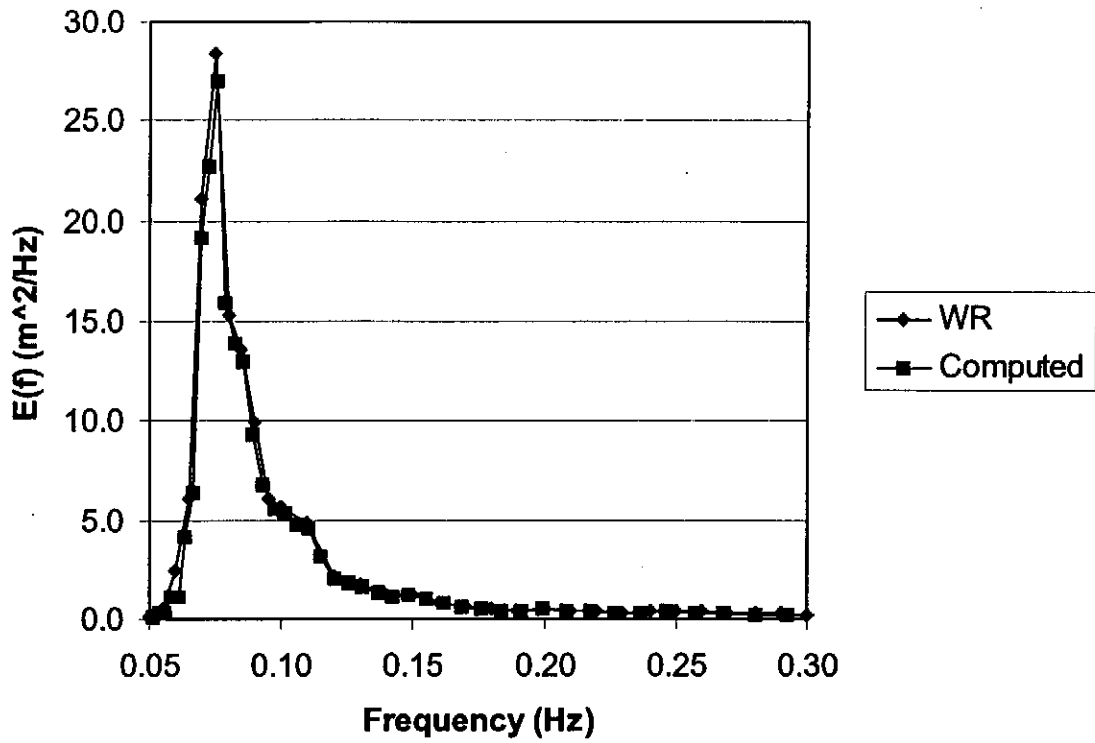
(b) Percentage absolute error in  $E(f)$  due to total discretization



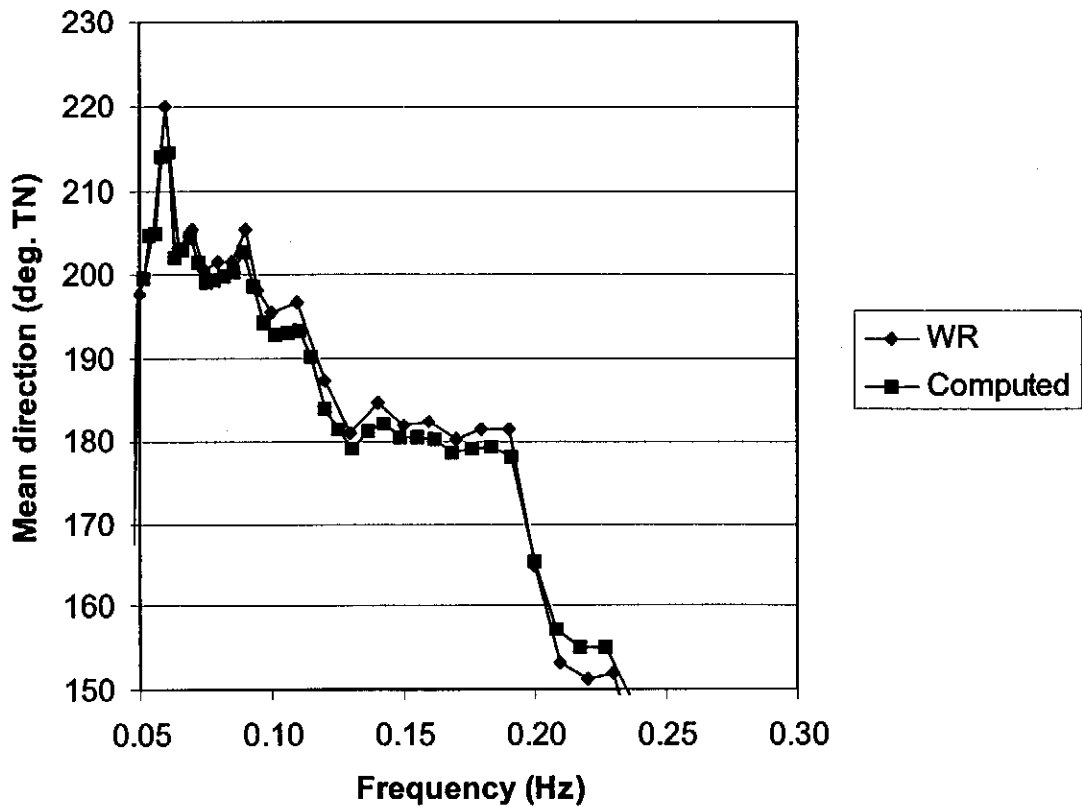
(c) Absolute error in mean direction due to total discretization



(a) Energy density spectrum at boundary

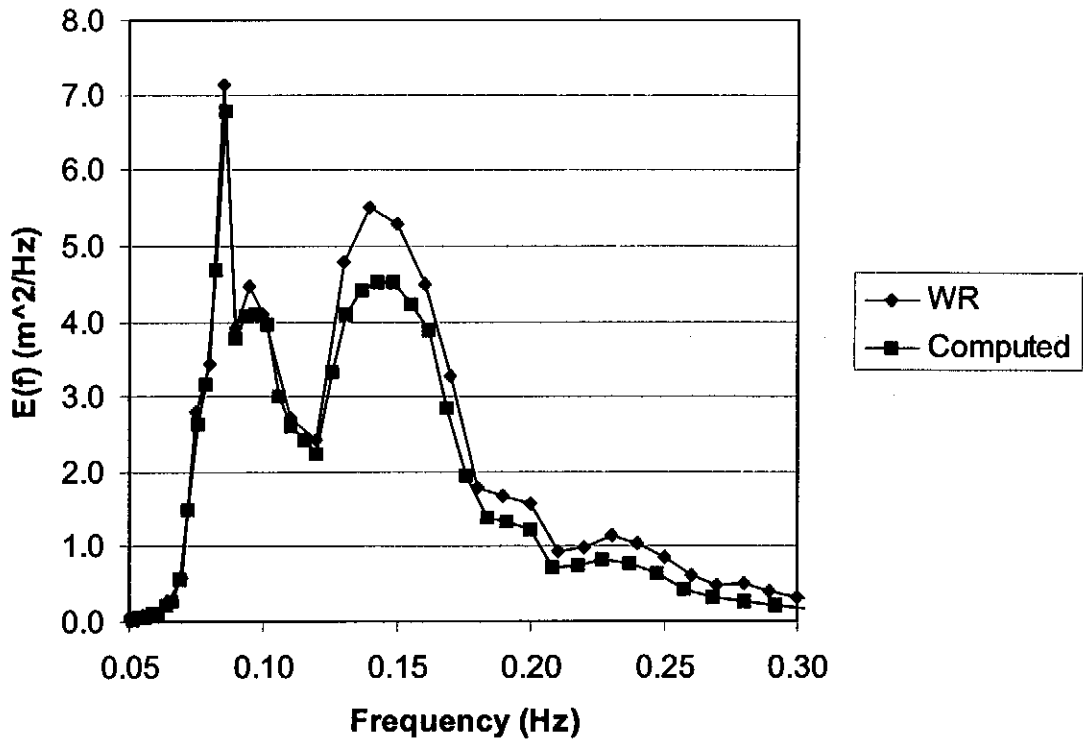


(b) Mean direction per frequency component

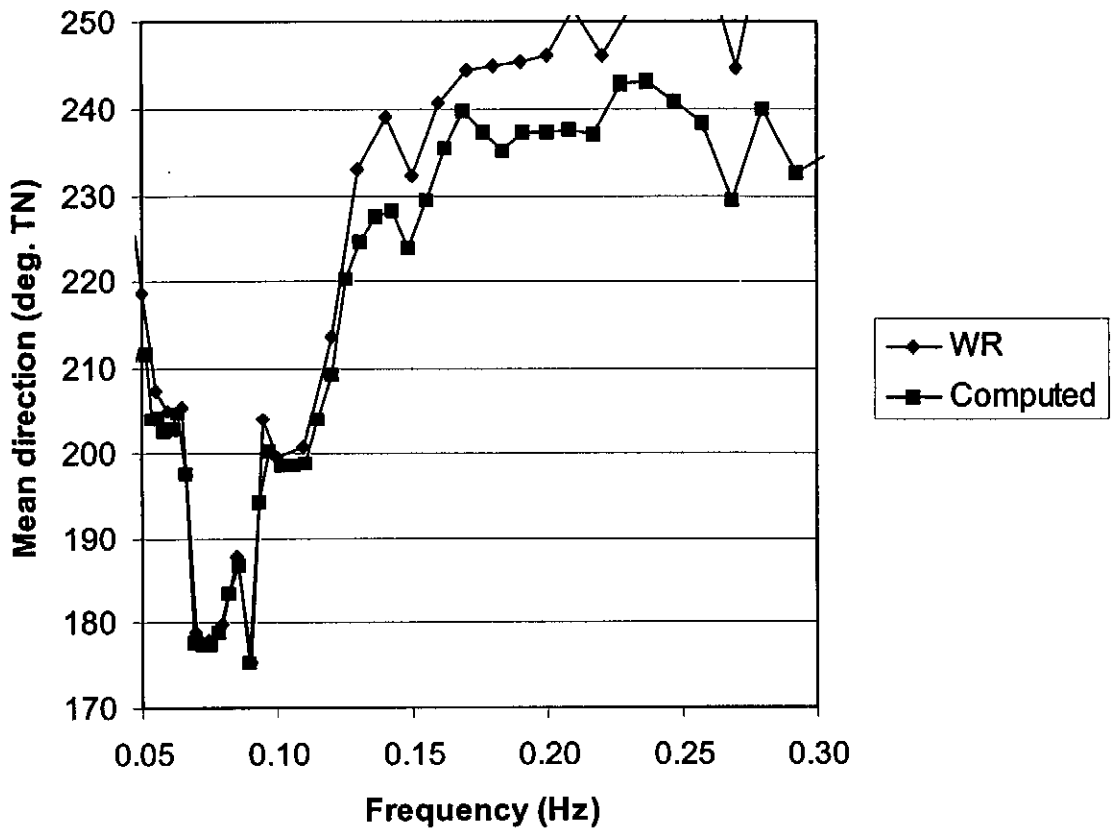




(a) Energy density spectrum at boundary



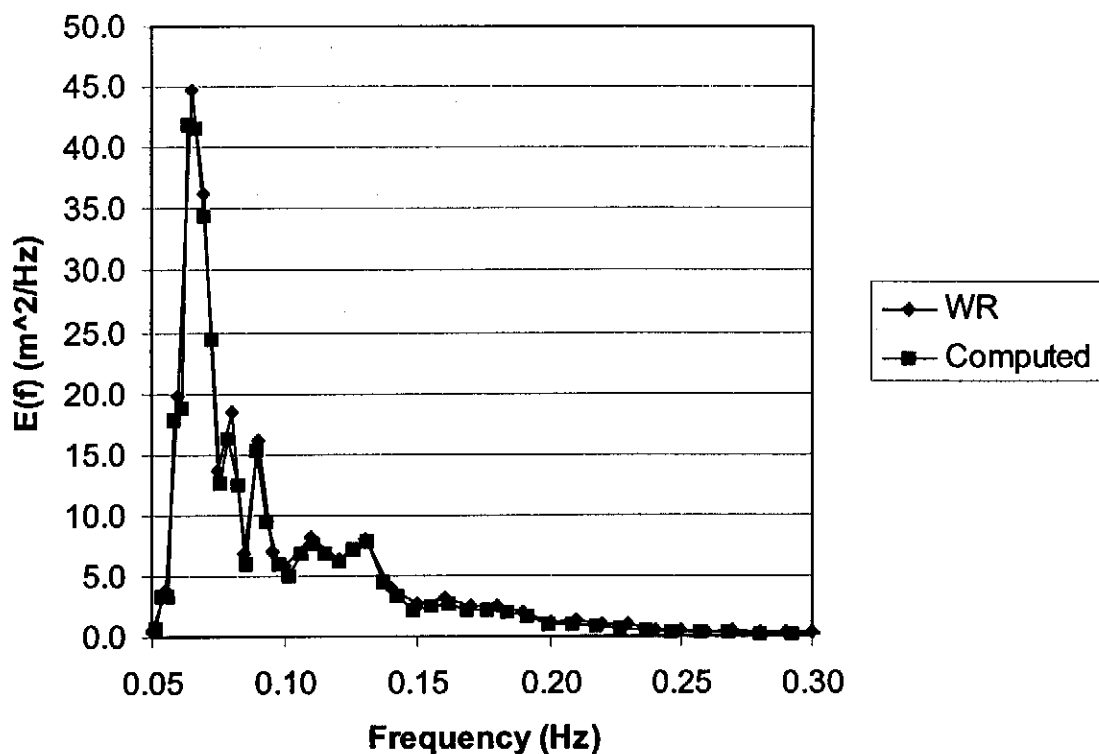
(b) Mean direction per frequency component



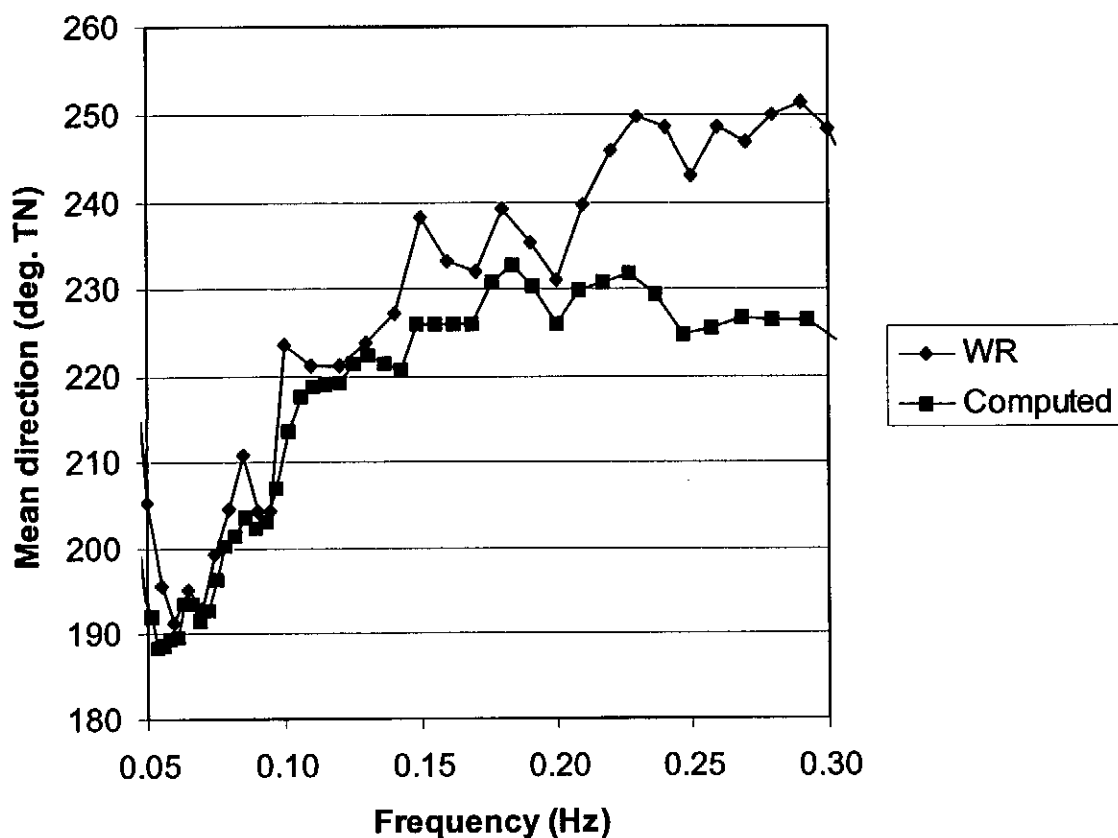
ALGOA BAY FIELD CASE: MODEL SETUP  
Simulated and measured boundary values  
for Case 7 (SSW/SW)

FIGURE  
5.15

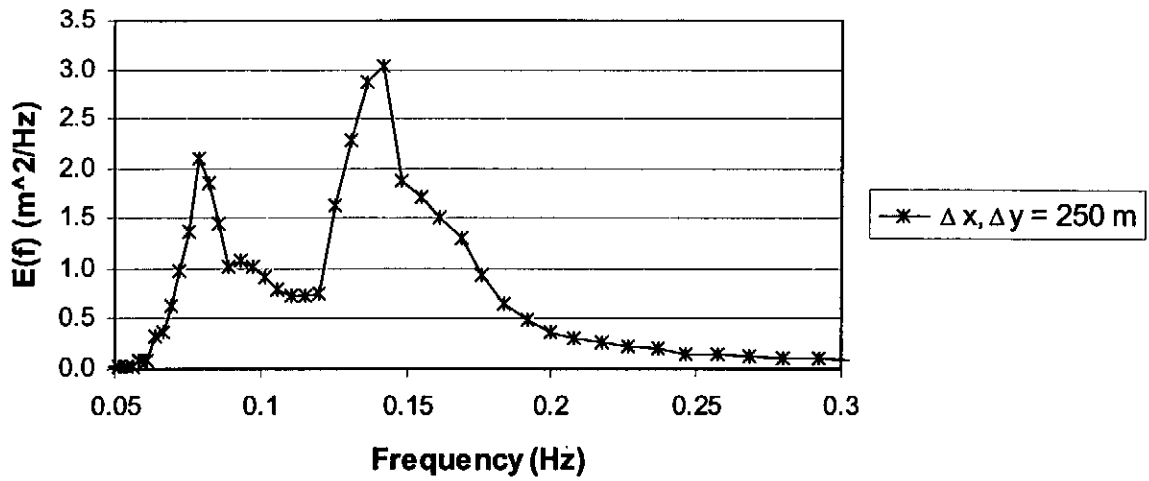
(a) Energy density spectrum at boundary



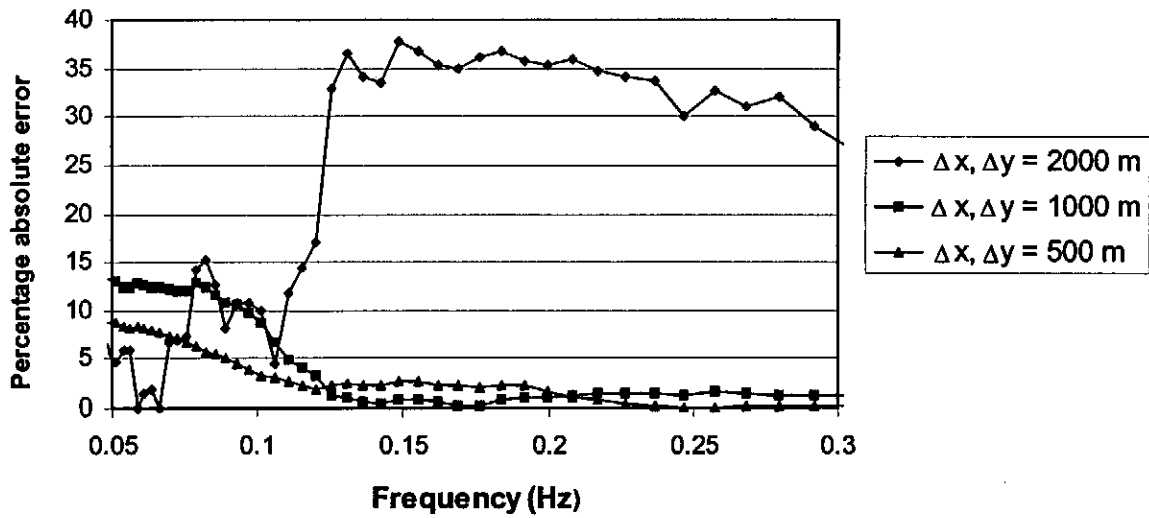
(b) Mean direction per frequency component



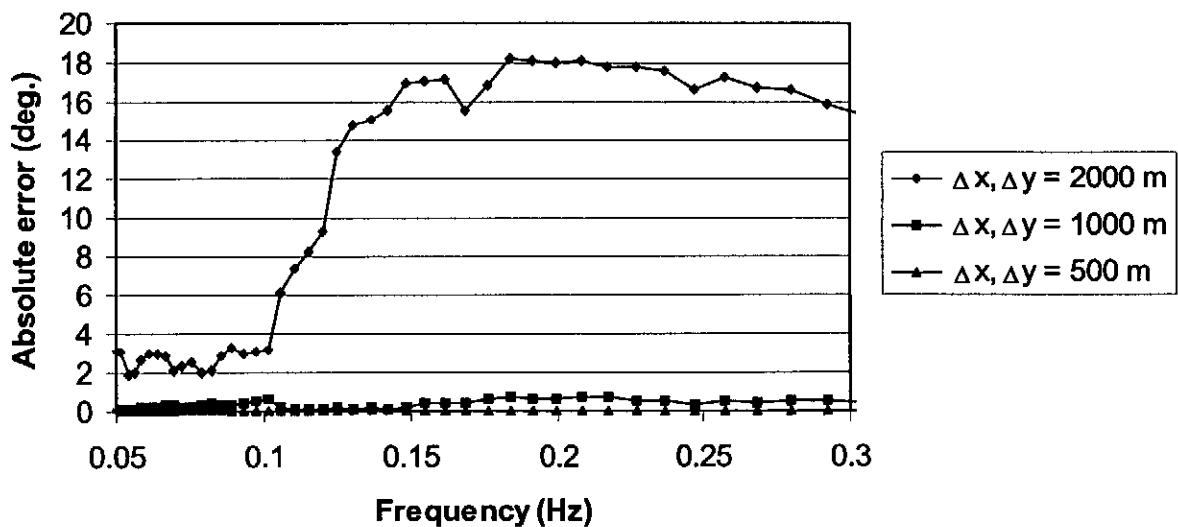
(a) Energy density spectrum at S4, calculated by fine SWAN simulation



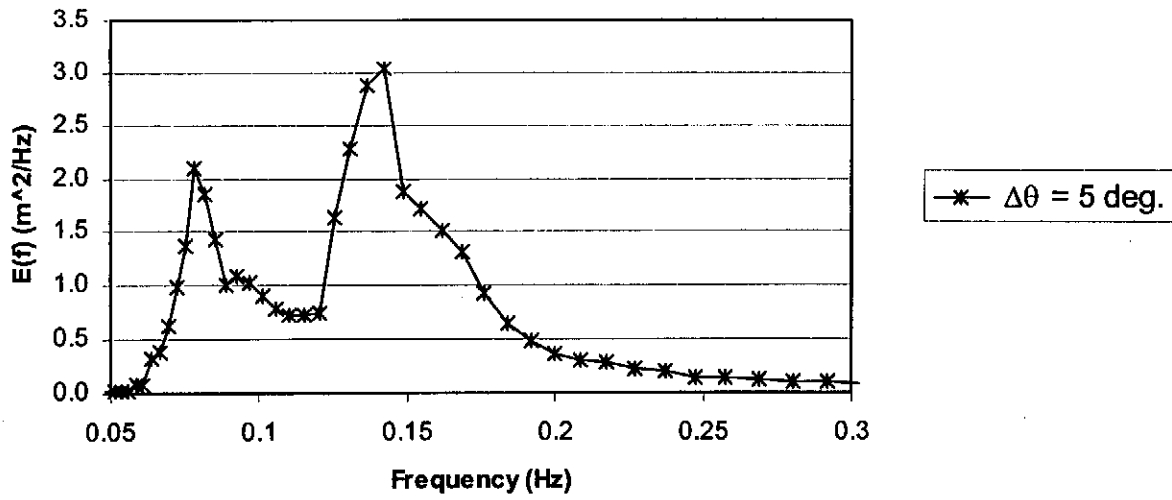
(b) Percentage absolute error in  $E(f)$  due to spatial discretization



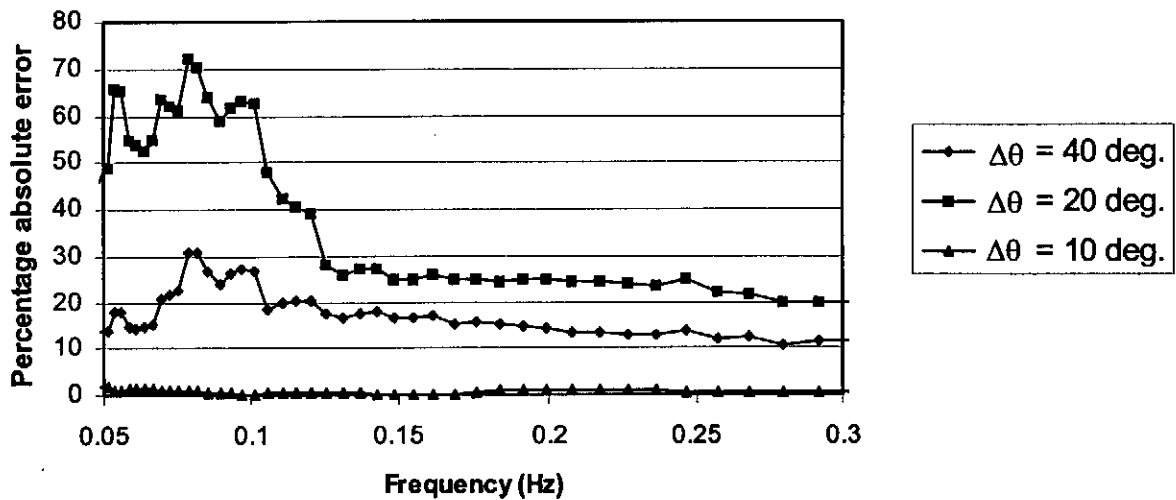
(c) Absolute error in mean direction due to spatial discretization



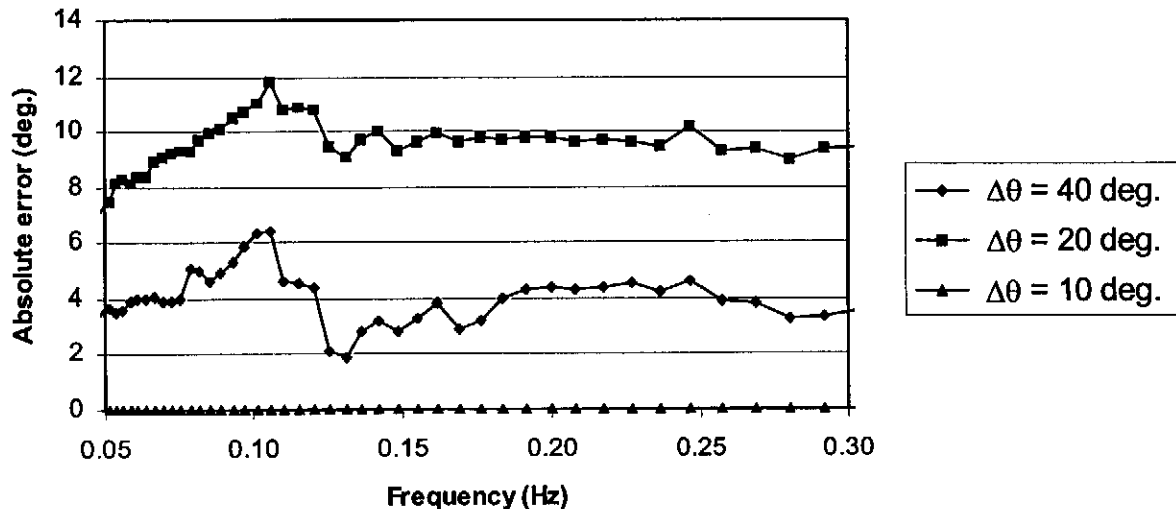
(a) Energy density spectrum at S4, calculated by fine SWAN simulation

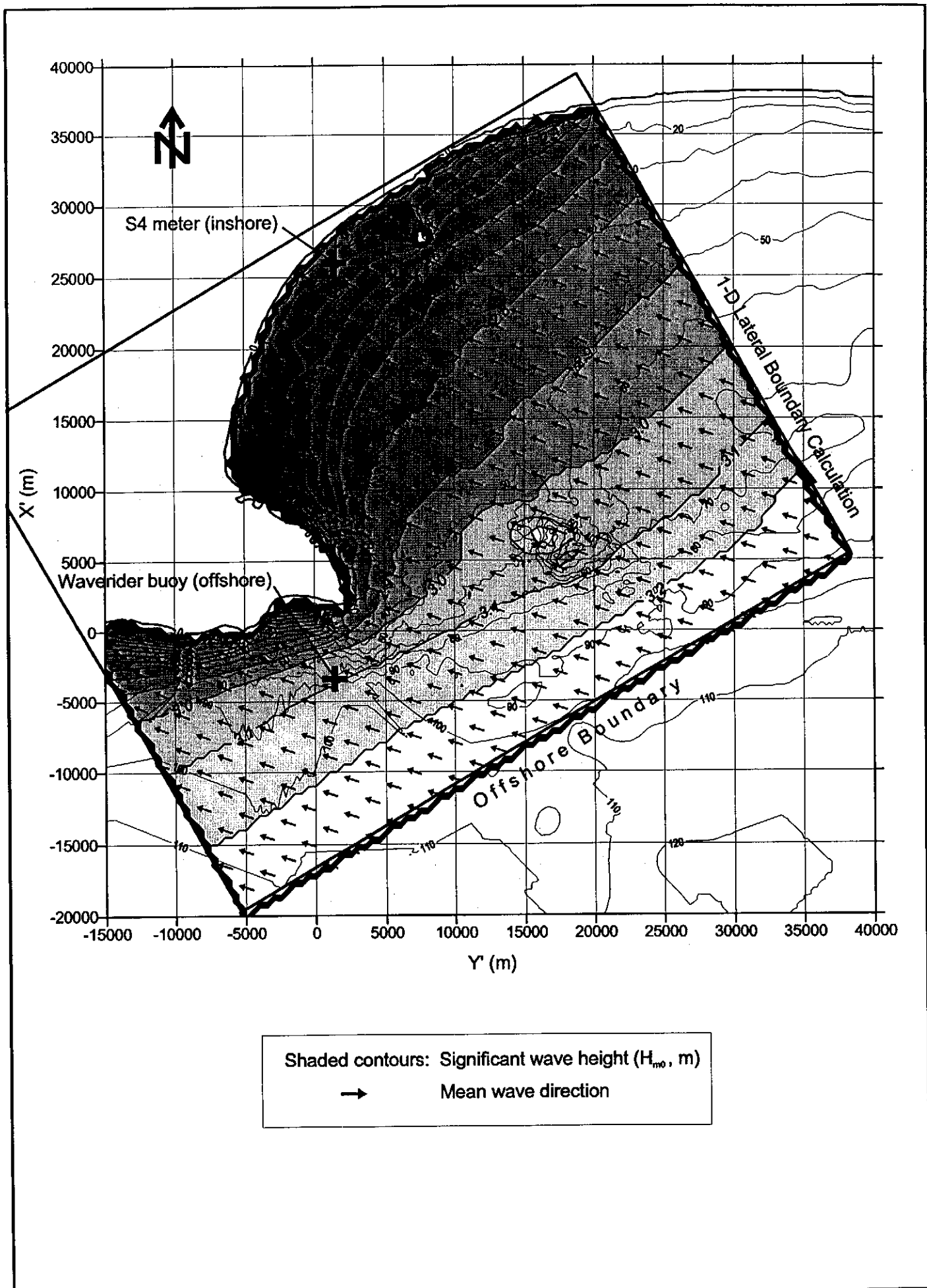


(b) Percentage absolute error in  $E(f)$  due to directional discretization



(c) Absolute error in mean direction due to directional discretization

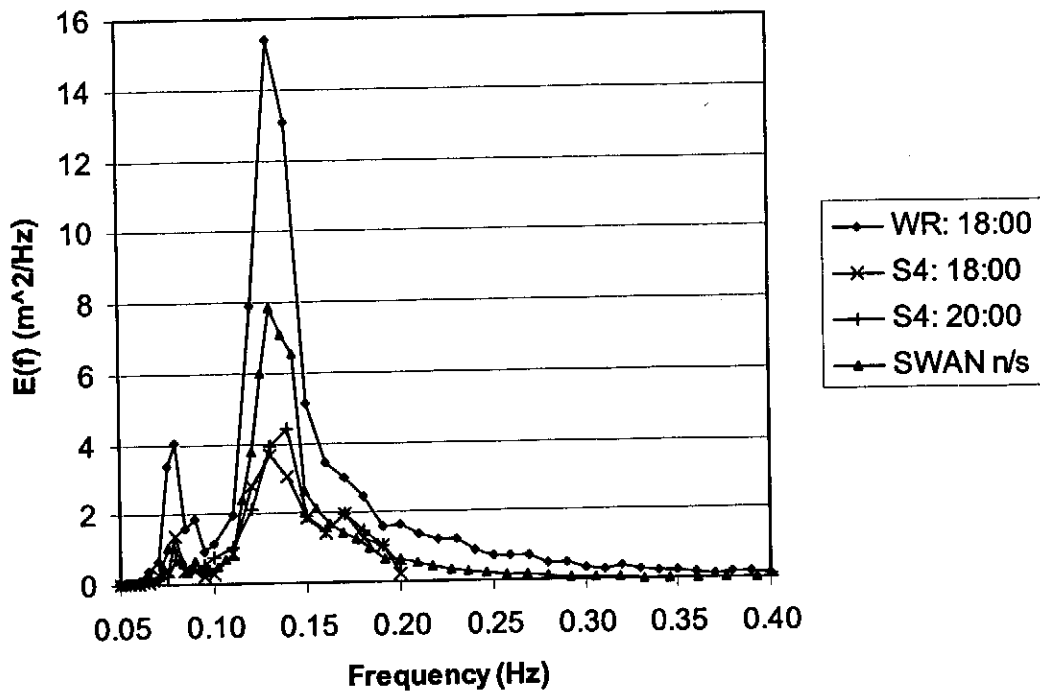




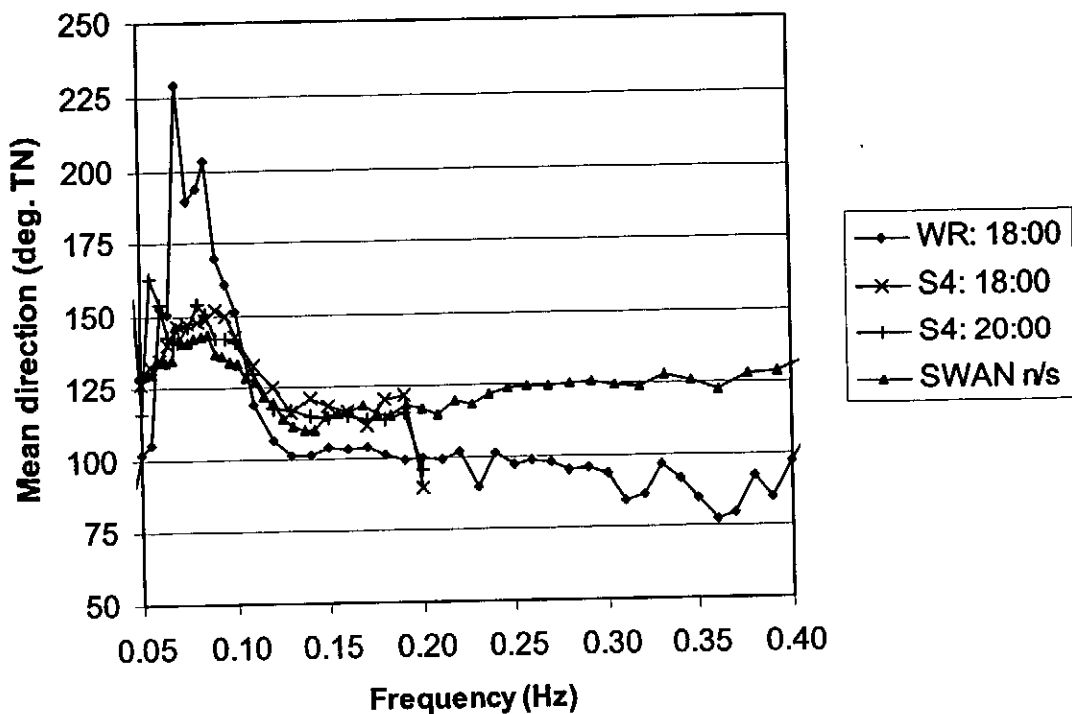
ALGA BAY FIELD CASE: FIRST ESTIMATE  
 Case 1 (ESE): Spatial solution of significant wave height and mean wave direction

FIGURE  
 6.1

(a) Energy density spectra: observed and calculated values



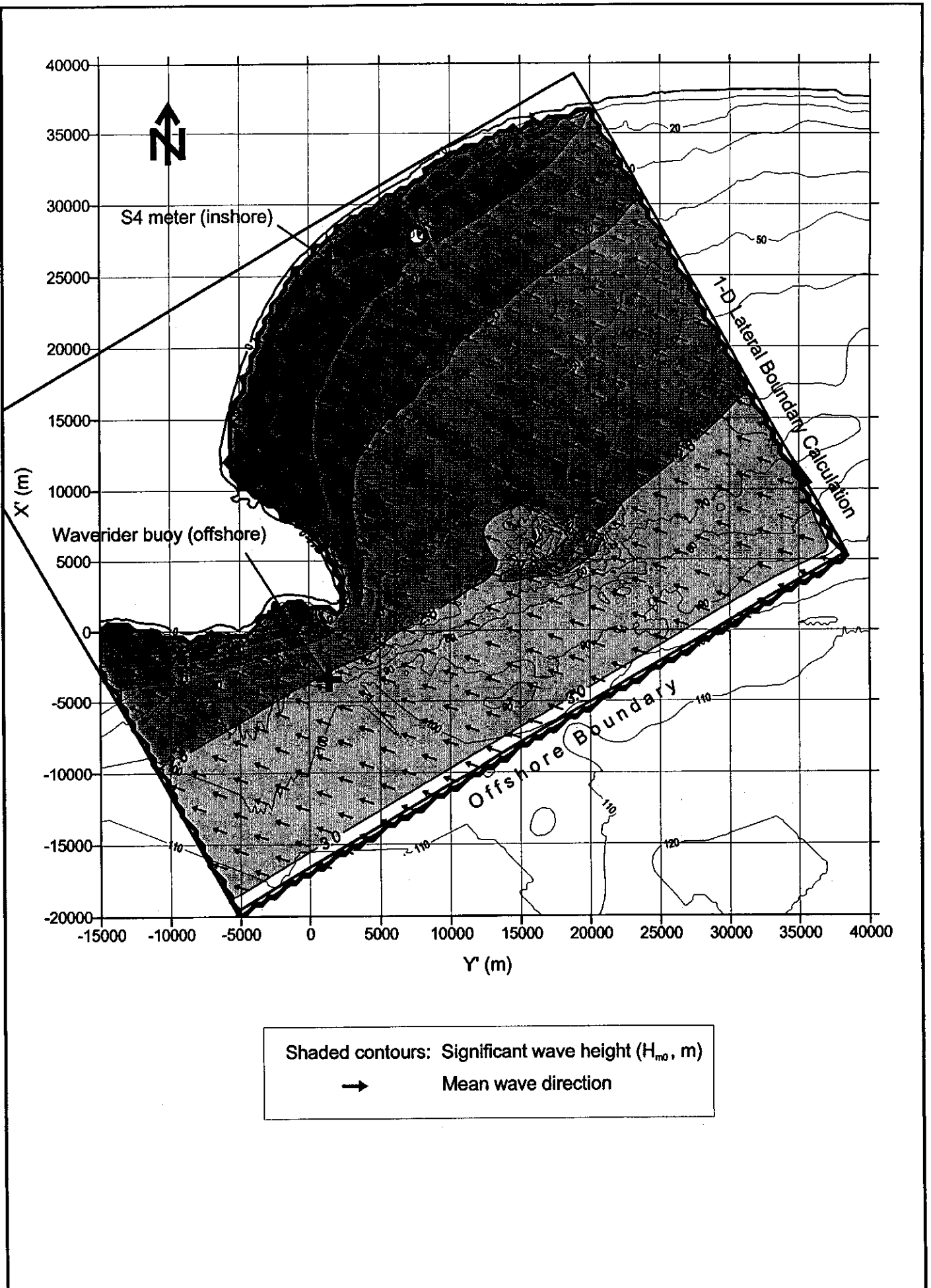
(b) Mean direction per frequency: observed and calculated values



ALGOA BAY FIELD CASE: FIRST ESTIMATE

Case 1 (ESE): Spectral solution of SWAN simulation at the nearshore (n/s) S4 station

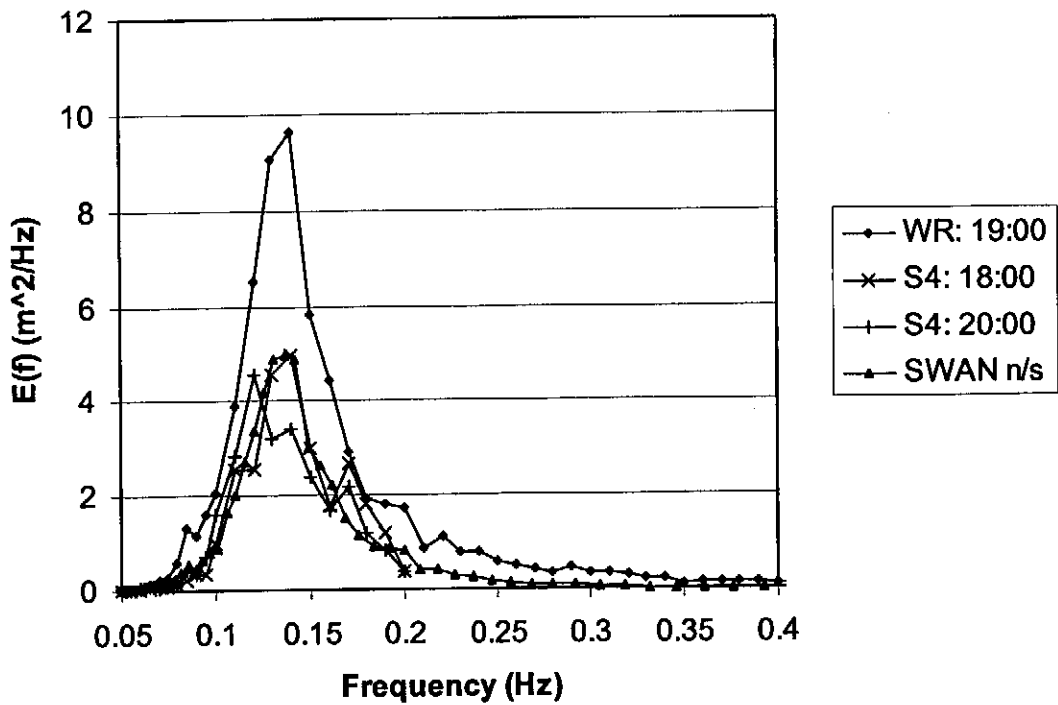
FIGURE 6.2



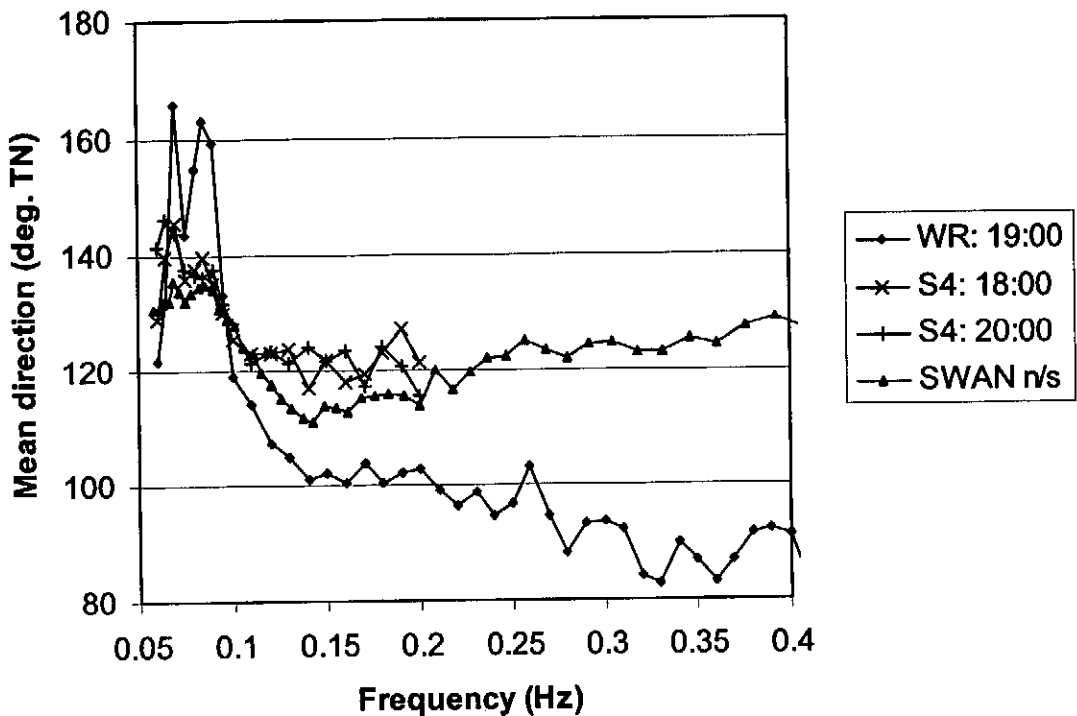
ALGOA BAY FIELD CASE: FIRST ESTIMATE  
 Case 2 (ESE): Spatial solution of significant wave height and mean wave direction

FIGURE  
 6.3

**(a) Energy density spectra: observed and calculated values**



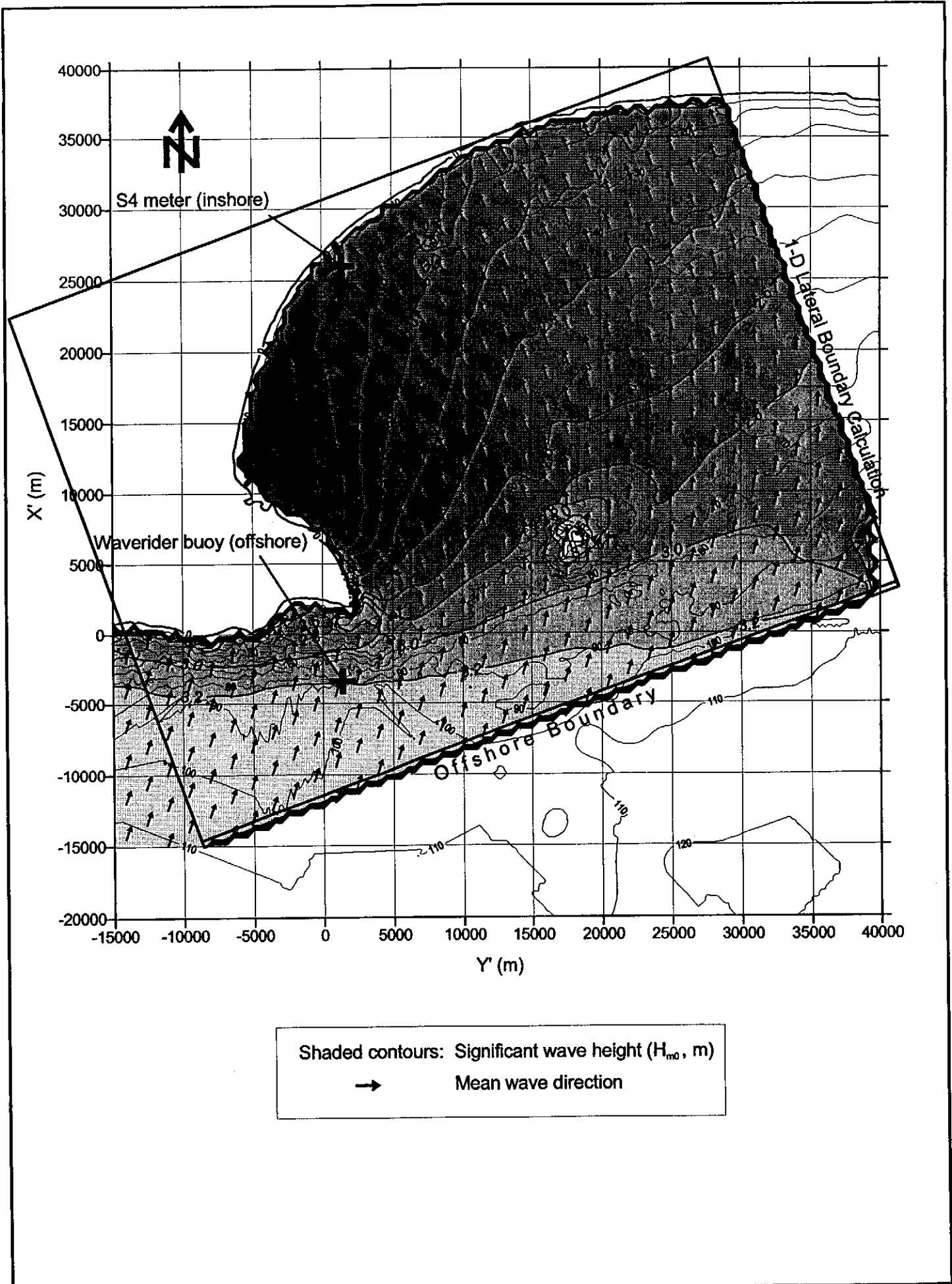
**(b) Mean direction per frequency : observed and calculated values**



ALGOA BAY FIELD CASE: FIRST ESTIMATE  
 Case 2 (ESE): Spectral solution of SWAN simulation  
 at the nearshore (n/s) S4 station

FIGURE  
 6.4

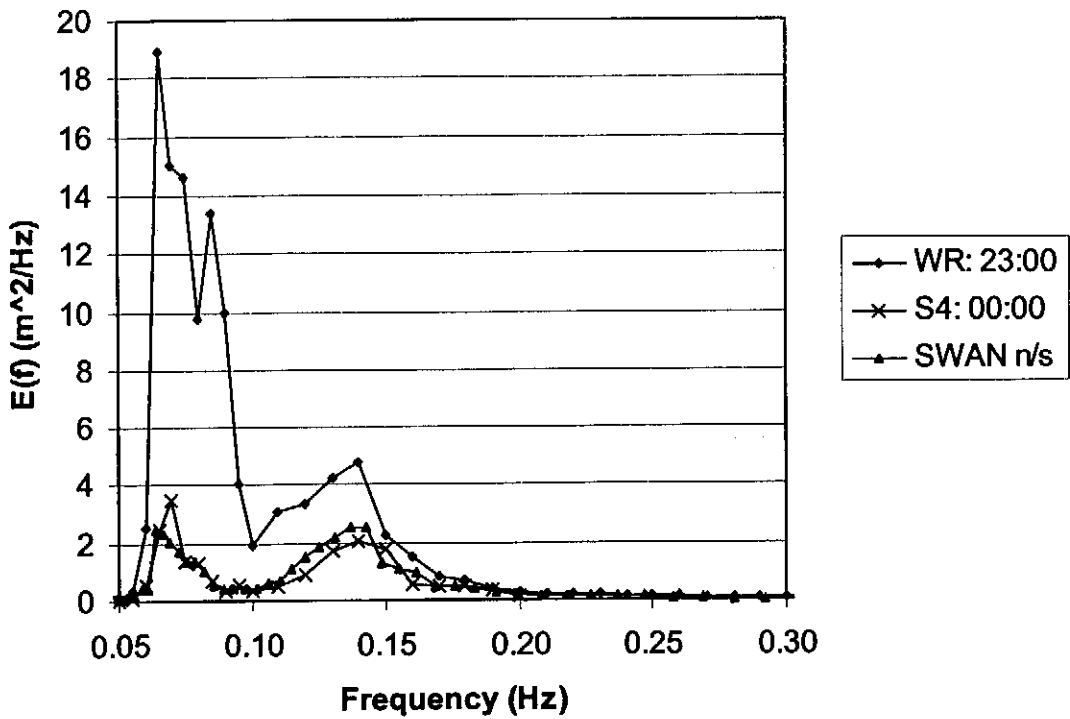




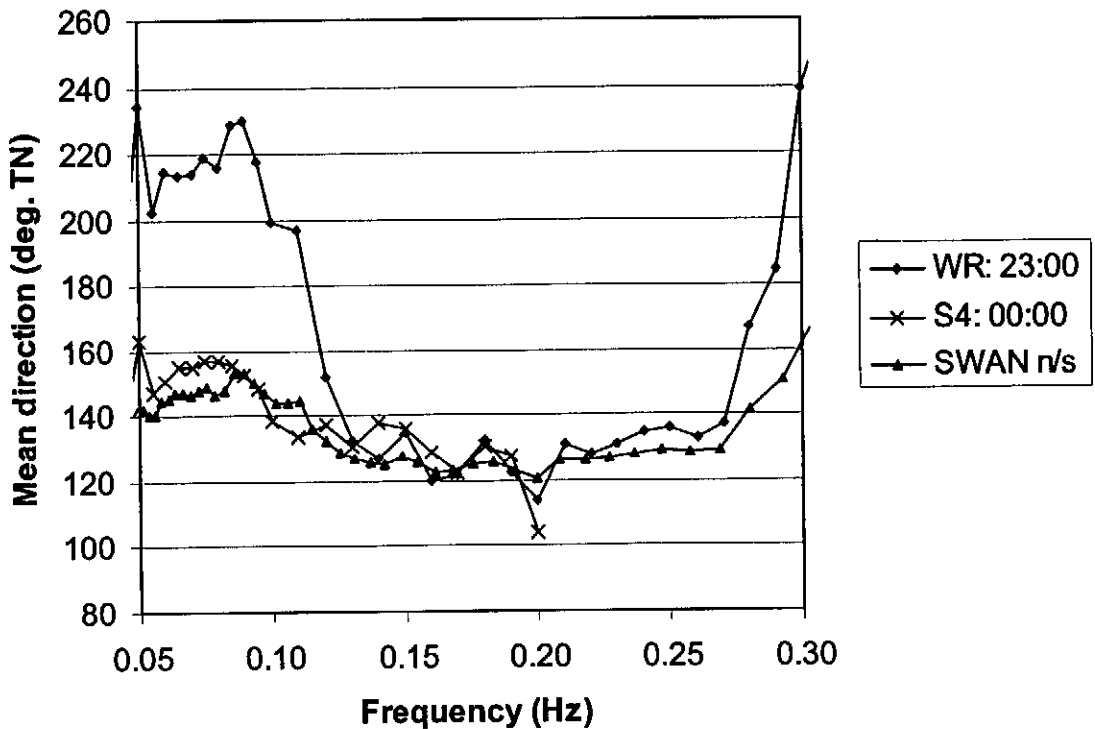
ALGOA BAY FIELD CASE: FIRST ESTIMATE  
 Case 3 (SSW/SE): Spatial solution of significant wave height and mean wave direction

FIGURE  
 6.5

**(a) Energy density spectrum: observed and calculated values**



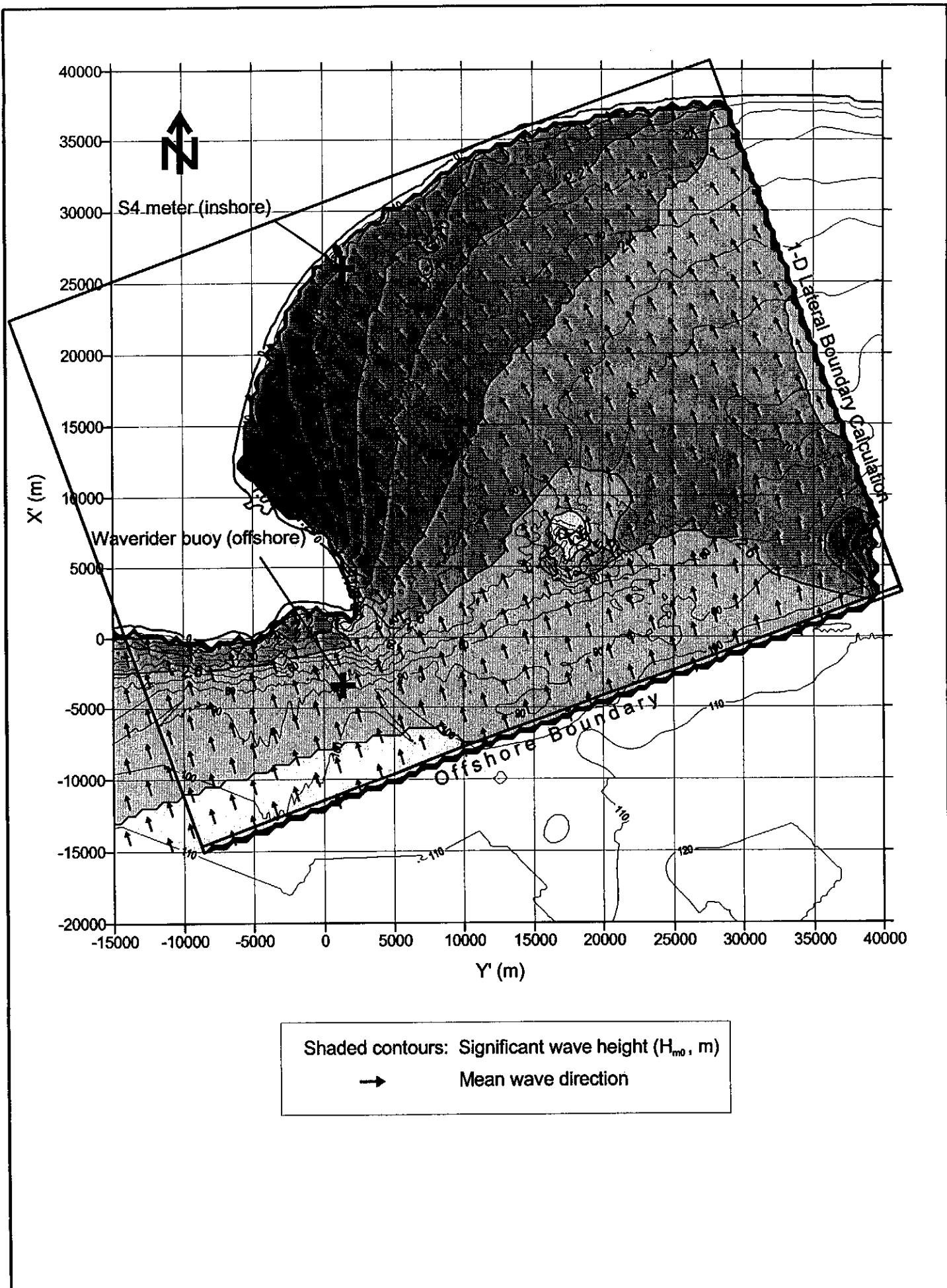
**(b) Mean direction per frequency: observed and measured values**



ALGOA BAY FIELD CASE: FIRST ESTIMATE

Case 3 (SSW/SE): Spectral solution of SWAN simulation  
at the nearshore (n/s) S4 station

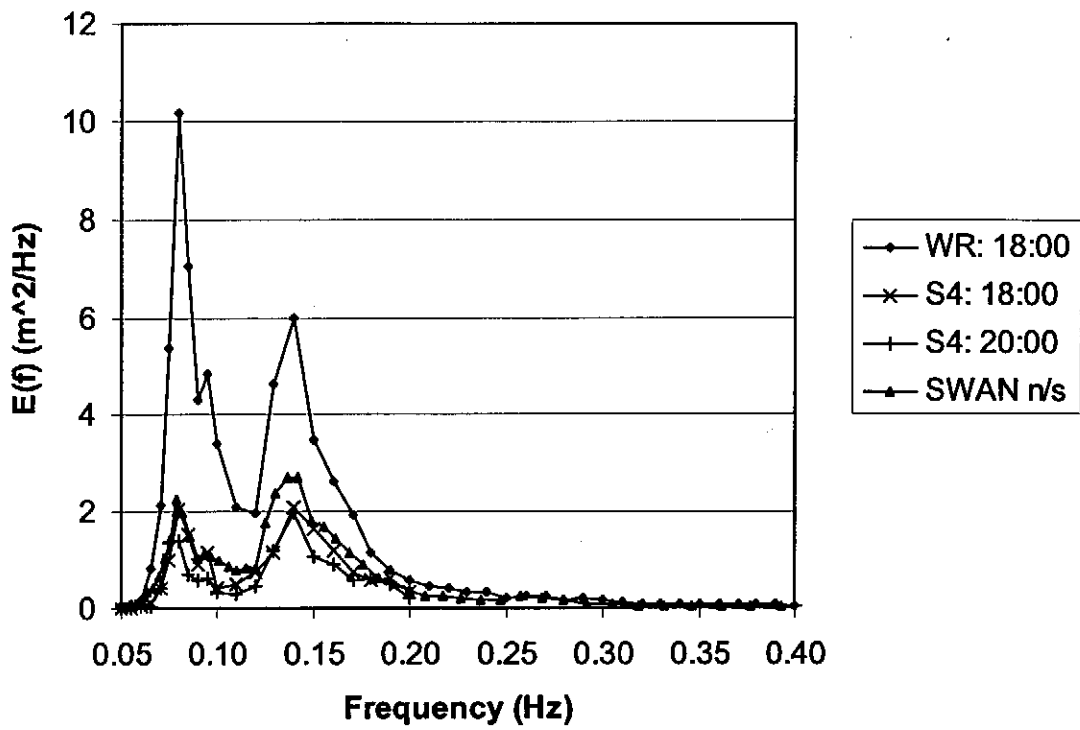
FIGURE  
6.6



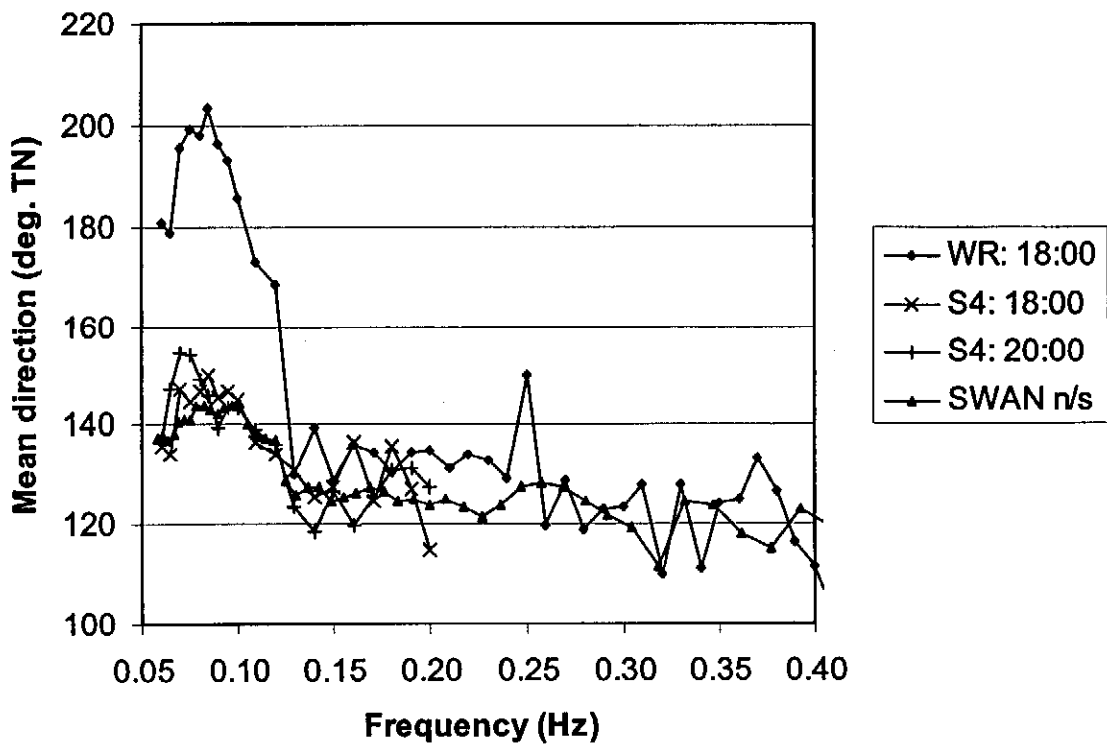
ALGOA BAY FIELD CASE: FIRST ESTIMATE  
Case 4 (SSW/SE): Spatial solution of significant wave height and mean wave direction

FIGURE 6.7

**(a) Energy density spectra: observed and calculated values**



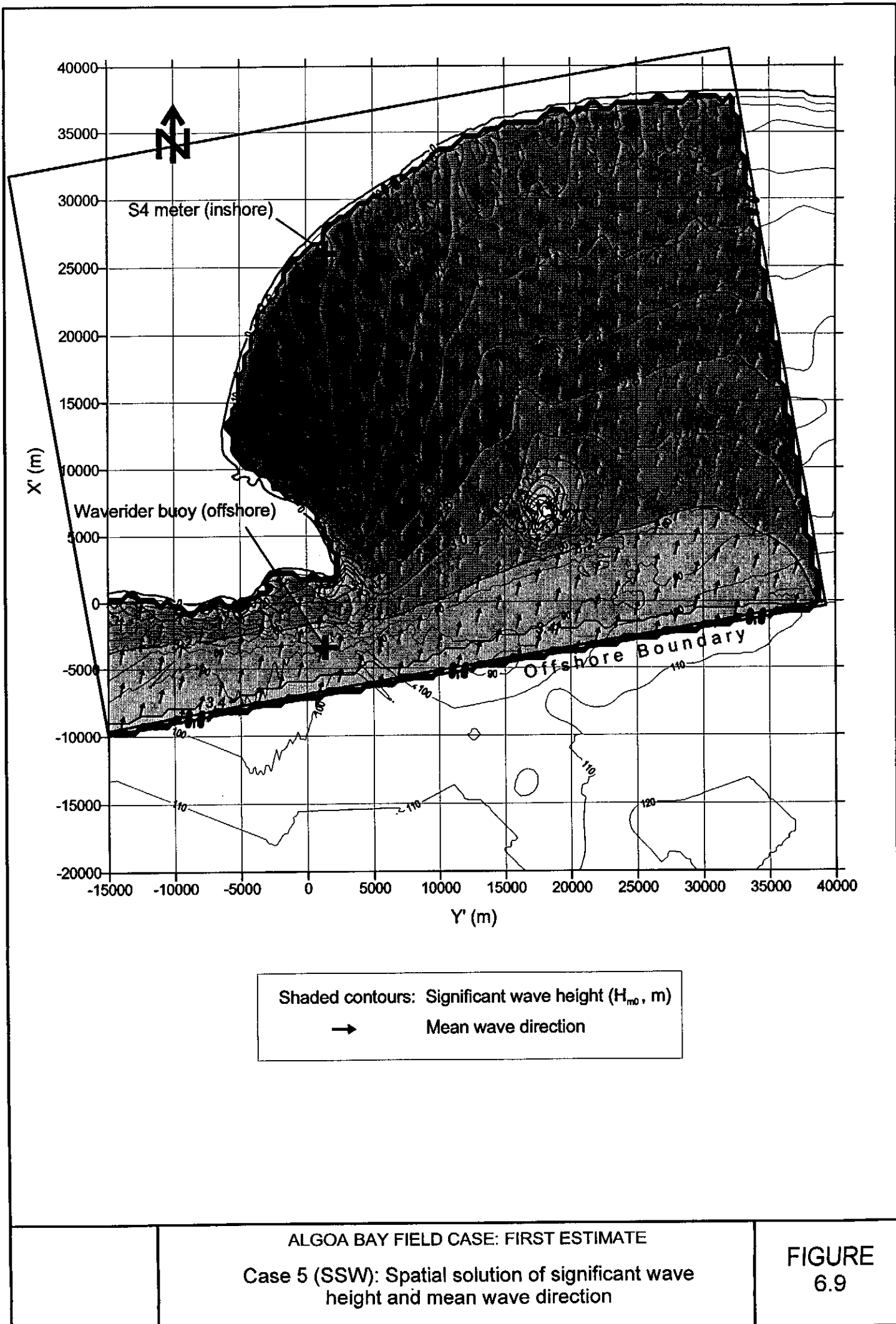
**(b) Mean direction per frequency: observed and calculated values**



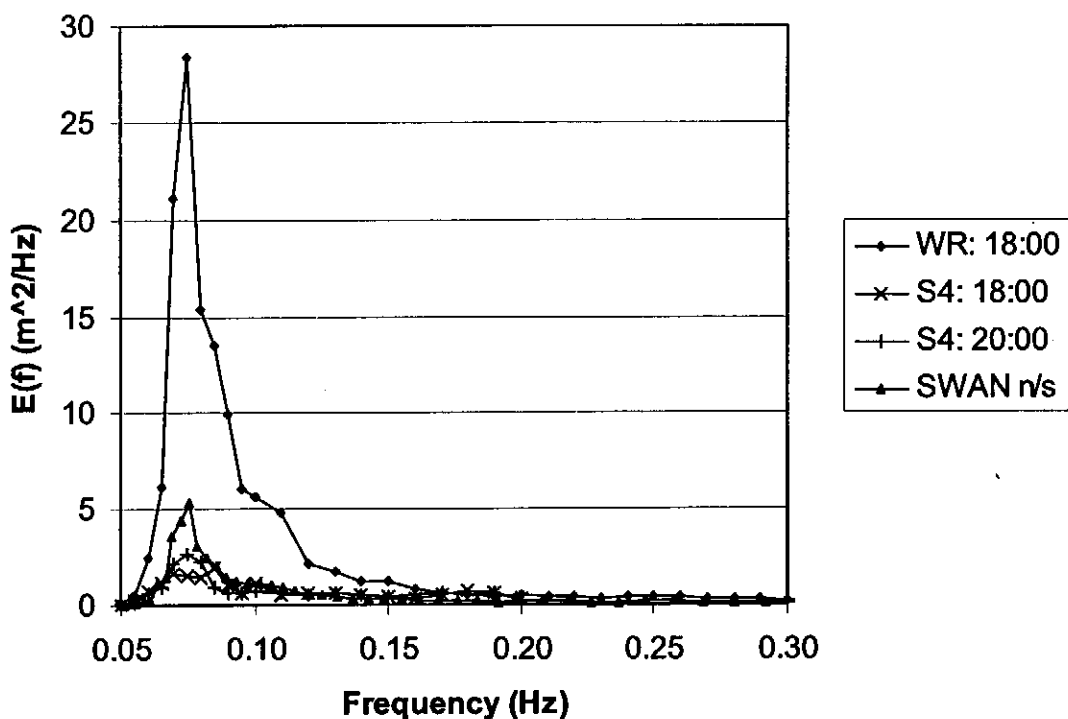
ALGOA BAY FIELD CASE: FIRST ESTIMATE

Case 4 (SSW/SE): Spectral solution of SWAN simulation at the nearshore (n/s) S4 station

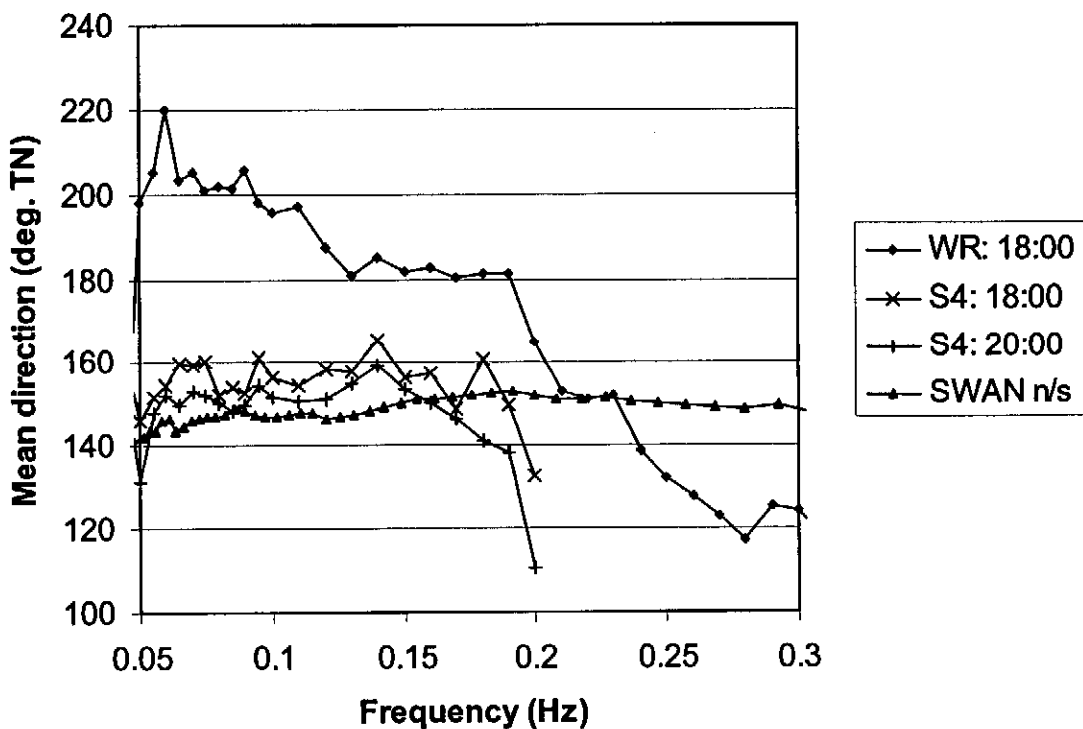
FIGURE 6.8



(a) Energy density spectrum: observed and calculated values



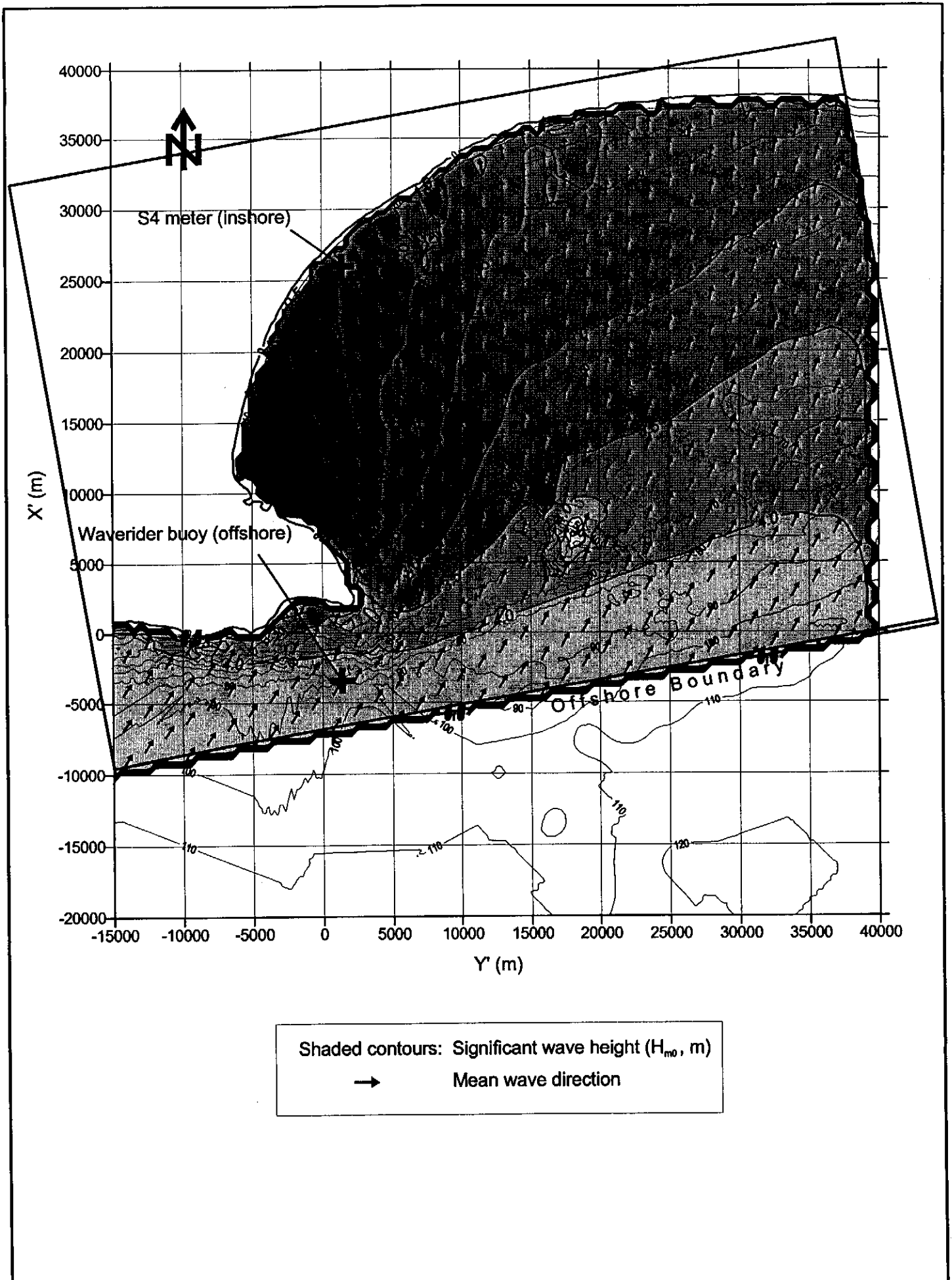
(b) Mean direction per frequency: observed and calculated values



ALGOA BAY FIELD CASE: FIRST ESTIMATE

Case 5 (SSW): Spectral solution of SWAN simulation  
at the nearshore (n/s) S4 station

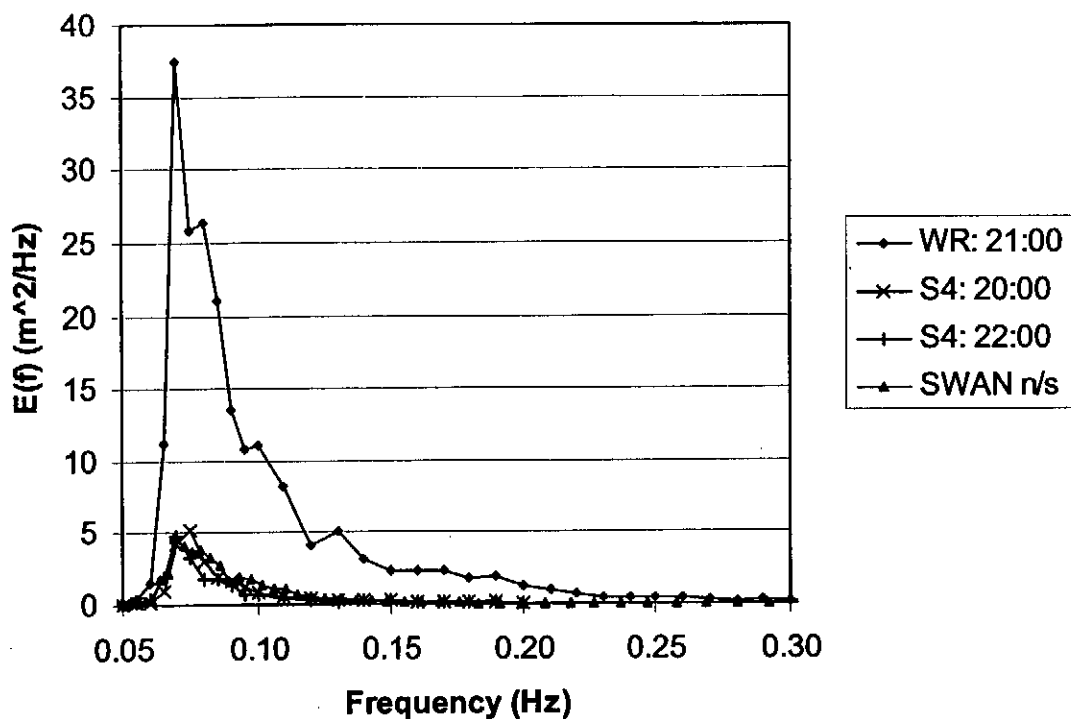
FIGURE  
6.10



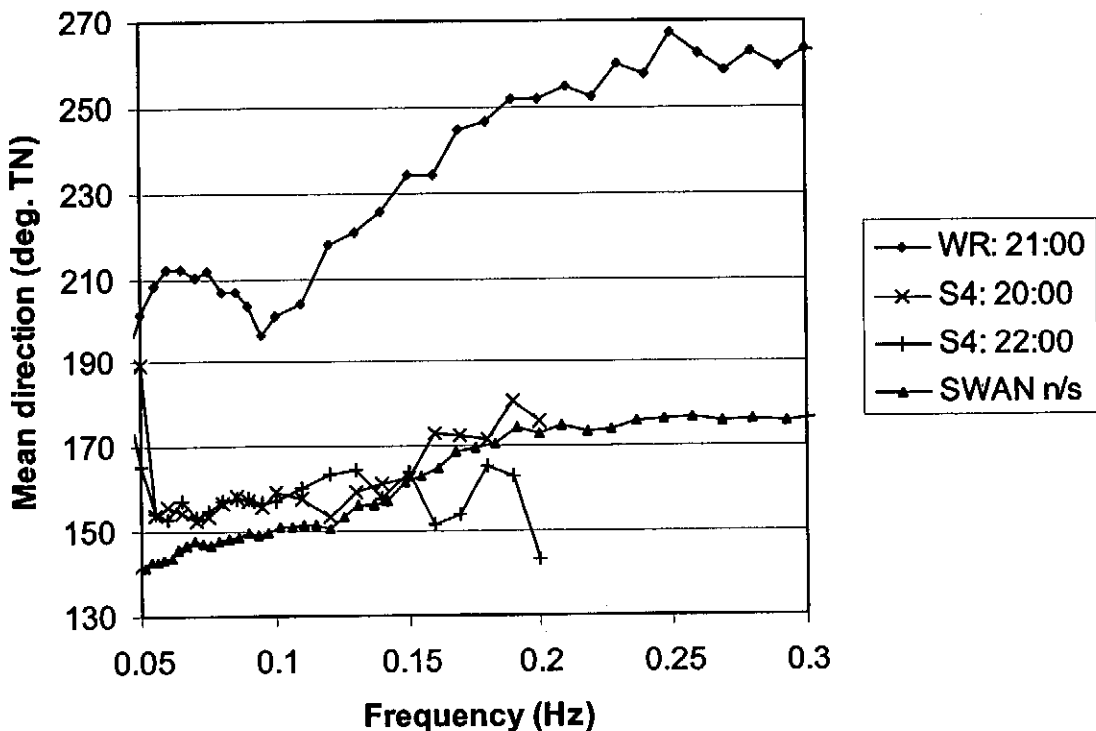
ALGOA BAY FIELD CASE: FIRST ESTIMATE  
 Case 6 (SSW/SW): Spatial solution of significant wave height and mean wave direction

FIGURE  
 6.11

**(a) Energy density spectra: observed and calculated values**



**(b) Mean direction per frequency: observed and calculated values**

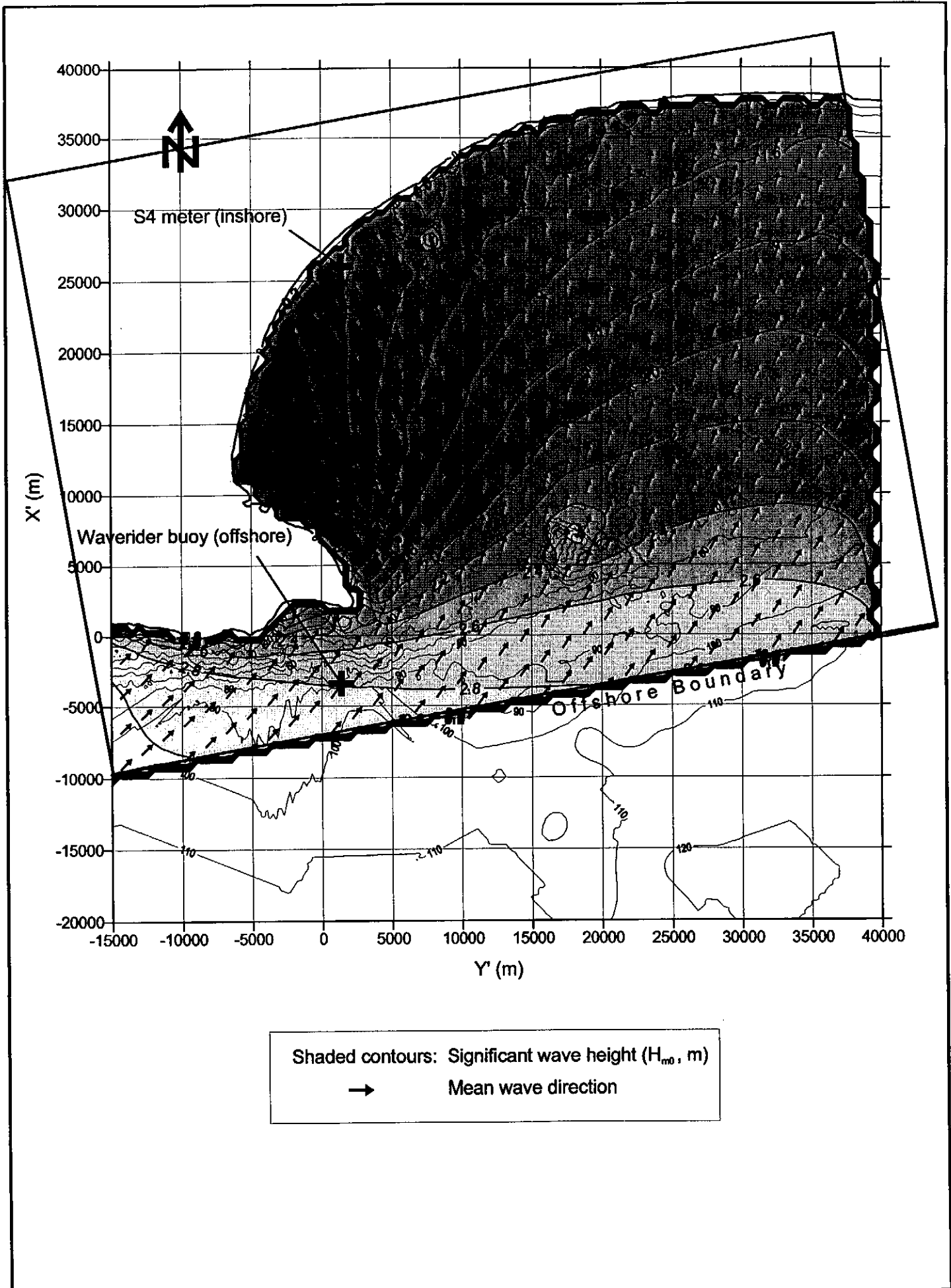


ALGOA BAY FIELD CASE: FIRST ESTIMATE

Case 6 (SSW/SW): Spectral solution of SWAN simulation at the nearshore (n/s) S4 station

FIGURE 6.12

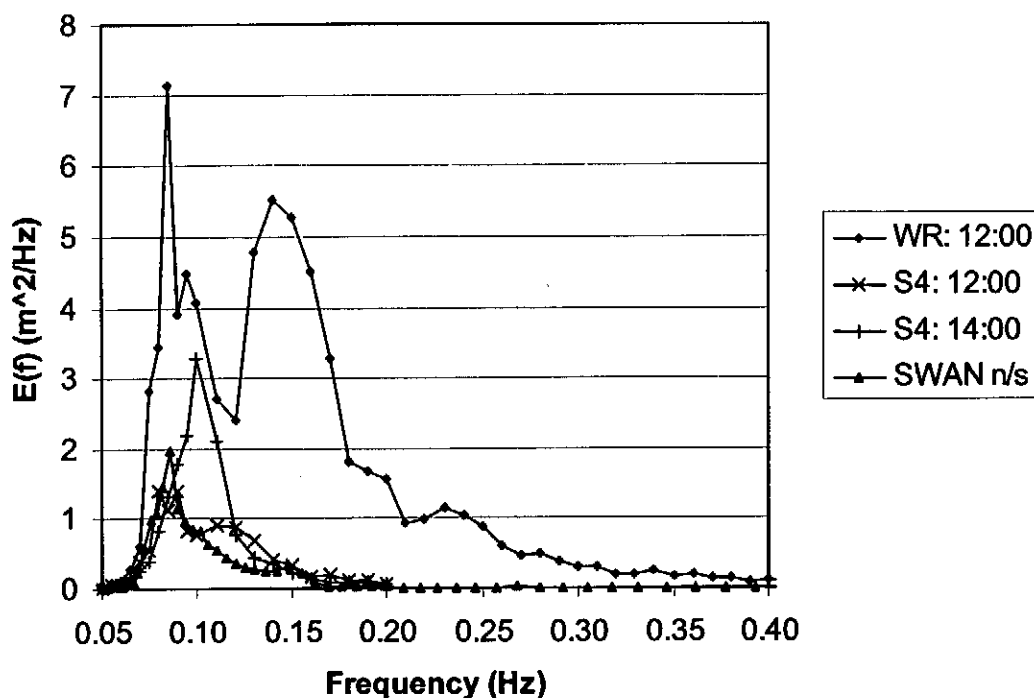




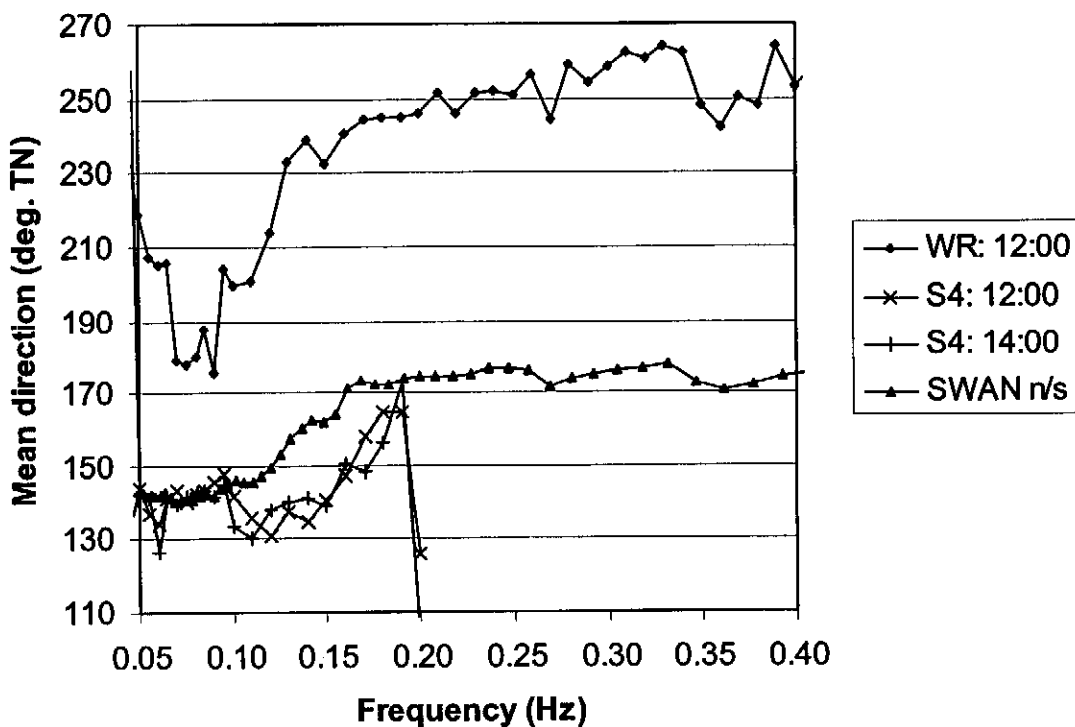
ALGOA BAY FIELD CASE: FIRST ESTIMATE  
 Case 7 (SSW/SW): Spatial solution of significant wave height and mean wave direction

FIGURE  
 6.13

**(a) Energy density spectra: observed and calculated values**



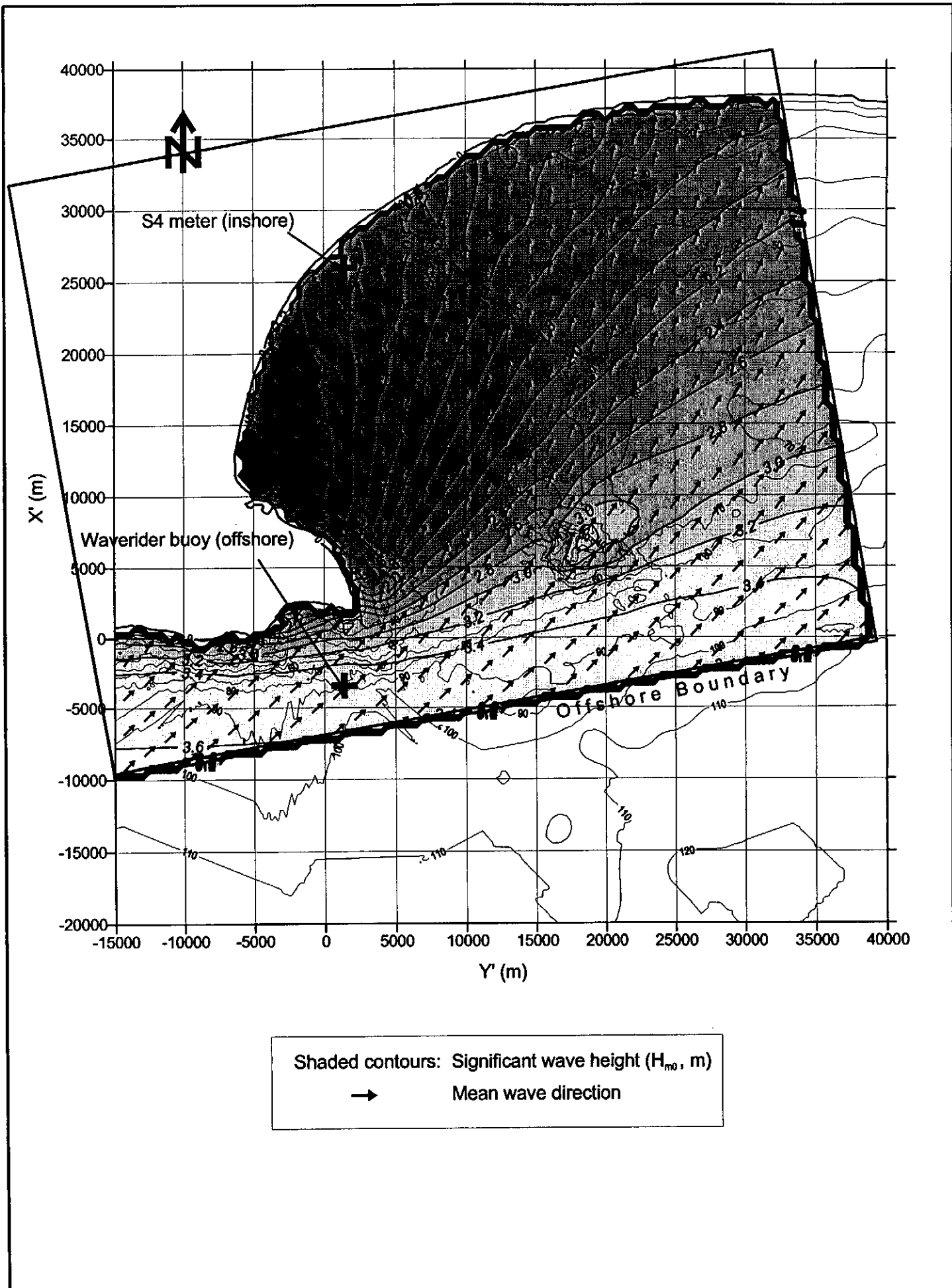
**(b) Mean direction per frequency: observed and calculated values**



ALGOA BAY FIELD CASE: FIRST ESTIMATE

Case 7 (SSW/SW): Spectral solution of SWAN simulation  
at the nearshore (n/s) S4 station

FIGURE  
6.14



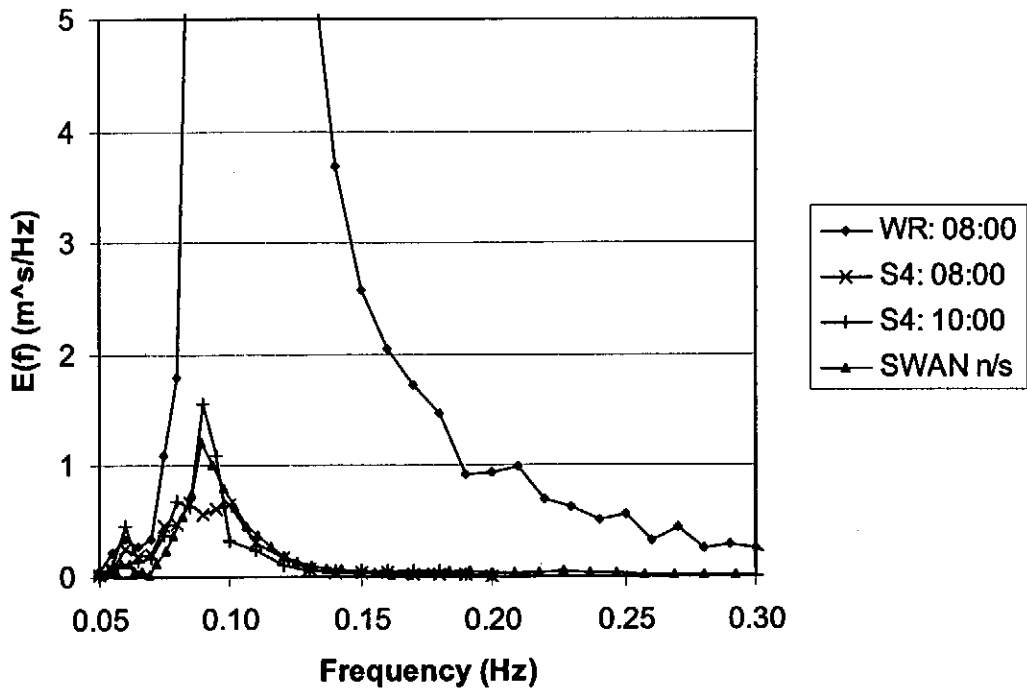
Shaded contours: Significant wave height ( $H_{m0}$ , m)  
 → Mean wave direction

ALGOA BAY FIELD CASE: FIRST ESTIMATE

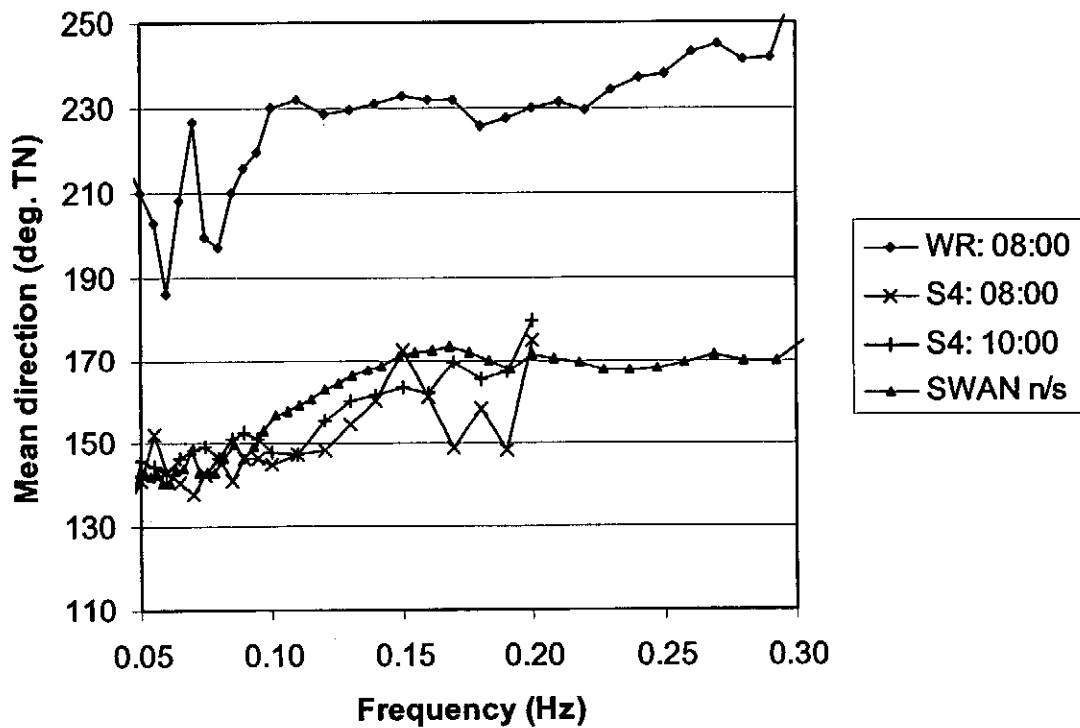
Case 8 (SSW/SW): Spatial solution of significant wave height and mean wave direction

FIGURE 6.15

(a) Energy density spectra: observed and calculated values



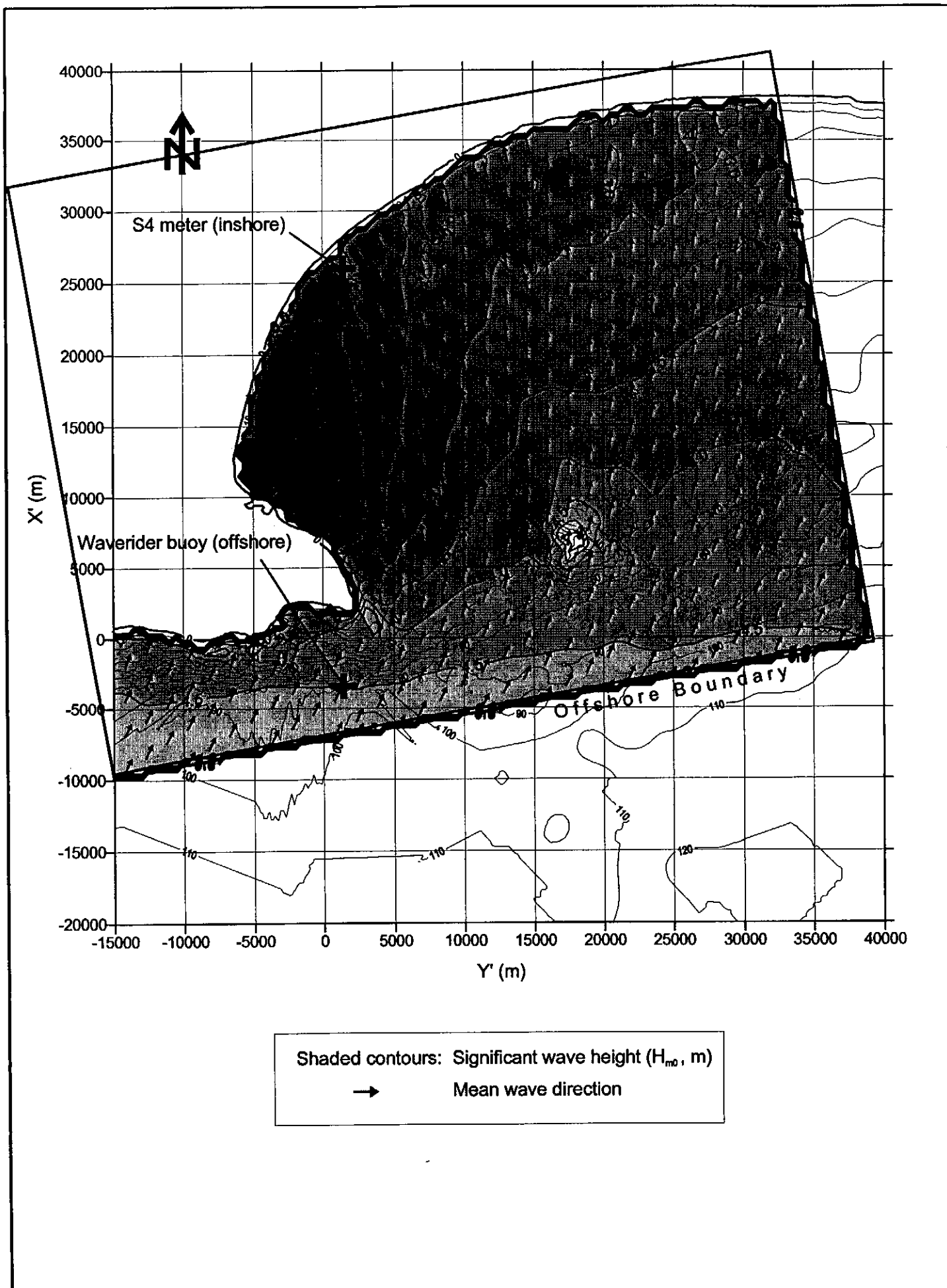
(b) Mean direction per frequency: observed and calculated values



ALGOA BAY FIELD CASE: FIRST ESTIMATE

Case 8 (SSW/SW): Spectral solution of SWAN simulation at the nearshore (n/s) S4 station

FIGURE 6.16

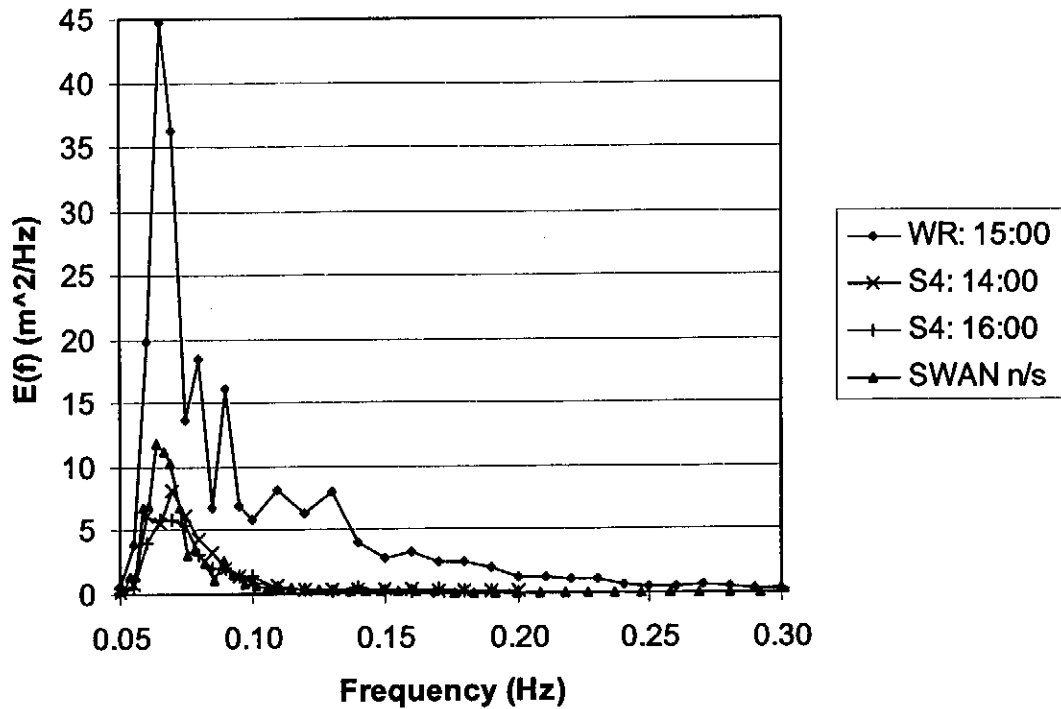


ALGA BAY FIELD CASE: FIRST ESTIMATE

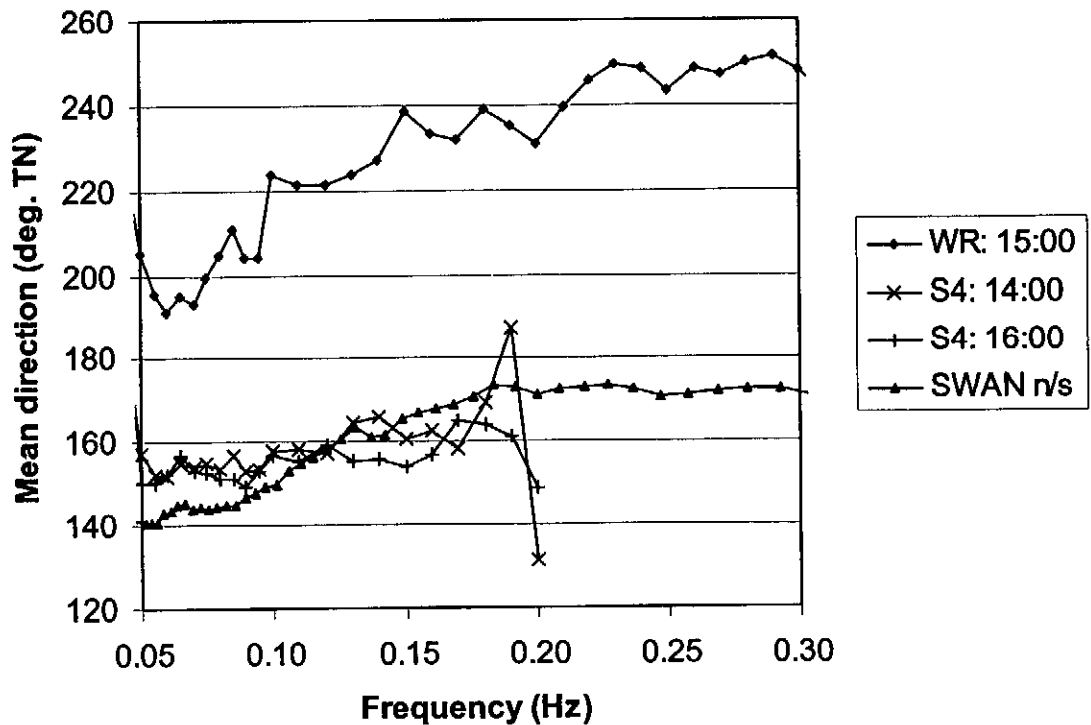
Case 9 (SSW/SW): Spatial solution of significant wave height and mean wave direction

FIGURE  
6.17

(a) Energy density spectra: observed and calculated values



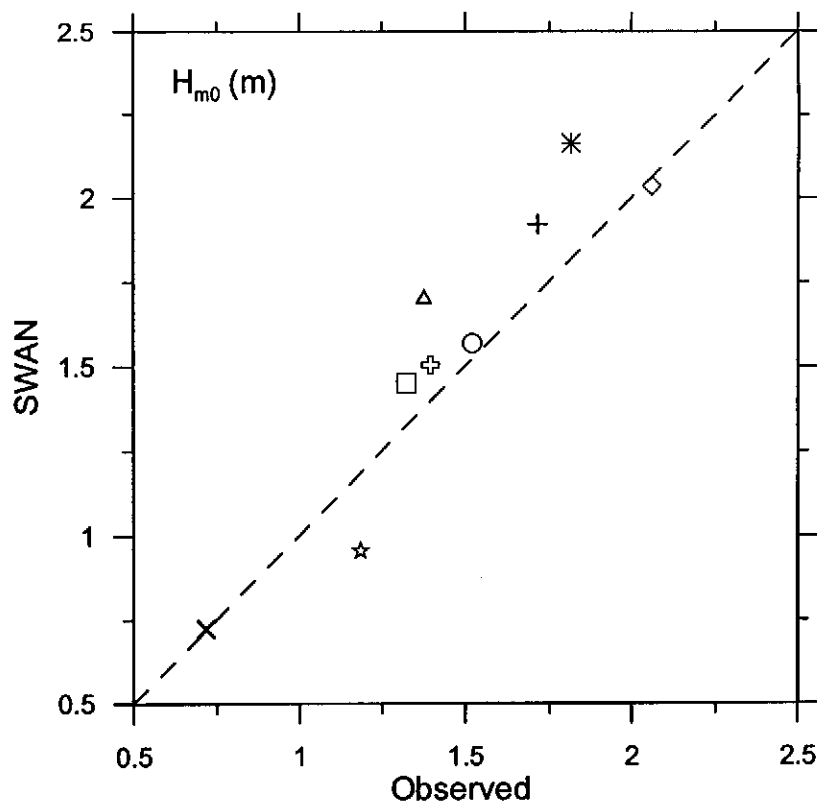
(b) Mean direction per frequency: observed and calculated values



ALGOA BAY FIELD CASE: FIRST ESTIMATE

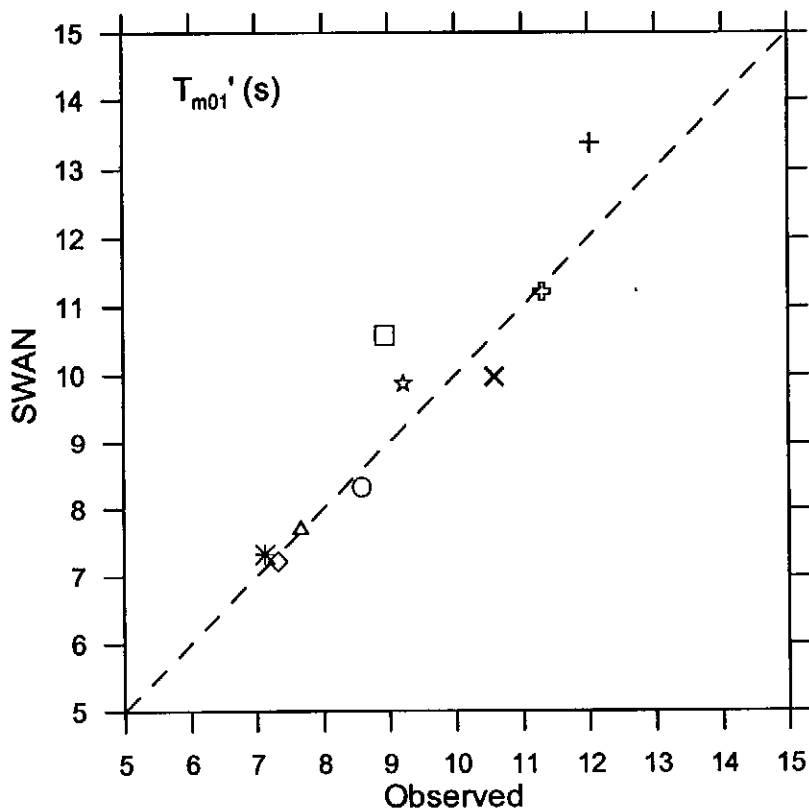
Case 9 (SSW/SW): Spectral solution of SWAN simulation  
at the nearshore (n/s) S4 station

FIGURE  
6.18



Case and offshore wave direction

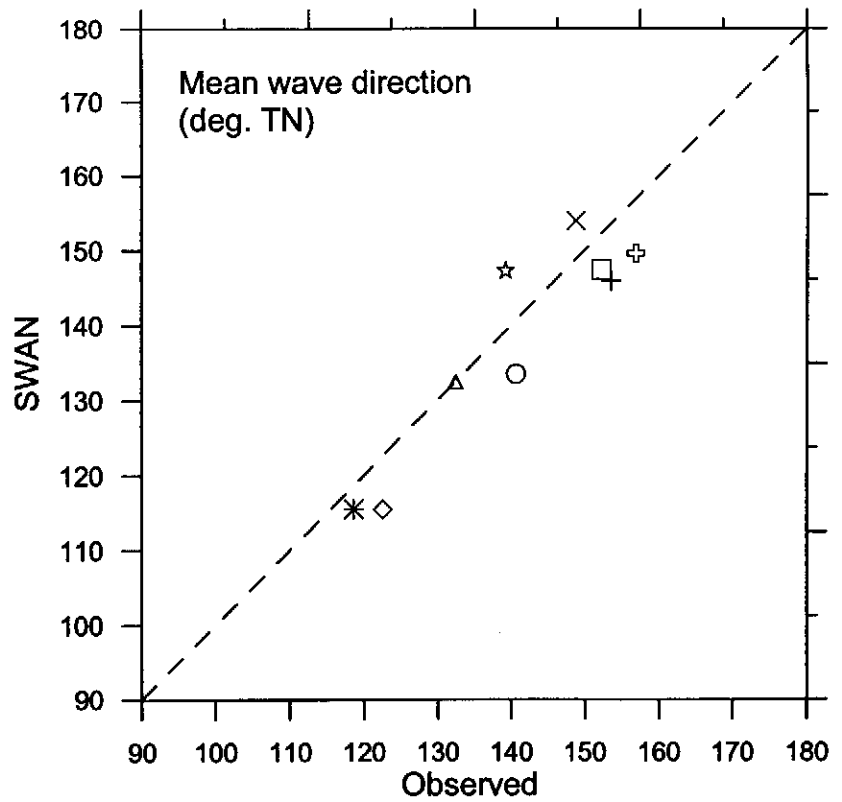
- \* Case 1 (ESE)
- ◇ Case 2 (ESE)
- Case 3 (SSW/SE)
- △ Case 4 (SSW/SE)
- Case 5 (SSW)
- ⊕ Case 6 (SSW/SW)
- ☆ Case 7 (SSW/SW)
- × Case 8 (SSW/SW)
- + Case 9 (SSW/SW)



ALGOA BAY FIELD CASE: FIRST ESTIMATE

Correlation between simulated and observed  
 $H_{m0}$  and  $T_{m01}'$

FIGURE  
6.19(a)



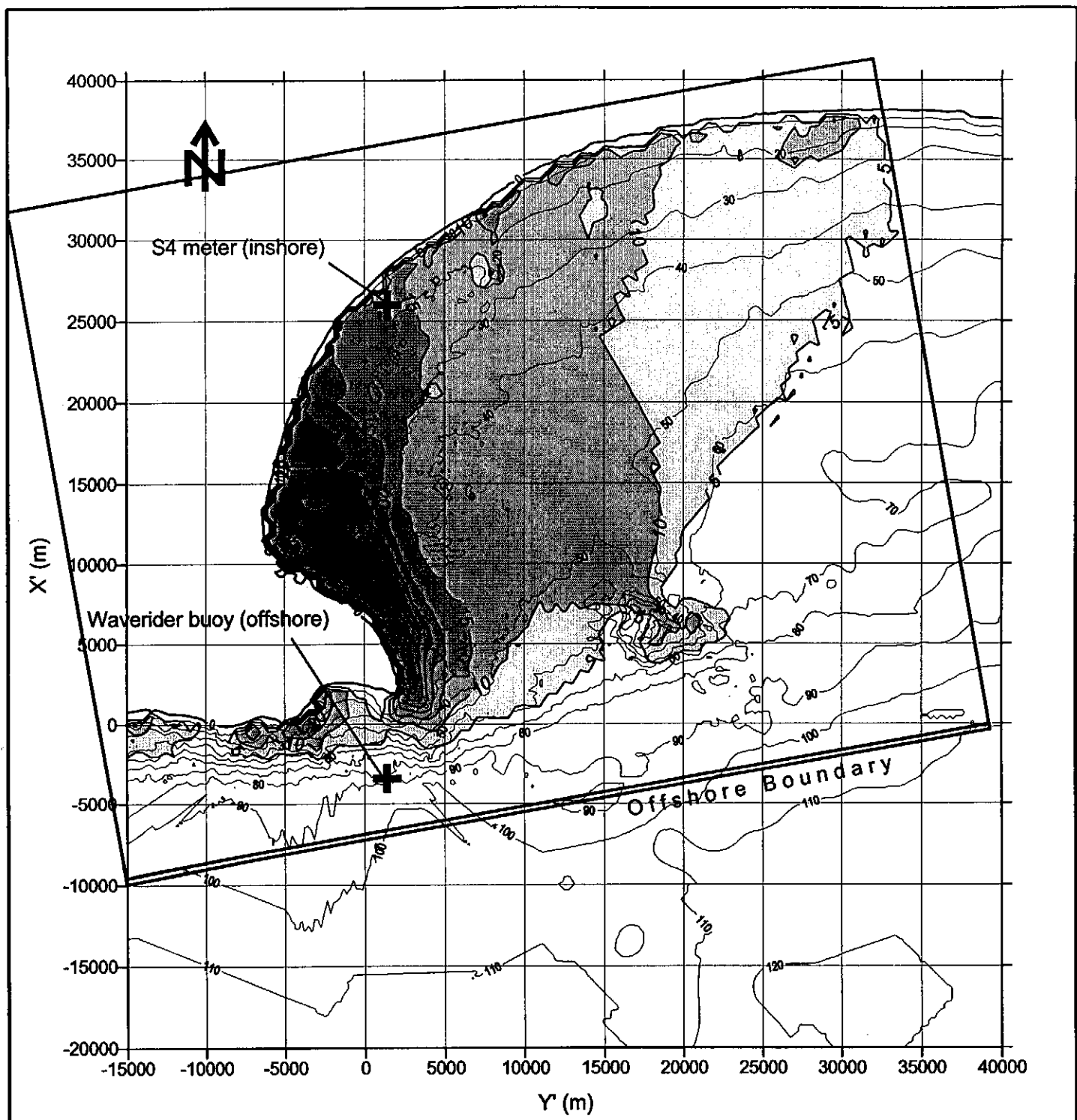
Case and offshore wave direction	
*	Case 1 (ESE)
◇	Case 2 (ESE)
○	Case 3 (SSW/SE)
△	Case 4 (SSW/SE)
□	Case 5 (SSW)
⊕	Case 6 (SSW/SW)
☆	Case 7 (SSW/SW)
×	Case 8 (SSW/SW)
+	Case 9 (SSW/SW)

ALGOA BAY FIELD CASE: FIRST ESTIMATE

Correlation between simulated and observed mean wave direction

FIGURE 6.19(b)



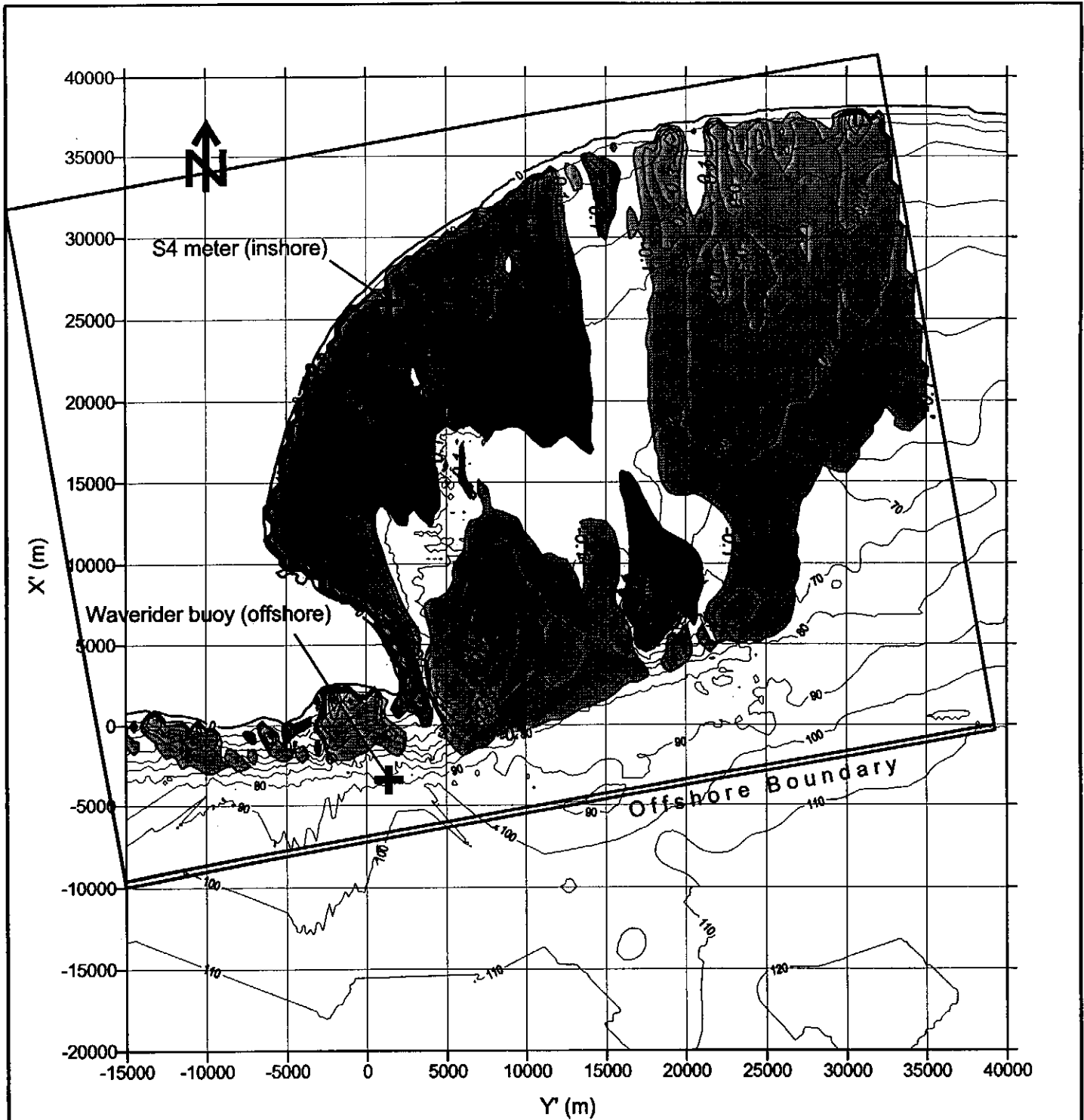


Difference plot: Absolute difference in mean wave direction (degrees) between simulations with and without depth-induced refraction

ALGOA BAY FIELD CASE: SENSITIVITY TESTS

Case 9 (SSW/SW): Absolute change in mean direction due to depth-induced refraction

FIGURE  
7.1



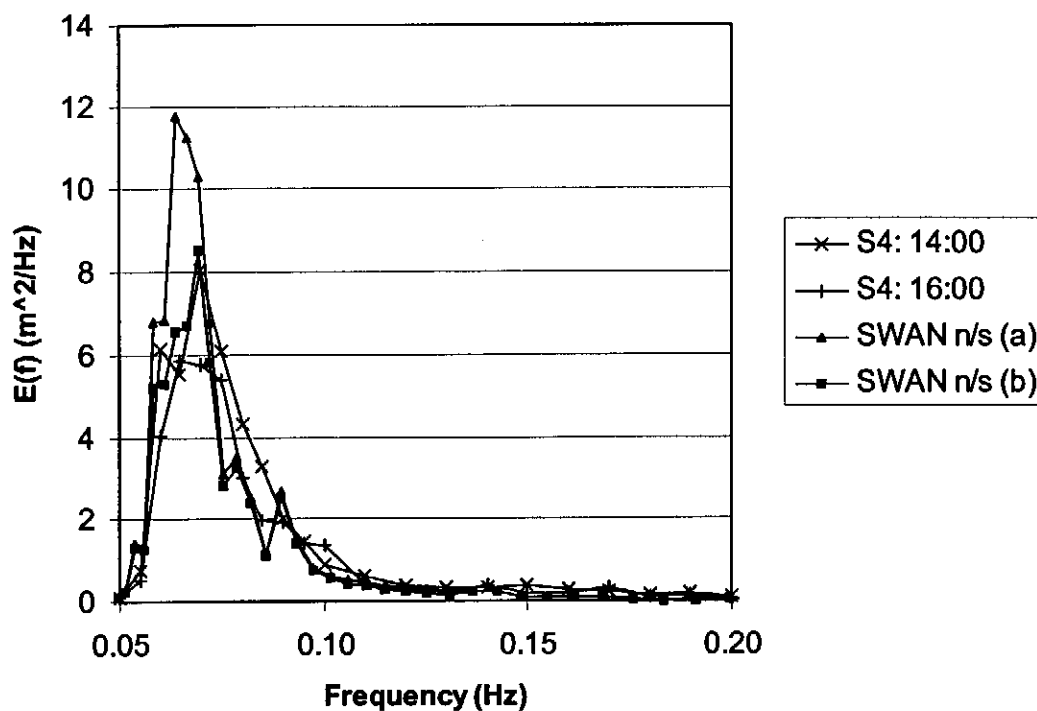
Difference plot: Difference in significant wave height ( $H_{m0}$ , m) between simulations with and without depth-induced refraction

ALGOA BAY FIELD CASE: SENSITIVITY TESTS

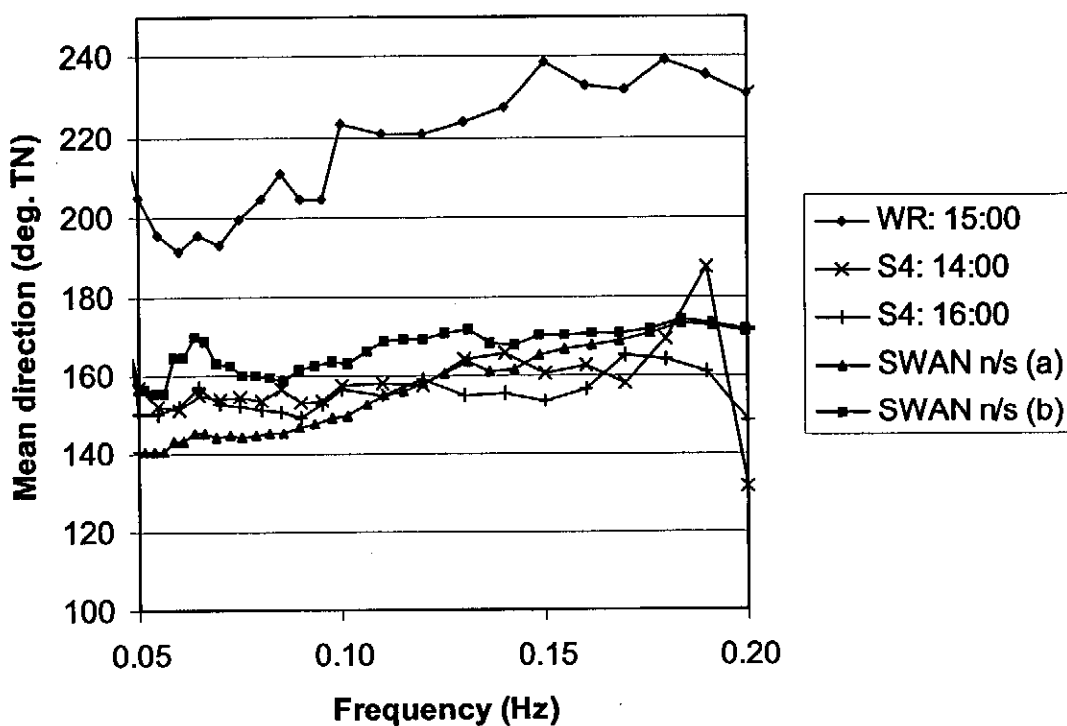
Case 9 (SSW/SW): Change in significant wave height due to depth-induced refraction

FIGURE  
7.2

(a) Energy density spectra: observed and calculated values



(b) Mean direction per frequency: observed and calculated values

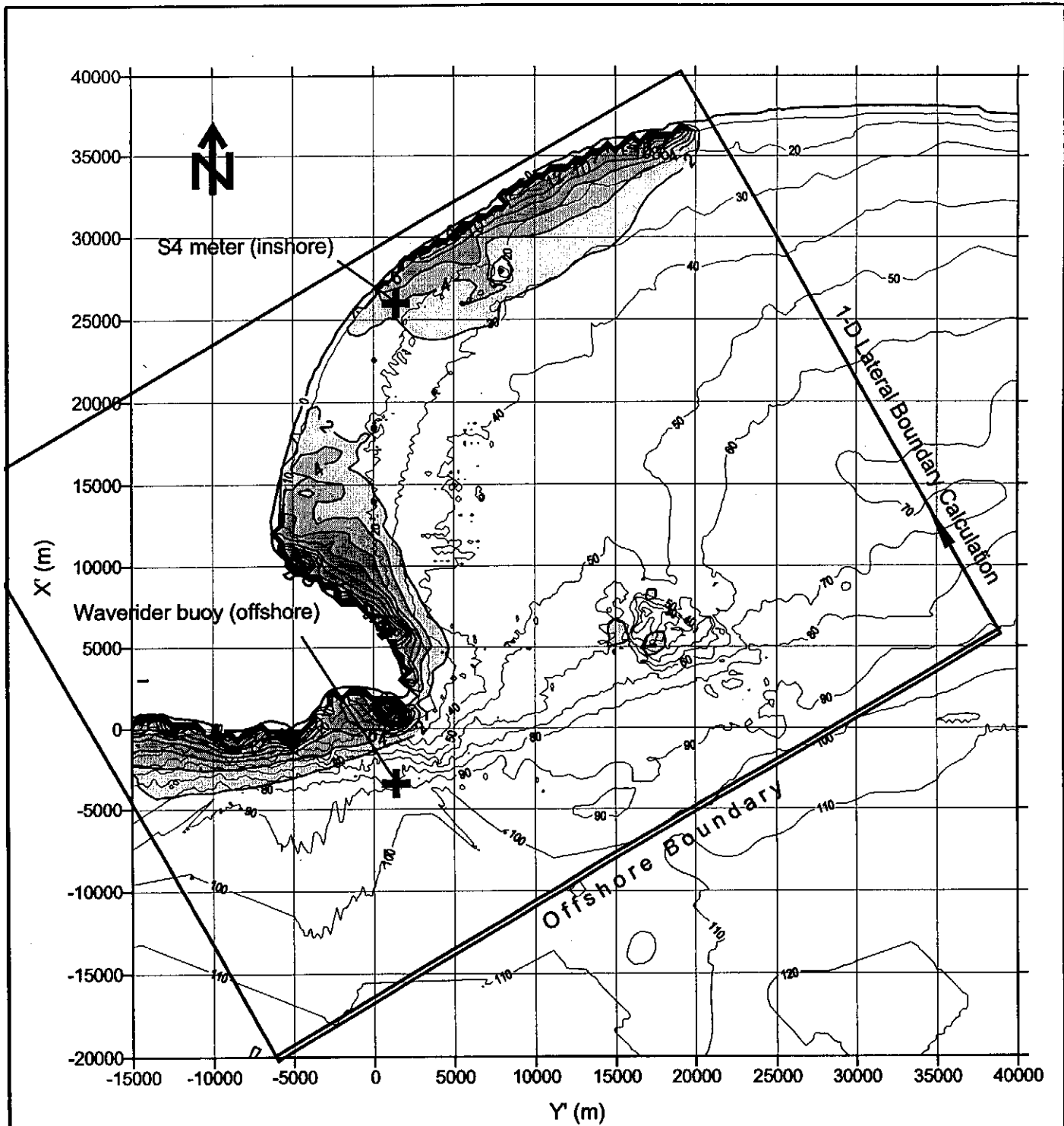


Note: Refer to Table 7.1 for SWAN test conditions

ALGOA BAY FIELD CASE: SENSITIVITY TESTS

Case 9 (SSW/SW): Spectral solution at nearshore S4 station, with and without depth-induced refraction

FIGURE 7.3

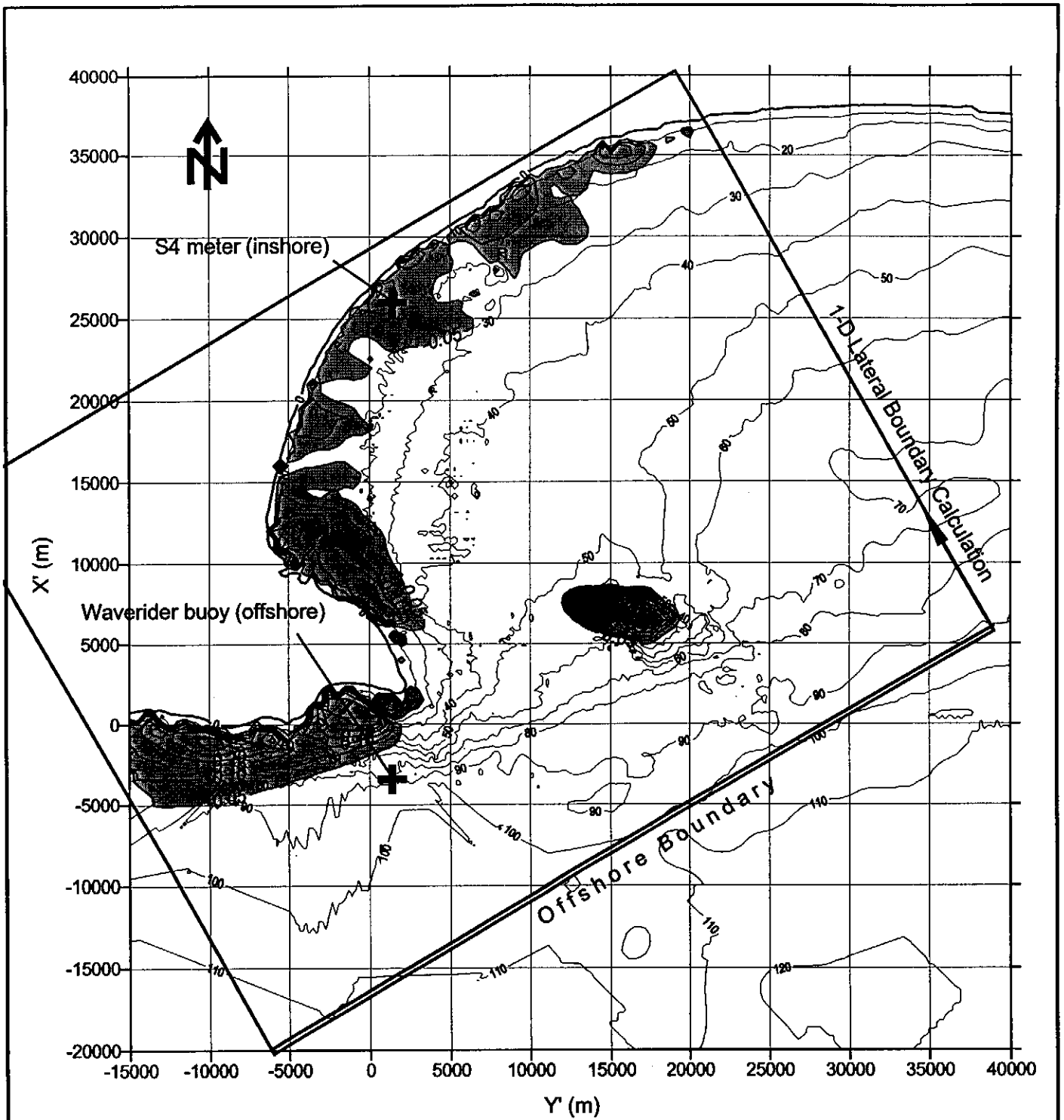


Difference plot: Absolute difference in mean wave direction (degrees) between simulations with and without depth-induced refraction

ALGOA BAY FIELD CASE: SENSITIVITY TESTS

Case 1 (ESE): Absolute change in mean wave direction due to depth-induced refraction

FIGURE  
7.4



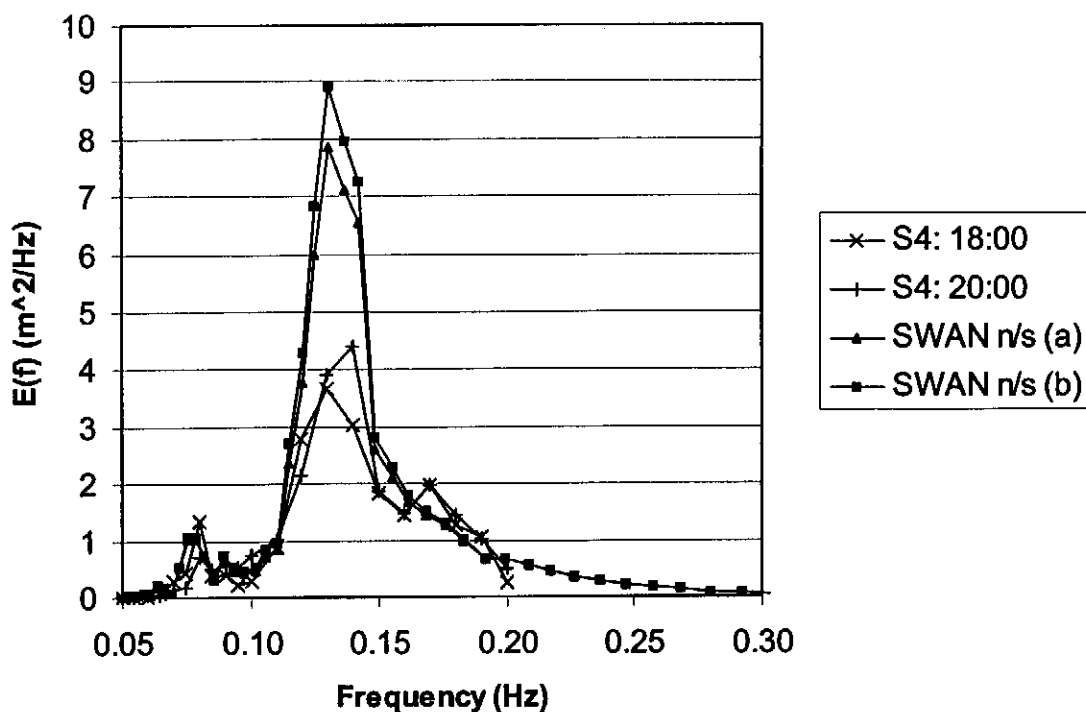
Difference plot: Difference in significant wave height ( $H_{m0}$ , m) between simulations with and without depth-induced refraction

ALGOA BAY FIELD CASE: SENSITIVITY TESTS

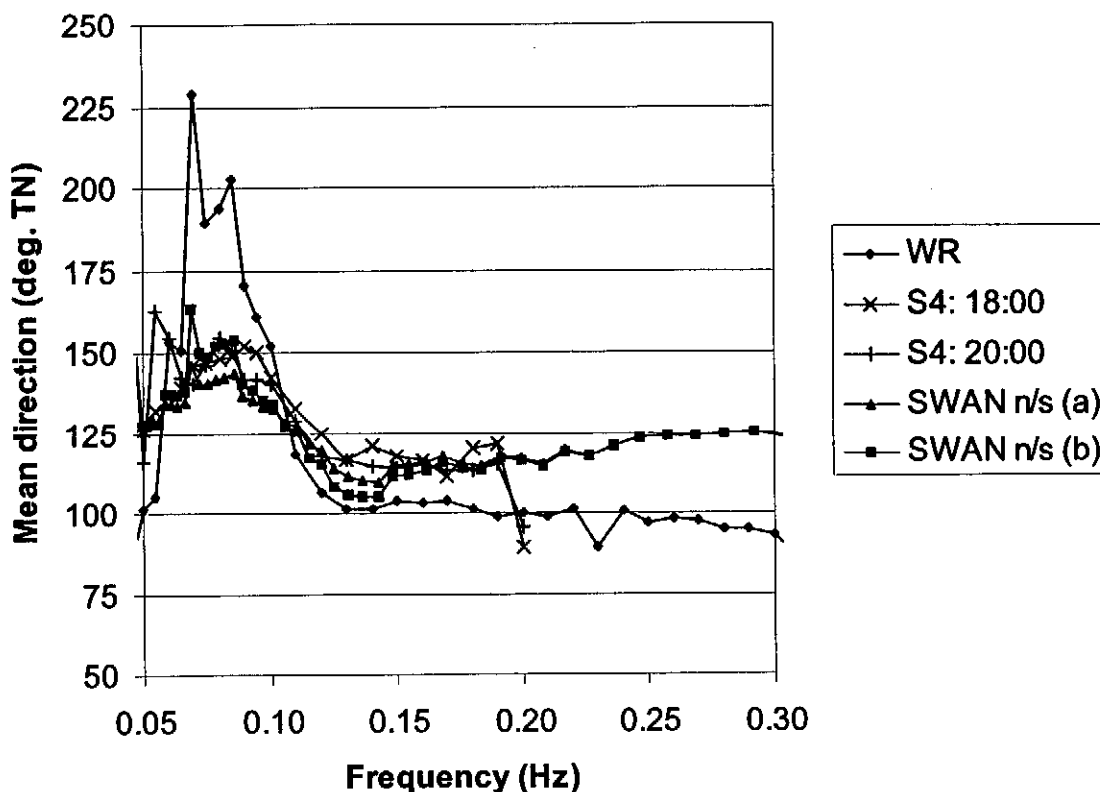
Case 1 (ESE): Change in significant wave height due to depth-induced refraction

FIGURE  
7.5

(a) Energy density spectra: observed and calculated values



(b) Mean direction per frequency: observed and calculated values



Note: Refer to Table 7.1 for SWAN test conditions

ALGOA BAY FIELD CASE: SENSITIVITY TESTS

Case 1 (ESE): Spectral solution at nearshore S4 station, with and without depth-induced refraction

FIGURE 7.6